Electrochemical water oxidation with transition-metal based catalysts: structure-function relations by electrochemistry combined with X-ray absorption spectroscopy and UV-visible spectroscopy

Im Fachbereich Physik der Freien Universität Berlin
eingereichte Dissertation von

Diego González-Flores

For the degree of

Dr. rer. nat.

Berlin, January 2017

Prof. Dr. Holger Dau (Betreuer, Erstgutachter)

Prof. Dr. Peter Strasser (Zweitgutachter)

Datum der Disputation: 17.01.2017

Table of contents

Glossary

ATR-FTIR	Attenuated total reflectance Fourier transform infrared spectroscopy
BESSY	Berliner Elektronenspeicherring-Gesellschaft für Synchrotronstrahlung
CoCat	The cobalt oxide catalyst, deposited in KP_i (0.1 M, pH7)
CV	Cyclic voltammetry or cyclic voltammogram
ε	Molar extinction coefficient
E_0	Energy shift in EXAFS simulations
EDTA	Ethylenediaminetetraacetic acid
EDX	Energy dispersive X-ray spectroscopy
EXAFS	Extended X-ray absorption fine-structure
E_w	Interaction energy
FT	Fourier-transform
FTO	Fluorine doped tin oxide
FEFF	Program used for calculation of phase functions
$\hbar$	the Planck constant divided by 2π
GIXRD	Grazing incidence X-ray diffraction
HZB	Helmholtz-Zentrum Berlin für Materialien und Energie
ITO	Indium tin oxide
ICR	In-coming rate
J	Current density
KP_i	Potassium phosphate buffer pH 7
N	Coordination number
NHE	Normal hydrogen electrode
OCP	Open circuit potential
OCR	Out-coming rate
OCV	Open circuit voltage

OER	Oxygen evolution reaction
Pak	Pakhomovskyite, $Co_3(PO_4)_2 \cdot 8H_2O$
PSII	Photosystem II
ϕ_i	phase shift
q	Charge in general
q_{red}	Charge passed during electrochemical reduction
RHE	Reversible hydrogen electrode
R_f	Fit quality of EXAFS simulations
R_i	Distance between absorbing atom and backscattering atom of element i
σ_i	Debye-Waller parameter in EXAFS simulations
S_0^2	Amplitude reduction factor in EXAFS simulations
SEM	Scanning electron microscopy
TOF	Turnover frequency
TXRF	Total reflection X-ray fluorescence
μ	X-ray absorption coefficient
XANES	X-ray absorption near-edge structure
XAS	X-ray absorption spectroscopy
XRD	X-ray diffraction
χ(E)	EXAFS fine-structure function

Chapter 1

Introduction

1.1 Hydrogen as a fuel

The global economic growth during the last century was sustained in great part by easily accessible fossil fuel reservoirs. Optimistic calculations, which include the most environmentally harmful sources of fuel, estimate that there are enough supplies to last throughout at least the next two centuries (Khatib, Barnes et al. 2000). However, inarguable scientific proofs have shown that the burning of fossil fuels has resulted in the accumulation of CO_2 in the atmosphere at levels never observed before in the past 650 000 years (now exceeding 400 ppm) (Siegenthaler, Stocker et al. 2005). According to this study, there also exists a direct correlation between the increase in CO_2 concentration in the atmosphere and the entire planets rising temperature, this process has become known as global warming. There are predictions that the unchanged continuation of a fossil fuel based economy will ultimately lead not only to the complete exhaustion of resources, but also to an accumulation of CO_2 at levels over 550 ppm, which might result in catastrophic consequences for the environment and life on the planet (Watson 2001). For this reason, one of the greatest challenges of our century is to find a way of matching the global economies ever growing energy needs, while at the same time mitigating and stopping the accumulation of CO_2 in the atmosphere (Hoffert, Caldeira et al. 1998).

Satisfying these energy needs requires not only the development of renewable energy sources, but also the development of carriers and new fuels to store clean energy. These new energy carriers will have to be used on a global scale, while at the same time being carbon neutral (Petit, Jouzel et al. 1999, Siegenthaler, Stocker et al. 2005). Some of the most promising alternatives for large scale energy storage, for instance batteries, regularly use non environmental friendly materials. At the same time these materials have limited capacity which results in a low storage energy densitiy, with little room for improvement. Hydrogen (H_2) on the other hand has energy densities of around 142 MJ/kg, which is about two orders of magnitude higher than most batteries and at least three times higher than most fossil fuels, with the added advantage of producing water as a combustion product when burned (Turner 1999). Additionally, hydrogen can not only be burned, but it also can be used very efficiently within a fuel cell to produce electricity. There is also a possibility to use hydrogen

to reduce CO_2 and form small molecules – a process that facilitates the transport and storage of energy (Nocera 2009).

Since hydrogen element can be found in high abundance in the form of water, producing hydrogen gas through electrolysis appears to be one of the most logical methods for renewable energy production and storage (Lewis and Nocera 2006, Faunce, Lubitz et al. 2013). Currently, at a global scale most of the produced hydrogen is extracted from fossil fuels. Using water electrolysis for hydrogen production is comparatively more expensive. As a result of these differing production costs, only 4 % of the global hydrogen production is done by water electrolysis (Dunn 2002, Zeng and Zhang 2010). Making the technology for H_2 production competitive at a global scale means not only overcoming economical and political challenges, but also challenges at the scientific level. From the chemical point of view, the overall reaction of hydrogen production from water (water splitting) is composed of two semi-reactions: water oxidation (equation 1.1) and water reduction (equation 1.2). The water oxidation reaction requires the removal of 4 electrons from 2 water molecules coupled with the release of 4 protons and one dioxygen molecule. The complexity of this reaction leads to extremely slow kinetics, rendering the reaction of water oxidation the bottleneck of the overall reaction (equation 1.3). Usually, higher potentials than the thermodynamic value of the process of water oxidation (known as overpotentials) are required to increase the oxygen production rate, resulting in a noticeable loss of energy. Efficient water oxidation requires the development of water oxidation catalysts that lower the activation energy barrier and make the kinetics faster at low overpotential values, thus increasing oxygen production while minimizing entropic losses.

$$O_{2(g)} + 4H^+ + 4e^- \rightarrow 2H_2O_{(l)} \quad (1.1) \quad E_{anodic} = 1.23V - 0.059(pH)V \text{ vs NHE}$$

$$4H^+ + 4e^- \rightarrow 2H_{2(g)} \quad (1.2) \quad E_{cathodic} = 0\,V - 0.059(pH)V \text{ vs NHE}$$

$$2H_2O_{(l)} \rightarrow 2H_{2(g)} + O_{2(g)} \quad (1.3) \quad E_{rxn} = -1.23V$$

Since the recombination of hydrogen with oxygen results in water as a main product, burning of hydrogen is ideal method of clean and carbon neutral energy storage to combine with many different renewable energy systems. An example of this, is the coupling of water electrolysis with photovoltaic systems. Already some of these systems can be produced, but they work with relatively low efficiencies (Yilanci, Dincer et al. 2009, Pinaud, Benck et al. 2013). Making this technology commercially viable will require a lot of improvements. Since photosynthesis is the best functioning model known which uses water oxidation and converts solar energy into chemical energy, it constitutes the optimal source of inspiration to overcome current limitations (Dau and

Zaharieva 2009). For this reason, we will briefly explain the most important details of the process of photosynthesis.

1.2 Inspiration in nature: biological catalysis for water oxidation

Plants, algae and cyanobacteria convert solar energy into chemical energy based on a light driven extraction of four electrons from water and the release of dioxygen and protons (Barber 2009). For this process, they have developed a multi-molecular complex, consisting of different proteins and lipids with a mass of about 700 kDa, known as photosystem II (PSII). Photosystem II is a transmembrane protein complex, which in plants is located in the inner chloroplast membrane, called tylakoid membrane (Figure 1.1). The machinery in charge of the electron transfer and water splitting is located inside the D1 and D2 protein subunits. The process of water oxidation occurs in the so-called donor side. The light absorption and charge separation begins in the pigment array named P680. Through the absorption of light P680 transfer electrons to what is called the acceptor side (a very complex arrangement of molecules which take care of the electron transfer). Once P680 is oxidized, it get reduced by a nearby tyrosine (Y_z) which oxidizes a Mn atom in the Mn_4CaO_5 cluster (Shen 2015).

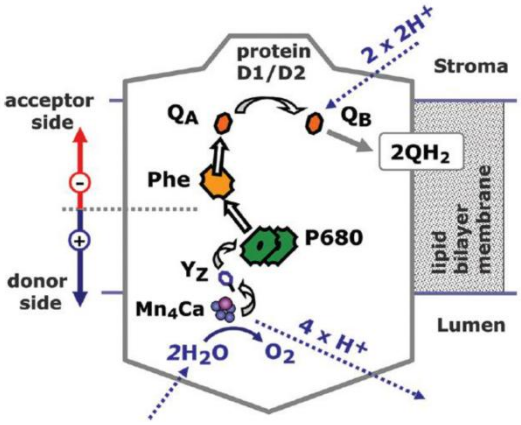

Figure 1.1. Scheme of the D1/D2 protein subunits of photosystem II. In the case of plants, it is located in a lipid bilayer at the inner chloroplast membrane (tylakoid membrane). This lipid bilayer separates the aquous phases at the acceptor side (Stroma) and at the donor side (Lumen). A simplified illustration of the redox factors inside these subunits is also shown. The charge separation is started in P680. The electrons are transferred to the acceptor side (composed in this case by Phe, Q_A and Q_B). At the donor side, P680 is reduced by a tyrosine (Y_z) that oxidizes a Mn atom in the Mn_4Ca cluster. Image taken from (Dau and Zaharieva 2009).

The process of water oxidation occurs in this μ-oxo bridged tetrametric complex (Figure 1.2.A), which contains 4 manganese and 1 calcium ions connected by oxide or hydroxide bridges and constitutes the catalytic centre of PSII (Dau, Grundmeier et al. 2008, Umena, Kawakami et al. 2011, Suga, Akita et al. 2015). Three manganese ions (Mn_1, Mn_2 and Mn_3) together with one Ca form a distorted cubane type of structure where the fourth manganese (Mn_4) resides in a dangling position. This cluster is bound to the protein structure through the coordination to seven amino acids. The cuboidal structure of the PSII complex was first identified in 2004 from a 3.5 Å resolution crystal structure (Ferreira, Iverson et al. 2004). The most accurate structure, with a resolution of 1.95 Å was obtained in 2015 using femtosecond X-ray pulses, and made it finally possible to locate more unambiguously the position of the atoms and bonds (Suga, Akita et al. 2015). Before the water oxidation process takes place, four electrons are removed from the cluster one by one (Haumann, Müller et al. 2005, Zaharieva, Chernev et al. 2016). The oxidation process is also associated with proton removal. Every turnover, the system goes through four main states known as S states of the Kok cycle (Figure 1.2.B) (Kok, Forbush et al. 1970). The S_0 state is the most reduced one, containing three Mn^{III} ions and one Mn^{IV}, and the oxidizing equivalents are accumulated one by one until all Mn atoms are in a +4 oxidation state (S_3 state) (Haumann, Müller et al. 2005). Once the oxidizing equivalents has been accumulated, two water molecules are split into four protons and one oxygen molecule during the transition from S_3-(S_4)-S_0.

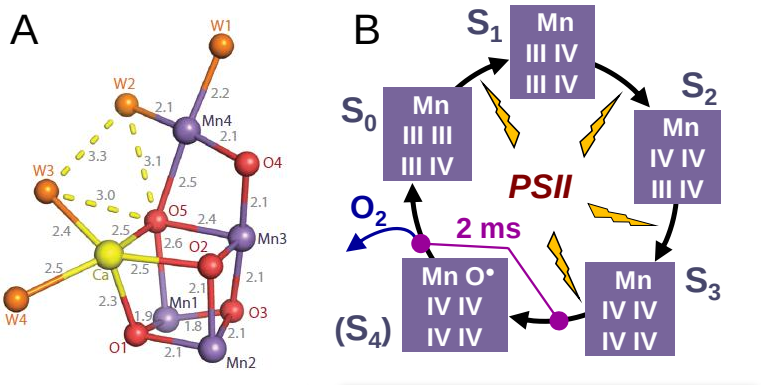

Figure1.2. (A) Core structure of the Mn_4CaO_5 cluster active centre in PSII in S3 state (Umena, Kawakami et al. 2011). (B) Kok cycle showing the change in the oxidation state of the manganese with every laser flash modified from (Zaharieva, González-Flores et al. 2016).

The Mn_4CaO_5 cluster of PSII is a highly efficient catalyst. In terms of TOF for example, it is at least one order of magnitude higher than the best known synthetic oxide particle base catalyst, working at an overpotential of about 0.3 V (Dau, Limberg et al. 2010, Hong, Risch et al. 2015). This makes the PSII complex the perfect referent for the understanding the mechanism of catalytic

water oxidation and development of optimal catalysts. However, the complete mechanistic details are yet to be completely understood (Yachandra and Yano 2011). For example, the role calcium plays in this process is still not clear. Studies in PSII particles suggest that Ca has an important role in the charge balance and might also act as a Lewis acid in the mechanism of water splitting, by binding and activating water molecules (Debus 1992, Pecoraro, Baldwin et al. 1998, Limburg, Szalai et al. 1999, Vrettos, Stone et al. 2001, Yocum 2008). Experiments in model compounds with structures similar to the PSII complex also suggest that redox inactive metals can modulate the redox properties of the manganese atoms according to their Lewis acidity (Tsui, Tran et al. 2013).

1.3 Biomimetic Catalyst for water oxidation

The Mn_4CaO_5 cluster of PSII also features many useful characteristics besides its high efficiency, like the use of abundant and inexpensive materials, benign conditions, carbon neutrality and the use of solar power as a driving force. For these reasons, mimicking the structure of the Mn_4CaO_5 cluster of PSII has been one of the most interesting synthetic challenges for decades. The main advantage of having a molecular model system is that it can be easily studied, both structurally and functionally. Since the cubane structure of the Mn_4CaO_5 cluster of PSII is known, most synthetic efforts failed to accurately replicate the positions of its atoms and ligands (Tsui and Agapie 2013, Tsui, Tran et al. 2013). In 2015 a more accurate synthetic model version was developed that was able to replicate not only the atoms positions and connectivity, but also some of its spectroscopic characteristics (Zhang, Chen et al. 2015). However, all these synthetic models failed to reproduce the water splitting catalytic activity of the Mn_4CaO_5 cluster. In most cases when these synthetic compounds were tested under water oxidation conditions (aqueous solution and/or presence of oxidant) they decomposed forming amorphous inorganic metal oxides. Until today, the synthesis of a molecular system which mimics both the structural and catalytic properties of PSII seems rather unlikely. The only families of compounds that have approached the performance of PSII are mononuclear and dinuclear molecular complexes of ruthenium, whose structure is far from similar to the Mn_4CaO_5 cluster. (S. W. Gestern, G. J. Samuels et al. 1982, Zong and Thummel 2005, H.-W. Tseng 2008, Concepcion, Jurss et al. 2009).

Efforts to mimic the structure of Mn_4CaO_5 cluster of PSII also involve amorphous inorganic metal oxide particles with water oxidation properties. These particles show water oxidation activity when suspended in an aqueous solution containing a chemical oxidant. These oxides can be obtained

through the amorphisation of different crystalline precursors which occurs under water oxidation conditions (Hocking, Brimblecombe et al. 2011, Menezes, Indra et al. 2014, Najafpour, Moghaddam et al. 2014, Shevchenko, Anderlund et al. 2014). Alternatively, they can be designed and prepared through numerous synthetic chemical routes (Rossouw, de Kock et al. 1992, Ching, Landrigan et al. 1995, Luo, Zhang et al. 1999, Devaraj and Munichandraiah 2008, Spiro, Bargar et al. 2009, Najafpour, Ehrenberg et al. 2010, Zaharieva, Najafpour et al. 2011). Directed chemical synthesis under controlled conditions (i.e. optimized temperature or concentrations of the starting compounds in the solution) also allows the tuning of electrochemical properties. For example, the introduction of inert cations, like Ca, Sr, Mg and Na, affects the catalytic activity for water oxidation in a similar fashion to that in PSII, with the Ca containing materials being the most active (Wiechen, Zaharieva et al. 2012). This type of oxides are typically very amorphous. Their structure was determined by EXAFS and resembles layered manganese oxides of birnesite type, which consists of MnO_6 octahedra interconnected by di-μ_3-oxo bridges with the manganese atoms mostly in +4 oxidation state. In these structures water and different ions can enter the interlayer space.

Figure 1.3.A shows the structure of an ideal birnessite lattice with no defects. Differing from it, active catalysts have shown to be formed by small fragments which can be seen as versions of the birnessite structure, with an increased portion of defects in it. The positions of possible defects can be occupied by calcium, and presumably also by low-valent manganese atoms (Bergmann, Zaharieva et al. 2013). Figure 1.3.B shows an illustrative scheme of possible defects in the birnessite structure occupied by calcium atoms as determined through EXAFS experiments. The Ca atoms are introduced into the layer structure, forming cubane-like $Mn_3Ca(\mu\text{-}O)_5$ features similar to the Mn_4CaO_5 cluster of PSII (labelled as α), or compensating the charge deficiency on top of Mn vacancies, as shown in the feature labelled as γ (Zaharieva, Najafpour et al. 2011). The binding to peripheral positions (β and δ) is also likely, according to studies in biogenic birnessites (Toner, Manceau et al. 2006).

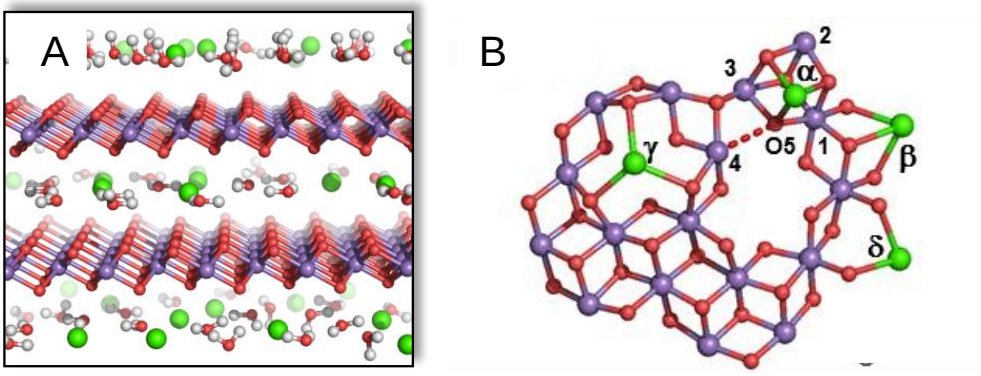

Figure 1.3. (A) Structure of an idealized birnessite (based on coordinates of ref. (Post and Veblen 1990); **(B)** Ilustration of different defects (α, β, δ, γ) in water-oxidizing Mn(Ca) oxides based on X-ray absorption data (Zaharieva, Chernev et al. 2012). Color codes are the following: manganese, purple; oxygen, red; calcium, green; protons, white. Images taken from (Zaharieva, González-Flores et al. 2016).

The presence of low ordered layers, with open coordination sites where water can bind (similar to the one labelled with 4 in Figure 1.3.B), might allow the amorphous Mn oxides to be involved in the water oxidation process. The presence of di-$\mu_{2/3}$-oxo bridging between metal ions at a distance of 2.86 Å seems to be a requirement for efficient catalysis (Bergmann, Zaharieva et al. 2013, Robinson, Go et al. 2013). Recently, many studies have also described the importance of the stabilization of the Mn^{+3} oxidation state for catalysts working at neutral pH (Takashima, Hashimoto et al. 2011, Takashima, Hashimoto et al. 2012, Najafpour, Moghaddam et al. 2014, Park, Kim et al. 2014, Indra, Menezes et al. 2015, Li, Liu et al. 2015, Mattioli, Zaharieva et al. 2015, McKendry, Kondaveeti et al. 2015, Mahdi Najafpour, Jafarian Sedigh et al. 2016). However, the exact characteristics of the active sites of catalysis in this type of oxides are far from being fully understood.

1.4 Electrodeposited transition metal (oxy)hydroxide catalysts for water oxidation

Inorganic amorphous metal oxy(hydroxides) with similar low ordered birnessite type of structure, as described in the previous section, can also be prepared electrochemically. This not only applies to manganese, but also to some other first row transitions metals, for instance cobalt, nickel and iron (Trotochaud and Boettcher 2014, Roger and Symes 2016). Electrosynthesis protocols are especially advantageous due to their simplicity, low cost, good reproducibility and control over the film thickness, which make them ideal for both technological applications and functional studies.

Electrodeposition of amorphous manganese oxide catalysts has been performed before applying constant oxidation potential in an aqueous solution of Mn^{+2} ions (Gorlin and Jaramillo 2010, Zaharieva, Chernev et al. 2012, Gorlin, Lassalle-Kaiser et al. 2013, Huynh, Bediako et al. 2014). However, the activity of these catalysts was remarkably low. A special cycling protocol described in ref. (Zaharieva, Chernev et al. 2012) was required to obtain manganese oxide films with catalytic activity for water oxidation comparable to cobalt (Kanan and Nocera 2008) or nickel oxides (Bediako, Lassalle-Kaiser et al. 2012).

Amorphous cobalt oxides (CoCat) on the other hand, can be very easily prepared applying constant oxidizing potential on different substrates, at different pH values and employing different electrolytes and deposition potentials (Gerken, Landis et al. 2010, Esswein, Surendranath et al. 2011, Gerken, McAlpin et al. 2011, Ramírez, Hillebrand et al. 2014). This high flexibility in preparation together with other special characteristics, like their high efficiency at neutral pH and low cost, makes Co oxides a very interesting material. Especially important are their self assembly and self healing properties, in which the phosphate or electrolyte base likely plays a key role (Lutterman, Surendranath et al. 2009, Surendranath, Lutterman et al. 2012). For these reasons, CoCat has to be included in any discussion regarding developments in the field of electrocatalysis for water oxidation with amorphous transition metal oxides.

Even though the use of amorphous cobalt oxides for water oxidation was first reported more than 100 years ago (Coehn and Gläser 1902), the burst of investigations on their structure and function came after their rediscovery by Kanan and Nocera in 2008 (Kanan and Nocera 2008). The electrodeposited CoCat is highly amorphous. The structure in its resting state, as determined by EXAFS, is composed of octahedrally coordinated Co(III) ions interconnected by di-μ-oxo-bridges, similar to the case of the manganese birnessites (Risch, Khare et al. 2009, Kanan, Yano et al. 2010). Films deposited in a pH 7 phosphate buffer are composed of oxo clusters of about 9-16 cobalt atoms (Risch, Khare et al. 2009). The oxo layers might also possibly involve defects, different ions in the interlayer space and also ions bound in different positions of the layer (Risch, Klingan et al. 2012), as described for the manganese based oxides.

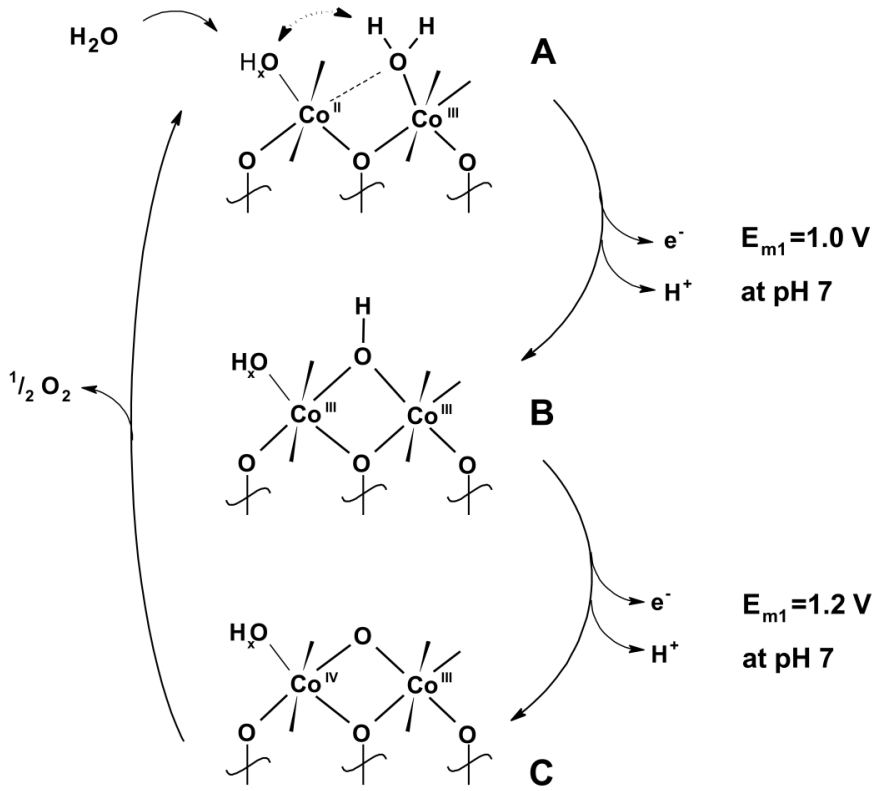

Figure 1.4. Structural motifs A, B, and C in the CoCat during the OER. Oxygen evolution occurs in the transition from C to A. The shown structural changes probably arise at the margins of Co-oxo fragments (9-16 Co ions). Figure reproduced from (Risch, Ringleb et al. 2015) with permission from The Royal Society of Chemistry.

The CoCat is one of the transition metal oxide catalysts that has been mechanistically studied more compared to other catalysts. Based on in-situ XAS measurements together with in-situ UV-visible and differential electrochemical mass spectroscopy, the mode of catalysis for CoCat has been described recently as the interconversion between three main motifs, which are described in Figure 1.4 (Risch, Ringleb et al. 2015). These motifs are possibly located in the margins of the Co-oxo cluster. Each kind of motif prevails at a certain potential. Under resting state conditions the catalysts is in all +3 oxidation state. If the potential is increased over 1.2 V versus NHE at pH 7, a fraction of Co ions are oxidized to +4, which is then also followed by deprotonation. The catalysis is described to be dependent on the accumulation of neighbouring Co(IV) species and the probability that this high oxidation state species form an active site. The limiting step is the O-O bond formation and release of O_2, which happens during the transition from C to A. After this, the cobalt involved in the O_2 formation are reoxidized by the electrode potential and return to equilibrium conditions (this is all Co^{III}). The conversion of A into B occurs around 1.0 V versus NHE at pH 7, and consists of a deprotonation step associated to an oxidation of cobalt to an

average oxidation state of +3. The process of oxidation is markedly faster than the limiting step, which leads to the accumulation of redox equivalents before the release of oxygen takes place. The striking similarities of this catalytic cycle to the catalysis in the Mn_4CaO_5 cluster of PSII, including a stepwise increase of oxidation state of cobalt coupled to deprotonation, are noteworthy and suggest not only analogous structural changes during turnover, but also similarities in the functioning and mode of catalysis.

Heterogeneous water oxidation happening in nano or micrometric particles composed of crystallites is assumed to happen on the surface of some of the faces of the crystals which are determined by the bulk structure of the crystal and its elemental composition (Trasatti 1980, Trasatti 1984, Harriman, Pickering et al. 1988, Suntivich, May et al. 2011, Gardner, Go et al. 2012, Landon, Demeter et al. 2012, Trotochaud, Ranney et al. 2012, Bajdich, García-Mota et al. 2013, Calle-Vallejo, Inoglu et al. 2013, Louie and Bell 2013, Robinson, Go et al. 2013, Smith, Prévot et al. 2013). Amorphous transition metal (oxy)hydroxides on the other hand seem to have properties in between traditional solid state materials and synthetic organometallic homogenous catalysts. The special structural features composed of these small aggregates of highly amorphous oxide clusters forming a layered structure that contains water and ions in between the layers seem to be important in determining the electrocatalytic properties. Recent reports have shown that the catalysis of water oxidation can happen not only at the surface but also in the bulk of the oxide material (Klingan, Ringleb et al. 2014). At high overpotentials however, the proton transfer to the electrolyte becomes determinant in the reaction rate. It is feasible to imagine that these structural features surrounded by water allows catalysis to happen in the volume of the oxide in a similar way to homogeneous catalysis.

In recent years, an increasing number of studies report the surface amorphisation of crystalline materials during water oxidation catalysis. In the case of perovskites (Lee, Carlton et al. 2012) and $LiCoO_2$ (May, Carlton et al. 2012) for example, an amorphous layer with similar structure to CoCat was obtained. Similar observations have been made in materials based on manganese were MnO was transformed into an amorphous active oxide (Indra, Menezes et al. 2013) and in heterometallic oxides containing iron and cobalt. Crystalline Co_3O_4 also undergoes reversible surface amorphisation under operation (Bergmann, Martinez-Moreno et al. 2015). In addition, it is well documented that many complexes of transition metals during water oxidation conditions are transformed into amorphous oxides (Hocking, Brimblecombe et al. 2011, Najafpour, Moghaddam et al. 2014). All this evidence seems to imply that water oxidation by transition metal based catalyst is always connected to formation of amorphous oxide phases. If this is the case, the catalysis

happening at the surface of crystals would be influenced not only by the surface contribution determined by the atomic structure, but also by the rate of amorphisation and formation of an amporhous phase that eventually contributes with bulk catalysis. These dynamic processes and transformations also raise the question whether surface catalysis or bulk catalysis prevails and constitutes the major contribution in the activity during the water oxidation process.

Several other parameters can affect the catalytic activities besides surface catalysis and bulk catalysis, for example preparation methodology, pH, catalyst load, substrate and electrolyte. The high variability of conditions across studies makes a direct comparison of catalysts difficult. However, being able to compare conditions is of major importance for the development of technological applications. Currently, the best known solar power electrolyser fabricated achieved a conversion efficiency of 12 % solar to hydrogen, with a current of about 10 mA cm^{-2} and a potential of about 1.7 V provided by two perovskyte solar cells in series (Luo, Im et al. 2014). This means that catalysts which can hold the aforementioned current with the lowest overpotential possible are both desirable and required.

Some groups have performed benchmarking efforts to be able to compare catalysts under similar conditions (McCrory, Jung et al. 2013). Some of the paramethers obtained in a comparative study of different metal oxides by Trotochaud are shown in Table 1.1 (Trotochaud, Ranney et al. 2012, Trotochaud and Boettcher 2014). In this study, the authors took special care to ensure that the films were tested under similar conditions with thin enough layers, so that the catalytic activity was not majorly influenced by bulk catalysis.

Table 1.1. Comparison of the catalytic performace of thin layers of metal oxide catalyst according to ref.(Trotochaud and Boettcher 2014)

Material	η (mV)	pH	TOF (s^{-1})
PSII*	300	~ 5.5	100
MnOx	300	14	0.0004
FeOx	300	14	0.0015
CoOx	300	14	0.0032
IrOx	300	14	0.0089
CoPi	300	7	0.00004
Ni0.9Fe0.1Ox	300	14	0.21

*The values for PSII were obtained from ref.(Dau, Limberg et al. 2010)

At pH 7 the best catalyst known are mostly cobalt based. However, the catalytic activity is far from fulfilling the requirements of a solar electrolyser device. As it can be observed in Table 1.1, even though transition metal oxides have quite low turnover frequencies (TOF) compared to the Mn_4CaO_5 cluster of PSII, in alkaline pH they display improved activities than at pH 7. Between them, NiFe based catalysts have repeatedly shown the best performances, even over iridium based catalysts, holding 10 $mAcm^{-2}$ currents at overpotentials below 0.3 V (Gong, Li et al. 2013, Song and Hu 2014). Since NiFe oxides have such promising properties, they will be discussed in more detail in the following section.

1.5 NiFe oxides as the most active catalysts: pH dependence of the catalytic activity

One of the mayor goals in the field of water splitting is the rational design of non precious metal based catalyst for water oxidation. Accomplishing this goal will definitively require a better understanding of the catalysts function, especially those catalysts that present a high activity. From this perspective, NiFe oxide based catalysts are interesting candidates due to their high activity at low overpotentials in alkaline conditions at levels comparable or superior to most efficient noble metal based catalyst (Trotochaud, Ranney et al. 2012, Gong and Dai 2014, Song and Hu 2014, Swierk, Klaus et al. 2015). The high catalytic activity of NiFe oxides is well known since more than 60 years. Early discovery reports can be traced back to the 50's (Tichenor 1952). However it was studied more in depth until the 80's when the interest in water splitting was rising (Młynarek, Paszkiewicz et al. 1984, Corrigan 1987). With the ever increasing interest in water splitting, more recent works have focused on understanding the function of this kind of catalyst. Understanding the function of the catalyst requires insights in the structure and specially identification of the active site and mechanism.

The story of the identification of the active phase in NiFe oxides is rather a very complicated story full of debate. One of the reasons for this is that most of the time different synthesis protocols lead to mixed phases. Also transformation to other phases under operation can be observed. In some reports formation of the $NiFe_2O_4$ inverse spinel has been associated with the catalytic activity (Landon, Demeter et al. 2012). However, Raman spectroscopic evidence suggests this is not the main active phase (Louie and Bell 2013). It has also been observed that nickel iron oxides with rock salt structure are converted to the oxyhydroxide phase under operation (Trotochaud, Ranney et al. 2012). Most of the recent investigations agree in pointing the oxyhydroxide phase like the

responsible of the catalytic activity. In the case of the oxyhydroxide phases for a long time was stated that the active phase consists of the β-NiOOH (Lu and Srinivasan 1978). However, a more recent report indicates the γ-NiOOH as the active one (Bediako, Lassalle-Kaiser et al. 2012). The group of Bell suggest that iron is incorporated into this phase (Friebel, Louie et al. 2015).

The effect of Fe in enhancing the catalytic activity is undeniable. However the reason for this improvement is not clear. It has been suggested it is related to an increment of the conductivity of the film with the incorporation of Fe. However, the improvement in the activity cannot be solely explained based in a conductivity increment (Trotochaud, Young et al. 2014, Klaus, Cai et al. 2015). Some groups have suggested the formation of Fe^{+4} with Fe-O bonds of covalent nature related to the catalytic activity (Balasubramanian, Melendres et al. 2000, Wang, Zhou et al. 2015). Meanwhile the group of Bell have suggested that during operation the iron containing α-$Ni(OH)_2$ is transformed into γ-NiOOH. The nickel increases its oxidation state to 3.6 and iron remains in +3 oxidation state with unusually short Fe-O distances. The short distances in the iron result from the constrains imposed by the γ-NiOOH structure. These Fe^{+3} sites have been proposed as the active sites for catalysis (Friebel, Louie et al. 2015). A more recent Mössbauer spectroscopy study shows the formation of Fe^{+4} in NiFe catalysts under catalytic potential (Chen, Dang et al. 2015). In this study, it is proposed that Fe^{+4} is located at edges or defects in the NiOOH structure forming highly active sites. However these species were not directly seen in the measurements due to their fast kinetics. The authors only observed the slow Fe^{+4} species which they propose are inside of the structure of the layer (Chen, Dang et al. 2015).

What can be definitively stated is that a better understanding of the structure and function are still required. This includes also the effect of the pH on the activity of the catalysts. Most electrochemical studies suggest that amorphous first row transition metal oxides are affected in a very different way by changes of pH (Burke, Zou et al. 2015, Giordano, Han et al. 2016). For example in the case of the NiFe oxide catalyst, the catalytic properties at pH 7 are similar to other catalyst, and much better than other catalysts at pH 14 (Görlin, Gliech et al. 2016). Raman studies by Trzésniewski in 0.1 M KOH and in 0.5 M borate buffer with pH 9.2 suggest the formation of active species in nickel-iron oxides under applied potential (Trześniewski, Diaz-Morales et al. 2015). The formation of such species was previously described by Merrill and were named as “active oxygen” (Merrill, Worsley et al. 2014). Trzésniewski and co-workers also observed that the formation of such species is strongly pH dependent and is inhibited by borate anions. Even thought the nature of the species is not known the authors suggest that they are formed by deprotonation of

the nickel hydroxide and might have peroxide or superoxide nature. The possibility of an important deprotonation step involved by turnover in the catalytic cycle is also supported by recent data in which nickel iron oxides with different anions in the interlayer space were prepared and studied under controlled atmosphere conditions (Hunter, Hieringer et al. 2016). The authors observed a sigmoidal behaviour of the catalytic activity as a function of the basicity of the corresponding anions. All this data raises important questions about the role of the pH in the electrocatalytic performance of these amorphous oxide catalysts which will also be addressed in this thesis with a comparative study in the last chapter.

1.6 Scope and organisation of the thesis

The main scope of this thesis is to contribute to the field of water oxidation with first row transition metal oxides catalyst by addressing some important questions like "What is the role of Ca in the electrochemical properties of manganese-calcium oxides?", "How is the oxidation state of Mn related to the activity of the manganese oxide films?" "Is the catalysis in crystalline materials always associated to amorphisation and restructuring of the surface of the crystal?", "How is the activity of different transition metal oxides affected by the pH?" All this topics are addressed with the ambition of understanding better the function of the catalysts and extrapolate some structure-function relationships.

The chapters are organised as follows:

Chapter 2 Describes in detail the experimental details and theoretical background in the X-ray absorption measurements.

Chapter 3 Describes a new protocol for the electrodeposition of biomimetic manganese-calcium oxide catalyst for water oxidation. The chapter also studies more in depth the role of Ca ions in the catalytic activity of manganese oxides by combining electrochemistry with X-ray absorption spectroscopy and UV-visible spectroscopy. Besides, the effect of active site creation by annealing and some structure-function relationships are outlined.

Chapter 4 Examines screen-printed electrodes of previously prepared and optimized Ca-birnessite on a conductive FTO substrate. The main focus of the chapter is studying

by XAS the effect of the grafting protocol and electrochemical operation on the structure of the catalyst.

Chapter 5 Investigates the modes of catalysis in a crystalline cobalt phosphate mineral upon long term operation and scrutinises the role of surface catalysis, volume catalysis and dynamical restructuring during long term operation at catalytic potentials.

Chapter 6 Addresses the question of the role of the pH in the catalytic activity of cathodically deposited transition metal oxides making emphasis in NiFe oxides. The study combines spectroelectrochemistry and *in-situ* XAS with electrochemistry.

Chapter 2

X-ray absorption spectroscopy

This introduction to X-ray absorption spectroscopy is based mostly on (Rehr and Albers 2000, Calvin 2013, Newville 2014)

2.1 X-ray absorption and the EXAFS equation

When an X-ray hits an atom with an energy equal or higher to the binding energy of a core electron, then absorption of X-rays can occur. The absorption depends on the availability of energetically higher electronic states. The quantized nature of the transitions results in a sharp absorption of X-rays forming what is called an edge. The name of the absorption edges are usually given according to the principal quantum number, n. For example the K-edge is related to transitions from the 1s orbital, meanwhile the L edge is related to transitions from the 2s and 2p orbitals (see Figure 2.1).

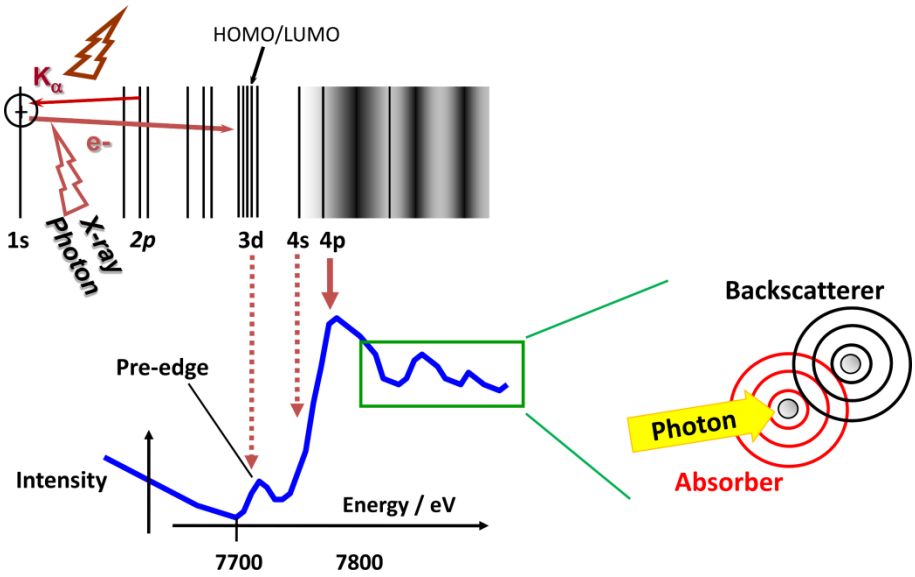

Figure 2.1. X-ray absorption K-edge of Co. In this case the red arrow represents a forbidden transition from 1s→3d resulting in the pre-edge feature observed. The K_α fluorescence emission as a result of the relaxation of 2p electrons into the core-hole is also represented. At high enough energies the photo-electron can leave the atom and is backscattered by surrounding atoms resulting in the interference EXAFS region highlighted in the green box.

The transitions of the electron follow the dipole transition selection rules: $\Delta l = \pm 1$, $\Delta j = \pm 1$, $\Delta s = 0$.Where s is the spin quantum number, l is the azimuthal quatum number and j is the total angular momentum of the electron (given by the sum of its orbital and spin angular momenta j=l+s). La Porte rule for example says that in molecules with a center of symmetry, transitions within a subshell are forbidden when $\Delta l = 0$. In the case of octahedral molecules for example transitions 3p→3p and 3d→3d are forbidden. The transition from 1s to 3d is also forbidden according to the rules described; however, it can be sometimes observed due to 3d to 4p orbital mixing and direct quadrupolar coupling. In those cases the forbidden transitions result in a pre-edge feature at lower energies than the main edge, which contains also information about the symmetry of the system.

The features observed at the pre-edge, the main edge and about 30 eV further are called X-ray near-edge structure (XANES). Since the energetic levels are sensitive to the element of the scatter atom, its oxidation state and coordination environment, a lot of structural information is encoded in the position and shape of the edge. Simulations, of the edge and pre-edge features to extract structural information are normally complicated. For that reason the experimental spectra of samples with unknown structure are usually analyzed in comparison with reference spectra of samples of known structure, coordination environment and oxidation state. This will be described in detail later in section 2.6.

The absorption of X-rays is a function of the thickness of the sample (Figure 2.2). The attenuation of the intensity can be described according to the equation

$$I = I_0 e^{-\mu x} \quad (2.1)$$

Where x represents the thickness of the sample, I_0 the initial intensity and μ is the X-ray absorption coefficient, which is proportional to the following factors

$$\mu \approx \frac{\rho Z^4}{A E^3} \quad (2.2)$$

where ρ is the density of the material, Z the atomic number, A the atomic mass and E the energy of the incoming beam.

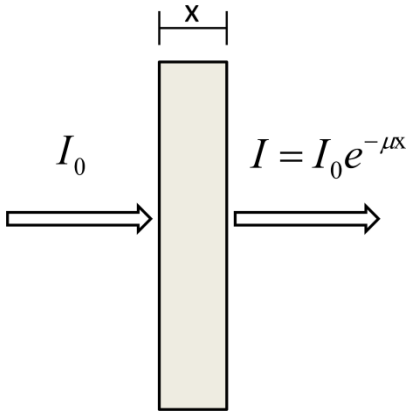

Figure 2.2. Attenuation of an incoming X-ray beam with initial intensity I_0 after having passed through a sample of a certain thickness x, where μ represents the X-ray absorption coefficient.

If the energy is further increased after the edge, it becomes high enough that the 1s electrons are expelled from the atom (e.g. generation of a photo-electron). The surrounding atoms can scatter the emitted wave. The scattered wave interferes with the emitted one resulting in constructive or destructive interference and modulations of its amplitude depending on how the scanning energy affects the wavelength of the scattered photo-electron. The characteristics of the scattering effect depend also on the nature of the surrounding atoms and the distance from the main scattering center. As a result, if the energy is scanned after the edge and about 1000 eV after, a constructive-destructive oscillatory pattern is obtained which is usually called extended X-ray absorption fine-structure (EXAFS). This spectrum contains information about the neighboring atoms around the main scattering center like identity of the scatterers, distance to the absorber and quantity of them.

The EXAFS region can be phenomenologically described with the EXAFS fine-structure function χ(E)

$$\chi(E) = \frac{\mu(E) - \mu_0(E)}{\Delta\mu_0(E)} \quad (2.3)$$

where μ(E) is the measured absorption coefficient defined as μ(E)= -log (I/I_0), $\mu_0(E)$ is a background function that represents the absorption of an isolated atom, and $\Delta\mu_0(E)$ is a normalization factor related to the increase in the absorption which is approximated as the jump in absorption at the corresponding edge.

Since the absorption process represents an electronic transition between two quantum states, the absorption coefficient can be mathematically described as proportional to an expression determined by the Fermi's Golden Rule as

$$\mu(E) \propto \left|\langle i|H|f\rangle\right|^2 \quad (2.4)$$

where $\langle i|$ represents the initial state (an X-ray, a core electron and a no photo-electron), $|f\rangle$ is the final state (no X-ray, a core-hole and a photoelectron) and H is the interaction term, that represents the process of changing between two energy momentum states. Solving this equation results in the EXAFS equation 2.5 (for more details about the derivation see ref (Newville 2014)). For instance, the patterns observed in the EXAFS spectrum can be modelled as the addition of the contribution of different scatterers at certain distances called shells. Every shell produces a scattering event that contributes to the whole spectrum. The modelling of those events can be described with the so called EXAFS equation χ(k)

$$\chi(k) = S_0^2 \cdot \sum_i^{n_{shell}} A(R_i,k)_i \cdot N_i \cdot e^{-2\sigma_i^2 \cdot k^2} \cdot \sin(2k \cdot R_i + \phi_i) \quad (2.5)$$

S_0^2 …Amplidude reduction factor

$A(R_i,k)_i$ …Scattering amplitude for the *i*-shell

N_i …Coordination number or degeneracy

σ_i …Debye-Waller parameter, the mean square root in the bond distance

R_i …half path length or distance between absorber and scatterer

ϕ_i …phase shift

The photo-electron wave-vector k is given by

$$k = \sqrt{\frac{2m(E-E_0)}{\hbar^2}} \quad (2.6)$$

where $\hbar$ is the Planck constant divided by 2π, E is the

When the photo-electron is ejected from the 1s core, the scattering of that electron is described by equation (2.5). The scattering function will depend on the distance R of the scatterer from the

absorber and the energy of the photo-electron (the photo-electron wave vector k). When the photo-electron is scattered, it will also experience a phase shift ϕ due to the change of direction, but also due to the interaction with the potential field created by the atoms.

The scattering amplitude function as represented in equation 2.5 contains the probability of scattering as well as the contribution of the mean free path of the electron (related to the lifetime of the core-hole state) which decays exponentially with k and its responsible of making EXAFS a local effect technique.

The degeneracy or coordination numbers N accounts for the number of scatterers at a certain distance. The distances between different scatterers can be slightly different due to thermal effects (thermal disorder) which result in a distribution of similar distances. This distribution is represented by the Debye-Waller factor (σ). It is also strongly correlated to the coordination number N and related to the disorder of the material.

When the photoelectron leaves the atom, the remaining electrons have to adjust to the presence of the core hole, this changes the overlapping between the initial and final state which results in a reduction in the amplitude of the oscillations. This relaxation of the system after creating the core-hole is taken into account by the amplitude reduction factor S_0^2. Other less understood factors can contribute (shake up and shake off effects) and some of the experimental conditions as well (like inhomogenity and self-absorption for example).

The structural information in the EXAFS can be better visualized if the data is Fourier transformed from the energy domain to the space domain. The presence of a certain kind of neighbor atom is then visualized as a peak. This peak contains information about the distance at which the neighbor is located, the quantity of neighbors and also to the distribution of the average of similar distances. The data has to be specially treated before being Fourier transformed, this will be explained later in section 2.5.

2.2 Experimental details

All of the X-ray absorption spectroscopy experiments in this thesis were performed in the KMC-1 or KMC-3 bending-magnet beam line of the BESSY synchrotron (Helmholtz-Zentrum Berlin). The energy of the beam is adjusted with a double-crystal (Si-111) monochromator.

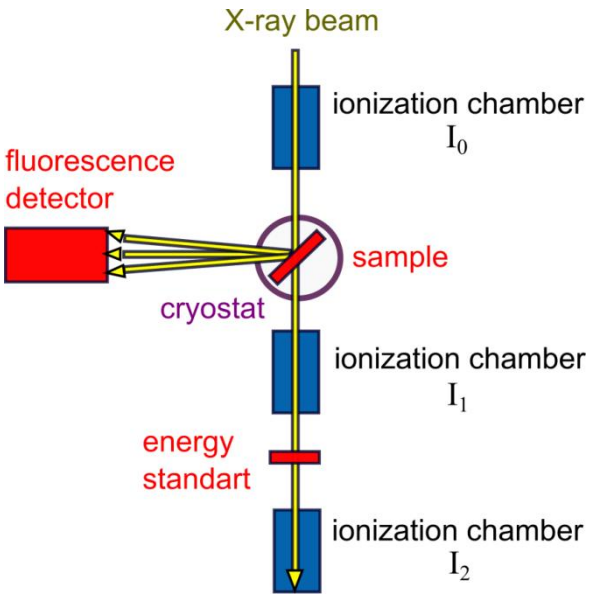

Figure 2.3. Scheme of the basic set up used for the X-ray absorption spectroscopy measurements. The absorption in the sample is taken from A_1=-log(I_1/I_0). The absorption for the energy standard measured at the same time as A_2=-log(I_2/I_1). The sample is place in a cryostat at 20 K and can also be measured at the same time in fluorescence mode by using an energy resolving fluorescence detector placed orthogonal to the incident X-ray beam.

A scheme of a typical X-ray absorption spectroscopy set up is shown in Figure 2.3. The monochromatic beam passes first through an ionization chamber, which consists basically of a chamber with two parallel plates at high voltage and a low pressure of a gas (N_2 or Ar). When the beam hits the camber (I_0), ionization of the gas generates a current response which is proportional to the intensity of the coming beam. Then, the beam hits the sample and the change in the signal due to the sample is recorded by a second ionization chamber (I_1). For a precise adjustment of energy values and energy standard with a known edge position is used to calibrate the energy of the measurements. The absorption due to the energy standard is recorded with a third ionization chamber (I_2).

A second phenomenon can occur when the 1s electron is ejected from the atom, then an electron at higher energetic states can relax to the 1s state, resulting in fluorescence emission. The probability of the fluorescence emission is proportional to the probability of the ejection of the 1s electron. As a result, the fluorescence spectrum is proportional to the absorption one. This condition holds only in the case of samples that are thin enough so that the same sample does not re-absorb the fluorescence again (self-absorption).

The possibility of measuring the absorption spectra through fluorescence measurements opens up a lot of experimental possibilities for measuring complicated samples that cannot be easily measured in absorption mode.

For fluorescence measurements a fluorescence detector with 13 germanium elements (Ultra-LEGe deterctor elements, Canberra GmbH) was used. The detector is placed orthogonal to the set-up as depicted in Figure 2.3. The sample is placed in an angle of 45 degrees in respect to the incoming beam. Two main measuring approaches are used in this work; experiments at 20 K and in-situ measurements at room temperature.

2.3 Measurements at 20 K

For this type of measurements, a liquid helium cryostat is used (Oxford Danfysk, heat conduction by helium gas at 200 mbar in the sample compartment). Measurements at low temperature have some advantages like prevention of radiation damage and favoring the preservation of the conditioning of the sample and its structure (by avoiding thermal disorder for example). For this type of measurements a special kind of sample holder is used. These sample holders are normally made of polymethylmethacrylate with a size of 3.2x1.9x0.2 cm and can be used to condition the catalyst electrodes at certain potential conditions. In the back side of the holder, an X-ray transparent substrate and working electrode (like glassy carbon) is usually used for electrodeposition of the sample. A platinum wire is used as counter electrode as shown in the Figure 2.4. To condition the sample at a certain potential, the sample frame with the catalyst already deposited is place in horizontal position. The volume of the sample frame that works as a electrochemical cell is filled with the desired electrolyte. The working and counter electrode are connected to the potentiostat. Before doing the conditioning of the sample a reference electrode is used. The desired potential versus the reference electrode is applied (V_R) and the corresponding potential value at the counter electrode is also recorded (V_C). After this, the reference electrode is removed to avoid damage when the liquid nitrogen is poured; the electrochemical cell is used in a two electrode system and a potential equal to V_R-V_C is applied between the two electrodes. After some stabilization time the sample is frozen by pouring liquid nitrogen when the potential is still applied. Then it is kept frozen under liquid nitrogen until the measurements are performed. We call this quasi in-situ approach for sample preparation freeze-quench approach. In our group we have previously shown with cobalt oxide catalyst samples that by using this approach it is possible to preserve the samples in certain states and obtain similar results as in in-situ measurements (Risch,

Ringleb et al. 2015). This sample preparation procedure is also described in detail in reference (Zaharieva, Gonzalez-Flores et al. 2016).

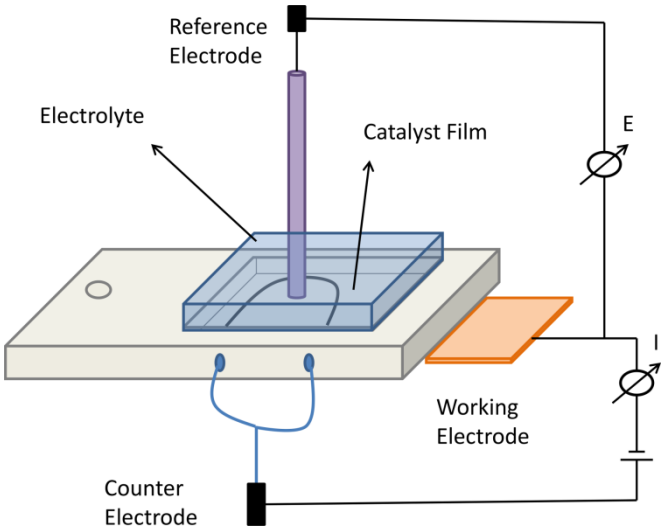

Figure 2.4. Sample holder (electrochemical cell) used for the freeze quench approach for sample preparation. The sample holder with the working electrode in the back side is placed horizontally, the cavity is filled with the corresponding electrolyte, and connected to the potentiostat as shown.

2.4 In-situ measurements at room temperature

For this type of measurements some modifications are required in the set up. An picture of the set up in KMC-3 is shown in Figure 2.5. In this case, the measurements are performed only in fluorescence mode. The measurement of the energy standard is performed ex-situ after the measurement of the sample in a separate measurement. For that reason only the ionization chamber before the sample I_0 is kept in the set up. To perform the in-situ XAS measurements while electrochemistry is performed, a special kind of electrochemical cell was designed. The cell is made of Teflon and has a window where a working electrode substrate transparent to X-rays (like glassy carbon or carbon paper) is placed. The sample catalyst is deposited in this substrate and measured from the back side, as shown in Figure 2.6. The counter and reference electrode are also placed inside the electrochemical cell. The fluorescence measurements are performed orthogonal to the incident beam.

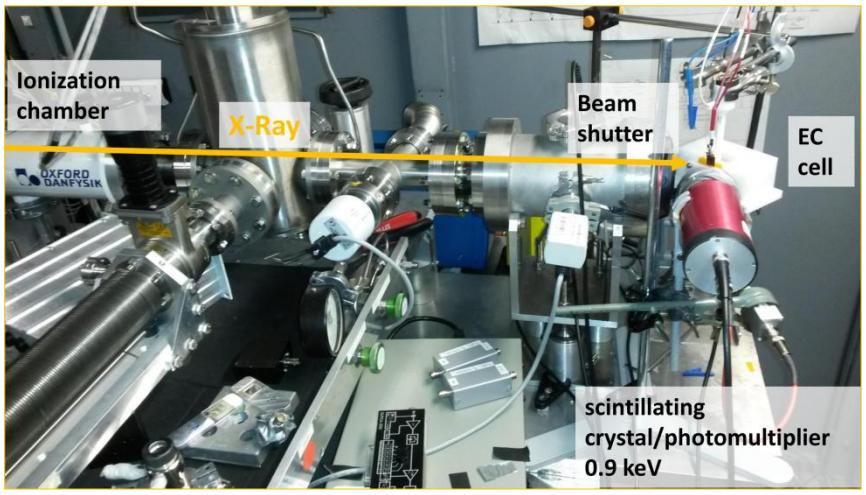

Figure 2.5. Picture of the set-up used for the in-situ measurements. The direction of the X-ray beam is illustrated with the yellow arrow. The main components like ionization chamber, scintillating detector, beam shutter and electrochemical cell are shown.

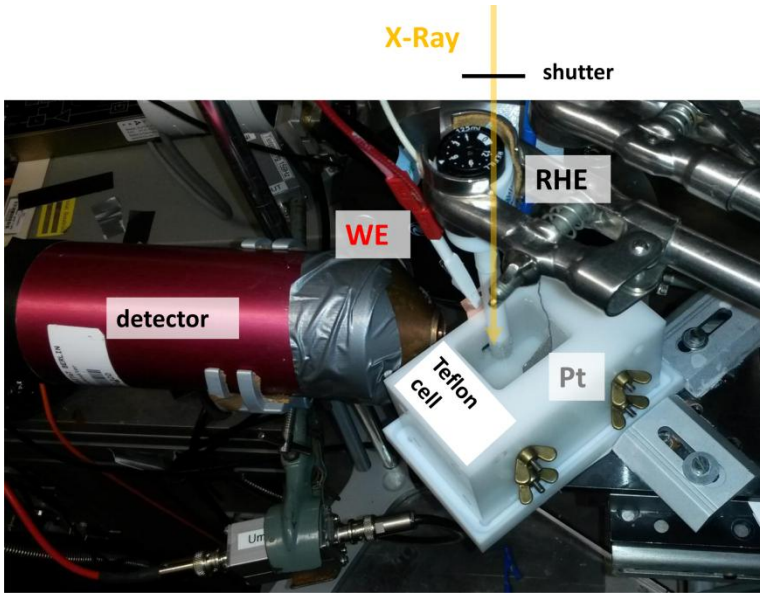

Figure 2.6. Close-up of the home-made Teflon electrochemical cell used during the in-situ measurements. The position of the electrodes and detector can be observed.

In this case, the fluorescence signal is recorded by a scintillating detector. The scattered light is filtered by using a metal foil properly selected for every kind of transition metal. The current is passed through a 1 MΩ resistance and converted to voltage. The signal is amplified with 6dBlock 10 Hz low-pass filter. The system allows measurements with 10 to 40 ms time resolution. More details of the measurements are described in the experimental part of chapter 6.

2.5 Treatment of the data

During the XAS measurements the signals of four ionization chambers are recorded: I_0, I_1, I_2 and another ionization chamber (I_{00}) before the set-up used by the beam line to control the intensity and calibration of the beam. In case of the measurements at low temperature, also the total incoming count rates and raw fluorescence signals of the 13 elements of the detector are recorded (in total 26 signals). Meanwhile the ICR signals correspond to all the fluorescence counts measured by every element, the fluorescence signal corresponds to a selected window at the K_α emission of the corresponding metal of interest. An example of an I_1 measurement is shown in Figure 2.7.A.

Dead time correction: Energy resolving detectors count and analyze the photons at the same time, therefore, they have a dynamic range and sometimes can fail to count photons producing nonlinearities. The treatment of the data starts with a dead time correction of the fluorescence data where the photon counts are corrected for the number of non-detected photons due to possible dead time of the detector elements. The out-coming data (OCR) is corrected by an exponential fit from the ICR values (equation 2.7). The calibration saturation plot is obtained by measuring time scans at a fixed energy for the corresponding shaping time of the 13 element detector.

$$OCR = A \cdot (1 - e^{-k \cdot ICR}) \quad (2.7)$$

Calculation of the absorption: The intensity of the ionization change after the sample is converted to absorbance by A_1=-log(I_1/I_0). The absorption for the energy standard is calculated as A_2=-log(I_2/I_1). The fluorescence signals are normalized by dividing by I_0. The absorption spectra A_1 is shown in Figure 2.7.B.

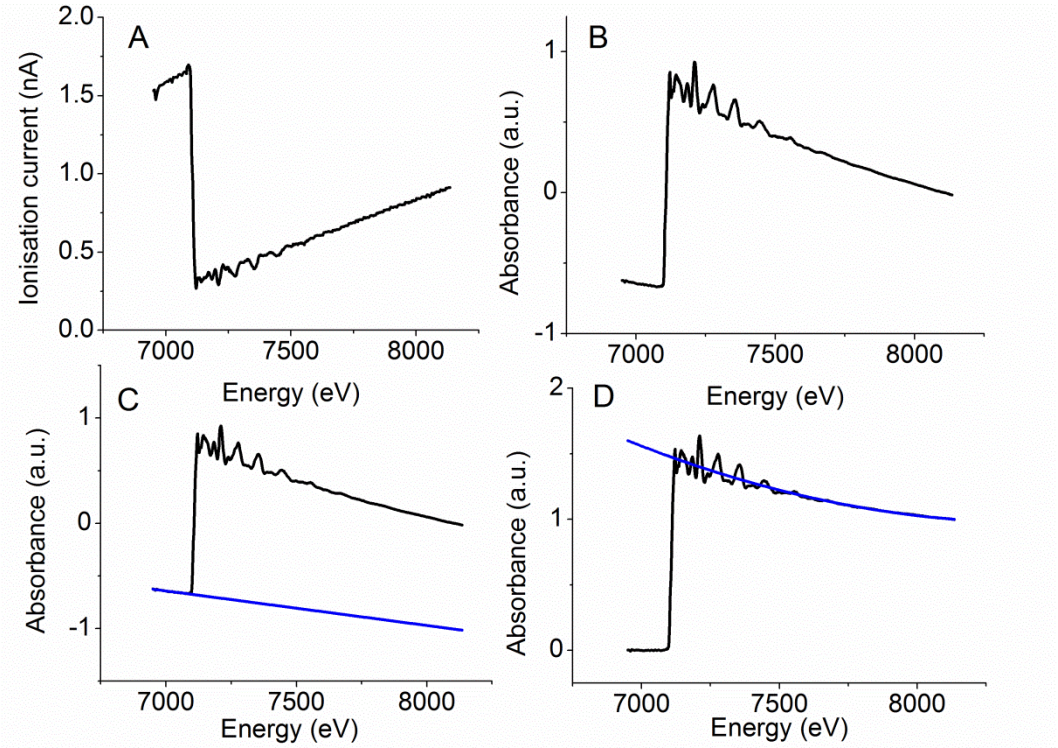

Figure 2.7. A) Raw absorption spectrum for a metallic Fe sample. B) Absorbance in the sample calculated as A_1=-log(I_1/I_0). C) Background subtraction with a straight line in the region before the edge rising. D) Normalization to 1 by dividing by a polynomium of second order.

Energy calibration: The energy calibration of the data is performed by calculating the derivative of the absorption spectra of A_2. The first peak of the derivative is fitted with the combination of a linear and Gaussian function, and shifted to the literature value of the corresponding edge. All the experimental data is then shifted the same as the reference spectra are shifted. Finally, the fluorescence and absorption spectra are processed in the same way. An in-house software (Bessy) developed by Dr. Petko Chernev (AG Dau) was used for data treatment.

The extraction of X-ray spectra starts with a background subtraction in the regions before the edge rising (Figure 2.7.C). Then, the spectra are normalized to 1 by dividing by a polynomial function grade 1, 2 or 3 depending on the data (Figure 2.7.D). In a third step, the data is averaged, and weighted by its signal to noise ratio. The signal is calculated as the ratio between the absorption at the end of the scan and the absorption before the rise of the edge. The noise is calculated by fitting a line in the data at the end of the spectra were the oscillations have a small amplitude and calculating the mean square root.

2.6 Estimation of the edge position

After this normalization, the spectrum can be used to estimate the edge position (Figure 2.8). This is accomplished by using a step integral function (Dau, Liebisch et al. 2003). For each energy point in the interval [E_1,E_2], the edge energy is defined by the integral

$$E^{edge} = E_1 + \frac{1}{\mu_2 - \mu_1} \int_{E_1}^{E_2} \mu_2 - \tilde{\mu}(E) dE \quad (2.8)$$

Where $\tilde{\mu}(E)$ is defined as

$$\tilde{\mu}(E) = \begin{cases} \mu_1 & \text{for } \mu(E) \langle \mu \\ \mu_2 & \text{for } \mu(E) \rangle \mu_2 \\ \mu(E) & else \end{cases} \quad (2.9)$$

By using the limits μ_1=0.15 and μ_2=1, one of the main advantages of this methodology it's insensitive to noise effects.

Estimation of the oxidation state can be achieved by comparison with reference samples (Figure 2.9). By using references that contain the desired metal surrounded by the same kind of ligands and the same geometry expected for the sample, it is possible to make a calibration plot of the dependence of the edge position on the oxidation state of the metal. The measured sample can be then interpolated in this plot and its oxidation state can be determined. The accuracy of the oxidation state will depend on the quality and purity of the references used.

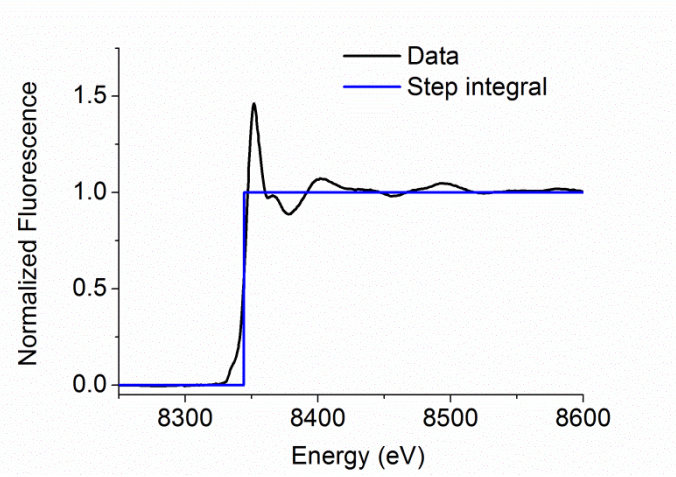

Figure 2.8. Illustration of the step function used to determine the edge position in a nickel oxide.

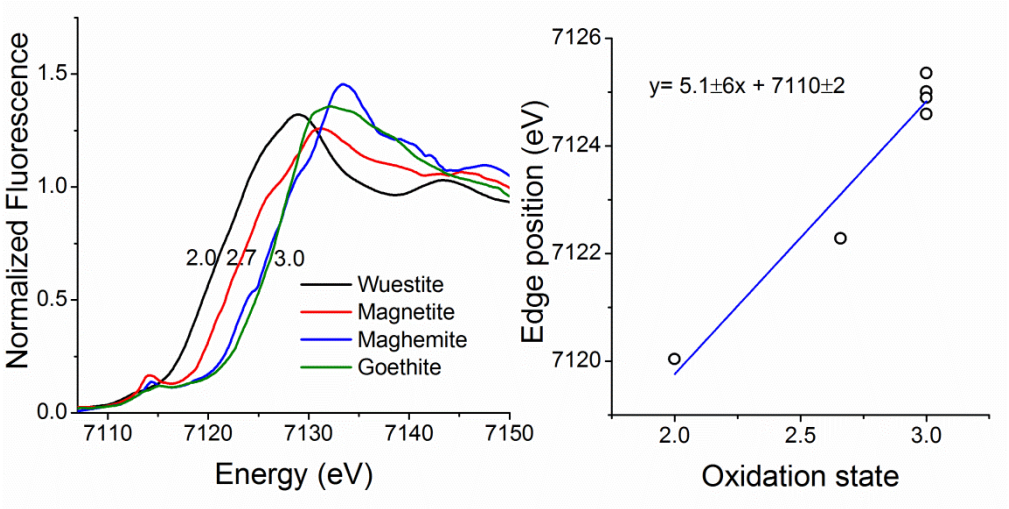

Figure 2.9. Example of reference XANES spectra used to calibrate the edge position of samples in the Fe K-edge: Westite (FeO), Magnetite (Fe_2O_3), Hematite (α-Fe_2O_3), Goethite (α-FeO(OH)) and Ferrihydride ($Fe_2O_3 \cdot 0.5\ H_2O$). The fitting of the edge position versus the oxidation state is shown in the right graph.

2.7 Extraction of the EXAFS spectra

Once the spectrum has been normalized, the data in the EXAFS region is fitted with a spline function (with number of knots between 3 and 7 depending on the sample) going through the middle of the oscillations of the data and starting from an energy about 20 eV after the rising of the edge (Figure 2.10.A). The spline function is set as the zero and represents the absorption of a single atom. Oscillations bellow the spline have a negative value and oscillations above it are positive. The spline region is cut off. The energy scale is changed to a scale respect to the edge energy as $E-E_0$, where E_0 is the edge energy (Figure 2.10.B). Then, the x axis is changed to an axis of the magnitude of the photo-electron wave vector as described in equation 2.5 (Figure 2.10.C).

In most of the cases the y axis of the spectrum is weighted by k^3 to compensate the damping of the oscillations at high k values. This corresponding k^3 weighted spectra is used to perform the simulations. The structural data can be more easily visualized, if it is Fourier transformed. The peaks observed in the Fourier transformed data correspond to every type of scatterer located at a certain distance from the absorbing atom (Figure 2.10.D). In this case the x axis is usually called reduced distance. The position of the peaks of the Fourier transform of the data usually falls at lower distances than the real distance. Usually, at higher k values the phase shift is less pronounced resulting in an effect that mimics a shorter distance when the Fourier transform is applied. This happens due to the dependence of the phase shift with k. Due to the effect of the phase shift on the geometrical distance, the data must be corrected by a theoretical or experimental standard. This is

usually performed using the FEFF program (version 8.4, self-consistent field option activated) that calculates the corresponding phase functions with theoretical models. The Fourier transform has a magnitude and a phase but normally only the magnitude is plotted, as observed in the Figure 2.10.D.

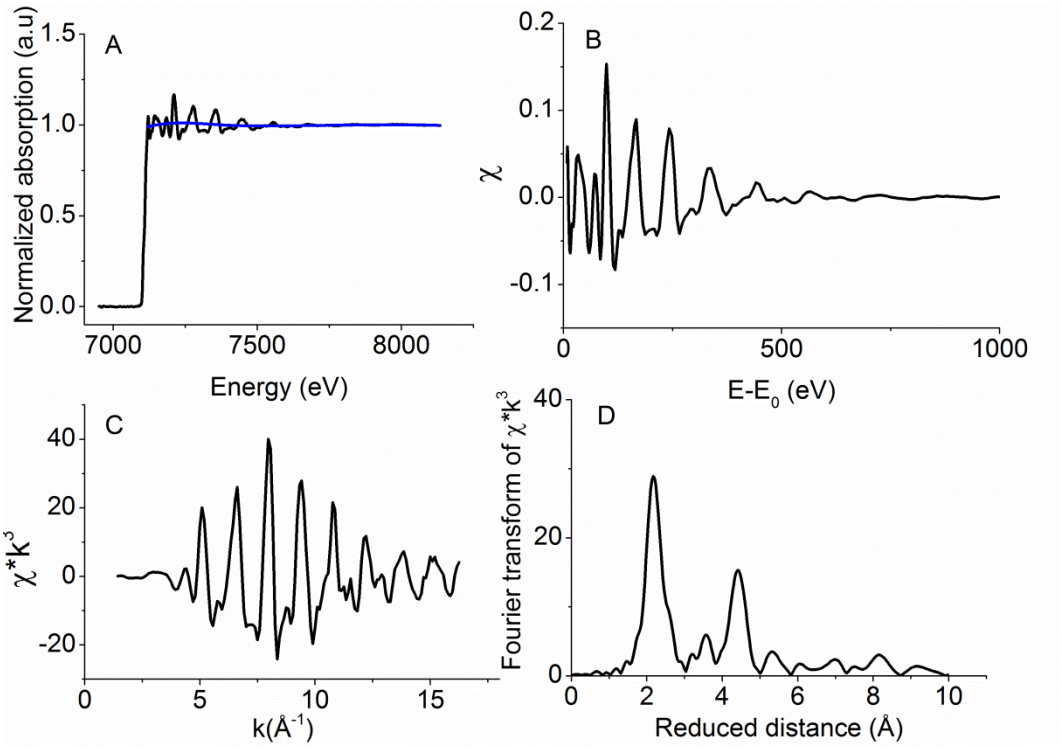

Figure 2.10. Extraction of the EXAFS data for a metallic Fe K-edge. A) Fitting of the absorption data with the spline function. B) Cut-out of the EXAFS oscillations, the so called χ spectrum. The energy axis is substituted by an energy offset $E-E_0$. C) The energy offset scale is transformed to the photo-electron wave vector and the spectrum is k^3 weighted. D) Fourier transformation of the spectrum.

Since the data available is finite, the Fourier transform also has to be calculated over a finite range of k. However, it might not be necessarily obvious which frequencies are present in that range of data, especially if the experimental set of data has abrupt ends. This means that the k range used to analyze the data might also affect the results in case it does not contain a whole number of oscillations of a certain periodic function. The solution to such a problem is to use a window function that smoothly reduces the ends of χ(E) to zero or a small value to avoid sharp discontinuities and avoid a strong dependence on the k-range chosen. Equation 2.10 represents the window function W(k) used in the simulations.

$$W(k) = \begin{cases} \left[0.5\left(1 - cos\left(\pi\frac{k-k_0}{a}\right)\right)\right]^p & \text{when } k_0 \le k < k_0 + a \\ \left[0.5\left(1 - cos\left(\pi\frac{k_n-k}{b}\right)\right)\right]^p & \text{when } k_n - b < k \le k_n \\ 1 & \text{when } k_0 + a \le k \le k_n - b \end{cases} \quad (2.10)$$

where p is the cosine exponent, k_0 and k_n are the starting and ending k-values and a and b are the starting and ending regions over which the cosine is applied:

$$a = (k_n - k_0)L$$
$$b = (k_n - k_0)R$$

L and R values of 0.1 are commonly used, meaning that the starting 10% and the ending 10% of the weighted EXAFS oscillations are dampened by the cosine function. Possible values for L and R are between 0 (no dampening) and 0.5 (strong dampening; L=R=0.5, p=1 is the Hann window). p is usually 1.

2.8 Simulation of the data

The parameters S_0^2, N_i, σ_i and R_i from the EXAFS equation (2.5) are used to simulate the specta. The phase functions were calculated using the FEFF program (version 8.4, self-consistent field option activated). Models obtained from crystal structure of appropriate reference compounds were used to generate the input coordinates for the phase function calculations. The error in the fitting was estimated according to the equation 2.11, where the error between the measured and simulated value is minimized via a least-square approach using Levernberg-Marquardt algorithm

$$\delta = \sum_i^n (m_i - e_i)^2 \quad (2.11)$$

m_i …data point of simulated EXAFS spectrum

e_i …data point of experimental EXAFS spectrum

To quantify the error in the EXAFS simulations, the Fourier-filtered R-factor described in equation (2.12) and elsewhere (Press, Teukolsky et al. 1992) was used. This factor corresponds to the relative difference in the real and simulated EXAFS spectrum after Fourier-filtering.

The filtered R-factor is calculated as

$$R_f = 100\frac{\Sigma\left|m_i^{ff} - e_i^{ff}\right|}{\Sigma\left|e_i^{ff}\right|} \quad (2.12)$$

m^{ff} and e^{ff} are the Fourier-filtered model and experimental k-weighted EXAFS curves. The sums run over all points in the fit region.

The "measurement error" can be estimated by assuming that the Fourier-filtered simulation reasonably well reproduces the Fourier-filtered experimental weighted EXAFS data. For a perfect reasonable fit, the number of degrees of freedom ν should be equal to the chi-squared value χ^2_{ff} of a fit that compares the Fourier-filtered model m^{ff} to the Fourier-filtered experiment e^{ff}:

$$\nu = \chi^2_{ff} = \frac{N'}{N}\sum_i \left(\frac{m_i^{ff} - e_i^{ff}}{\sigma}\right)^2 \quad (2.13)$$

which allows the measurement error σ to be estimated. Where N is the total number of points in these k-ranges and N´ represents the number of independent points, estimated as

$$N' = \frac{2\ \Delta R\ \Sigma\Delta k}{\pi} \quad (2.14)$$

where ΔR represents the useful R-space range. In the above formulas, $\Sigma\Delta k$ is the sum of all k-ranges being fitted. The measurement error determined in this way will depend on the number of fit parameters N_{fit} that are currently selected, because this number is used in the calculation of the degrees of freedom:

$$\nu = N' - N_{fit} \quad (2.15)$$

For each fit parameter, the respective 1σ-error range (68% confidence interval) corresponds to an increase in the normalized sum by one. The 1σ-error range was obtained from the square root of the corresponding diagonal element of the covariance matrix of the system in the Levenberg-Marquardt algorithm. This error was normalized by using the normalized error sum as a norm and calculated as:

$$\varepsilon = \nu\frac{\delta}{\sigma} \quad (2.16)$$

Chapter 3

Electrosynthesis of Biomimetic Manganese-Calcium Oxides for Water Oxidation Catalysis- Atomic Structure and Functionality

Inorganic materials mimicking the Mn_4Ca-oxo core of biological water-oxidation catalysis are of high interest. We obtained amorphous MnCa oxide films with adjustable Ca content using a simple electrochemical method involving anodic electrodeposition followed by transformation into electrocatalytically active oxide films through annealing at moderate temperatures. X-ray absorption spectroscopy (XAS) at the *K*-edges of Mn and Ca suggests an activation mechanism: The annealing causes Mn^{IV}-Mn^{III} reduction coupled to strong disordering of the birnesite-type oxides; thereby more terminal water coordination sites and likely also especially reactive metal-oxo motifs are created. Ca-XAS supports that the reactive motifs may include Mn_3CaO_4 cubanes, in close analogy to the biological catalysts. Nonetheless, Ca is inessential for water oxidation activity but rather tunes electrocatalytic properties. For increasing Ca:Mn molar ratios, both Tafel slopes and exchange current densities decrease gradually, resulting in optimal catalytic performance at Ca:Mn molar ratios close to 10%. Tracking UV-vis absorption changes during electrochemical operation suggests that inactive oxides reach their highest, all-Mn^{IV}, oxidation state already at comparably low electrode potentials. The ability to undergo redox transitions and the presence of a minority fraction of Mn(III) ions at catalytic potentials is identified as a prerequisite for catalytic activity.

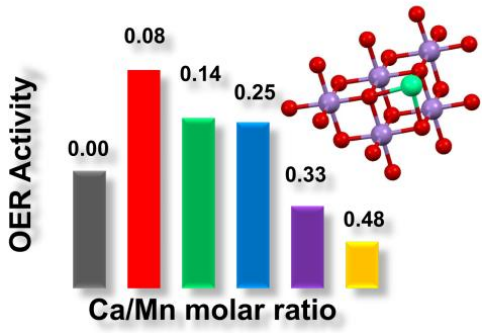

Complemented by additional information this entire chapter has been published as:

D. González-Flores, I. Zaharieva, J. Heidkamp, P. Chernev, E. Martínez-Moreno, C. Pasquini, M. R. Mohammadi, K. Klingan, U. Gernet, A. Fischer, H. Dau, *ChemSusChem* **2015**, 9(4), 379-387.

http:\\dx.doi.org\10.1002/cssc.201501399

D.G.-F. made EC, XAS, and UV-visible experiments and wrote the article

I.Z., J.H., P.C., E.M-M., C. P., M. R. M and K.K supported the synchrotron measurements

H.D. supervised and co-wrote the article

3.1 Experimental Methods

3.1.1 Materials

Reagents: ($Mn(CH_3COO)_2 \cdot 4H_2O$ (Fluka, ≥99%), H_2KPO_4 (Roth, ≥99%), K_2HPO_4 (Roth, ≥99%), $Mg(CH_3COO)_2 \cdot 4H_2O$ (Fluka, 99%), H_3BO_3, (Merck, p.A.), KOH (Sigma Aldrich, ≥86%). All reagents where used without further purification. Solutions were prepared with 18 MΩ·cm Milli-Q water.

3.1.2 Electrodeposition of the films

The electrochemical experiments were performed at room temperature using a potentiostat (SP-300, BioLogic Science Instruments) controlled by EC-Lab v10.20 software package. The metal oxide films were deposited electrochemically on glass covered with ITO (Visiontek Systems Ltd) using a three-electrode cell and constant potential of 1.99 V vs RHE applied for 15 min. The electrolyte was 0.1 mol/L borate buffer (pH 9.2) containing 0.5 mM manganese acetate. The amount of Ca incorporated was controlled by the concentration of calcium acetate added in the electrolyte. The Mn incorporated in the film was in the range of 97 ± 8 $nmolcm^{-2}$. After deposition, all films were initially essentially inactive in water oxidation. They became active after (annealing) to 210°C for 3h in air.

3.1.3 Electrochemical measurements

Catalytic activity of the cobalt oxide was tested in 0.1 M phosphate buffer (pH 7.0) solution using single-compartment three-electrode electrochemical cell. A high surface Pt mesh was used as a counter electrode and $Hg/HgSO_4$ (saturated) as a reference electrode. The electrochemical experiments were performed at room temperature using a potentiostat (SP-300, BioLogic Science Instruments) controlled by EC-Lab v10.20 software package. Test runs were carried out with the typical electrolyte resistance (incl. the electrode) of about 40 Ω; iR compensation at 85% was applied. The solution was not stirred during the experiments. In the case of the measurements in 1 M KOH a Ag/AgCl (saturated) reference electrode was used instead.

3.1.4 Ca and Mn quantification

Elemental analysis was done using the PicoFox Spectrometer (Bruker) for total reflection X-ray fluorescence (TXRF) measurements. For the Ca quantification the samples were deposited in 1 cm^2 platinum electrodes to avoid interference of In or Sn from the ITO in the measurements. The CaMn

oxides were dissolved in 500 μl of 30% HCl by exposing the films to the acid for several minutes and then 500 μL of Ga standard ($Ga(NO_3)_3$, concentration of 10 mg/l was added and 5 μL of the mixture were deposited on a silicon coated quartz glass sample plate. The acquisition time was 30 min per sample. The Ca content in the films was corrected with a calibration plot using a $CaCO_3$ (Sigma Aldrich, 99.999) standard (Figure 3.1).

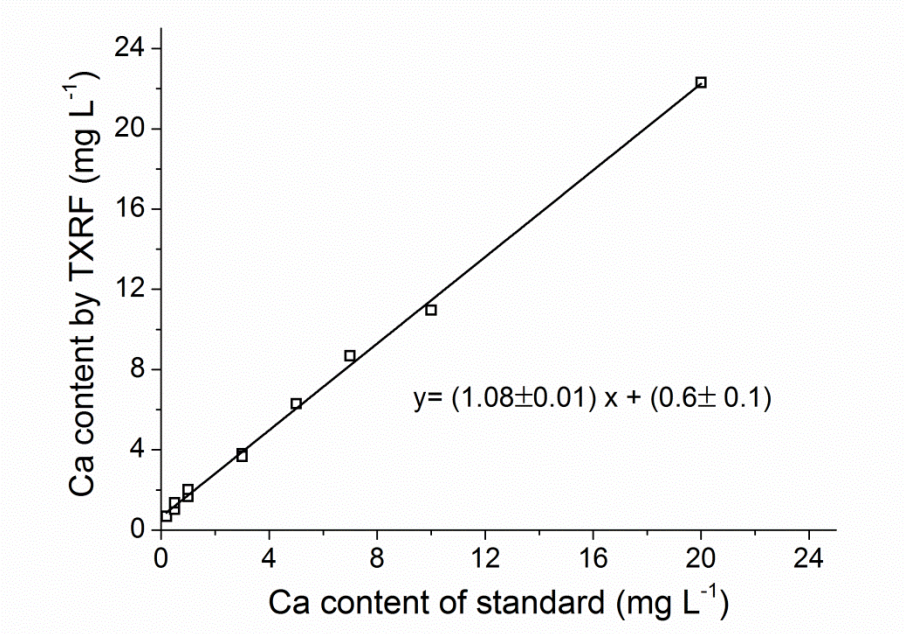

Figure 3.1. Calibration plot for the correction in the Ca content in the Ca/Mn films. The x axis shows the Ca content obtained by the measurements in the TXRF equipment; meanwhile the y axis shows the real Ca content according to the prepared $CaCO_3$ standard solutions.

3.1.5 UV-vis spectroscopy

UV-vis measurements were performed using Varian Cary 50 UV-vis Spectrophotometer according to reference (Zaharieva, Chernev et al. 2012). For these measurements the samples were deposited on transparent glass substrates covered with ITO (Visiontek Systems Ltd).

3.1.6 SEM images and elemental analysis

Scanning electron microscopy (SEM) and energy dispersive X-ray analysis (EDX) were performed with a JEOL 7401F scanning electron microscope operated at 10 kV and equipped with a Bruker Quantax 400 EDX detector.

3.1.7 XAS measurements

XAS measurements at the K-edge of manganese were performed at the KMC1 beamline at the BESSY synchrotron (Helmholtz-Zentrum Berlin, Germany) at 20 K in a liquid-helium cryostat in fluorescence detection mode employing a 13 element ultra-low energy resolving Ge detector (Canberra). The samples were deposited on glassy carbon substrates 1.5 cm^2 of glassy carbon of 100 μm thickness (HTW Hochtemperatur-Werkstoffe GmbH). The data range used in the simulation of the EXAFS spectra was the 2-12 $Å^{-1}$ k range. Further details concerning the synchrotron experiment and the EXAFS simulations are described in ref (Wiechen, Zaharieva et al. 2012).

For the measurements in the K-edge of Ca the films were deposited for 2 h on a platinum substrate (Labor platina Kft, Hungary, 99,95 % purity) to avoid interferences from Ca contaminations present in most of commercial glassy carbon substrates.

3.2 Results and Discussion

3.2.1 Electrosynthesis of the calcium-manganese oxides

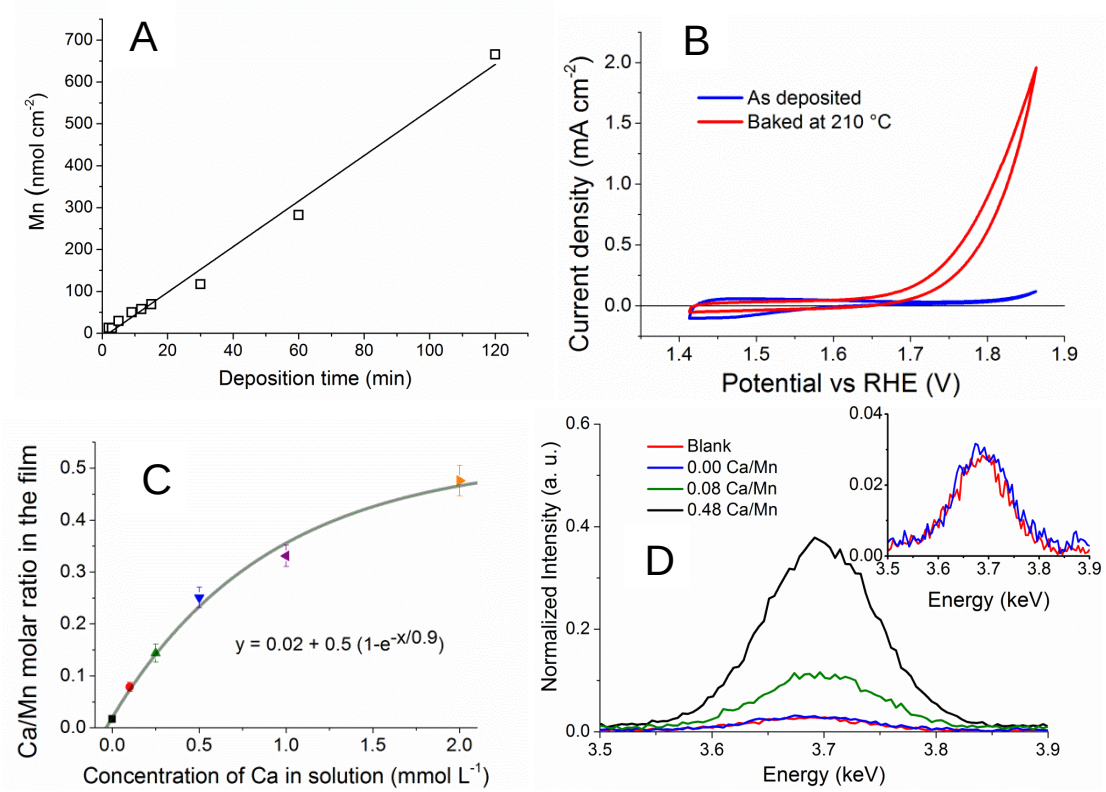

Figure 3.2. A) Quantity of manganese deposited on the film depending on the deposition time. **B)** CV for the Mn with 0.08 Ca/Mn molar ratio before and after annealing at 210 °C. Measurments at 20 mVs^{-1} scan rate in 0.1 $molL^{-1}$ and pH 7 phosphate buffer. **C)** Incorporation of Ca in the film depending on the concentration of Ca during deposition (films deposited for 15 minutes). In all cases the concentration of Mn during deposition was 0.5 $mmolL^{-1}$. The Mn incorporated in the film was in the range of 97 ± 8 $nmolcm^{-2}$. The solid line was obtained by a least-square fit assuming exponential concentration dependence **D)** Ca TXRF peak for solutions prepared by dissolution of oxide films previously deposited on blank platinum substrate (original Pt substrate, red) the 0.00 Ca/Mn sample (blue), the 0.08 Ca/Mn sample (green) and the 0.48 Ca/Mn sample (black). The intensity of the peak was normalized by the intensity of the Ga standard peak. The blank sample consists of a platinum substrate that was treated in a similar way than the catalyst films. The similarity in the Ca peak intensity for the blank sample compared to the 0.00 Ca/Mn electrode suggests that most of the Ca in this electrode results from a spurious Ca background and not from Ca incorporated into the Mn oxide.

Ca-Mn oxides were electrodeposited at constant potential in borate buffer at pH 9.2, see Figure 3.2 and Experimental section. The activity of the resulting films is low, but heat treatment at 210 °C for

3 h (in air) increases strongly the OER activity (Figure 3.2.B). This new protocol is advantageous for two reasons: (i) the quantity of material on the electrode can be controlled by the deposition time (Figure 3.2.A) and (ii) this procedure allows the controlled variation of the Ca:Mn stoichiometry by variation of the concentration of Ca in the deposition solution, as shown in Figure 3.2.C. The incorporation of Ca in the films shows a saturation behavior and can be modeled according to the equation depicted in the inset of Figure 3.2.C. Similar saturation behavior has been observed for conventional synthesis of oxide particles, with a maximal value of the Ca/Mn ratio of 0.63 (Frey, Wiechen et al. 2014). We note that a 1:1 ratio of the Mn and Ca concentrations in solution results in a molar ratio of 4:1 (Mn:Ca) in the deposited catalyst film, matching (presumably coincidentally) the Mn:Ca ratio in the biological catalyst.

3.2.2 Electrochemical characterization

Figure 3.3 shows how different Ca/Mn molar ratios (in the films) affect the catalytic function of the oxide films. The Tafel slope of the Mn-only oxide is similar to values reported before for OER catalysis in the neutral pH regime (Zaharieva, Chernev et al. 2012, Huynh, Bediako et al. 2014). The film with a Ca/Mn molar ratio of 0.08 excels by the highest overall activity, whereas the Mn-only oxide is characterized by the lowest Tafel slope. Interestingly a continuous increase of the Tafel slope is observed for increasing Ca content. We conclude that Ca affects the electrocatalytic properties of the catalyst leading to a gradual increase in Tafel slope, which may be viewed as an unfavorable consequence of Ca incorporation. However for low overpotentials and at Ca/Mn molar ratios below 0.3, the decreased Tafel slope is clearly overcompensated by a favorable increase in J_{ex}, the (formal) exchange current density. The Ca enhancing influence on J_{ex} and the opposing influence on the Tafel slope explain that there is an optimal Ca/Mn molar ratio for OER catalysis at intermediate overpotentials (around 0.08). The opposing effect of Ca ions on Tafel slope and J_{ex} likely also explains the finding of Kurz and coworkers, who found an optimal Ca content for OER catalysis (driven by chemical oxidants) of Ca-Mn oxide particles prepared conventionally by a wet synthesis route (Frey, Wiechen et al. 2014).

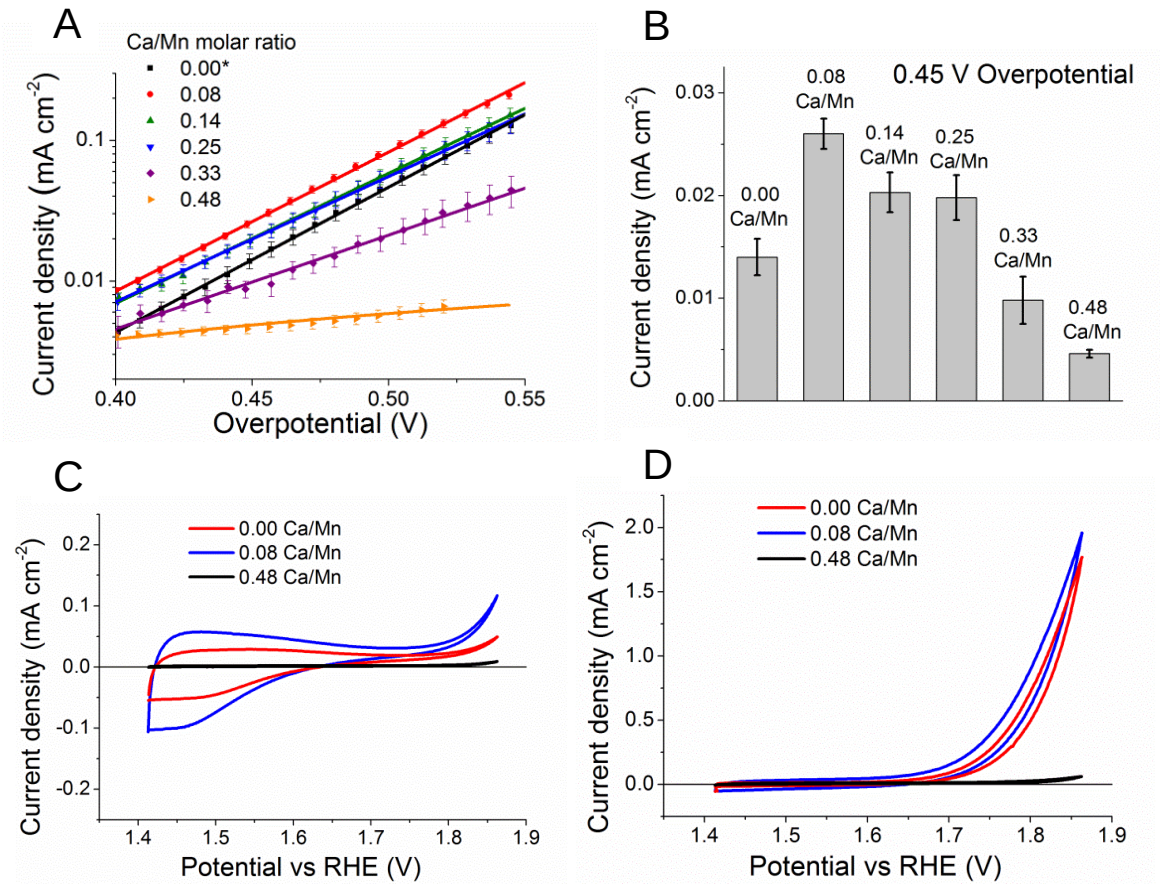

Figure 3.3. A) Tafel plots collected for films with different Ca/Mn molar ratios. The plots were collected in 0.1 mol L^{-1} phosphate buffer at pH 7 with 1 mV s^{-1} scan rate. The anodic and cathodic scan differed slightly and the respective mean value of the current density was used in the Tafel plot analysis. The plots correspond to the average of 3-7 measurements, the corresponding standard deviation is indicated. **B)** OER activity measured (current density per cm^{-2}) at 0.45 V overpotential for the different Ca/Mn molar ratios ranging from 0.0 (Mn-only film) to 0.48. **C)** CVs for oxide films in 0.1mol L^{-1} and pH 7 phosphate buffer with Ca/Mn molar ratio of 0.01, 0.08 and 0.48(20 mV s^{-1}, 2nd CV cycle, films deposited for 15 min) before and **D)** after annealing at 210 °C. Note the difference in the y-axis scaling when comparing C) and D).

Table 3.1. Tafel slope for the films with different Ca/Mn molar ratios.

Ca/Mn molar ratio	**Tafel slope (mV/decade)**
0.00	96.9 ± 0.2
0.08	101.1 ± 0.2
0.14	108.1 ± 0.4
0.25	112.2 ± 0.3
0.33	150 ± 1
0.48	649 ± 30

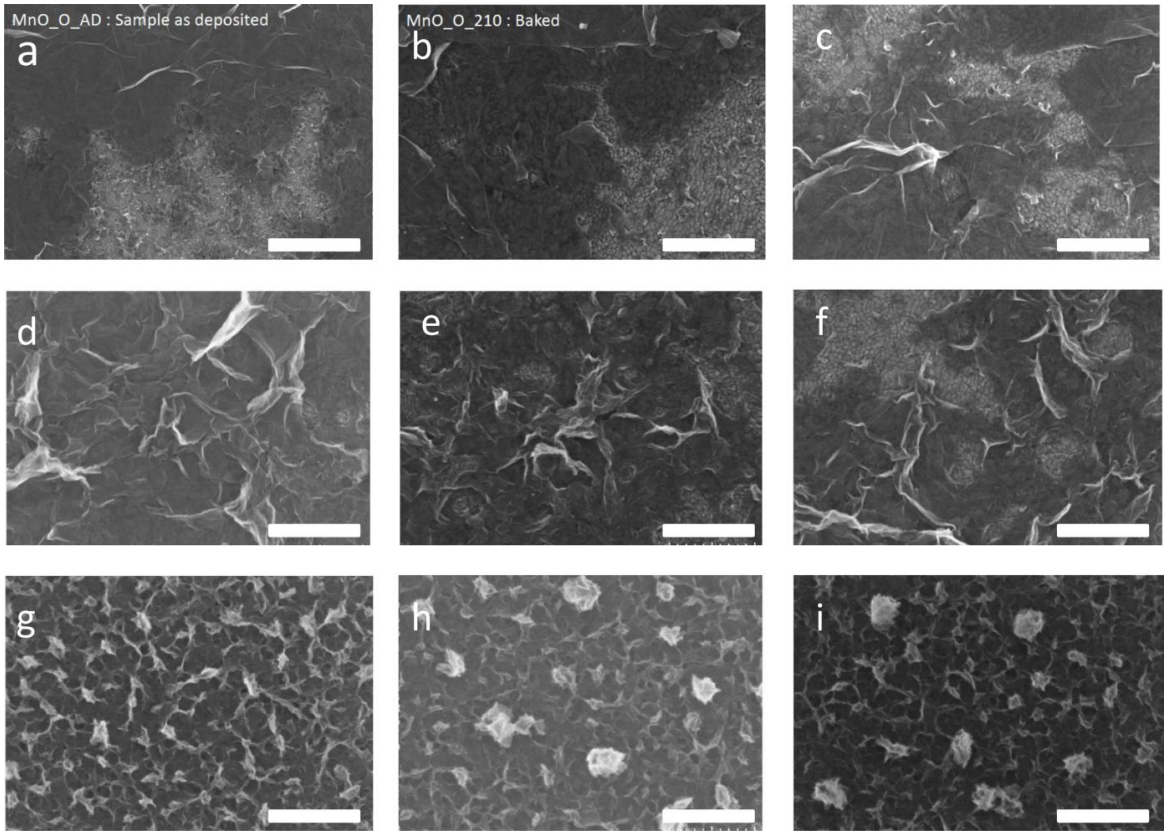

Figure 3.4. SEM image for the 0.00 Ca/Mn oxide film a) as deposited, b) after baking at 210 °C and c) after baking at 210 °C and electrochemical conditioning at 1.76 V vs RHE per 5 min. The 0.08 Ca/Mn ratio film d) as deposited, e) after baking at 210 °C and f) after baking at 210 °C and electrochemical conditioning at 1.76 V per 5 min. The 0.48 Ca/Mn ratio film d) as deposited, e) after baking at 210 °C and f) after baking at 210 °C and electrochemical conditioning at 1.76 V per 5 min. The white bar represents 300 nm.

Figure 3.4 shows SEM images for the only manganese film, the most active film and the film with higher Ca content. The images were taken for samples deposited for 15 minutes i) as prepared, ii) after heating to 210 °C and iii) samples treated with this annealing procedure and exposed to 1.76 V vs RHE for 5 min. In Figures 3.4.a, b, c, e and f portions of the ITO surface are visible. The films in the samples with only manganese and 0.08 Ca/Mn molar ratio look like thin corrugated layers of oxide. The morphology of the films changes importantly in the case of the inactive sample with higher Ca content. In this case the films look more like porous structures. Based on the images we cannot confirm any change in the samples due to the different conditionings, in all cases the morphology stays almost the same as in the samples after deposited.

3.2.3 Effect of the temperature in the catalytic activity

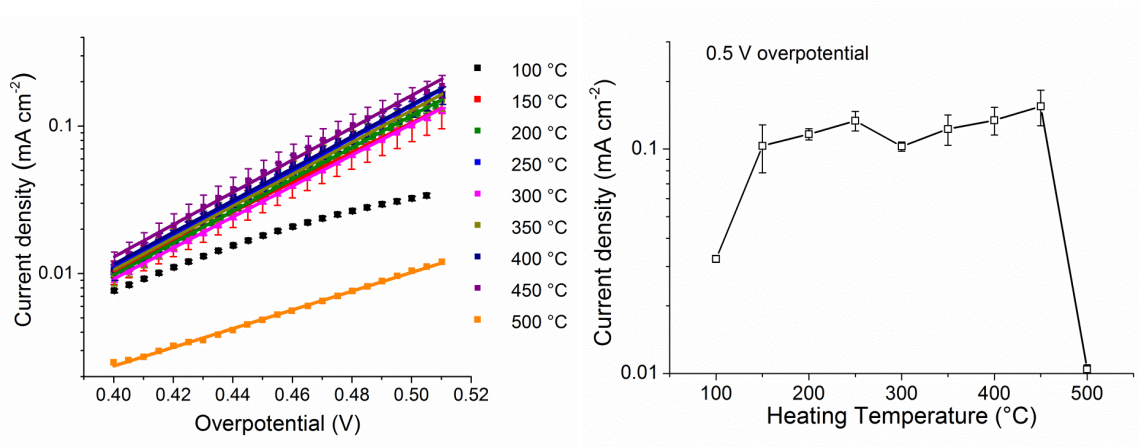

Figure 3.5. Effect of the annealing temperature in the performance of the most active 0.08 Ca/Mn molar ratio electrode. Films heated over 500 °C showed a dramatic decrease in the activity; films heated to 700 °C were melted with the glass substrate.

The beneficial effect of heat treatment (annealing) of Mn oxide films has been described previously. Zaharieva et all (Zaharieva, Chernev et al. 2012) annealed electrodeposited Mn oxides at 90 °C and reported improved catalytic activity. Spiccia and coworkers (Zhou, Izgorodin et al. 2013) studied the influence of annealing of Mn oxides at temperatures below 120°C on alkaline OER catalysis; they did not detect structural reasons for improved catalytic rates and suggested mere dehydration as an explanation. We scrutinized the effect of the heating temperature on OER activity of the 0.08 Ca/Mn film. Temperatures ranging from 150 °C to 450 °C caused a similar improvement in the catalytic activity. A further increase in the temperature resulted in a decrease of the catalytic activity (Figure 3.5). Structural changes likely explaining the improvement in catalytic activity by annealing are described further in section 3.2.6.

3.2.4 Effect of the thickness in the catalytic activity

We deposited different thicknesses of the most active (with 0.08 Ca/Mn ratio) catalyst. We observed an increase in the catalytic activity with the thickness of the deposited material. For the thicker samples we observed deviations from the Tafel behavior at high overpotentials. However, in the linear regime all samples show very similar Tafel slopes (Figure 3.6 and Table 3.2).

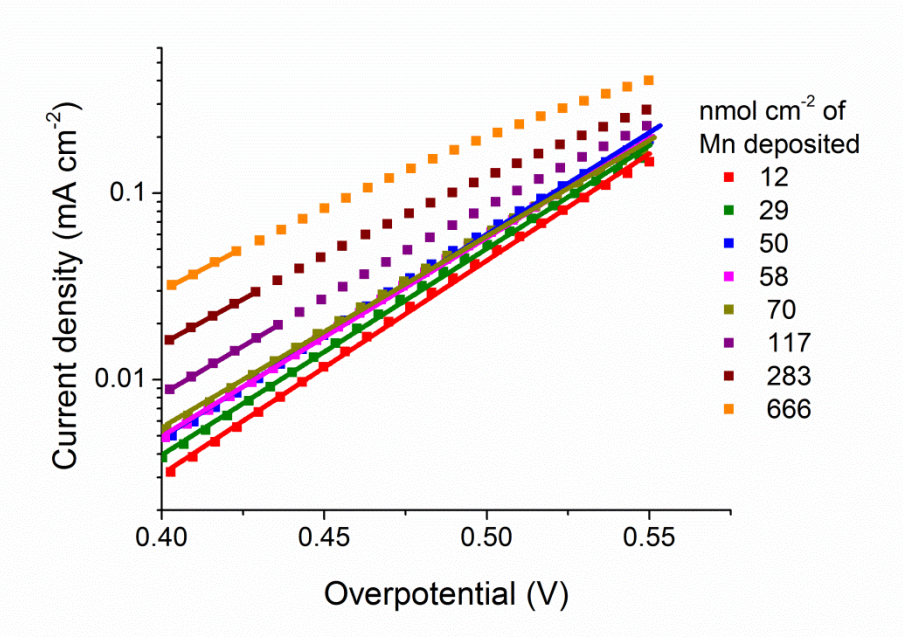

Figure 3.6. Tafel plots for Mn oxide films prepared employing different deposition times without any Ca in the deposition solution. The plots were collected in 0.1 mol L^{-1} phosphate buffer at pH 7 with a scan rate of 1 mV s^{-1}. The anodic and cathodic scan differed slightly and the respective mean value of the current density was used in the Tafel plot analysis.

Table 3.2. Tafel slopes for the Mn oxide films of different thicknesses refered to in Figure 3.6.

Deposition time (min)	Mn deposited (nmol cm^{-2})	Tafel slope (mV/decade)
2	12	87
5	29	90
9	50	92
12	58	94
15	70	97
30	117	96
60	283	104
120	666	108

3.2.5 Studies under alkaline conditions

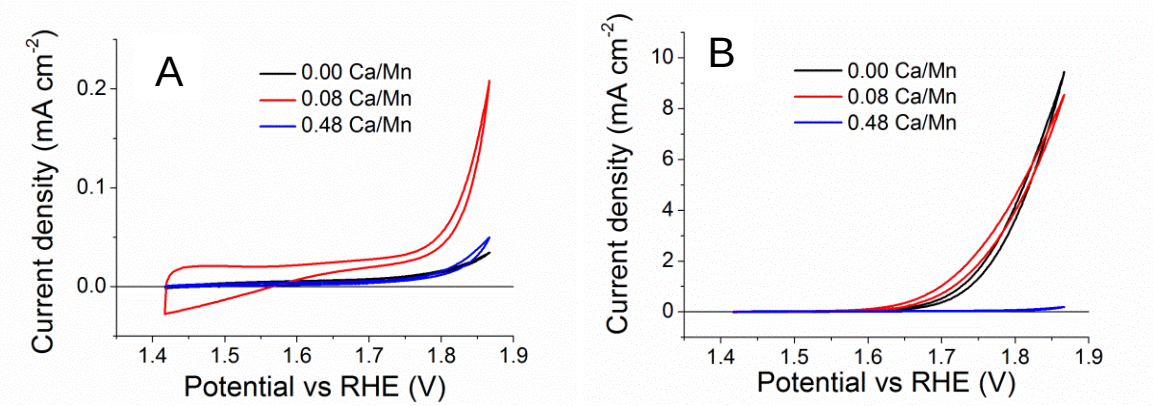

Figure 3.7. CVs for the 0.00, 0.08 and 0.48 Ca/Mn molar ratio films **A)** before and **B)** after baking at 210 °C. Measurments at 20 mVs^{-1} scan rate in 1 $molL^{-1}$ KOH (Second cycle). Measurements in samples deposited for 15 min.

To scrutinize the relationship between the Ca concentration and the OER activity of the films also in alkaline water oxidation, electrochemical experiments were performed in 1 mol L^{-1} KOH. These experiments show that the Ca content and the activation by annealing at 210°C affect the catalytic properties at pH 7 (Figure 3.3) and in the alkaline regime (Figure 3.7) in essentially the same way.

3.2.6 Structural characterization by XAS

For insight in the atomic structure and the oxidation state of the amorphous oxide films, X-ray absorption spectroscopy (XAS) measurements at the Mn *K*-edge were performed for (i) the as-deposited (inactive) oxide electrodes, (ii) the oxide films after annealing at 210°C, and (iii) the oxide electrodes after operation at 1.76 V vs RHE pH 7 in 0.1 mol L^{-1} phosphate buffer. After rapid freezing of the samples in liquid nitrogen, the XAS measurements were performed at 20 K for the oxide films on the working electrode of the electrochemical experiment (quasi-in-situ approach). The XANES (X-ray absorption near-edge structure) of the Ca-Mn oxides with molar ratios of 0.00, 0.08 and 0.48 are shown in Figure 3.8.A, B and C, respectively.

Table 3.3. Change in the oxidation state depending on the conditioning of the samples.

Condition	MnOx	0.08 Ca/Mn ratio	0.48 Ca/Mn ratio
As deposited	3.7	3.6	3.9
210 °C	3.2	3.3	3.1
after electrolysis	3.4	3.6	3.7

In the XANES spectra, the X-ray edge position reflects the mean Mn oxidation state. Mn^{III}/Mn^{IV} oxidation/reduction shifts the Mn-edge position to higher/lower energies. After calibration employing reference compounds of well-known oxidation state (MnO_2, Mn_2O_3, $MnCO_3$, MnO as well as molecular complexes) (Zaharieva, Najafpour et al. 2011), the experimentally determined X-ray edge position allows an estimate of the mean Mn oxidation state (Table 3.3). Visual inspection of the edge spectra as well as the quantitative oxidation-state estimates (summarized in Table 3.3) reveal that the annealing procedure results in reduction of Mn^{IV} to Mn^{III}. Operation at catalytic potentials, however, largely restores the high-valent Mn^{IV} oxidation state. This behaviour was observed at all Ca/Mn ratios. We note that the oxide with a Ca/Mn ratio of 0.48 shows an especially high oxidation state (close to IV), after deposition as well as after exposure to catalytic potentials.

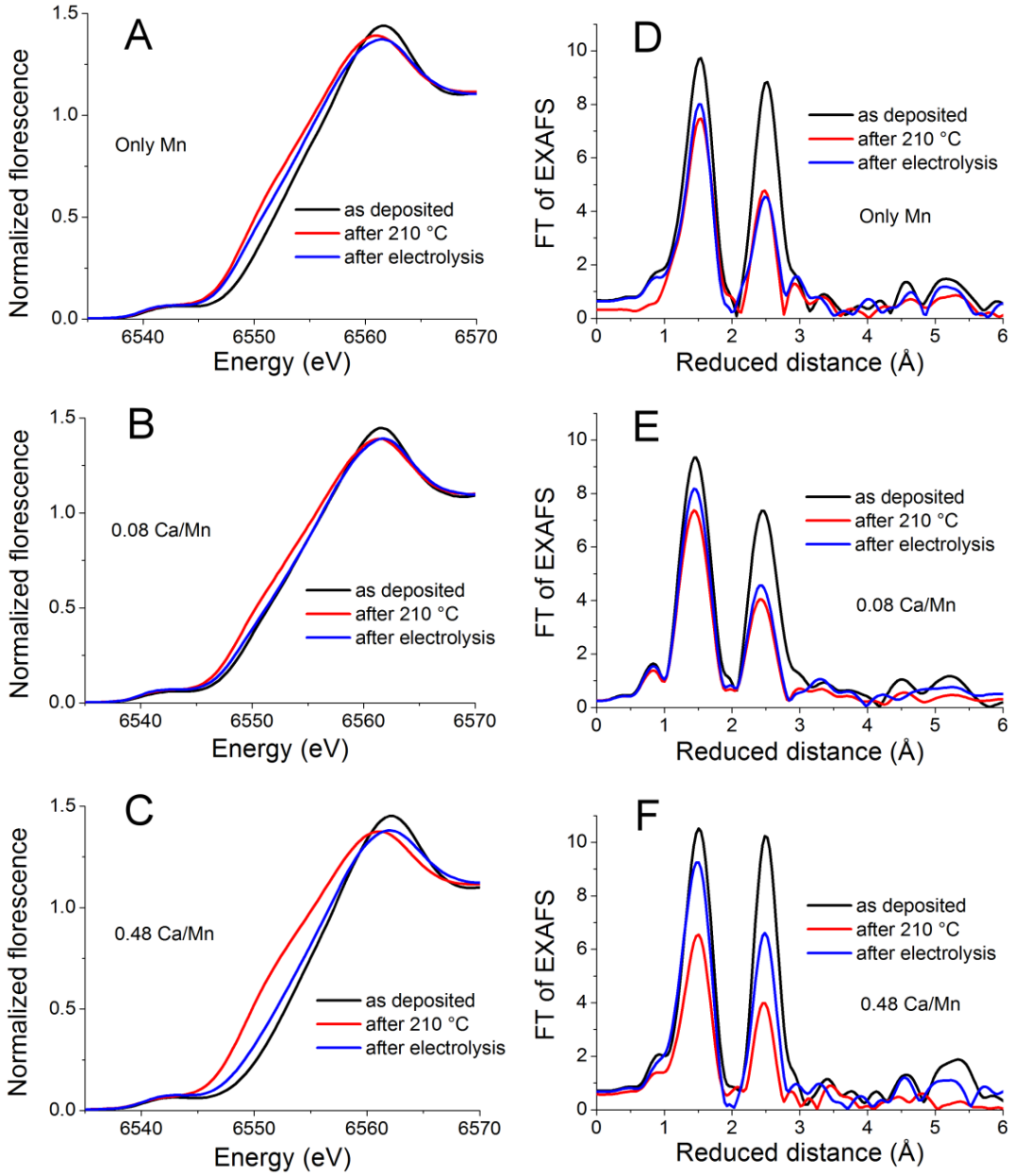

Figure 3.8. XANES spectra for the samples deposited with different Ca/Mn ratios: **A)** 0.00 Ca/Mn ratio, **B)** 0.08 Ca/Mn ratio and **C)** 0.48 Ca/Mn ratio. Fourier-transformed EXAFS spectra for **D)** 0.00 Ca/Mn ratio, **E)** 0.08 Ca/Mn ratio and **F)** 0.48 Ca/Mn ratio.The figures show the results for the samples as deposited, after baking at 210 °C for 3 h and the samples after baking and exposing them to 1.76 V vs RHE for 5 min. Measurements in the Mn K-edge with samples deposited for 15 min.

In the Fourier-transformed (FT) extended X-ray absorption fine structure (EXAFS), significant differences are visible when comparing the three states of the catalyst film (as-deposited, after annealing at 210°C and after operation at oxidizing potentials; Figure 3.8.D-F). The basic structure type, however, is the same in all herein discussed oxide films, namely amorphous birnessite-type Mn-oxides with extensive di-μ-oxo bridging between high-valent Mn ions. The same basic structure has been detected before in Mn-Ca-oxide particles (Zaharieva, Najafpour et al. 2011, Wiechen, Zaharieva et al. 2012) and electrodeposited Mn-only oxides (Zaharieva, Chernev et al. 2012, Gorlin, Lassalle-Kaiser et al. 2013).

The FT-EXAFS spectrum consists of two main peaks corresponding to Mn-O distances found in MnO_6 octahedra and to Mn-Mn distances found for di-μ-oxo bridged Mn ions, respectively. The first Mn-O (1.9 Å) distance can be simulated with one type (shell) of oxygen ligands in the as-deposited oxide. However, after annealing two types of oxygen shells are required, corresponding to Mn-O distances around 1.9 Å and around 2.3 Å, respectively. The latter distance accounts for the Jahn–Teller elongation typical for Mn^{III} ions. The simulation results confirm the XANES analysis: Annealing results in a $Mn^{IV} \rightarrow Mn^{III}$ reduction, while exposure to catalytic potentials partially restores the initial high-valent oxidation state by $Mn^{III} \rightarrow Mn^{IV}$ oxidation. The results from the simulations are shown in Figure 3.9 and Table 3.4.

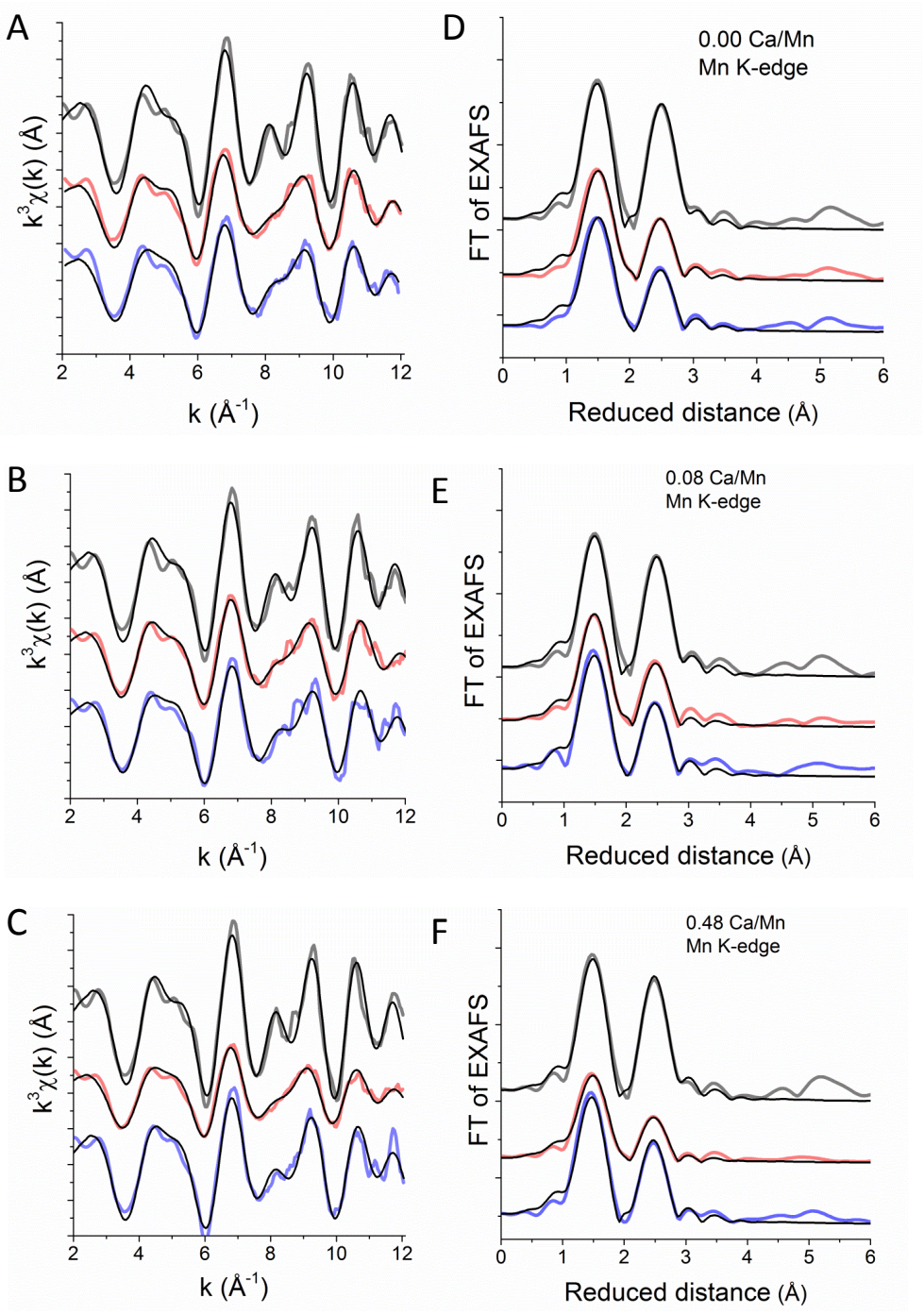

Figure 3.9. k^3-weighted EXAFS spectra of **A)** Mn-only oxide films, **B)** oxides with a Ca/Mn molar ratio of 0.08 and **C)** oxides with a Ca/Mn molar ratio of 0.48. Fourier-transformed EXAFS spectra of **D)** Mn-only oxide films, **E)** oxides with a Ca/Mn molar ratio of 0.08 and **F)** oxides with a Ca/Mn molar ratio of 0.48 (a cosine window covering 10% on the left side and 30% on the right side of the EXAFS spectra was used to suppress the side lobes in the Fourier transforms). The black lines represent the EXAFS simulations. Color code: grey, as deposited; red, after 210 °C; blue, after electrolysis (Data collected at the Mn *K*-edge).

Table 3.4. Estimated Mn-Mn μ-oxo bridge bond distances and change in the coordination number with the different conditioning procedures. The Debye–Waller parameter σ was set to 0.063 Å for all bond lengths to avoid overparametrization. The number in parenthesis corresponds to the uncertainty in the last digit. The asterisk (*) indicate the parameters which were fixed during the simulations (in the case of the second Mn-O distance the asterisk indicate that the sum of the coordination numbers of the first two shells was fixed to 6).

	Mn-O	Mn-O	Mn-Mn	Mn-Mn
0.00 Ca/Mn ratio				
as deposited				
R [Å]	1.896(4)	-	2.885(5)	3.11(2)
N	6.1(4)	-	5.2(5)	1.2(6)
after 210 °C				
R [Å]	1.909(8)	2.27(3)	2.89(1)	3.09(2)
N	4.9(2)	1.1(2)*	3.2(4)	1.8(5)
after electrolysis				
R [Å]	1.902(8)	2.30(4)	2.89(1)	3.10(2)
N	4.9(3)	1.1(3)*	2.9(4)	1.3(5)
0.08 Ca/Mn ratio				
as deposited				
R [Å]	1.901(7)	-	2.887(6)	3.16(2)
N	6.0(3)	-	5.2(4)	1.9(7)
after 210 °C				
R [Å]	1.901(9)	2.25(4)	2.87(1)	3.11(3)
N	5.1(3)	0.9(3)*	2.7(4)	1.4(6)
after electrolysis				
R [Å]	1.891(8)	2.31(5)	2.871(9)	3.14(2)
N	5.2(3)	0.8(3)*	3.3(4)	1.7(6)
0.48 Ca/Mn ratio				
as deposited				
R [Å]	1.901(7)	-	2.887(6)	3.16(2)
N	6.0(3)	-	5.2(4)	1.9(7)
after 210 °C				
R [Å]	1.901(9)	2.25(4)	2.87(1)	3.11(3)
N	5.1(3)	0.9(3)*	2.7(4)	1.4(6)
after electrolysis				
R [Å]	1.891(8)	2.31(5)	2.871(9)	3.14(2)
N	5.2(3)	0.8(3)*	3.3(4)	1.7(6)

The second FT peak corresponds to the distance vectors of about 2.89 Å length found for pairs of Mn ions connected by di-μ_3-oxo bridging. In an ideal Mn(μ-O)$_2$ oxide layer, the corresponding EXAFS coordination number ($N_{2.89}$) should be 6. The as deposited films show a value close to 6 (Table 3.4), indicating relatively well-ordered and extended Mn(μ-O)$_2$ oxide layers. The annealing

protocol, however, results in a strongly decreased value of $N_{2.89}$ implying a transition to smaller or more defect-rich Mn(μ-O)$_2$ oxide fragments. Qualitatively this decrease in $N_{2.89}$ can be concluded already by means of visual inspection of the FT-EXAFS data shown in Figure 3.8. D-F, where a pronounced decrease in the magnitude of the second FT peak is apparent; quantitative analysis is facilitated by EXAFS simulations (Table 3.4). Importantly, in the Mn-only and 0.08 Ca/Mn oxides, the long-range order is not recovered by exposure to an oxidizing potential of 1.76 V vs RHE. Only in the 0.48 Ca/Mn oxide, partial recovery of the initially high value of $N_{2.89}$ is observed, which is reflected by a significant increase in the second FT-peak upon exposure to the oxidizing potential.

From the XAS measurements at the Mn *K*-edge we conclude:

(i) The electrodeposition results in initially well-ordered Mn(μ-O)$_2$ oxide layers with a mean oxidation state close to Mn^{IV}.

(ii) Annealing at moderate temperatures (here 210 °C) does not induce formation of crystalline phases. It causes Mn reduction resulting in a mean oxidation state close to Mn^{III}.

(iii) The Mn^{IV} reduction is coupled to formation of a highly disordered Mn oxide, where the extent of di-μ-oxo bridging is comparably small. This behavior is observed at all investigated Mn/Ca stoichiometries.

(iv) Upon application of oxidizing potentials in the catalytic regime, the Mn^{IV} oxidation state is partially restored, but structurally the Mn-only and 0.08 Ca/Mn oxide remain disordered. Only at high Ca content (0.48 Ca/Mn), the return to extended fragments of Mn(μ-O)$_2$ oxide layers is observable.

In the present study, we have exclusively used a quasi-in-situ approach for XAS data collection on the complete electrolyte/catalyst/electrode assembly, which prevents modification of the water-containing oxide catalyst by vacuum exposure. At the Mn *K*-edge, this approach facilitates collection of high-quality spectra also for relatively thin oxide films, but it is associated with severe signal-to-noise problems at *K*-edges in the energy region below 5 keV. We could not collect high-quality XAS data Ca *K*-edge for MnCa oxides prepared by electrodeposition for 15 min because the total Ca amount was too low. Therefore we measured thicker films deposited for 2 h, with Ca/Mn molar ratios of 0.070±0.003 and 0.31±0.01 for the most-active and the least-active MnCa oxide, respectively. We verified that the structural and electrochemical properties of the two thick oxide films are comparable to the corresponding thin oxide films formed by electrodeposition for only 15 min (Figures 3.10, 3.11 and Table 3.5).

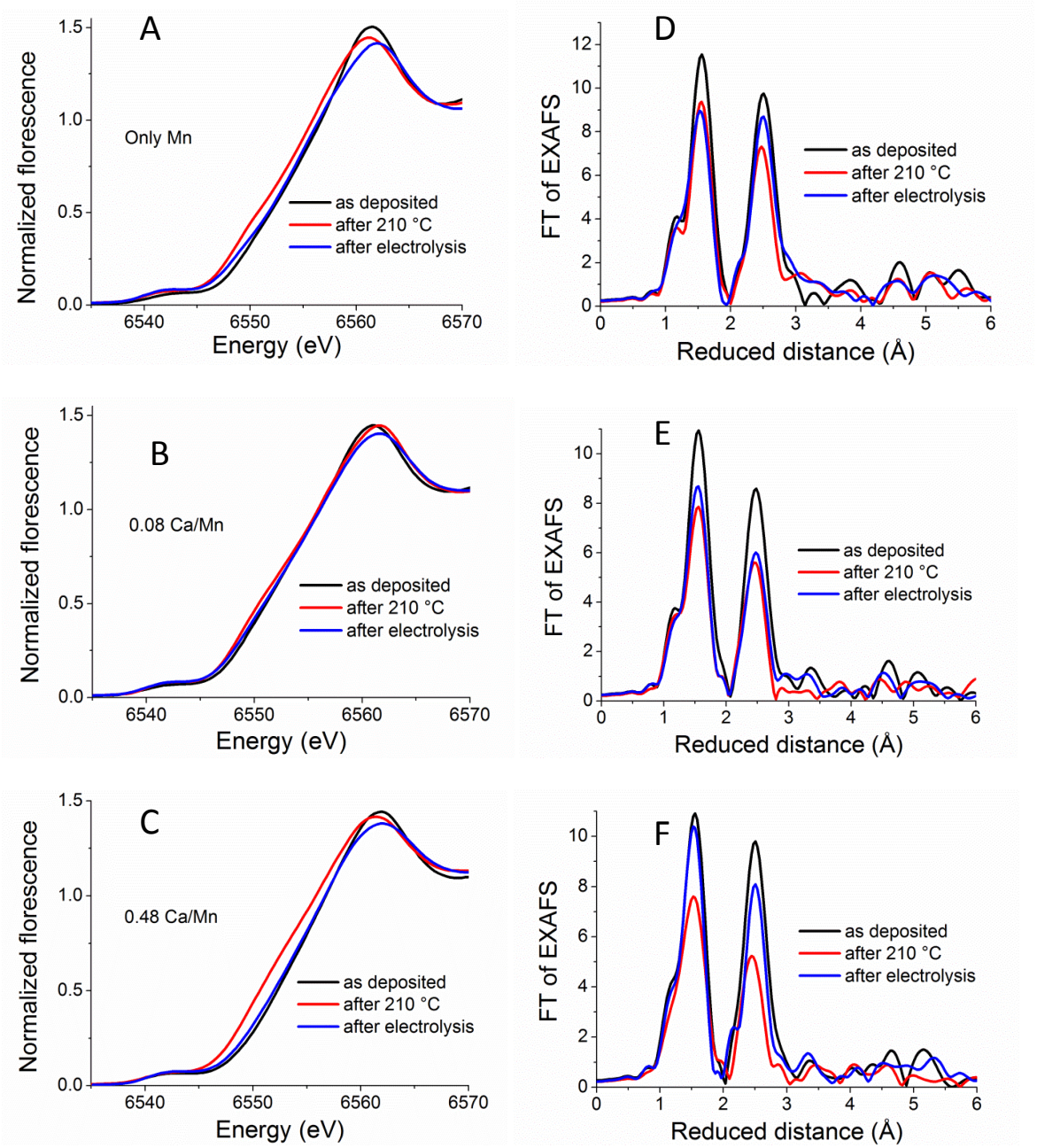

Figure 3.10. X-ray absorption data collected at the Mn *K*-edge on oxide-covered electrodes for the oxide films deposited for 2 h (thick films) with various Ca/Mn molar ratios. In A-C, XANES spectra are shown for samples with different Ca/Mn molar ratios: **A)** 0.01 Ca/Mn, **B)** 0.08 Ca/Mn, and **C)** 0.48 Ca/Mn. The corresponding Fourier-transformed EXAFS spectra are shown in **D)**, **E)** and **F)**. Each panel shows spectra for the as-deposited oxide films (black line), the oxide films after annealing for 3 h at 210°C (red line), and the annealed oxide exposed to 1.76 V vs RHE for 5 min (black line).

Table 3.5. Mean Mn oxidation states estimated from the energy position of the XANES spectra of Figure 3.10.

Condition	MnOx	0.07 Ca/Mn ratio	0.31 Ca/Mn ratio
As deposited	3.7	3.5	3.8
210 °C	3.4	3.3	3.4
210 °C + electrolysis	3.6	3.4	3.6

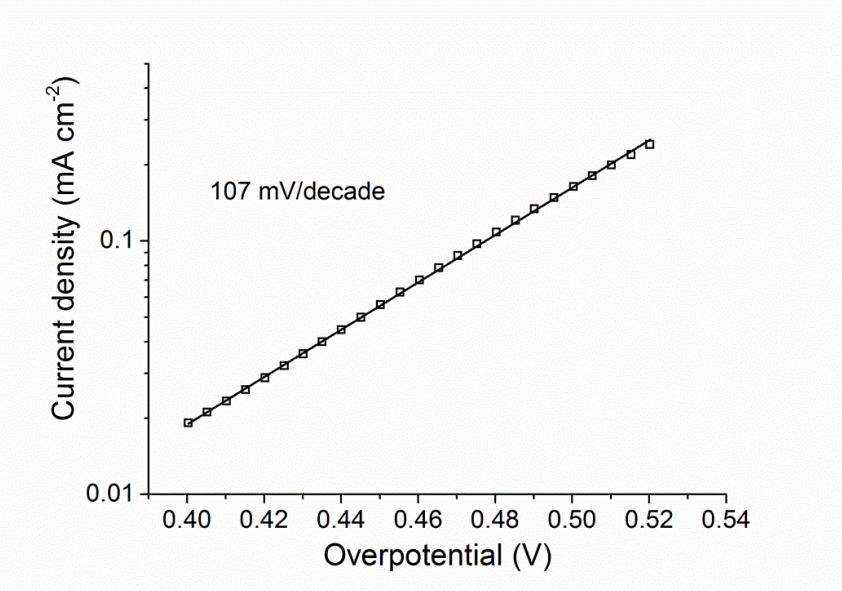

Figure 3.11. Tafel plots for the 0.07 Ca/Mn film deposited for 2h. The plots were collected in 0.1 mol L^{-1} phosphate buffer at pH 7 with 1 mV s^{-1} scan rate. The anodic and cathodic scan differed slightly and the respective mean value of the current density was used in the Tafel plot analysis.

Figures 3.12.A and 3.12.B show the Ca *K*-edge XANES spectra for the thick oxide films with Ca/Mn ratios of 0.07 and 0.31. In the 0.07 Ca/Mn film, annealing increases the magnitude of the pre-edge feature (at about 4035 eV) but decreases the intensity of the principal edge maximum (at about 4045 ev). These changes indicate a significant change in the Ca coordination environment and are clearly less pronounced in the 0.31 Ca/Mn sample. In a series of Ca model compounds with differing coordination environments, the Ca pre-edge was found to be highly sensitive to coordination number and ligand geometry of the Ca ion (Martin-Diaconescu, Gennari et al. 2015). Seven-coordinated Ca compounds in a cubane type structures showed higher pre-edge intensity when compared with non-cubane 8- and 7-coordinated compounds. The XANES spectra of ref (Martin-Diaconescu, Gennari et al. 2015) display strong similarities to the here described spectra. It

is conceivable that the XANES changes caused by annealing relate to formation of Mn_3CaO_4 motifs. This structural change may relate to most Ca ions in the low-Ca oxide, but only to a minority of Ca centers in the high-Ca oxide.

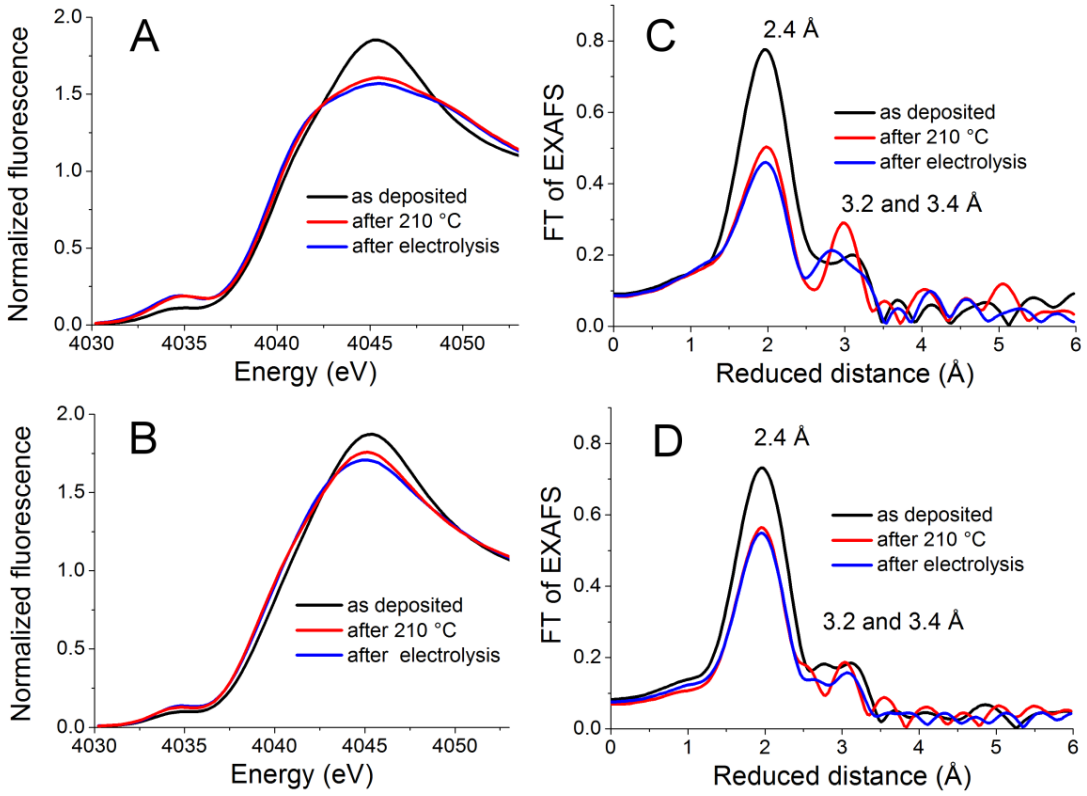

Figure 3.12. Studies in the Ca K-edge for films deposited for 2h. In this case thicker films are required to be able to measure in the Ca edge. XANES spectra for samples with Ca/Mn ratios: **A)** 0.07 Ca/Mn and **B)** 0.31 Ca/Mn. Fourier-transformed k^2 weighted EXAFS spectra for **C)** 0.07 Ca/Mn ratio and **D)** 0.31 Ca/Mn ratio. The figures show the results for the samples as deposited, after baking at 210 °C for 3 h and the samples after baking and exposing them to 1.76 V vs RHE for 5 min. The position of the edge was adjusted according to the position reported for the Ca acetate in the reference (Sowrey, Skipper et al. 2004).

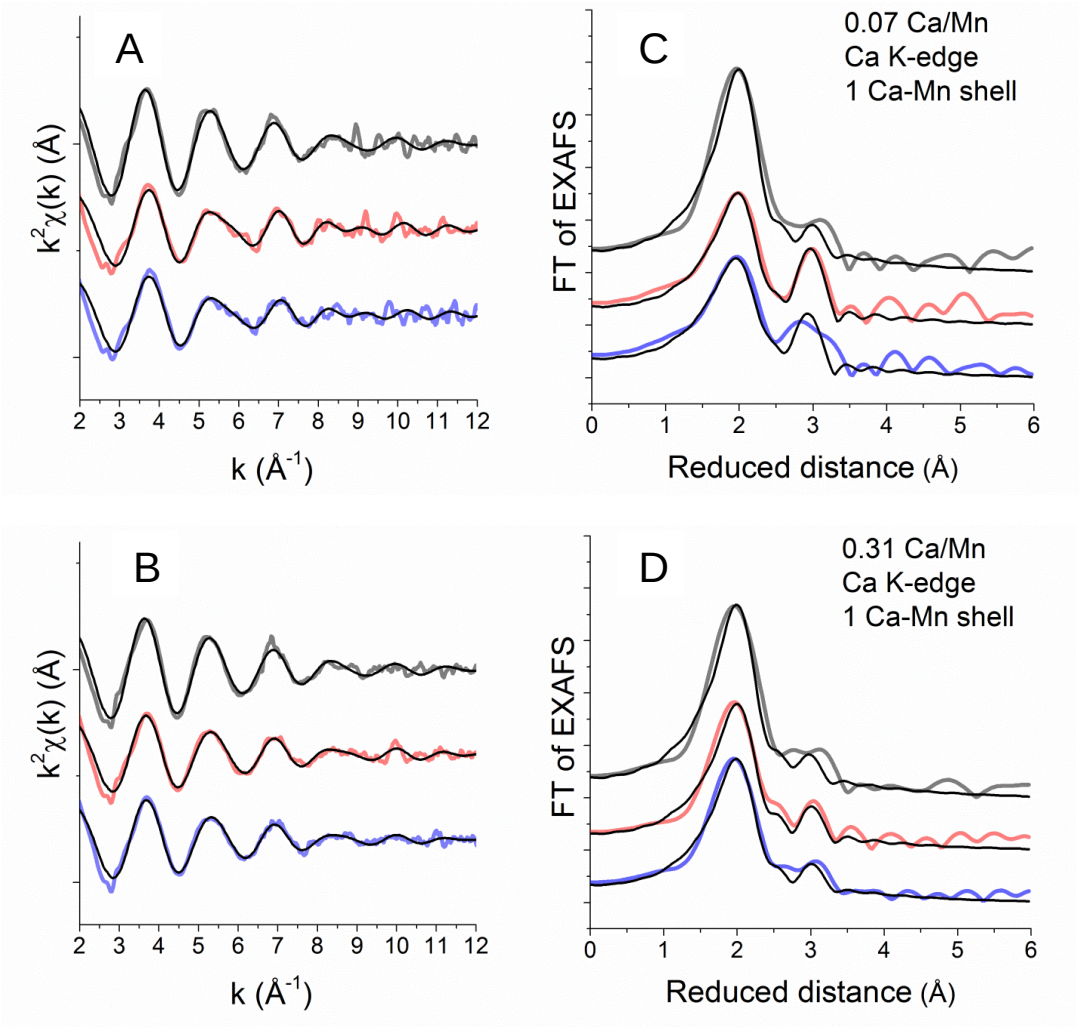

Figure 3.13. k^2-weighted EXAFS spectra of **A)** oxides with a Ca/Mn molar ratio of 0.07 and **B)** oxides with a Ca/Mn molar ratio of 0.31 (deposited for 2 h) for XAS at the Ca *K*-edge deposited. Fourier transformed EXAFS of **C)** oxides with a Ca/Mn molar ratio of 0.07 and **B)** oxides with a Ca/Mn molar ratio of 0.31. The black lines represent the EXAFS simulations. Color code: grey, as deposited; red, after 210 °C; blue, after electrolysis. **Simulations using one Ca-Mn shell are shown in black.**

Table 3.6. Bond distances and coordination numbers from EXAFS simulations. Simulation using only one Ca-Mn shell. The number in parenthesis corresponds to the uncertainty in the last digit.

	As deposited			After 210 °C			After electrolysis		
	R [Å]	**N**	**σ[Å]**	**R [Å]**	**N**	**σ[Å]**	**R [Å]**	**N**	**σ[Å]**
				0.07 Ca/Mn					
Ca-O	2.43(1)	8.7(8)	0.094(9)	2.41(2)	6.0(8)	0.10(1)	2.40(2)	6(1)	0.11(2)
Ca-Mn	3.36(4)	0.5(3)	0.0632*	3.32(2)	1.4(7)	0.07(3)	3.30(3)	1.0(3)	0.0632*
				0.31 Ca/Mn					
Ca-O	2.43(1)	8.2(6)	0.093(6)	2.42(1)	6.0(5)	0.09(1)	2.42(1)	6.3(6)	0.09(1)
Ca-Mn	3.35(3)	0.4(2)	0.0632*	3.36(2)	0.6(2)	0.0632*	3.37(3)	0.5(2)	0.0632*

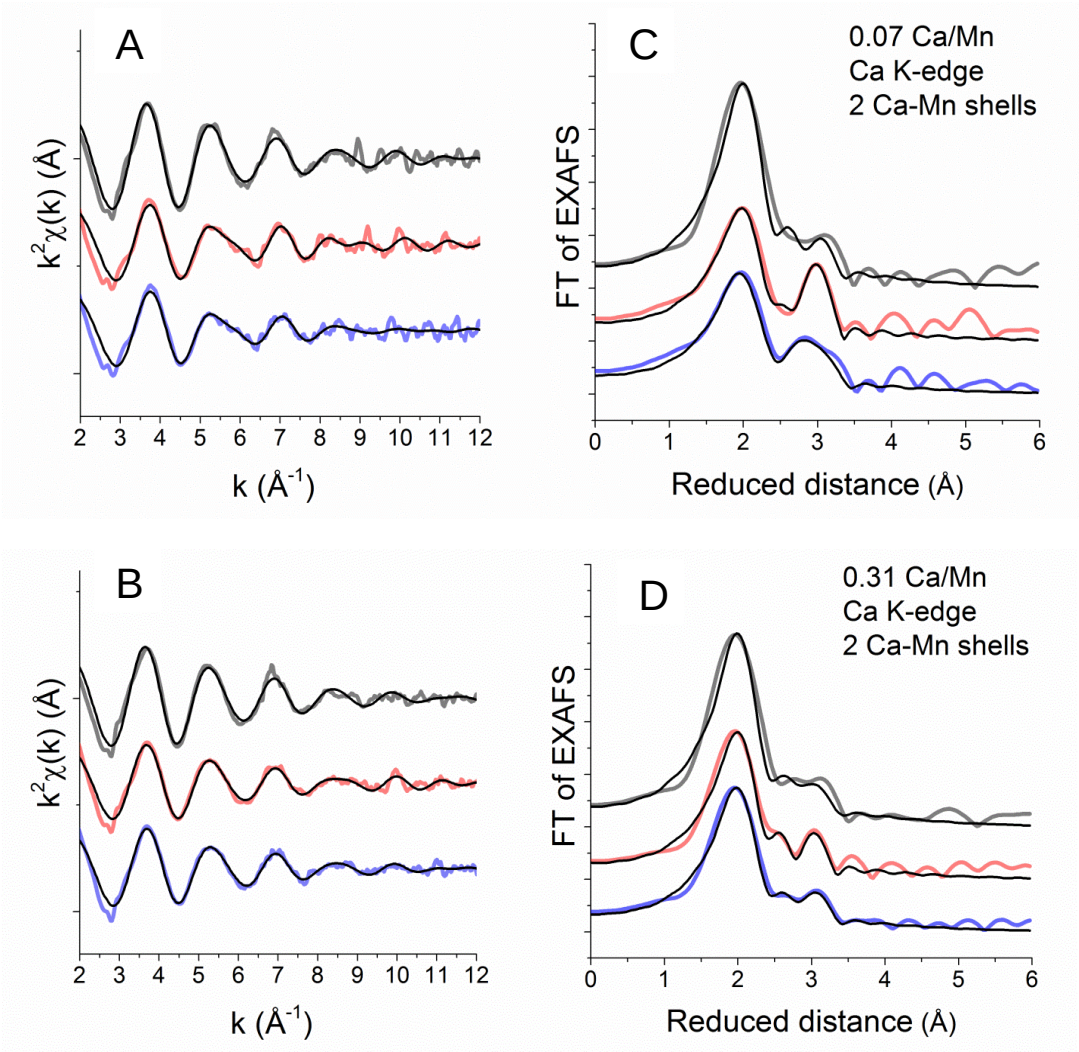

Figure 3.14. k^2-weighted EXAFS spectra of **A)** oxides with a Ca/Mn molar ratio of 0.07 and **B)** oxides with a Ca/Mn molar ratio of 0.31 (deposited for 2 h) for XAS at the Ca *K*-edge deposited. Fourier transformed EXAFS of **C)** oxides with a Ca/Mn molar ratio of 0.07 and **B)** oxides with a Ca/Mn molar ratio of 0.31. The black lines represent the EXAFS simulations. Color code: grey, as deposited; red, after 210 °C; blue, after electrolysis. **Simulations using two Ca-Mn shells are shown in black.**

Table 3.7. Bond distances and coordination numbers from EXAFS simulations. Simulation using two Ca-Mn shells. The number in parenthesis corresponds to the uncertainty in the last digit.

	As deposited			After 210 °C			After electrolysis		
	R [Å]	N	σ[Å]	R [Å]	N	σ[Å]	R [Å]	N	σ[Å]
				0.07 Ca/Mn					
Ca-O	2.43(1)	8.5(7)	0.092(8)	2.41(2)	5.9(8)	0.10(1)	2.40(2)	6.0(9)	0.11(1)
Ca-Mn	3.18(4)	0.6(4)	0.0632*	3.16(9)	0.3(4)	0.0632*	3.22(4)	1.1(4)	0.0632*
Ca-Mn	3.37(3)	1.0(4)	0.0632*	3.33(2)	1.6(4)	0.0632*	3.38(4)	1.1(4)	0.0632*
				0.31 Ca/Mn					
Ca-O	2.43(1)	8.0(7)	0.091(8)	2.42(1)	5.9(7)	0.09(1)	2.42(1)	6.2(7)	0.09(1)
Ca-Mn	3.22(5)	0.6(4)	0.0632*	3.13(4)	0.5(4)	0.0632*	3.20(6)	0.5(4)	0.0632*
Ca-Mn	3.40(4)	0.9(4)	0.0632*	3.35(3)	1.0(4)	0.0632*	3.39(4)	0.8(4)	0.0632*

The EXAFS spectra in Figure 3.12.C and 3.12.D indicate highly amorphous material; formation of an ordered CaO_xH_y phase can be excluded. Interestingly, the EXAFS spectra are similar to the ones collected for the protein-bound Mn_4CaO_5 cluster of biological water oxidation (Yachandra and Yano 2011). The Ca-Mn oxide EXAFS spectra are dominated by two main peaks corresponding to Ca-O and, most likely, Ca-Mn distances. We find that the first ligand shell is dominated by 2.4 Å Ca-O distances. Unfortunately EXAFS simulations could not provide an unambiguous determination of the Ca coordination numbers. Upon annealing, this shell becomes more disordered (more heterogeneous distance distribution) resulting in the clearly visible reduction of the magnitude of the first Fourier peak. A disordering or rather increased Ca-O distance heterogeneity also is in line with the decrease in the principal edge maximum of the XANES spectra. The second peak cannot be simulated as a Ca-Ca distance as found, e.g., in $Ca(OH)_2$ (3.6 Å). It is clearly better modeled by assuming 3.2 Å and 3.4 Å Ca-Mn distances (Figure 3.14 and Table 3.7).

Using a single Ca-O and single Ca-Mn ligand shell (Figure 3.13 and Table 3.6) gives a poor fit, which suggests that at least one additional ligand shell is required. The introduction of a second Ca-Mn shell (Figure 3.14 and Table 3.7) gives a distance of 3.2 Å, which matches the distance resolved in the measurements in the Mn K-edge. Addition of a second shell also gives a Ca-Mn distance of 3.4 Å, which corresponds well to distances observed in minerals like marokite; especially the 3.2 Å distance has been observed before in Mn_3CaO_4 cubane motifs (Zaharieva, Najafpour et al. 2011, Baktash, Zaharieva et al. 2013). We conclude that the XANES and EXAFS of the Ca-Mn oxides support the possibility of having the Ca incorporated in the structure of the Mn oxide in form of Mn_3CaO_4 cubanes or closely related structural motifs. The annealing protocol causes a restructuring resulting in a more heterogeneous coordination environment, especially in

the low-Ca oxide. These structural changes are mostly not reversed upon Mn oxidation by application of a positive potential (1.76 V vs RHE).

Our analysis of X-ray absorption data collected at the Mn and Ca *K*-edges suggests that structural changes of the oxide fragments underlie catalyst activation by low-temperature annealing. As opposed to formation of well-ordered, crystalline phases observed upon annealing to clearly higher temperatures (Najafpour, Ehrenberg et al. 2010, Baktash, Zaharieva et al. 2013), annealing results in disordering by formation of an increased number of defects in the $Mn(\mu_3\text{-}O)_2$ parent structure and/or oxide fragments of reduced size. Thereby the number of sites for terminal coordination of water species increases strongly ($Mn\text{-}OH_2$, Mn-OH, Mn=O) and special structural motifs of high reactivity may be formed. Previously it has been proposed (Zhou, Izgorodin et al. 2013) – for low-temperature annealing of electrodeposited Mn-only oxides – that dehydration of the amorphous oxide is the source of increased catalytic activity. We consider it more likely that the annealing activation relates directly to the herein reported structural changes of the oxide.

3.2.7 In-situ UV-visible measurements

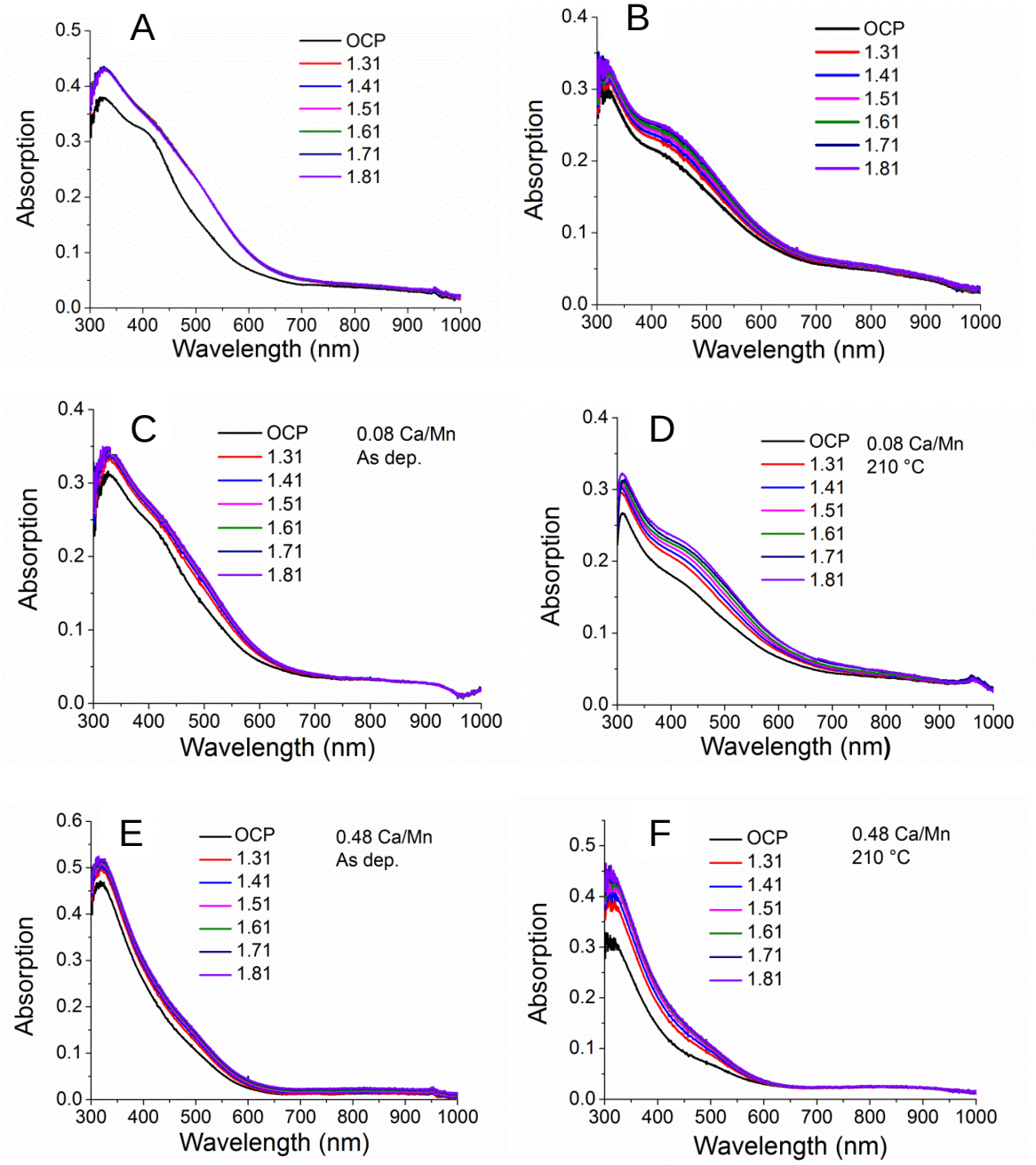

Figure 3.15. UV-vis absorption spectra of the Mn-only oxide films A) before and B) after baking at 210 °C, the 0.08 Ca/Mn ratio film C) before and D) after baking at 210 °C and the 0.48 Ca/Mn ratio film E) before and F) after baking at 210 °C. Each electrode potential was applied for 3 min prior to recording the corresponding spectrum. The open-circuit potential (OCP) was around 1.05 V vs. RHE. The oxide film had been electrodeposited for 15 min.

Previous spectro-electrochemical experiments involving UV-vis absorption studies on water-oxidizing transition metal oxides have shown that changes in absorption under applied potential can be used as a convenient *in-situ* probe of changes in the metal oxidation state (Takashima,

Hashimoto et al. 2011, Zaharieva, Chernev et al. 2012, Risch, Ringleb et al. 2015). For a structurally related Co oxide, the absorption changes were found to reflect closely oxidation state changes, with the oscillator strength increasing approximately linearly with increasing oxidation state of the transition metal (Risch, Ringleb et al. 2015).

There are differences between the UV-vis spectra of not-annealed, inactive oxide films (Figures 3.15.A, C and E), on the one hand, and annealed, OER-active oxide films (Figures 3.15.B, D and F), on the other hand. This observation confirms that the annealing results in significant structural changes which are not reversed upon application of oxidizing potentials.

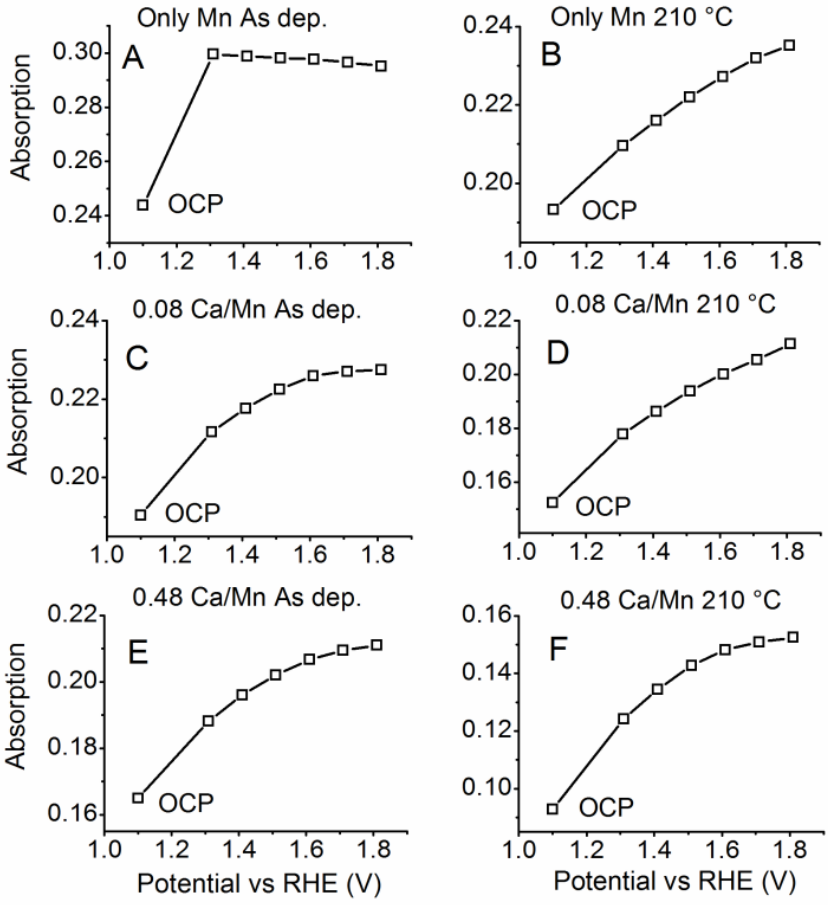

Figure 3.16. *In-situ* UV-vis experiments - potential dependence of the absorption at 450 nm for the Mn-only oxides, A) as deposited and B) after heating at 210 °C, for oxides with 0.08 Ca/Mn ratio, C) as deposited and D) after heating at 210 °C, and for oxides with 0.48 Ca/Mn, E) as deposited an F) after heating at 210 °C. The absorption values for the plots were taken from the data in Figure 3.15.

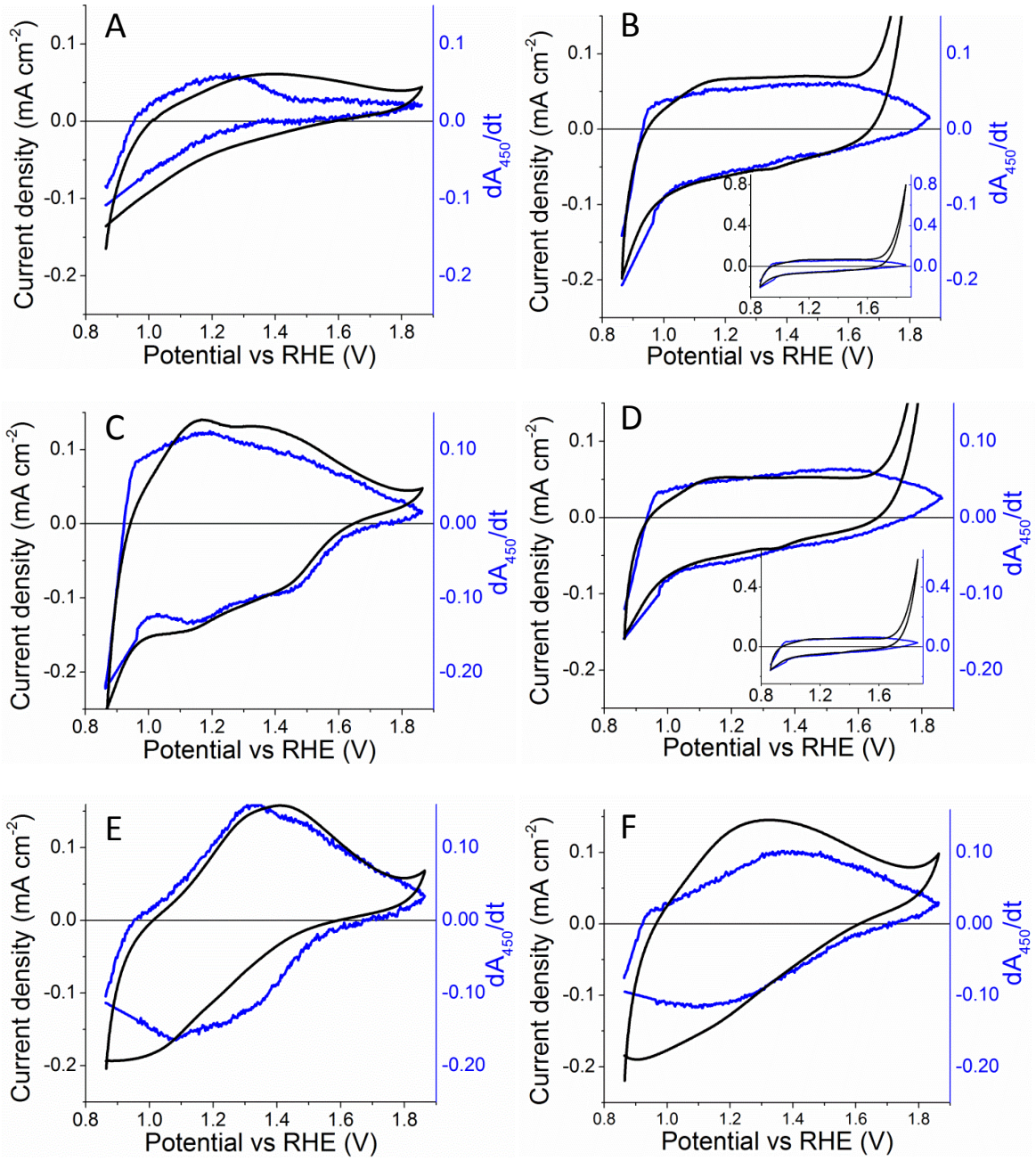

Figure 3.17. Cyclic voltammograms of the oxide films compared to simultaneously detected absorption changes. The current density is shown in black. The time derivative of the absorption at 450 nm is shown in blue. It is assumed that the absorption derivative reflects the current flow assignable to changes in the Mn oxidation state. The Mn-only oxide films before and after annealing at 210 °C are shown in **A)** and **B)**, respectively. The 0.08 Ca/Mn-ratio oxide films before and after annealing at 210 °C in B) and C), respectively. The 0.48 Ca/Mn-ratio oxide before and after annealing at 210 °C in **E)** and **F)**, respectively.

For the as-deposited Mn-only sample (Figure 3.15.A), application of 1.31 V vs RHE results in an abrupt increase in the absorption oscillator strength over the complete spectral range covered by the measurement; further increase of the potential does not cause any further changes in the spectrum. The as-deposited Ca oxides, however, respond clearly more gradually to increasingly positive potentials (Figure 3.16, A versus C and E), indicating significant changes in the redox properties caused by incorporation of Ca ions. Differences in the redox properties are also supported by the CVs shown in Figure 3.17.

Figure 3.17 compares the current density ($I = dQ/dt$, per cm^2) and the first time derivative of the absorption (dA_{450}/dt). Similarly to previous reports (Zaharieva, Chernev et al. 2012), the appropriately normalized derivative of the absorption follows closely the current and both reflect the accumulation of redox equivalents with increasing potential.

For the inactive Mn-only films (Figure 3.17.A), most of the oxidation state changes are observable below 1.31 V (vs RHE), which agrees with the results of the steady-state experiments shown in Figure 3.16.A. After annealing, the oxidation state changes detected during the CV are of increased magnitude and they also extend to higher potentials (Figure 3.17.B).

In the case of the 0.08 Ca/Mn inactive film (Figure 3.17.C), the incorporation of Ca promotes more pronounced oxidation state changes at higher potentials (more pronounced than before annealing) with two redox waves relating to midpoint potentials of about 1.15 and 1.45 V vs RHE. Similar observations have been described in Zaharieva et al (Zaharieva, Chernev et al. 2012), where the inactive films exhibited more pronounced oxidation state changes than the catalytically active ones. The catalytic currents in the 0.08 Ca/Mn oxide are strongly increase after the annealing (Figure 3.17.D), and also the shape of the derivative of the absorption becomes similar to that of the catalytically active 0.00 Ca/Mn oxide, without well separated redox waves. In clear contrast, the 0.48 Ca/Mn oxide film exhibits a completely different CV shape with only a single, exceptionally broad redox transition; its properties change only slightly after the annealing step, without increase in the catalytic activity (Figure 3.17.C and 3.17.D).

We conclude that both the steady-state and the CV absorption experiment lead to the same conclusions. Both suggest that active oxides are characterized by a gradual increase of the Mn oxidation state when increasing the applied potential within the catalytic potential regime. In clear contrast, the least-active oxide film (not annealed Mn-only oxide) shows complete saturation of the oxidation state changes already at low electrode potentials (below 1.31 V vs RHE) and no further increase in the oxidation-state level in the catalytic potential range.

In the Mn-only oxide, the annealing procedure strongly modifies the response to application of positive potentials (Figure 3.16A versus Figure 3.16B). We interpret this difference as follows: the inactive films reaches a high-valent Mn oxidation state (Mn^{IV}) already at comparatively low potentials, meanwhile active films are characterized by a gradual increase in the oxidation state within the catalytic potential range. Similar trends are observed for the 0.08 Ca/Mn and 0.48 Ca/Mn oxide films (Figure 3.16). Only for the two catalytically active oxide forms (annealed Mn-only oxide, Figure 3.16.B; 0.08 Ca/Mn oxide, Figure 3.16.C), the oscillator strength increases monotonously up to the highest applied potentials; in all the essentially inactive oxide forms (Figures 3.16 A, C, E, and F), the absorption increase saturates at about 1.6 V (or earlier in the Mn-only oxide). This finding suggests that the ability to undergo oxidation state changes at electrochemical potentials in the catalytic regime may be a prerequisite for catalytic activity. Measurements of the oxide films in 1 mol L^{-1} KOH also confirm the observations at pH 7 (Figures 3.18 and 3.19, the region of interest in Figure 3.19 is signaled in red).

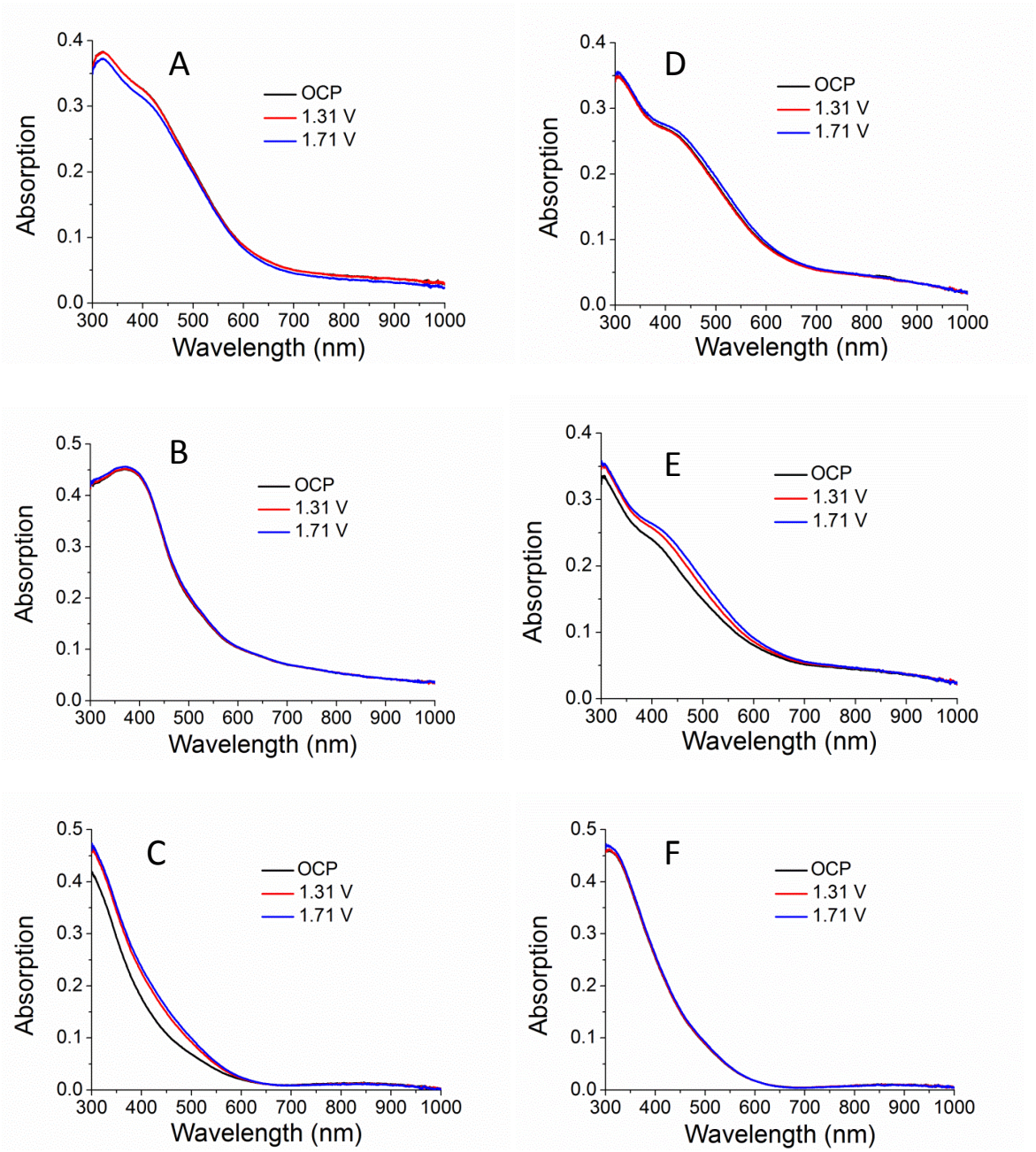

Figure 3.18. UV-vis spectro-electrochemistry by *in-situ* detection of UV-vis absorption spectra after equilibration at the indicated electrode potential (vs RHE) in KOH. Spectra of the following oxide films are shown: **A)** 0.00 Ca/Mn, **B)** 0.08 Ca/Mn, and **C)** 0.48 CaMn as deposited; **D)** 0.00 Ca/Mn, **E)** 0.08 Ca/Mn, and **F)** 0.48 Ca/Mn after 210 °C annealing. All spectra were collected in ***1 mol L^{-1} KOH*** solution; a clean ITO substrate was inserted in the spectro-electrochemical cell for recording the baseline spectrum. Each electrode potential was applied for 3 min prior to recording the corresponding spectrum. The oxide films had been electrodeposited for 15 min.

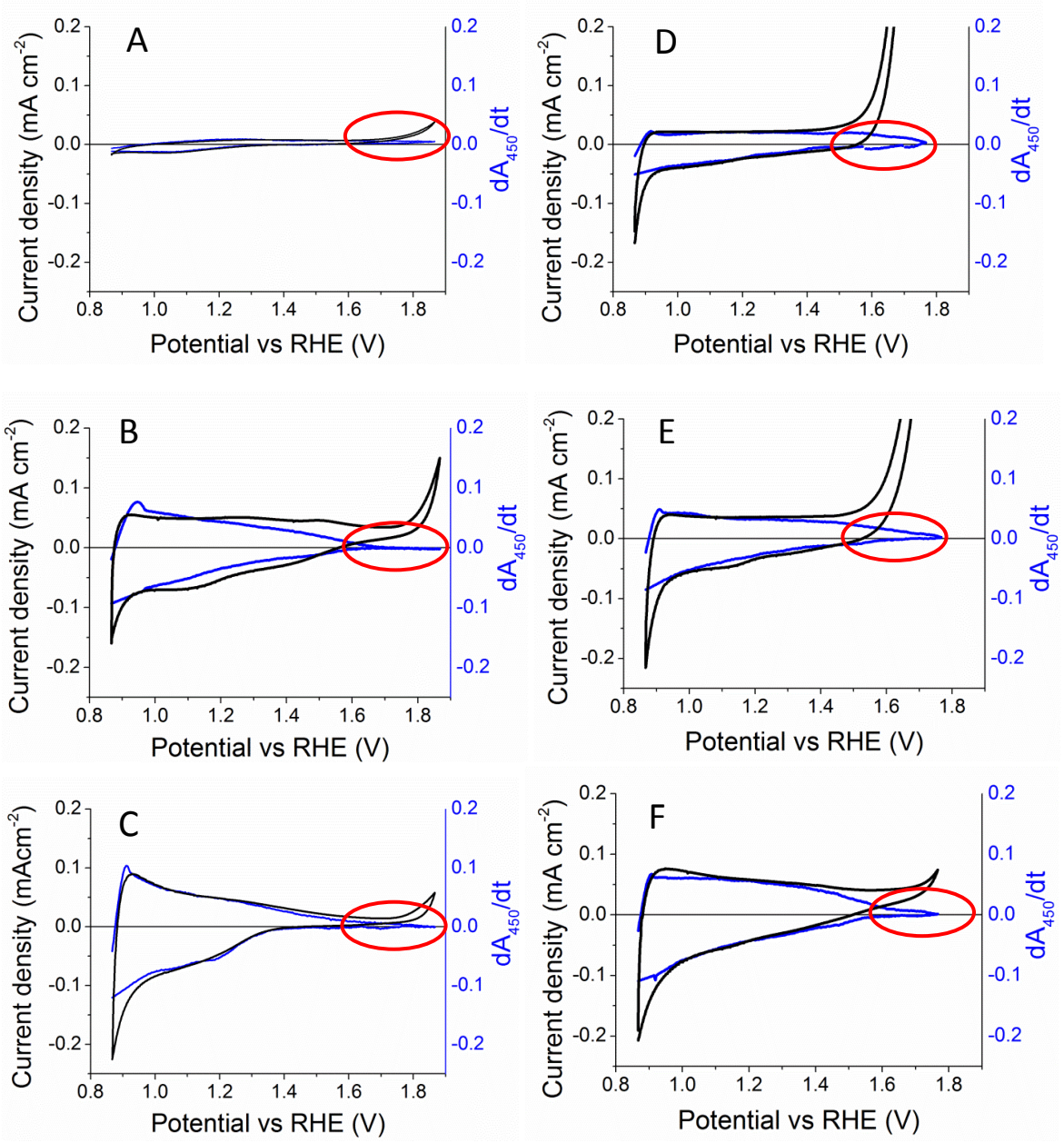

Figure 3.19. Cyclic voltammograms (black lines) and time derivatives of the absorption detected at 450 nm for the following oxide films in 1 molar KOH: **A)** 0.00 Ca/Mn, **B)** 0.08 Ca/Mn, and **C)** 0.48 CaMn as deposited; **D)** 0.00 Ca/Mn **E)** 0.08 Ca/Mn and **F)** 0.48 CaMn after 210 °C annealing. The sweep rate was 20 mV s^{-1} (second CV scan); the electrolyte was ***1 mol L^{-1} KOH***. Both the current (black line) and the absorption at 450 nm (blue line in the inset) were recorded. The derivative of the absorption reflects the current flow assignable to changes in the Mn oxidation state.

Comparison of panels A and C in Figure 3.16 suggests that Ca ions prevent the sharp increase in the oxidation state of Mn ions observed in Mn-only films at catalytic potentials. Accordingly we propose that the potentially beneficial role of Ca in these heterogeneous catalysts is the tuning of the redox potentials of Mn ions. It is indeed plausible that formation of a $Mn_3Ca(\mu\text{-}O)$ cubane by binding of a Ca^{2+} ion to $Mn_3(\mu\text{-}O)_4$ motif could render the Mn^{III}-Mn^{IV} redox potential significantly more positive. This redox-tuning role of Ca or other cations (X) is in line with synthetic model chemistry on molecular complexes comprising $Mn_3X(\mu\text{-}O)_4$ heterocubanes (Tsui and Agapie 2013) or similar metal-oxo motifs (Tsui, Tran et al. 2013). Also in the biological metal-oxo complex, the Ca ion likely will affect the redox potentials of the Mn^{III}-Mn^{IV} transition significantly (without excluding the possibility of additional roles of the Ca ion in photosynthetic water oxidation). In a recent investigation on oxidant-driven water oxidation by suspensions of Mn oxide particles, Ca was found to be a more effective promotor of water oxidation than other redox-inert cations but also the other cations could facilitate water oxidation (Wiechen, Zaharieva et al. 2012). In the present investigation and in earlier work (Zaharieva, Chernev et al. 2012), we found that additional bivalent cations are not required for water oxidation by Mn oxides, but specific active sites present only in highly disordered oxides appear to be essential. (Due to the use of a potassium phosphate buffer or KOH, we cannot exclude that a monovalent cation, namely potassium, is incorporated into the catalyst film). This means that the required redox-tuning can be achieved also in the absence of bivalent cations (see Fig. 3.16.B).

Taking into account the clear differences between the UV-vis absorption spectra of all the herein investigated Mn-based catalyst films (Figure 3.20), the relation between absolute values of the UV/vis absorption and absolute Mn oxidation states likely will be specific for each catalysts and may depend not only on atomic and electronic structure, but also on film thickness and morphology. Quantitative determination of the relation between Mn oxidation state and electrochemical potential by means of X-ray absorption experiments could clarify the issues discussed above and thus appears as highly desirable, but is beyond the scope of the present investigation.

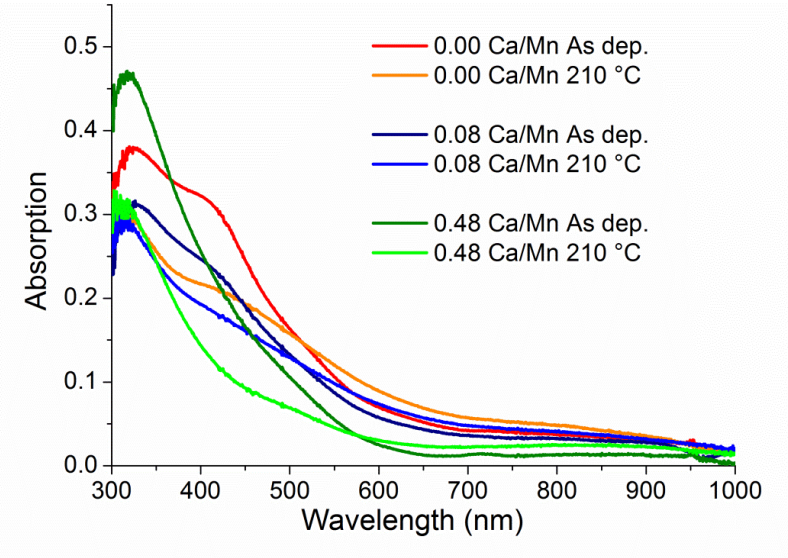

Figure 3.20. *In-situ* UV-vis absorption spectra in open-circuit-potential conditions for the samples as deposited and annealed at 210 °C. Spectra for samples with 0.00 Ca/Mn, 0.08 Ca/Mn and 0.48 Ca/Mn molar ratios are shown. The shown spectra were taken from Figure 3.15.

3.3 Summary

We synthesized Ca-Mn oxides with adjustable Ca content and film thickness using a simple electrochemical method involving anodic electrodeposition followed by annealing at moderate temperatures (150 °C to 450 °C).

All the herein described Ca-Mn oxides are amorphous at the atomic and nanoscopic level. They resemble layered manganese oxides of birnessite type with structures similar to the Mn oxide particles investigated before (Zaharieva, Najafpour et al. 2011, Wiechen, Zaharieva et al. 2012). The activation by annealing involves $Mn^{IV} \rightarrow Mn^{III}$ reduction and a pronounced decrease of the atomic order of the birnesite-like oxides resulting in (i) more terminal coordination sites for potentially reactive water species and likely also (ii) formation of especially reactive metal-oxo motifs. Application of catalytic potentials partially restores the high-valent oxidation state, but does not reverse the changes in structural order. The Ca *K*-edge XAS data support the possibility of having Ca ions incorporated in a Mn_3CaO_4 cubane, in close analogy to the biological PS II catalysts. Local structures resembling metal-oxo cubanes thus could be decisive for catalytic activity.

The electrochemical properties of the oxides are determined by the Ca:Mn molar ratio. A ratio of 0.08 results in an increase in activity while a ratio of 0.48 leads to almost complete inhibition of the

catalyst. By increasing the Ca:Mn ratio, Tafel slopes and exchange current densities are gradually increased. We conclude that the catalyst composition allows tuning of mechanistic properties.

The UV-vis in-situ experiments suggest that active oxide films are characterized by a gradual increase of the oxidation state with applied potential, whereas inactive films reach the highest oxidation state (Mn(IV)) already at comparably low electrode potentials. The ability to undergo redox transitions and the presence of a minority fraction of Mn(III) ions at catalytic potentials appears to be a prerequisite for catalytic activity.

Chapter 4

XAS Study in Screen Printed Electrodes from Pre-synthesized Ca-Birnessite

Procedures for coating conductive electrodes with pre-synthesized and structurally optimized catalyst are of general interest for the field of water splitting. Since some of these procedures might involve harsh conditions, some structural changes can be induce during coating. We present here an example case, in which synthetically optimized powders of calcium manganese oxide (Ca-birnessite) were screen printed onto conductive substrates and used as anodes in water electrolysis at pH 7. To study the effect of the screen printing procedure on the structure of the catalyst we used X-ray absorption spectroscopy measurements at the Mn K-edge. The screen printing results in the amorphisation of the birnessite structure and reduction of the Mn oxidation state compared to the original powder. Operation of the electrode restores the high valent Mn oxidation state but the structure remains amorphous. The screen-printing procedure proves to be non-innocent and important for structural and electrochemical properties of the catalyst.

Complemented by additional information this entire chapter has been published as:

S. Y. Lee, D. Gonzalez-Flores, J. Ohms, T. Trost, H. Dau, I. Zaharieva, P. Kurz, *ChemSusChem* **2014**, *7* (12), 3442-3451.
http:\\dx.doi.org\10.1002/cssc.201402533

With the original title:

Screen-Printed Calcium–Birnessite Electrodes for Water Oxidation at Neutral pH and an "Electrochemical Harriman Series"

S. Y. L., J. O., T. T. Made synthesis, electrode preparation and characterization, wrote paper
D.G.-F., I. Z. Made XAS experiments, data evaluation and contributed to the manuscript.
H.D., P.K. supervised and wrote paper.

4.1 Experimental details

4.1.1 Synthesis of the oxides

Previous studies in the group of Kurz showed that manganese-calcium oxides with formula $K_{0.20}Ca_{0.21}Mn_{2.21}$•1.4$H_2O$ prepared by a classical precipitation-comproportion methodology showed optimal catalytic activity respect to oxides with different Ca content (Frey, Wiechen et al. 2014). For this reason these samples were chosen for our study. All this samples were prepared in the group of Prof. Kurz.

4.1.2 Preparation of the electrodes

The electrodes were prepared in the laboratory of professor Kurz. The Ca-birnessite powder was synthesized as described ("$Ca_{0.21}$"), (Frey, Wiechen et al. 2014). The inks were prepared by mixing an amount of metal oxide powder (12.5 to 200 mg) with PEO (30 mg), distilled water (1 mL), acetyl acetone (0.1 mL) and Triton© X-100 (0.03 mL). The suspension was stirred for 12 h at room temperature and then a layer of ink was applied to fluorine doped tin oxide (FTO) coated glass slides (Aldrich), covering an area of 1cm² in each case. To guarantee a reproducible thickness and size of the printing, adhesive foil (thickness ~70μm) was used to cover the rest of the electrode surface. The wet electrodes were put in a cabinet dryer for 60minutes at 60°C and then sintered at 450°C for 60 min. Blank electrodes were prepared in the same way by just omitting the step of adding the metal oxide powder.

4.1.3 Electrochemical conditioning of the samples

The electrochemical experiments were performed at room temperature using a potentiostat (SP-300, BioLogic Science Instruments) controlled by EC-Lab v10.20 software package. Catalytic activity of the cobalt oxide was tested in 0.1 M phosphate buffer (pH 7.0) solution using a single-compartment three-electrode electrochemical cell. A high surface Pt mesh was used as a counter electrode and a Ag/AgCl (saturated) as reference electrode. Test runs were carried out with the typical electrolyte resistance (incl. the electrode) of about 40 Ω; iR compensation at 85% was

applied. The catalytic potential of 1.35 V versus NHE was applied for 5 h, after which the electrode was quickly frozen in liquid nitrogen.

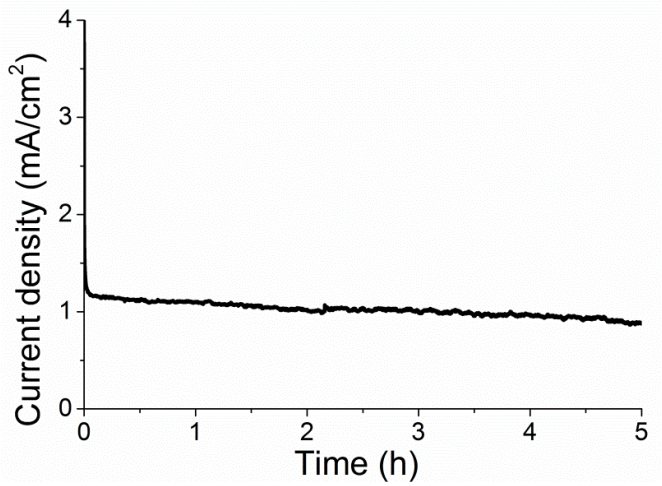

Figure 4.1. Chronoamperometry at 1.35 V versus NHE in 0.1 mol/L phosphate buffer pH 7 of the screen printed Ca-birnessite used for the XAS measurements.

4.1.4 XAS measurements

XAS measurements at the K-edge of manganese were performed at the KMC1 beamline at the BESSY synchrotron (Helmholtz-Zentrum Berlin, Germany) at 20 K in a liquid-helium cryostat. The samples were measured over FTO substrates in fluorescence mode. The data range used in the simulation of the EXAFS spectra was 3–14 $Å^{-1}$ k range. Details concerning the synchrotron experiment and the EXAFS simulations are described in reference (Zaharieva, Najafpour et al. 2011).

4.2 Results and Discussion

In the preparation of electrodes for water oxidation two main trends are common: in one hand the direct synthesis over the electrode and posterior characterization of the structure, or in the other hand, preparation of optimized materials and pasting over an electrode after the synthesis. Generally, the deposition of an already prepared material over an electrode faces a lot of stability and reproducibility challenges. Besides, most grafting methodologies result to be material specific, meaning that the same electrode preparation might not be optimal for different types of catalyst. The electrode preparation methodology can also change the structural and electrochemical properties of the original material. In this work we present a study by EXAFS of an already optimized Ca-birnessite and the effect in the structure of the screen-printing protocol used for the electrode preparation. The screen printing procedure consists in the formation of an ink that is painted over an FTO electrode and calcinated at 450°C for 60 min as described in the experimental section. This screen printed electrodes were also used to perform water electrolysis in phosphate buffer at pH 7. The importance of studying this type of catalyst is not only related to the cheap materials they are made of and the high activity they show at pH 7, but also to their structural resemblance to the $CaMn_4O_5$ cluster in PSII.

To study the structural changes of the birnessite anode material under different conditions in more detail, we performed X-ray absorption measurements at the Mn *K*-edge of the pre-synthesized Ca-birnessite powder and the screen printed electrode before and after electrochemical treatment at 1.35 V versus NHE for 5 h in 1/15M phosphate buffer (pH 7).

The XANES (X-ray absorption near-edge structure) spectra shown in Figure 4.2 indicate that the screen printing procedure causes a reduction of the average manganese oxidation state in the material from +3.6 for the synthetic oxide powder to +3.3 in the fabricated anode. However, electrochemical operation of the electrode at +1.35 V versus NHE in phosphate buffer (pH7) for 5h increases the oxidation state back to +3.6 (The average Mn oxidation state were determined by comparison of the Mn K-edge-energy positions with those of MnO_2, Mn_2O_3 and $MnCO_3$ reference compounds as reported before (Zaharieva, Najafpour et al. 2011)).

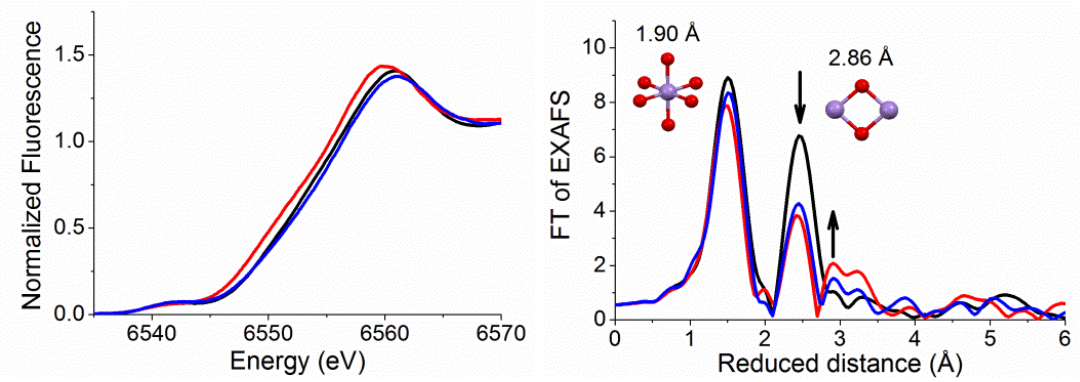

Figure 4.2. *left:* Mn *K*-edge XANES and *right:* Fourier-transformed EXAFS spectra for the Ca-birnessite oxides. Color code: black: pre-synthesized Ca-birnessite powder used for the ink preparation; red: Ca-birnessite-coated FTO electrode; blue: anode after 5 h of electrolysis at +1.35 V versus NHE at pH 7.

The birnessite structure of the synthetic material can be confirmed by the characteristic shape of the EXAFS (extended X-ray absorption fine structure) spectrum. As illustrated in Figure 4.2, the Fourier-transformed EXAFS spectrum is dominated by two main peaks, corresponding to the Mn-O distance in MnO_6 octahedra and the short Mn-Mn distance in di-μ-oxo bridged Mn ions respectively.

After the screen printing procedure and even after 5h of water electrolysis, the EXAFS data provides evidence that the material in general keep their amorphous birnessite-type structures, but there are also some modifications. First the screen-printing results in a decrease of the amplitude of the second peak (di-μ-oxido Mn-Mn distance, left arrow in Figure 4.2), and this change is not reversed after applying an oxidizing potential of +1.35 V versus NHE. In addition a third peak at higher reduced distance appears, which has been observed before in Mn anodes at water-oxidation conditions.

The described changes can be quantitatively analysed by simulations resulting in the data shown in Table 4.1. To obtain these values, we performed a joint fit of the three spectra keeping the number of shells and interatomic distances constant for all samples. The first peak (Mn-O distance) was simulated by two shells (1.90 Å and 2.28 Å) to account for the Jahn-Teller elongation typical for Mn^{III} ions. The sum of the coordination numbers in these two shells was fixed to 6, thus assuming an octahedral coordination for all Mn centres. The small increase of the fraction of longer Mn-O distances after screen-printing from 0.5 to 0.7 corresponds to the decrease in the average oxidation state (and thus an increase of the fraction of Mn^{III} ions) already observed in the XANES spectra.

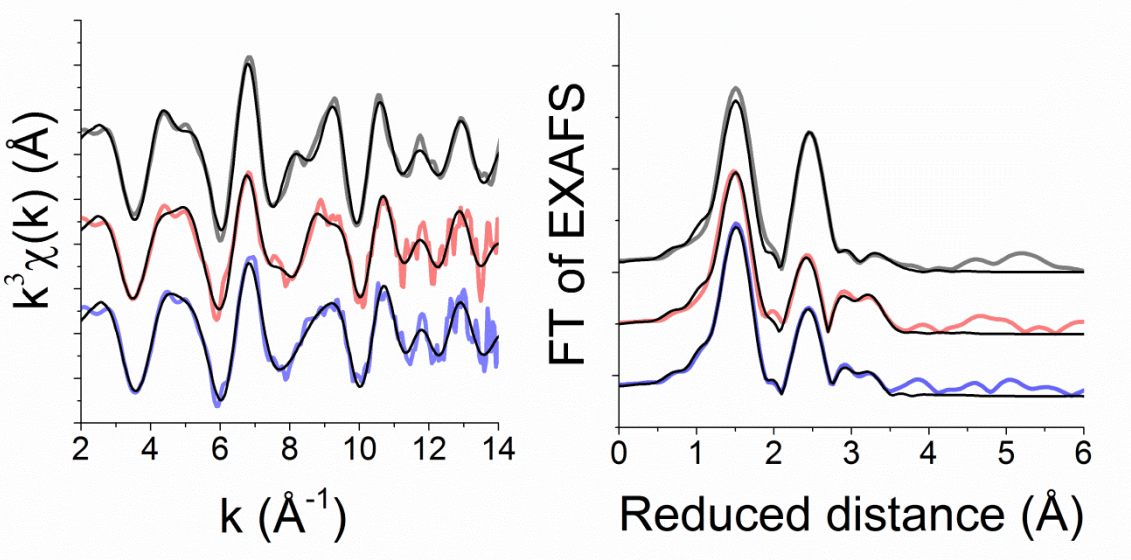

Figure 4.3. ***Left:*** *k^3-weighted* EXAFS spectra of Ca-birnessite at the Mn *K*-edge. ***Right***: Fourier-transformed EXAFS spectra of the Ca-birnessite oxides. The black lines represent the EXAFS simulations.Color code: grey: pre-synthesized Ca-birnessite powder used in the ink preparation; red: Ca-birnessite-coated FTO electrode; blue: anode after 5 h of electrolysis at +1.35 V versus NHE and pH 7.

Table 4.1. Coordination numbers and interatomic distances obtained by simulation of the k^3-weighted EXAFS spectra. The errors represent the 68% confidence interval of the respective fit parameter. The asterisk (*) indicate the parameters which were fixed during the simulations (in the case of the second Mn-O distance the asterisk indicate that the sum of the coordination numbers of the first two shells was fixed to 6). The Debye–Waller parameter, σ, was set to 0.063 Å for all bond distances to avoid overparametrization.

	R [Å]	pre-synthesized Ca-birnessite powder	Ca-birnessite-coated FTO electrode	anode after 5h of electrolysis at +1.35 V at pH 7
Mn-O	1.903(2)	5.5(1)	5.3(1)	5.4(1)
Mn-O	2.28(2)	0.5*	0.7*	0.6*
Mn-Mn	2.861(8)	4.3(4)	2.5(5)	2.7(3)
Mn-Mn	2.98(2)	2.0(4)	2.0(4)	1.5(4)
Mn-Ca	3.19(1)	1.8(4)	3.2(4)	2.3(4)
Mn-Ca	3.45(1)	0.0(3)	1.6(4)	0.9(4)
Mn-Ca	3.86(2)	0.9(4)	1.0(4)	0.2(4)

The second peak corresponds to di-µ-oxo bridges between the Mn atoms and similar to previous analysis (Wiechen, Zaharieva et al. 2012, Bergmann, Zaharieva et al. 2013), it was also simulated with two shells (2.86 Å and 2.98 Å). In a perfectly ordered birnessite structure consisting of layers of MnO_6-octahedra, the number of these short Mn-Mn distances per Mn ion should be 6 as found in the pre-synthesized material (Table 4.1). For the electrode coatings, the number of these vectors is markedly decreased to a total of about 4.5 which indicates a disruption in the long range order of the material. Unlike the oxidation state, this decrease of long-range order is not reversed under water oxidation conditions.

The longer metal-metal distances were simulated assuming backscattering by Ca^{+2} ions, but the possibility that Mn ions also contribute to these positions cannot be ruled out (if Mn is considered as backscatterer, the resulting distances are about 0.05 Å shorter). Here, we used three Mn-Ca shells for the simulations. The short (3.1 Å) and long (3.8 Å) distances were already identify before (Zaharieva, Najafpour et al. 2011) in catalytically active Mn-Ca oxide materials and have been assigned to two different binding positions for Ca^{+2} relative to Mn: a) a cubane-type $CaMn_3O_4$-motif (short distance) and b) the capping of vacancies of the birnessite layer created by missing Mn ions (long distance). As it can be seen in Table 4.1, there is a tendency to increase the number of these metal-metal vector for the electrode coatings in comparison to the synthesized oxide. However, the simulation results do not allow making an unambiguous statement about this change.

More significant is the appearance of the third, intermediate metal-metal distance (3.3 Å), which is absent in the starting materials and also in most of the previously investigated Mn-Ca oxides. Interestingly, such a third peak has been observed in the FT-EXAFS spectra of Mn-Ca oxides prepared by an alternative synthesis route and also in non-Ca^{+2} containing, electrochemically deposited Mn oxide films (Bergmann, Zaharieva et al. 2013). There, the intermediate metal-metal distance has been assigned to mono µ-oxido bridged Mn ions typical of oxides with tunnel structures and were found to affect both the electrocatalytic properties (Tafel slopes) and probably also the proton conductivity of the Mn oxide catalyst.

4.3 Summary

In conclusion, the presented characterization data clearly shows that the manganese oxides used to prepare the coated electrodes are birnessite-type, highly disordered, layered calcium manganese oxides with average Mn oxidation states of about +3.6. These general characteristics are neither affected by the screen-printing process nor by extended operation as water-oxidation anodes at pH

7. However, from a detailed look at the XAS spectra it can be concluded that fabrication method causes Mn reduction to +3.3 and clear order decrease (less di- μ-oxo-connnected Mn ions) which are accompanied by the appearance of an additional structural motif (3.45 Å metal-metal distance). Upon extended operation as anode for water-oxidation, the original Mn oxidation state of +3.6 is restored, but the structure remains less ordered in comparison to the starting material. The obtained results are in line with the discussion in chapter three and suggest the possibility of activation behaviour caused by the heating procedure also in this case with pre-synthesized Ca-birnessites.

Heterogeneous Water Oxidation: Surface Activity versus Amorphization Activation in Cobalt Phosphate Catalysts

In rationale development of catalyst for heterogeneous water oxidation, one basic question awaiting clarification is the role of surface reactivity versus catalysis within the bulk volume of the solid material. This question is addressed experimentally by synthesis and investigation of crystallites of pakhomovskyite ($Co_3(PO_4)_2 \cdot 8H_2O$, Pak). X-ray absorption spectroscopy reveals that exposure to oxidizing potentials transforms the initially crystalline Pak slowly (5-8 h) but completely into the amorphous phosphate-containing cobalt oxide (CoCat). Electrochemical analysis supports high-TOF surface activity in the initial crystalline state of Pak, whereas its amorphisation results in dominating volume activity of the thereby formed CoCat material. In conclusion, a complete picture of heterogeneous water oxidation catalysis by transition metal oxides requires insight in (i) catalysis at the electrolyte-exposed 'outer surface' of the oxide material, (ii) catalysis within an amorphous and hydrated volume phase, (iii) the modes and kinetics of restructuring and amorphisation of the catalyst material upon catalytic operation.

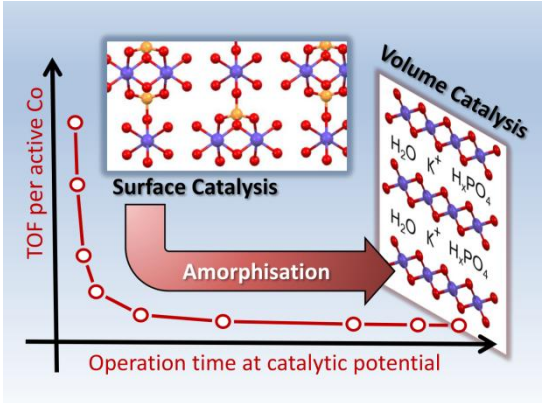

Complemented by additional information this entire chapter has been published as:

D. González-Flores, I. Sánchez , I. Zaharieva, K. Klingan, J. Heidkamp, P. Chernev, P.W. Menezes, M. Driess, H. Dau, and M.L. Montero, *Angew Chem Int Ed Engl.* **2015**, 54(8), 2472-2476.
http:\\dx.doi.org\10.1002/anie.201409333

D.G.-F. made EC, XAS, and ATR-FTIR experiments with the pakhomovskyites, wrote the paper
I.S. synthesised the pakhomovskyites, performed XRD, and SEM experiments
K.K. made all CoCat experiments
I.Z., J.H., P.C. supported the synchrotron measurements
P.C. wrote software for data evaluation
P.W.M. assisted in electro-preparation of pakhomovskyites
M.D., H.D., M.L.M. supervised

5.1 Experimental Section

5.1.1 Materials

$CoSO_4.7H_2O$, $CoCl_2.6H_2O$ ≥98.0%, $Na_2HPO_4.2H_2O$, H_4EDTA and $CaCl_2 \cdot 2H_2O$ was used as received from Sigma Aldrich. NaOH and $KClO_4$ were reagent grade and used as received. All electrolyte solutions were prepared with 18 MΩ·cm milliQ water.

5.1.2 Synthesis of sample A

Pakhomovskyite A was synthesized by a previously reported precipitation methodology (Riou, Cudennec et al. 1989) in which 7.11 g of $CoSO_4.7H_2O$ is dissolved in 10 mL of H_2O and heated to 75 °C and then mixed with a solution of 3.00 g of $NaHPO_4.2H_2O$ in 20 mL of H_2O. The obtained precipitate is filtrated, washed with mili-Q water and dried as well.

5.1.3 Synthesis of sample B

Electrolytic Reaction. The cell consists of a 100 mL beaker and two squared platinum electrode (2.5 cm^2) as anode and cathode, a water bath was necessary to maintain constant temperature (25°C). The electrolysis was performed at a fixed current density (J=0.280 A cm-2) for 3 h. An Agilent E3640A 30W DC Power Supply was used. The electrodes were submerged in 100 mL of 1.40:1.50:1.00:0.10 Co:EDTA:NaH_2PO_4:Ca ratio solution at pH 8.5 and an EDTA concentration of 0.25 M. The solid was separated by centrifugation, washed three times with mili-Q water and dried out in vacuum.

5.1.4 Electrochemical measurements and oxygen evolution reaction (OER)

Catalytic activity of the cobalt oxide was tested in 0.1 M phosphate buffer (pH 7.0) solution using single-compartment three-electrode electrochemical cell. The working electrode was prepared by taking 3 mg of the powder which was first dispersed in 2 ml of isopropanol under sonication (2 h) and then slowly drop-coated on the fluorinated tin oxide (FTO) surface. A few drops of 5 wt% of Nafion were also drop-coated on the surface to ensure the enhancement of mechanical stability of the electrodes. A high-surface Pt mesh was used as a counter electrode and a $Hg/HgSO_4$ (saturated) reference electrode was employed. The electrochemical experiments were performed at room temperature using a potentiostat (SP-300, BioLogic Science Instruments) controlled by the EC-Lab v10.20 software package. The typical electrolyte resistance (incl. the electrode) was of about 40 Ω; *iR* compensation at 85% was applied. The solution was not stirred during the experiments.

5.1.5 SEM analysis

Sample morphology and constituent elements were determined with a Low Vacuum Scanning Electron Microscope, HITACHI S-3700N, equipped with an energy dispersive X-ray analysis probe, Oxford (EDS) and a Hitachi S-570 with an Aspe model Sirius 10/7.5 EDS.

5.1.6 X-ray diffraction

XRD was performed on a Bruker AXS-D8 Advance with a copper X-ray tube using Göbel mirror and a Lynx-Eye detector. Locked coupled was used from 2Θ = 10º to 60º on increments of 0.019º and an equivalent time of 334 sec per step.

5.1.7 XAS measurements and simulations

X-ray absorption spectroscopy at the *K*-edge of cobalt was performed at the KMC-1 beamline at the BESSY synchrotron (Helmholtz-Zentrum Berlin, Germany) at 20 K in a liquid-helium cryostat as described elsewhere (Barra, Haumann et al. 2006). Spectra were recorded in fluorescence mode using a 13-element Ge detector (Canberra). The extracted spectrum was weighted by k^3 and simulated in *k*-space (E_0 = 7710 eV). All EXAFS simulations were performed using in-house software (SimX3) after calculation of the phase functions with the FEFF program (version 8.4, self-consistent field option activated). Atomic coordinates of the FEFF input files were generated for several reasonable structural models; the EXAFS phase functions did not depend strongly on the details of the used model. An amplitude reduction factor (S_0^2) of 0.7 was used. The data range used in the simulation was 20–548.7 eV (3–12 $Å^{-1}$). The EXAFS simulation was optimized by a minimization of the error sum obtained by summation of the squared deviations between measured and simulated values (least-squares fit). The fit was performed using the Levenberg-Marquardt method with numerical derivatives. The error ranges of the fit parameters were estimated from the covariance matrix of the fit, and indicate the 68 % confidence intervals of the corresponding fit parameters. The fit error was calculated as in ref (Risch, Klingan et al. 2011).

5.2 Results and Discussion

5.2.1 Synthesis and structural characterization of pakhomovskyite, $Co_3(PO_4)_2 \cdot 8H_2O$

We investigated crystalline cobalt phosphate with the formula $Co_3(PO_4)_2 \cdot 8H_2O$, which is classified in the vivianite group and denoted as pakhomovskyite, a rare mineral found at the Kola peninsula in Russia as reported in 2006 (Yakovenchuk, Ivanyuk et al. 2006). From a structural point of view pakhomovskyite composition can be indicated as $Co(1)Co(2)_2(PO_4)_2 \cdot 8H_2O$, with Co(1) and Co(2) cations lying on different crystallographic sites. Co(1) and Co(2) cations display octahedral environment, with Co(1) lying in an ideal equatorial plane formed by four terminally coordinated water molecules; in trans position, there are two oxygen atoms from two different phosphate groups (Figure 5.1). Co(2) is terminally coordinated by two water molecules; two oxygen atoms come from different phosphate groups, and two oxygen atoms from further phosphate groups in cis configuration with respect to the previously introduced plane. Two octahedral Co(2) share an oxygen thereby forming μ-oxo bridges between metal ions, and dimeric planar Co_2O_{10} octahedral units alternate with phosphate groups. The similarity of these dimeric Co_2O_{10} octahedral units with the structure of some of the published transition metal oxide catalyst for water oxidation (Gerken, McAlpin et al. 2011), makes this material very interesting in the study of the mechanistic details of the catalytic process.

The vivianite crystal packing can be described as a layered structure. Such layers are held together by an intricate network of H-bonds that result in a strong inter-layer interaction assuring the tightening of the layers within the three-dimensional framework. The hydrogen bonding structure of vivianite minerals allows them to undergo different structural transformations from condensation-dehydration to a complete phase change and some of these changes can be associated to redox and photo-catalytic processes (Frost, Weier et al. 2003, Frost, Weier et al. 2003).

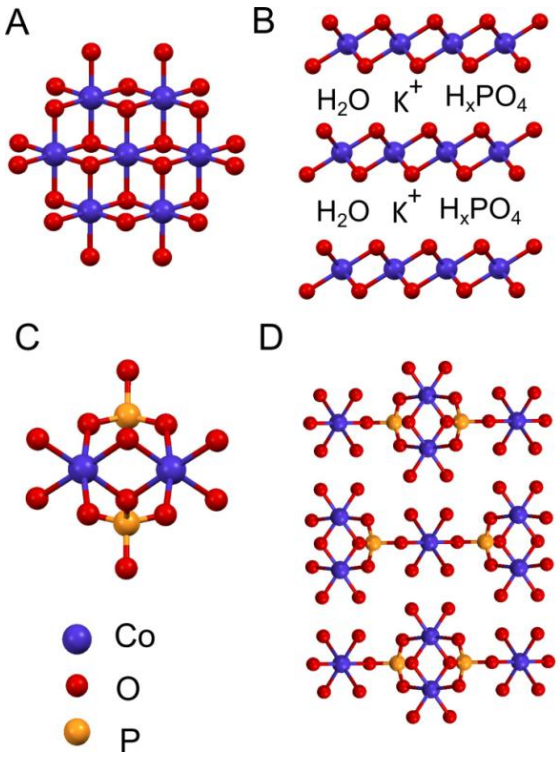

Figure 5.1. (A) Cobalt-oxo fragment of the CoCat. (B) Layered structure of the CoCat with ions and water intercalated between Co-oxide layers. (C) Phosphate binding and μ-oxo bridging in pakhomovskyit. (D) Layered structure of pakhomovskyite; the layers are joined by hydrogen bonds (not shown).

The relatively intricate atomic structure of pakhomovskyite (Pak) exhibits analogies to the CoCat structure (see Figure 5.1). Pakhomovskyite was prepared following either a previously reported precipitation procedure (sample A) (Riou, Cudennec et al. 1989) or a new electrosynthesis approach (sample B) described in the Experimental Section. The elemental composition and structural characterization by X-ray diffraction analysis are shown in Table 5.1 and Figure 5.2 respectively. SEM images of the powder samples are also shown in Figure 5.3.

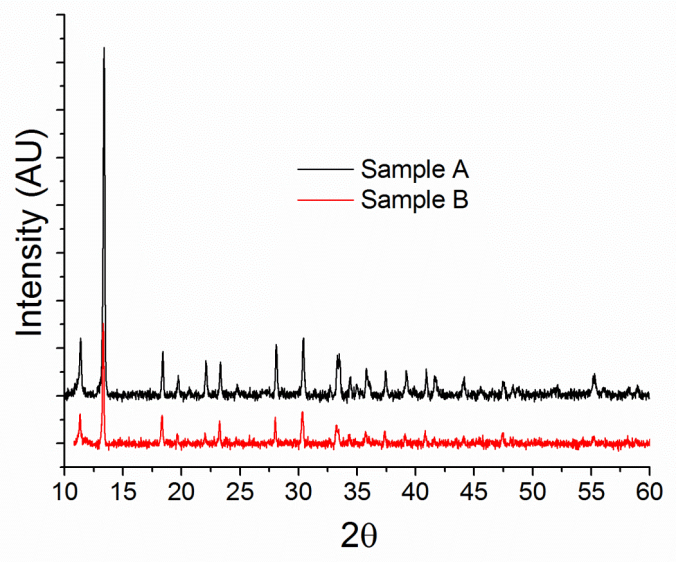

Figure 5.2. Powder X-ray diffractograms for catalyst A and B. The peak positions confirm that the pakhomovskyite mineral phase was synthesized.

Table 5.1. Elemental composition of synthesized catalysts compared to the ideal pakhomovskyite phase.

Catalyst	% P	%Co	% Ca	%Na
Pakhomovskyite	12,1	34,6	0	0
Sample A	11,8	33,7	0	1.0
Sample B	11,5	29,7	6.3	5.9

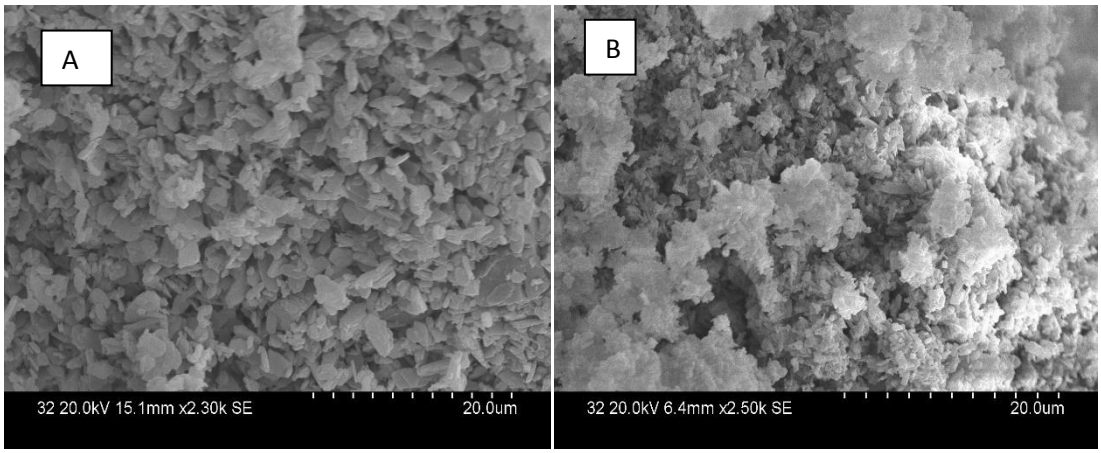

Figure 5.3. SEM images for powders of samples A and B.

5.2.2 Electrochemical properties of pakhomovskyite and transformation during operation at catalytic potentials

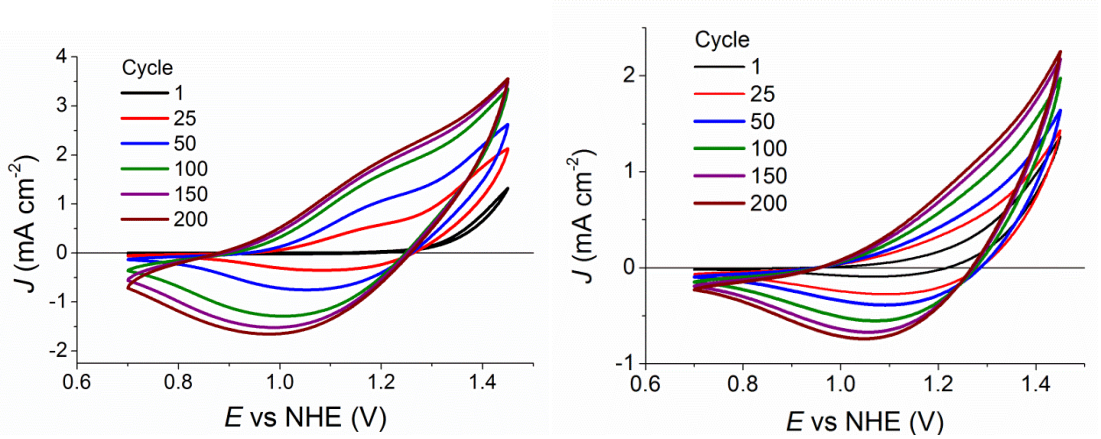

Figure 5.4. Series of cyclic voltammograms (CVs) of A) sample A and B) sample B deposited on FTO electrodes (*E* versus. NHE; CV with 10 mVs^{-1} in 0.1 M phosphate buffer at pH 7, 85% IR compensation).

To investigate the electrochemical properties of pakhomovskyite, we physically deposited microcrystalline sample A and B on FTO electrodes and investigated the respective catalyst-electrode assembly in a 0.1 $molL^{-1}$ phosphate buffer at pH 7. Cyclic voltammograms (CVs) are shown in Figure 5.4. Already during the first cycle, sample A exhibits a clear catalytic wave corresponding to a catalytic current exceeding 1 mA cm^{-2}. Interestingly, the catalytic current (at 1.45 V) increases with each CV cycle. This increase is accompanied by the rise of an oxidation wave (broad peak in the CV around 1.2 V) and reduction wave (broad negative peak around 1.0 V), which are assignable to cobalt oxidation and reduction, respectively; integration of the reductive currents provides a measure for the number of redox-active cobalt ions (Risch, Klingan et al. 2012, Klingan, Ringleb et al. 2014). We note that the observed behavior often is discussed in terms of a pseudocapacitance (Lee, Carlton et al. 2012). The increasing redox activity is typical for amorphisation processes in crystalline materials under electrochemical operation (Lee, Carlton et al. 2012, May, Carlton et al. 2012). A very similar behavior is observed in sample B; however, its initial redox activity is higher, explainable by either the smaller crystallite size (Figure 5.3) and thus higher surface area or faster amorphisation due to the presence of calcium and sodium ions.

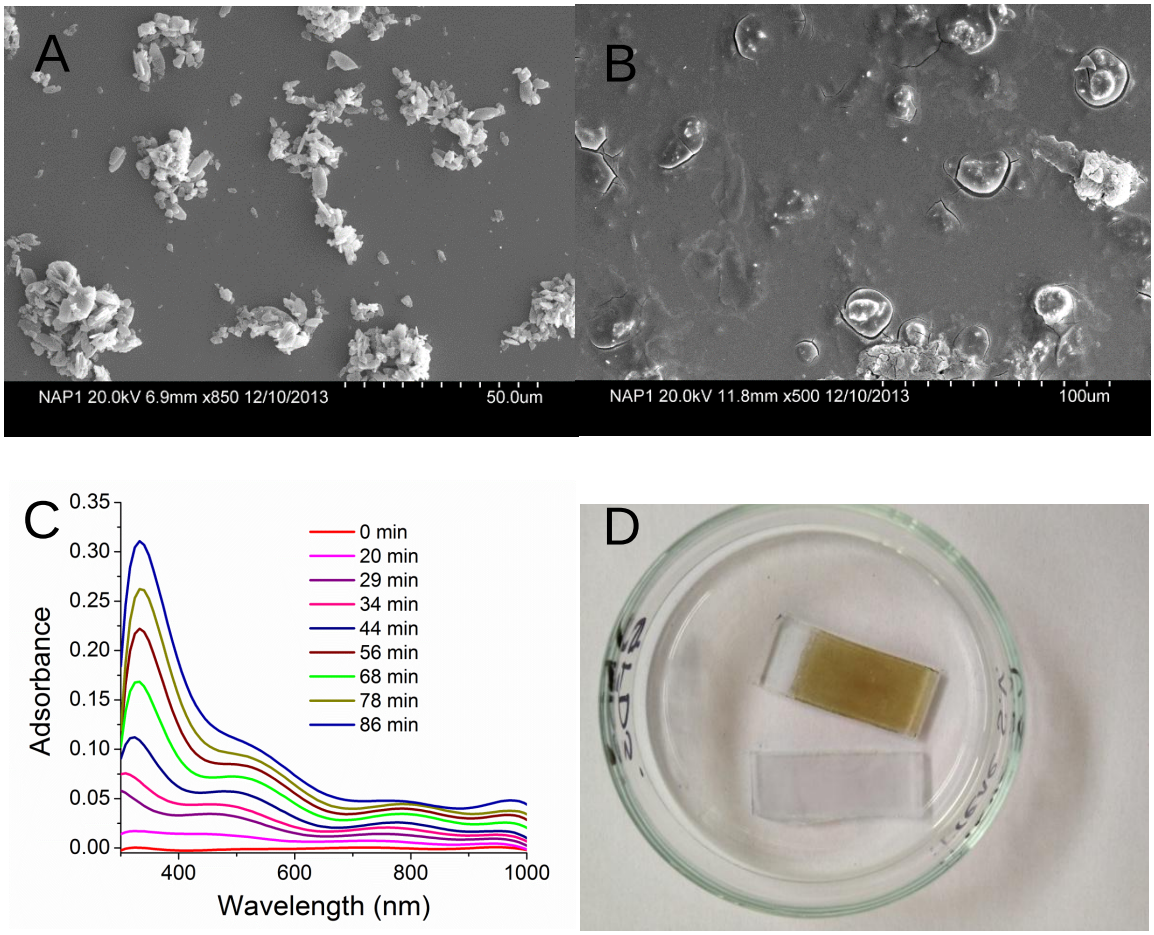

Figure 5.5. SEM images of **A)** sample A on the working electrode before the electrolysis, and **B)** after 6 hours of electrolysis . **C)** Spectra of sample A after various time periods of exposure to 1.35 V (versus NHE). The potential was set to 1.35 V versus NHE and spectra were collected every 30 s. **D)** Sample A before (transparent) and after (brown color) the electrolysis.

SEM images collected before and after catalytic operation show the transformation of small separated crystals into amorphous islands (Figure 5.5, A and B). Confirmed by powder XRD (Figure 5.6) and also ATR-FTIR measurements (Figure 5.7). The initially fully transparent film is transformed into a brownish material; UV/Vis spectra collected *in-situ* during catalytic operation suggest a continuous structural transformation of the catalyst material (Figures 5.5, C and D).

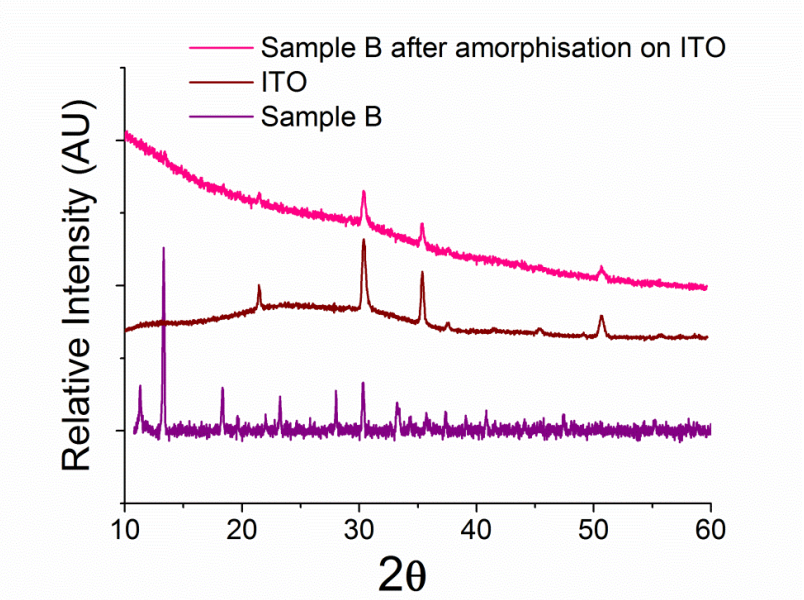

Figure 5.6. Powder x-ray diffractograms for catalyst B (purple line), catalyst B after 10 h of electrolysis on the ITO electrode (crimson), and the pure ITO substrate (brown). The diffractograms show how after the amorphisation process there remain no crystalline domains.

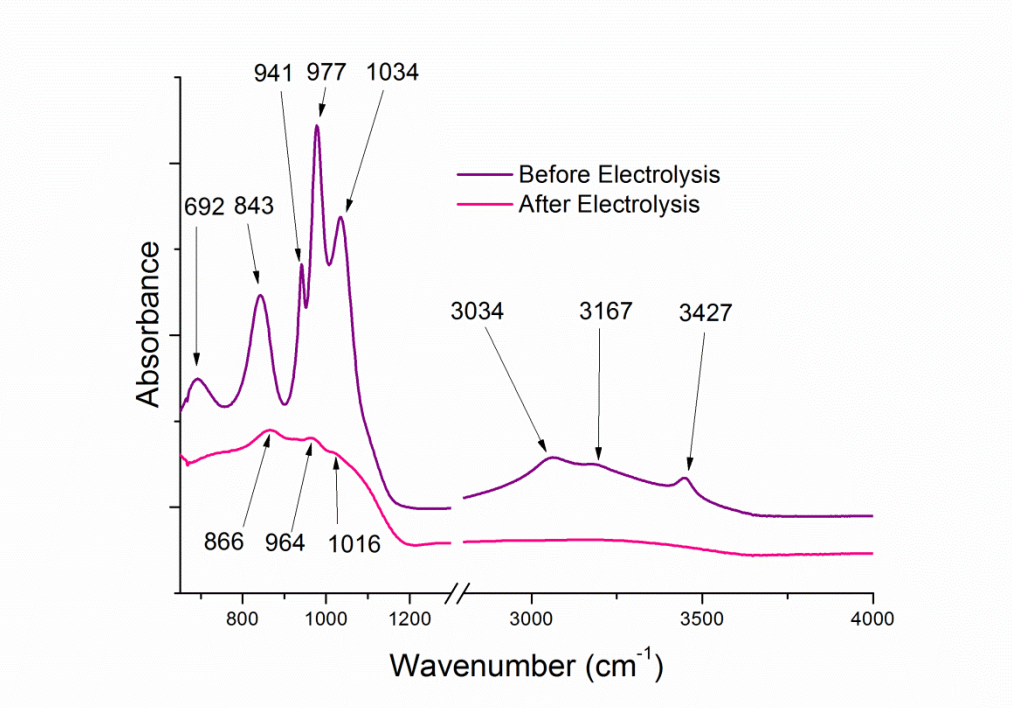

Figure 5.7. ATR-FTIR analysis for sample B before and after 16 hours of electrocatalysis at 1.35 V versus NHE.

We also performed long-term electrolysis at constant anode potential (1.35 V versus NHE), complemented by CV measurements at selected times (Figure 5.8). Starting at a low but clearly detectable level of catalytic current, the current increases with time (see Figure 5.8, A and B). The current increase likely relates to the increase in redox activity by the amorphisation of the catalyst material as scrutinized in more detail further below.

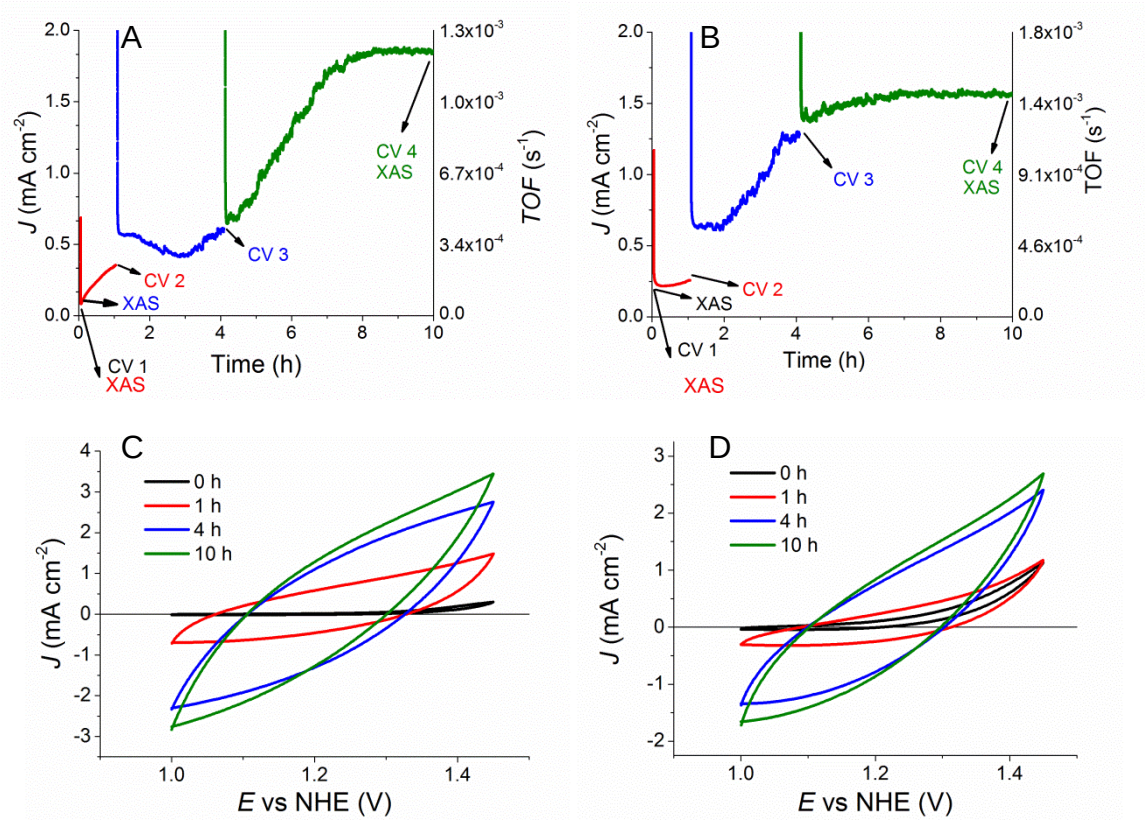

Figure 5.8. Long-term electrolysis for samples applying 1.35 V versus NHE for 10 h (in 0.1 M phosphate buffer at pH 7). Time course of the current density for **A)** sample A and **B)** sample B. At the indicated times CV were measured and samples rapidly frozen for analysis by X-ray absorption spectroscopy. CVs detected at a scan rate of 20 mVs^{-1} for **C)** sample A and **D)** sample B.

5.2.3 Structural studies by XAS

Upon exposure to catalytic potentials, catalyst activation is observed (Figures 5.8) and changing UV/Vis spectra suggests structural changes at the atomic and electronic level (Figures 5.5.C). To understand the structural changes coupled to catalyst activation, the electrochemical experiment was combined with X-ray absorption spectroscopy (XAS) at the cobalt *K*-edge. We performed low-temperature XAS measurements on electrodes of sample A and B which were rapidly frozen (i) before any electrochemical treatment, (ii) after 2 min, and (iii) after 10 h at 1.35 V (versus NHE).

The XANES spectra (X-ray absorption near-edge structure), Figure 5.9, A and B show a shift in the X-ray edge position (from 7717.6 to 7720.6 eV) suggesting that 10 h exposure to 1.35 V results in essentially complete conversion of the Co^{II} ions of Pak into Co^{III} ions; the Co^{III} spectra detected after 10 h resemble closely the XANES spectra of amorphous CoCat reported elsewhere (Risch, Khare et al. 2009). The transformation of the Pak mineral into the amorphous CoCat is confirmed by the Fourier transforms (FTs) of the extended X-ray absorption fine-structure (EXAFS) spectra (Figure 5.9 C and D). The spectrum of the sample A before electrolysis can be modeled according to the Pak crystal structure (Figure 5.10 and Table 5.2). After 10 h at 1.35 V, Co-O distance of 1.89 Å and Co-Co distance at 2.82 Å are detectable, which are identical to the previously reported distances of the CoCat.

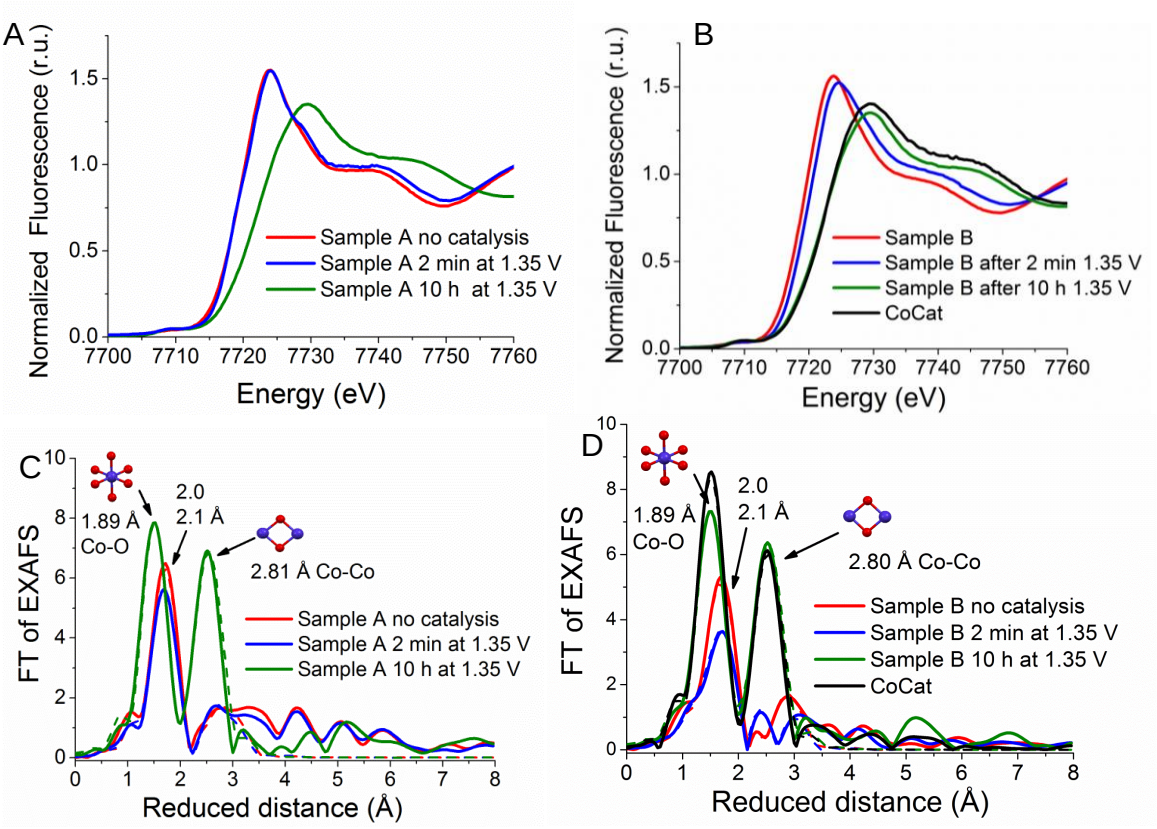

Figure 5.9. X-ray absorption spectra collected at the cobalt *K*-edge for pakhomovskyite samples deposited on FTO electrodes (red lines), after exposure to 1.35 V (vs. NHE, pH 7) for 2 min (blue) and 10 h (green). (**A**) XANES spectra for sample A and (**B**) XANES spectra for sample B. (**C**) Fourier-transformed EXAFS spectra for sample A and (**D**) Fourier-transformed EXAFS spectra for sample B. The indicated reduced distance is by about 0.4 Å shorter than the precise distance obtained by EXAFS simulations. The dotted lines results from EXAFS simulations (see Table 5.2 for parameters).

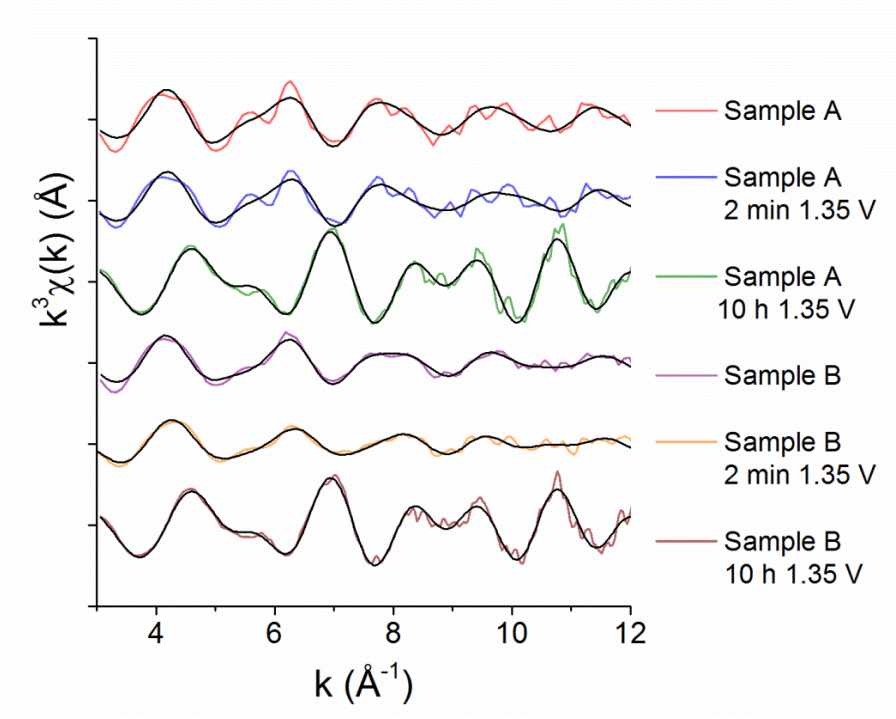

Figure 5.10. k^3-weighted EXAFS spectra of catalysts A and B recorded at the K-edge of cobalt. The black lines represent the respective EXAFS simulations.

Table 5.2. Parameters obtained by simulation of the k^3-weighted EXAFS spectra. The simulated spectra correspond to the Fourier-transformed EXAFS spectra shown in Figure 5.9. The errors represent the 68% confidence interval of the respective fit parameter (N, coordination number; R, absorber-backscatter distance; σ, Debye–Waller parameter)

		Co-O	Co-O	Co-Co	Co-P	Co-O
Sample A	**R (Å)**	2.07(1)	2.14(2)	2.93(4)	3.24(4)	3.51(6)
	N	4*	2*	0.7*	2*	3.25*
	σ (Å)	0.05*	0.05*	0.06(4)	0.06(4)	0.05*
Sample A after 2 min 1.35 V	**R (Å)**	2.05(5)	2.16(8)	2.95(3)	3.28(6)	3.47(1)
	N	4(2)	2(2)	1.1(5)	2(2)	1(3)
	σ (Å)	0.05*	0.05*	0.0592*	0.0592*	0.05*
Sample A after 10 h 1.35 V	**R (Å)**	1.892(7)		2.816(7)		
	N	5.5(7)		3.7(8)		
	σ (Å)	0.05(1)		0.05(1)		
Sample B	**R (Å)**	1.99(2)	2.10(1)	2.9(1)	3.27(5)	3.5(1)
	N	2*	4*	0.7*	2*	3.25*
	σ (Å)	0.05*	0.05*	0.10(5)	0.06(3)	0.09(7)
Sample B after 2 min 1.35 V	**R (Å)**	1.92(3)	2.08(2)	2.84(3)	3.25(4)	3.5(1)
	N	1.8(4)	3.9(5)	1.3(6)	1(1)	3(3)
	σ (Å)	0.05*	0.05*	0.0949*	0.0592*	0.0922*
Sample B after 10 h 1.35 V	**R (Å)**	1.894(8)		2.804(7)		
	N	5.9(7)		3.8(9)		
	σ (Å)	0.06(1)		0.06(1)		

We also compared the electrochemical properties of the amorphised pakhomovskyite with electrodeposited amorphous CoCat by measuring Tafel plots. We (i) deposited the pakhomovskyite material on the ITO electrode, (ii) amorphised it by electrolytic operation for 12 h, (iii) collected the Tafel plot data, and (iv) quantified the amount of cobalt on the electrode by X-ray fluorescence analysis. The amount of cobalt ions on the electrode was found to be equivalent to a deposition charge of 105 mC cm^{-2}. We then electrodeposited a CoCat film with this same deposition charge and collect its Tafel plot data. The Tafel plots were measured with 20 mV steps with 5 min equilibration time between steps and using the stabilized current at the end of the equilibration

time. Absolute currents and Tafel slopes are within the uncertainty range identical, which suggest both films have very similar electrochemical properties (Figure 5.11).

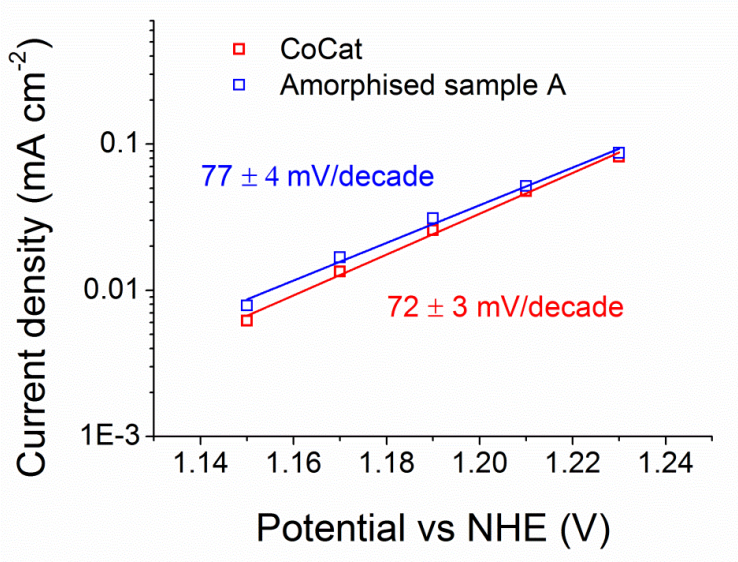

Figure 5.11. Comparison of the Tafel plot of amorphised pakhomovskyite (blue) and the directly electrodeposited CoCat (red).

We conclude that long-term exposure to catalytic potential results in complete conversion of the microcrystalline Pak (Figure 5.1.C and D) into the amorphous CoCat, which consists of fragments of a layered oxide with edge-sharing $Co^{III}O_6$ octahedra (Figure 5.1.A and B). This conversion requires several hours as verified by XAS analysis of the Pak samples exposed to catalytic potentials for 2 minutes only (Figures 5.9 C and D). The structural changes detected by XAS are also supported by the highly similar catalytic properties of amorphised Pak and directly electrodeposited CoCat (Figure 5.11).

5.2.4 Turnover frequency analysis in the pakhomovskyite sample

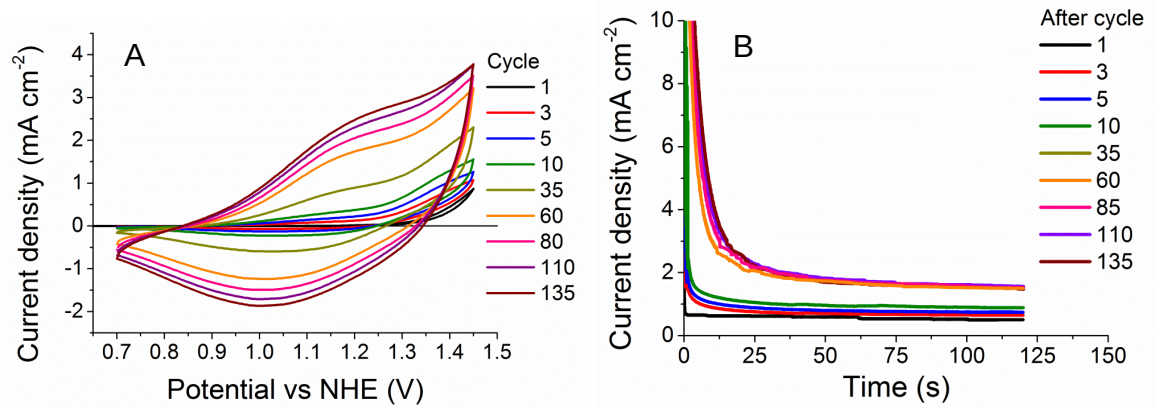

Figure 5.12. A) Series of cyclic voltammograms (CVs) of sample A deposited on FTO electrodes (E versus. NHE; CV with 10 mVs^{-1} in 0.1 M phosphate buffer at pH 7, 85% IR compensation). **B)** Chronoamperometries at 1.45 V versus NHE for sample A after the corresponding CV´s shown in panel A. Measurements in 0.1 M phosphate buffer at pH 7, 85% IR compensation.

For the CoCat and other materials, a close relation between redox activity and catalytic activity has been reported (Risch, Klingan et al. 2012, Klingan, Ringleb et al. 2014). This relation was investigated for the Pak material exposed for more than 8 h to a continuous sequence of CVs. In refs.(Risch, Klingan et al. 2012, Klingan, Ringleb et al. 2014) and herein, the redox activity was measured via integration of the reductive currents of the CV resulting in a redox charge, q_{red}, which provides N_{red}, the number of redox active cobalt ions undergoing oxidation state changes ($N_{red} = q_{red}/e$). The catalytic activity of the films was estimated as the current after two minutes stabilization in Figure 5.12.B. This methodology allows minimizing contributions from charging currents and pseudocapacitances in the catalytic current estimation. An initial catalytic current is clearly detectable, which is associated with a low level of redox activity. Subsequently, amorphisation results in the concomitant increase of both redox and catalytic activity. The red squares in Figure 5.13 indicate the ratio between catalytic current and redox charge, which may be viewed as a turnover frequency per redox active cobalt ion (TOF^{q}). It is clearly visible that the value of TOF^{q} is high before onset of amorphisation (red squares in Figure 5.13) and clearly lower at later times.

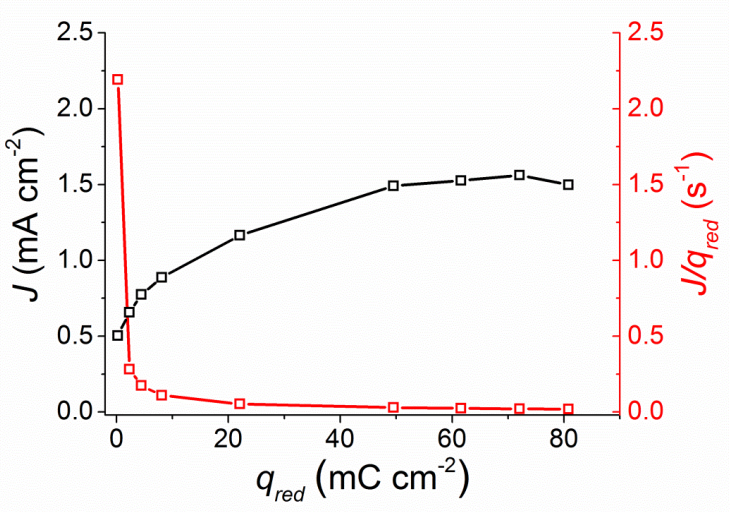

Figure 5.13. Relation between redox charge (q_{red}), catalytic activity (J), and TOF per redox-active site (J/q_{red}) during Pak→CoCat conversion. The redox charge was quantified by integration of the reductive currents of the six CVs shown in Figure 5.12.A. The catalytic activity was estimated activity was estimated from the chronoamperometry experiments shown in Figure 5.12.B and is indicated by open squares (left current-density axis). The red squares relate to the right y-axis and indicate the ratio between catalytic current density (J) and redox charge (q_{red}) in units of s^{-1} (= A C^{-1}). This ratio may be viewed as a turnover frequency (TOF^q, rate of catalytic electron flow per redox-active cobalt ion). Both q_{red} and J are normalized to the macroscopic electrode area.

We interpret the above findings as follows: in the initially crystalline material, water oxidation catalysis takes place at surface sites; the catalytic TOF per cobalt ion at the crystallite surface is high. Upon long-term operation at catalytic potentials, the catalytic material is progressively converted into an amorphous oxide of the CoCat type; after 10 h a complete conversion is achieved. In the amorphous catalyst, the TOF per cobalt ion is relatively low, but due to the high number of redox-active cobalt ions, the total rate of catalysis increases significantly by amorphisation.

5.2.5 Comparison of the TOF behavior of pakhomovskyite and CoCat

In previous work from Klingan it has been demonstrated the prevalence of volume catalysis in the amorphous CoCat material (Klingan, Ringleb et al. 2014). Since the conclusions from her data are important for the understanding and clarity of the present discussion we will proceed to explain some of the details in the following paragraphs.

In the experiments of Figure 5.14, the ratio between potential catalytic sites at the bulk-water—bulk-oxide interface (surface catalysis) and within the bulk phase of the CoCat film (volume catalysis) was altered by variation of the amount of deposited cobalt ions by more than three orders

of magnitude from 140 µC to 200 mC (per cm^{-2}). For deposition of 2 mC to 200 mC and if the current density stays below the level of proton transport limitation (1.20 V and 1.25 V data points in Figure 5.14), the catalytic current is proportional to the number of deposited cobalt ions; consequently, the TOF per cobalt ion remains fully constant. This is explainable by equal catalytic activity throughout the bulk volume of the catalyst film (Klingan, Ringleb et al. 2014). When the range of deposited cobalt ions was extended down to the level of 140 µC cm^{-2} it was observed an increase in the TOF per cobalt ion by one order of magnitude. X-ray absorption spectroscopy revealed that by deposition of small amounts of cobalt ions, the atomic structure and level of amorphicity of the catalytic material is not altered in any detectable way (Figure 5.15).

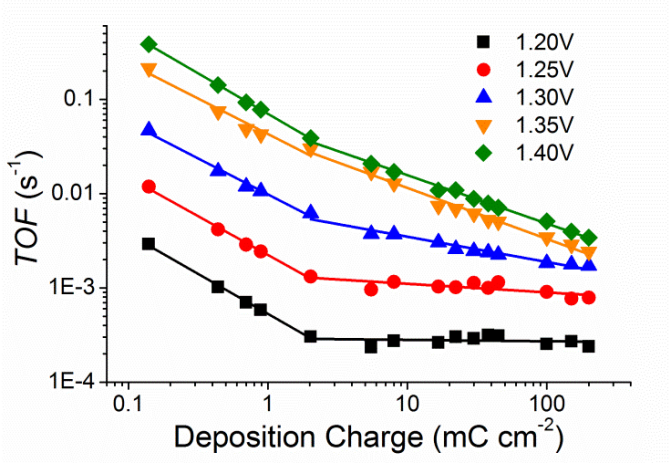

Figure 5.14. Turnover frequency (TOF) per cobalt ion and formed O_2 molecule for amorphous CoCat films of various thicknesses. The x-axis indicates the deposition charge which corresponds to the amount of cobalt ions electrodeposited on an ITO electrode; a deposition charge of 10 mC corresponds to about 100 nM cm^{-2} and to a thickness of the electrode film of about 70 nm (Klingan, Ringleb et al. 2014). The catalytic current was measured after equilibration for 60 s at the indicated electrode potentials (versus. NHE, pH 7); the TOF was calculated for the total amount of cobalt ions present in the catalyst film. The data relating to deposition charges ranging 2 mC to 200 mC has been discussed before in ref. (Klingan, Ringleb et al. 2014). The straight lines result from curve-fitting. All this experiments were performed by Katharina Klingan.

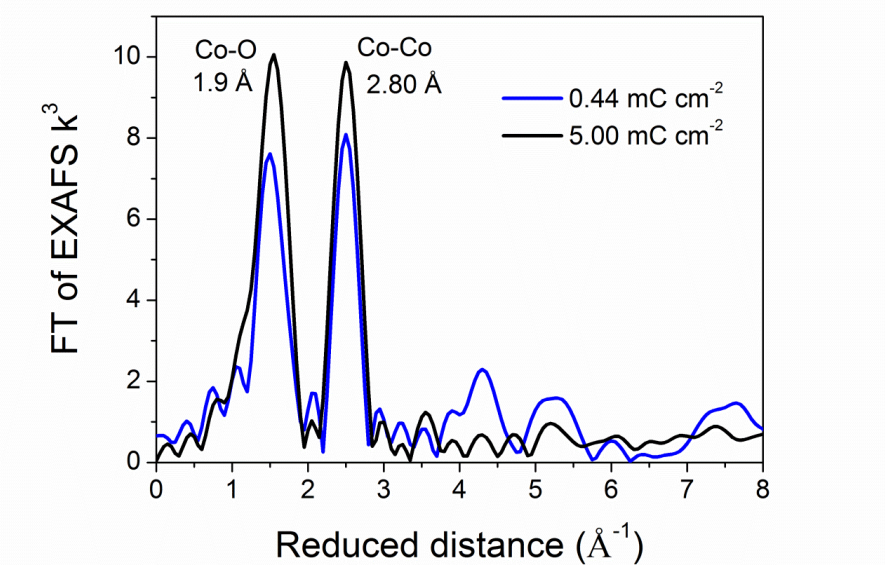

Figure 5.15. EXAFS data for the sublayer oxide prepared by depositing a charge of 0.4 mC/cm^2 and the layer oxide with 5 mC/cm^2.

The following explanation was proposed for the increased TOF at low deposition charge: for deposition of thick films (> 10 nm), catalysis within the bulk volume of the catalyst film is dominating; the corresponding TOF per cobalt ion is relatively low (10^{-3} s^{-1} at 1.25 V). At lower levels of deposited cobalt ions however, surface catalysis prevails and the corresponding TOF per cobalt ion is significantly higher than observed for volume catalysis (minimally by one order of magnitude; 10^{-2} s^{-1} at 1.25 V). This finding may or may not relate to the finding that in thin CoCat films enhanced catalysis could result from an influence of the electrode material on the electronic properties of the CoCat material (Yeo and Bell 2011). Our comparison of the CoCat performance for electrodeposition on ITO, gold or platinum did not provide evidence for a sizeable substrate influence (Figure 5.16).

In the case of the crystalline material we have shown that upon exposure to oxidizing potentials, the initially crystalline cobalt phosphate (Pak) is slowly (timescale of several hours) but eventually completely transformed into an amorphous phosphate-containing cobalt oxide (CoCat). The amorphisation is coupled to catalyst activation, meaning that a sizeable increase in the total catalytic activity is observed. In analogy to what is observed in the CoCat, and based on the observed electrochemical properties (Figure 5.11), we interpreted that in the initial crystalline state, surface activity of the catalysts prevails, whereas amorphisation results in later dominating volume activity of the bulk of the hydrated oxide material. We conclude that the differentiation between (a) catalysis at the electrolyte exposed, ‘outer surface’ of the oxide material and (b) catalysis within the amorphous bulk volume of the hydrated oxide is of critical importance when discussing

mechanistic aspects. The herein reported results suggest that functional investigations completed within tens of minutes indeed could probe catalysis of water oxidation at the surface of a crystalline material. However, control experiments are recommendable to assess the amorphisation rate, which likely will depend on (i) elemental composition and crystal structure, (ii) dimension of crystallites, and (iii) operation conditions (pH, electric potential and temperature). Whether fully amorphisation-resistant materials for heterogeneous water oxidation exist, remains an open question.

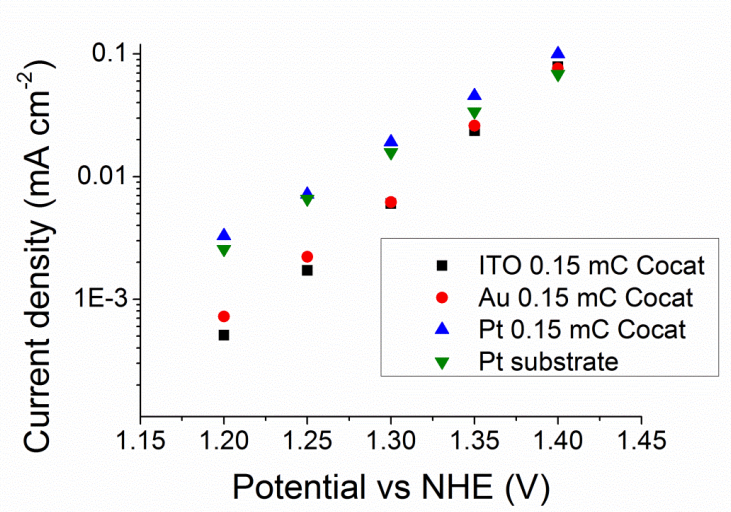

Figure 5.16. Comparison of the characteristics of the CoCat deposited on different substrate electrodes, namely ITO (black), gold (red) and platinum (green). We deposited the CoCat material with a total deposition charge of only 0.15 mC cm^{-2} and performed chronoamperometry for 60 s at 5 distinct potentials (same protocol as used for the data shown in Figure 5.14). At this low level of deposition charge, only a fraction of the electrode is covered by the CoCat material. Comparing the Au and ITO substrates, we do not detect any significant enhancement of the catalytic current that could result from an influence of the gold substrate. In the case of the platinum electrode, we observe a significant catalytic activity resulting from the bare platinum electrode (green data points). Therefore any interpretation of this Pt-electrode experiment is potentially ambiguous. However, we still can exclude that the catalytic activity of the CoCat material is enhanced several fold by deposition on a platinum electrode. (We note that for the Au and ITO substrate electrodes, the currents of the bare electrodes were always at least by one order of magnitude smaller than observed for these electrodes after deposition of 0.15 mC of the CoCat material.)

5.3 Summary

Recently in the work of Klingan it was demonstrated the prevalence of volume catalysis in the amorphous CoCat material (Klingan, Ringleb et al. 2014) for deposition charges ranging from 2-200 mC cm^{-2}. It was also reported an increased TOF at extremely low levels of electrodeposited cobalt ions (< 1 mC). This finding suggests that also in the amorphous CoCat the rate of catalysis could be enhanced significantly at surface exposed sites or domains. This, in turn, implies that high TOF surface catalysis of water oxidation is not restricted to surface sites of crystalline material.

Surface catalysis in pristine crystalline material either could occur at open coordination sites created by termination of the crystal lattice, involving only limited surface restructuring, or could involve more extended surface amorphisation. The latter option needs to be taken into account seriously when discussing catalysis by crystallites, as circumstantially evidenced by the enhanced TOFs at surface exposed sites in the amorphous CoCat material. In any event, our results presented herein demonstrate that a complete picture of water oxidation catalysis requires consideration of both surface and volume catalysis, including the dynamic restructuring and transformation of the catalyst material.

Chapter 6

pH dependence of OER activity in cathodically deposited transition metal oxides

Transition metal (oxy)hydroxides show very different trends in catalytic activity for water oxidation when compared at pH 7 and pH 14. The enhancement in the catalytic activity with the pH seems to be especially important for some of the catalyst like the nickel-iron based. To address these phenomena we made a comparative study with Co, Ni, Fe, Mn and NiFe cathodically deposited catalysts and observed that all of them show a similar increase in the normalized catalytic activity (in terms of TOF) of around 100 times when the pH is increased from 7 to 14. Combining *in-situ* UV-visible measurements and XAS (X-ray Absorption) together with electrochemistry we were able to study more in detail the pH dependence for the NiFe catalyst. We observed that the Ni redox transitions and the onset of the catalytic current are similarly shifted with the pH. The oxidation state changes in the nickel are associated to a phase transition which is favored at pH 14. The Fe atoms do not experience oxidation state changes but are structurally affected by the changes at the Ni. Both structural changes at the Ni and Fe edge follow similar kinetics. However, the Ohmic resistance of the electrochemical cell can become determinant to the reaction kinetics depending on the material of the substrate electrode.

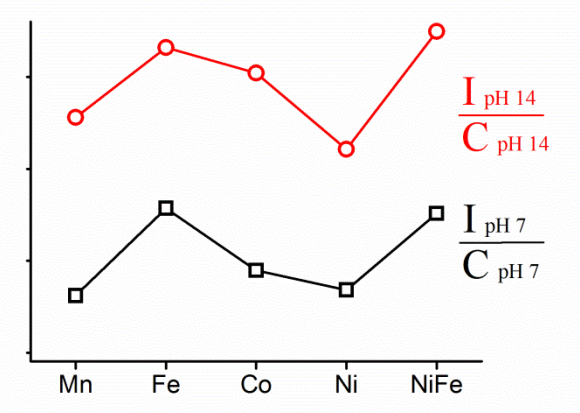

This work has been realized with the following contributions:

Susmita Das: collaborated in studies in the electrode deposition.
Samuel Ueberle: collaborated in pH dependence of NiFe oxide studies.
Aitziber Miguel Oyabide: collaborated in absorption measurements.
Mikaela Görlin: performed the XRD measurements.
Petko Chernev, Ivelina Zaharieva, Elías Martínez-Moreno, Chiara Pasquini, Mohammad Reza Mohammadi, Paul Kubella, Stefan Loos, Rodney D. L. Smith: Contributed to the XAS measurements.

6.1 Experimental Methods

6.1.1 Materials

Reagents: $MnSO_4$ (Merck, 99%), H_2KPO_4 (Roth, ≥99%), K_2HPO_4 (Roth, ≥99%), H_3BO_3, (Roth, ≥99%.), KOH (Sigma Aldrich, ≥86%), NH_4ClO_4 (Sigma-Adrich, 1 M reagent grade), $FeSO_4.7H_2O$ (Sigma-Aldrich, ≥99%), $NiSO_4.6H_2O$ (Riedel-deHaën, 99%), $CoSO_4$, H_2SO_4 (Roth, 37% techn), KNO_3 (Roth, ≥99%). All reagents where used without further purification. Solutions were prepared with 18 MΩ·cm Milli-Q water.

6.1.2 Electrodeposition of the films

The electrodepositions were performed in a two-electrode system. Both electrodes were made of platinum (Labor-Platina Kft Hungary, 99.95%) of 1x2 cm size. Before the deposition the electrodes were polished using DIAMANT-Paste SK-A 0,7µ (PAS0017 BDW-Binka Diamantwerkzeug GmbH) and washed with concentrated HCl and miliQ water. The deposition area was delimited to 1 cm^{-2} by using Kapton tape (IM301202 polyimid film Goodfellow, 683-465-79), and the back side of the electrodes was covered with Kapton tape as well. The electrodes were placed parallel to each other with a separation of 0.5 cm between them and connected to a power supply (Thursby-Thandar PL330DP). The current was held at 250 $mAcm^{-2}$ for 30 s as described by Merril (Merrill and Dougherty 2008) for all the films except the Ni electrodes in which we observed a higher electrodeposition rate and the deposition time was lowered to 7 s.

Table 6.1. Deposition conditions for the different metal oxides.

Oxide	Metal salt(s)	Electrolyte(s)	pH	Deposition time (s)	Deposition potential vs NHE(V)
Mn	18 mM $MnSO_4$	125 mM NH_4ClO_4	1.5 w/ H_2SO_4	30	-3.9
Fe	18 mM $FeSO_4$	100 mM NH_4ClO_4	1.5 w/ H_2SO_4	30	-3.5
Co	18 mM $CoSO_4$	35 mM NH_4ClO_4	6.8 w/ NH_4OH	30	-12.1
Ni	18mM $NiSO_4$	25 mM NH_4ClO_4	6.0 w/ NH_4OH	7	-12.4
NiFe	9 mM $NiSO_4$ & 9 mM $FeSO_4$	25 mM $(NH_4)_2SO_4$	2.5 w/ H_2SO_4	30	-9.0

6.1.3 Electrodeposition on FTO electrodes

For absorption measurements we deposited the NiFe oxide catalyst over FTO coated glass (SOLEMS, FTO TEC 7, 7-10 ohms thickness 600 nm on 2.2 or 3.1 mm-thick glass). The deposition was performed using a potentiostat (SP-300, BioLogic Science Instruments) controlled by EC-Lab v10.20 software package. The films were deposited cathodically using the same solution composition and current density as in the electrodes deposited on Pt. The deposition was performed for 1 s in order to have a thin enough film for the absorption measurements.

6.1.4 Electrochemical measurements

Catalytic activity of the different oxides was tested in 0.1 M phosphate buffer (pH 7.0) solution with 1 mol L^{-1} KNO_3 supporting electrolyte and in a 1 mol L^{-1} KOH solution using single-compartment three-electrode electrochemical cell. A high surface Pt mesh was used as a counter electrode and RHE (HydroFlex®, Gaskatel) as a reference electrode. The electrochemical experiments were performed at room temperature using a potentiostat (SP-300, BioLogic Science Instruments) controlled by EC-Lab v10.20 software package. Test runs were carried out with the typical electrolyte resistance (incl. the electrode) about 10-18 Ω; iR compensation at 85% was applied unless otherwise stated. The solution was not stirred during the experiments.

6.1.5 *In-situ* UV-vis absorption measurements

UV-vis measurements were performed using a commercial UV-vis spectrophotometer (Cary 60, Agilent). A quartz cuvette (2.5 cm × 2.5 cm × 4 cm height) filled with electrolyte (15 mL, 0.1 M phosphate buffer + 1 M KNO_3, pH 7 or 1 M KOH) was placed in the optical compartment of the spectrometer. The semi-transparent working electrode (FTO-coated glass with electrodeposited metal oxide film), a RHE reference electrode and a platinum counter electrode were immersed in the electrolyte-filled cuvette. The electrochemistry was controlled by a potentiostat (Biologic SP-300). The potential was applied for a stabilization time of 1 min prior to recording the spectrum. The spectrum was recorded under applied potential.

6.1.6 Quantification of deposited material by TXRF

Elemental analysis was done using a PicoFox Spectrometer (Bruker) for total reflection X-ray fluorescence (TXRF) measurements. For the samples deposited on Pt electrodes we proceeded to dissolve the samples using 1 mL of concentrated HCl, added 200 μL of Ga standard ($Ga(NO_3)_3$, concentration of 1000 mgL^{-1} and dilute to 10 mL. In the case of the electrodes prepared in FTO we dissolved the samples in 500 μL of 30% HCl. After dissolution of the film, 500 μL of a Ga standard ($Ga(NO_3)_3$, concentration of 40 mgL^{-1} was added. For all prepared solutions the final Ga standard concentration was 20 mgL^{-1} and 10 μL of the mixture was deposited on a silicon coated quartz glass sample plate for quantification. The XRF acquisition time was 30 minutes per sample.

6.1.7 X-ray absorption measurements

The metal oxide samples were deposited on Pt electrodes and the electrochemically activity was tested. We measured a CV with 1 mVs^{-1} scan rate from 1.413 to 1.863 V versus RHE for pH 7 and from 1.417 to 1.617 V versus RHE for 1 M KOH. After that a potential of 1.63 V versus RHE (0.4 V overpotantial) was applied for 5 min for samples in 1 M KOH and a potential of 1.83 versus RHE (0.6 V overpotential) for samples at pH 7. After applying this potential the samples were put inside liquid nitrogen within a few seconds and kept frozen until the XAS measurements. XAS measurements were performed at 20 K (Oxford He-flow cryostat) at the BESSY II synchrotron radiation source (Berlin-Adlershof) operated by the Helmholtz-Zentrum Berlin (at beamline KMC-1). A silicon (111) double-crystal monochromator was used for scanning the X-ray excitation energy. All X-ray absorption spectra were collected in the fluorescence mode, using 13-channel energy-resolving Ge detector (Canberra) with regions of interest adjusted at the corresponding metal K_α fluorescence emission. In each scan, the X-rays that passed the catalyst sample were used to measure the absorption of a reference, ($KMnO_4$ for Mn and a corresponding metal foil for the

other transition metals) placed between two home-made ionization chambers. The reference absorption was utilized for precise energy calibration. For further details on XAS data collection, data analysis and EXAFS simulations, see Refs. (Wiechen, Zaharieva et al. 2012, Zaharieva, Chernev et al. 2012).

6.1.8 *In-situ* X-ray absorption measurements

The measurements were performed at 20 °C at the BESSY II synchrotron radiation source at beamline KMC-3. A silicon (111) double-crystal monochromator was used for selecting a fixed X-ray excitation energy. The Ni-Fe oxide was deposited on Toray Carbon Paper 120 (with 5 wt% PTFE wet proofing and 370 µm thickness, 590437-FuelCellStore) for 5 s and was placed in a window covered with Kapton tape of a home-made Teflon electrochemical cell (filled with 1 M KOH) and placed in the path of the X-ray beam. The size of the area illuminated by the X-ray beam was approximately 11 x 3 mm. All X-ray absorption signals were collected in fluorescence mode. The excited X-ray fluorescence passed through the Kapton window and then through a 10 µm metal foil (Mn foil for measurements at Fe edge and Co for measurements at the Ni edge) shielding against scattered light. The fluorescence was monitored perpendicular to the incident beam by a scintillation detector (19.6 cm^2 active area, 51BMI/2E1-YAP-Neg, Scionix; shielded by additional 2 µm Al filter against visible light). The detector consisted of a scintillating crystal (YAP) converting X-ray photons into visible light (~50 % efficiency) detected by a fast photomultiplier operated at 0.9 kV. The signal from the photomultiplier passed through a 1 MΩ resistor for current-to-voltage conversion and was read by an amplifier (Stanford Research Systems, model SR560) with 6 dB/oct 10 Hz low-pass filter amplifying the signal by a factor of 20. The amplified signal was finally recorded with a time resolution of 10 ms by the potentiostat (BiologicSP-300) that also operated the electrochemical cell and recorded the signal from an ionization chamber monitoring the excitation X-ray beam intensity. With this 10 Hz low-pass filter the filtered signal had a step response about 30-40 ms with a signal to noise ratio of about 250. For details on this time-resolved *in situ* approach see Figure 6.1. Separately, short K-edge absorption spectra of the sample were recorded immediately before and after each time-resolved experiment in order to normalize the time-resolved data and to ascertain that there was no significant film dissolution. Absorption spectra of Ni and Fe metal foils were measured for precise energy calibration.

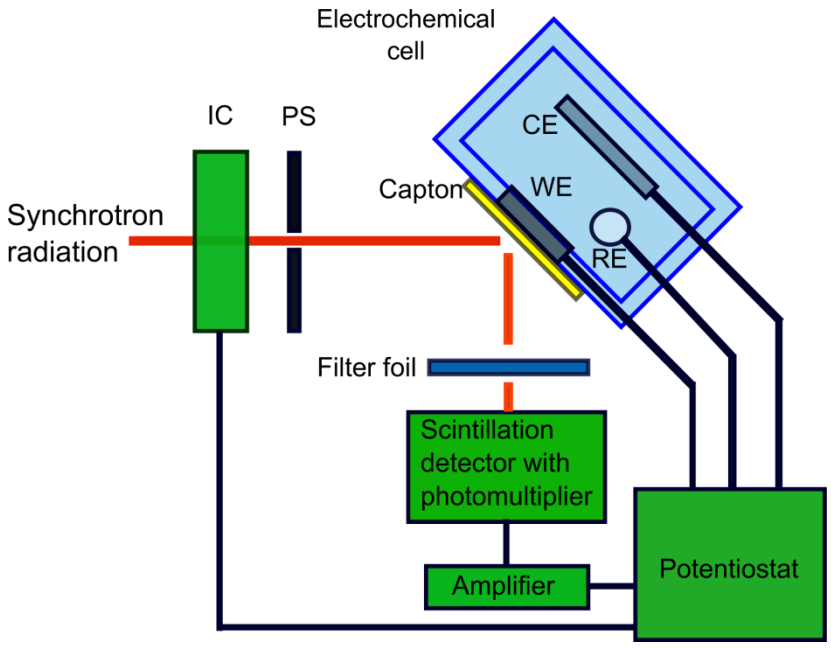

Figure 6.1. Simplified schematic representation of the experimental setup of the time-resolved X-ray absorption measurements. Monochromatic synchrotron radiation passes through an ionization chamber (IC, for recording the variations in the incoming beam intensity) and a photoshutter (PS) before hitting the catalyst film. The film is deposited on a carbon paper working electrode (WE) in a standard 3-electrode electrochemical setup, with a reversible hydrogen electrode as a reference electrode (RE) and a platinum mesh serving as counter electrode (CE). The cell is filled with 1 M KOH. Kapton tape covers a side window in the electrochemical cell. The excited Fe and Ni X-ray fluorescence passes through the Kapton window and then through a 10 μm metallic Mn or Co foil that filters out the majority of the scattered light. The fluorescence is monitored perpendicular to the incident beam by a scintillation detector. The detector consists of a scintillating crystal and a fast photomultiplier operated at 1.1 kV. The signal from the photomultiplier passes through a 1 MΩ resistor for current-to-voltage conversion and is read by an amplifier. The amplified signal is finally recorded by a potentiostat that also operates the electrochemical cell and records the signal from the reference ionization chamber (IC).

6.1.9 EXAFS Fourier-transforms and EXAFS simulations

The extracted spectrum was weighted by k^3 (except for samples in the Fe edge that were k^1 weighted) and simulated in *k*-space. All EXAFS simulations were performed using in-house software (SimX3) after calculation of the phase functions with the FEFF program (version 8.4, self-consistent field option activated). Phase functions were calculated using fragment of transition

metal oxides $MetalO_2$ layer with 10 metal atoms and 32 oxygen atoms as the one shown in Figure 6.2. The EXAFS phase functions did not depend strongly on the details of the used model. Cosine windows covering 10% at the low-*k* and high-*k* side of the spectra were applied before calculation of the Fourier transforms. An amplitude reduction factor (S_0^2) of 0.7 was used for all metals except for the Fe catalyst, were we used a factor of 0.8. The data range used in the simulation was 25–753.8 eV (2.17–14 $Å^{-1}$). In order to minimize the number of free parameters and to improve the significance of the simulation results, a joint fit approach was used where the interatomic distances were kept the same for all spectra of one data set (same type of metal oxide as deposited and after conditioning in pH 7 and 1 M KOH). Also The Debye-Waller parameters for all shells were fixed to 0.063 Å in to avoid overparameterization and to be able to study better the changes in coordination numbers under the different conditionings of the samples. The EXAFS simulation was optimized by a minimization of the error sum obtained by summation of the squared deviations between measured and simulated values (least-squares fit). The fit was performed using the Levenberg-Marquardt method with numerical derivatives. The error ranges of the fit parameters were estimated from the covariance matrix of the fit, and indicate the 68 % confidence intervals of the corresponding fit parameters. The fit error was calculated as in ref (Risch, Klingan et al. 2011). For calculation of the Fourier-filtered error (described in Ref. (Dau, Liebisch et al. 2003)), the range from 1 to 7 Å on the reduced distance scale was used.

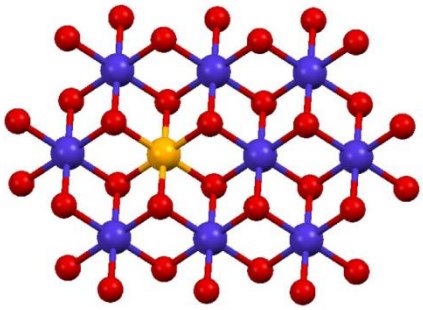

Figure 6.2. Structural model used for the calculation of the phase functions. In this case the red atoms represent the oxygen, the blue atoms correspond to Co and the orange atom correspond to the Co atom chosen as scattering atom for the phase functions calculations. For all the different transition metal oxides similar fragments were used with the corresponding metal.

6.1.10 Subtraction of the metallic contribution in the EXAFS

The metallic contribution in the extended X-ray absorption fine structure (EXAFS) spectrum can be artificially diminished by subtracting a weighted metal spectrum from the sample spectrum according to the following formula

$$corrected\ spectrum = \frac{1}{1-\alpha} * (sample\ spectrum - \alpha * metal\ spectrum)\ \ with\ \alpha < 1$$

Where the factor α represents the fraction of metallic contribution. The corrected spectrum is re-normalized by the factor 1/(1-α). This kind of corrections have been used before for cobalt based catalysts (Cobo, Heidkamp et al. 2012). An example of the effect of the correction in the XANES and EXAFS spectra for the NiFe catalyst is shown in Figures 6.3 and 4 where α was 0.1.

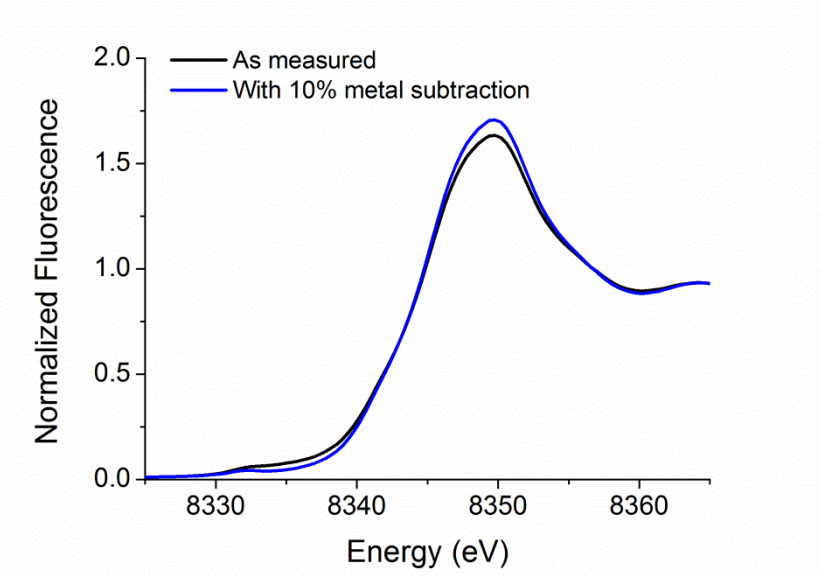

Figure 6.3. Nickel K-egde for the NiFe caltalyst in the in-situ measurements (with no potential applied) before (black) and after correction with a 10 % metallic contribution (blue).

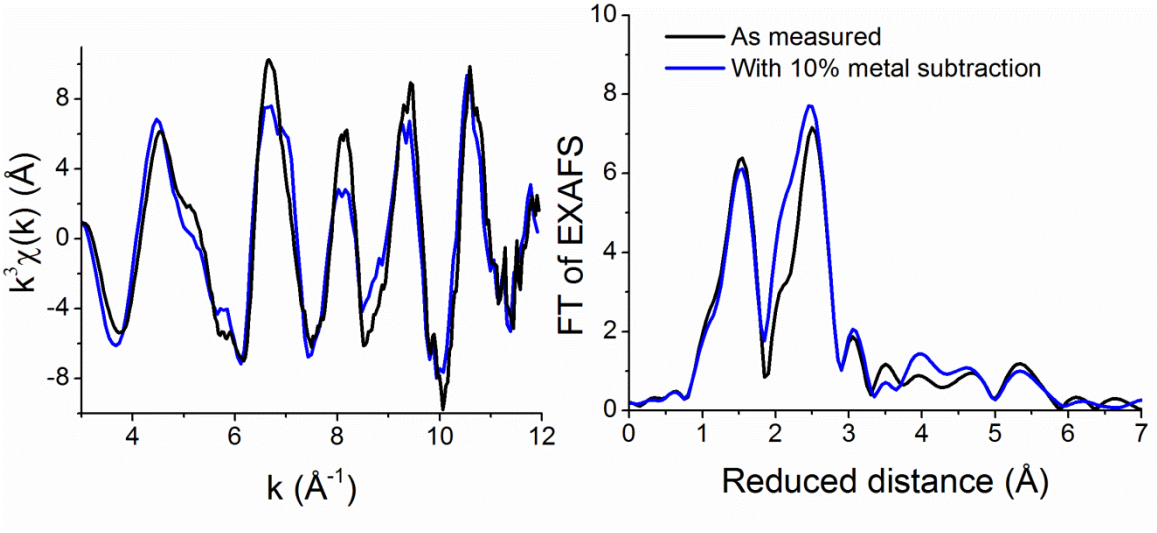

Figure 6.4. k^3-weighted EXAFS spectra (left) and FT of EXAFS for the NiFe catalyst at 1.55 V versus RHE before (black) and after correction with a 10 % metallic contribution (blue).

6.1.11 Time-resolved *in-situ* UV-vis absorption

NiFe oxide oxidation state changes induced by applied potential were tracked by absorption measurements. A film deposited on FTO was operated in a quartz glass electrochemical cell filled with 0.1 M phosphate buffer (pH 7) + 1 M KNO_3 or 1 M KOH at room temperature. The film together with the cell was placed on the path of a blue light (470 nm) beam coming from a pulse-driven (60 kHz) light-emitting diode. The transmitted light was detected by a photodiode connected to a lock-in amplifier. The amplified signal was recorded with time resolution of 1 ms (with 3 ms integration time constant of the lock in) by a potentiostat (BiologicSP-300) that also operated the electrochemical cell. We recorded CV together with absorption measurements at 470 nm at 40, 20 and 10 mV s^{-1} from 1.23 to 1.6 V versus RHE in 1 M KOH and from 1.3 to 1.85 V versus RHE in 0.1 $molL^{-1}$ phosphate buffer pH 7 with 1 $molL^{-1}$ KNO_3 supporting electrolyte. After this we did experiment with the stepping potential protocol. We stepped the potential 31 times between 1.55 and 1.2 V versus RHE and between 1.55 V and OCV for measurements in 1 M KOH and between 1.83 and 1.4 V versus RHE and between 1.83 V and OCV for measurements at pH 7.

6.1.12 Data treatment for the time-resolved *in-situ* UV-vis absorption measurements

To do the time-resolved absorption measurements we performed 31 times the step potential protocol between the two potential values or between the corresponding potential value and the OCP. After this we averaged the data excluding the first set of data as shown in Figure 5 and 6.

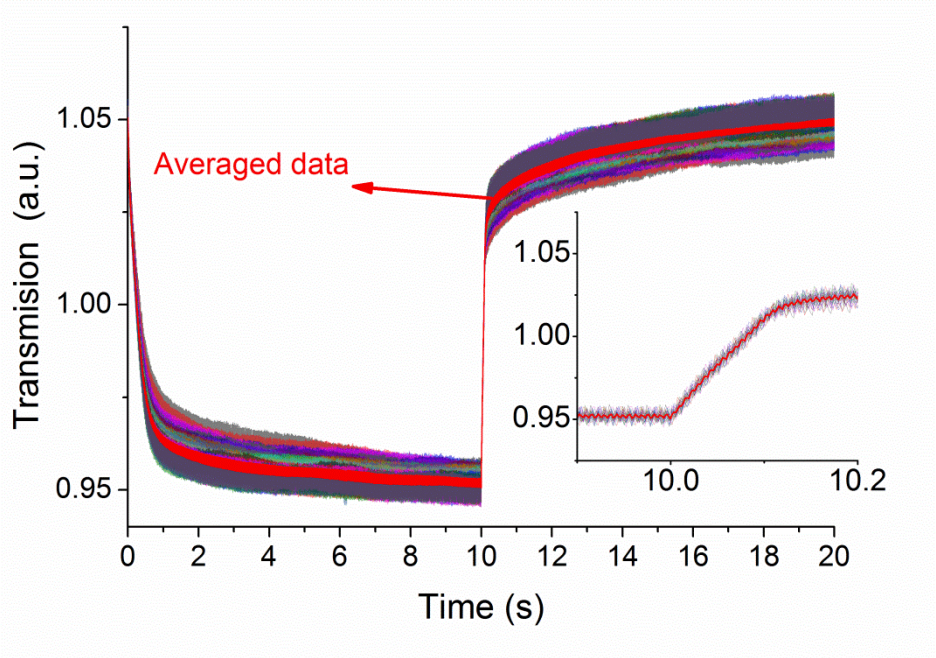

Figure 6.5. Example of averaging of the signals for the NiFe sample measured in 1 M KOH with jumping potential between 1.55 V and 1.20 V versus RHE. The different 30 data sets used for averaging are shown in different colors. The resulting averaged data is shown in red.

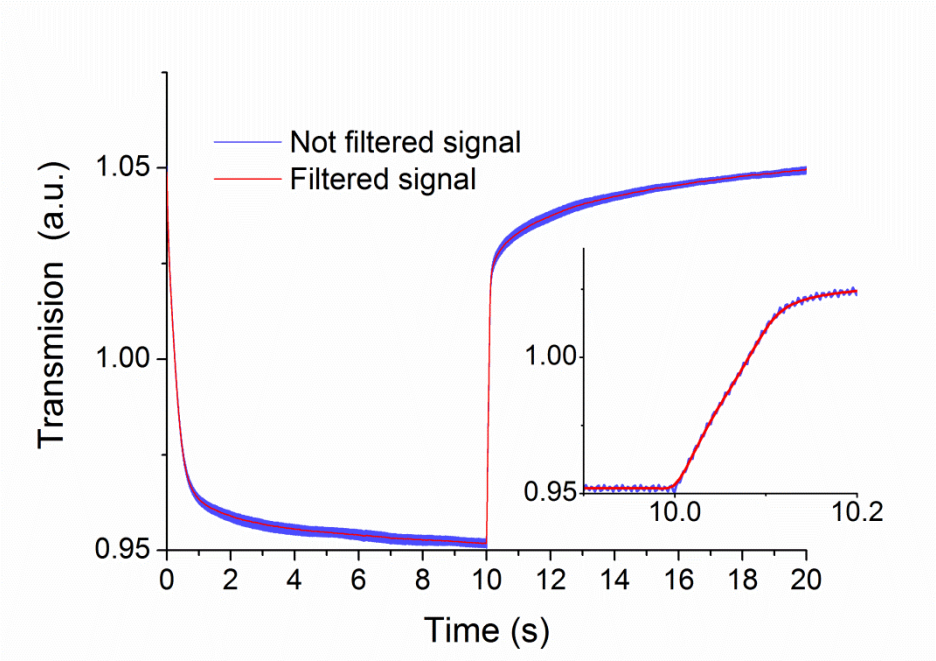

Figure 6.6. Example of filtering of the signals for the NiFe sample measured in 1 M KOH with jumping potential between 1.55 V and 1.20 V versus RHE. The filtered data is shown in red. Before the filtering the data was averaged every 2 data points.

To diminish the periodic noise we applied a filtering method that Fourier transform the data and filters out all frequencies higher than 80 Hz. The filtering was performed using the in-house software (BESSY).

6.2 Results and discussion

6.2.1 Electrochemical properties of the cathodically deposited catalysts

One of the major goals in the research area of water oxidation is to be able to fabricate integrated solar power electrolysers that capture solar energy and use this energy to split water and form hydrogen. A device with around 12 % solar to hydrogen conversion efficiency (which is an optimistic performance for a realistic device) will deliver a current of about 10 $mAcm^{-2}$ (Song and Hu 2014). However, since solar devices have a limited potential output, it is also desirable to deliver such a currents with the lower potentials possible. One of the major potential losses comes from the overpotential required for water oxidation. For this reason it is of high interest the development of catalyst that can help to decrease the overpotential required to deliver this 10 $mAcm^{-2}$ current densities (ideally below 300 mV). The lower the overpotential, the lower the energy losses and better the efficiency of the device. So far, with most of the known catalyst this seems difficult to accomplish at neutral pH. However, in strong alkaline conditions NiFe based catalyst has shown very promising performances (Gong, Li et al. 2013, McCrory, Jung et al. 2013).

We consider that cathodic deposition of transition metal catalyst at elevated current densities is of high technological importance, since high amounts of catalyst can be deposited quickly and easily with very good catalytic performance. To study this type of materials we followed the electrodeposition procedure described by Merrill for Ni, Fe, NiFe, Co and Mn based catalyst (Merrill and Dougherty 2008). The deposition solutions are described in the experimental part. It was already reported in that article that the catalytic activity in case of the FeNi is superior compared to any other metal oxide. However, some reports have shown that the catalytic activity of NiFe oxide is not especially high at neutral pH (Görlin, Gliech et al. 2016). We consider that a better understanding of these phenomena by comparison of the behavior with other metals at neutral and basic pH can be helpful in the designing of catalysts that work optimally at certain desired pH. For practical effects, in this chapter we use the notations 1M KOH and pH 14 as roughly equivalents.

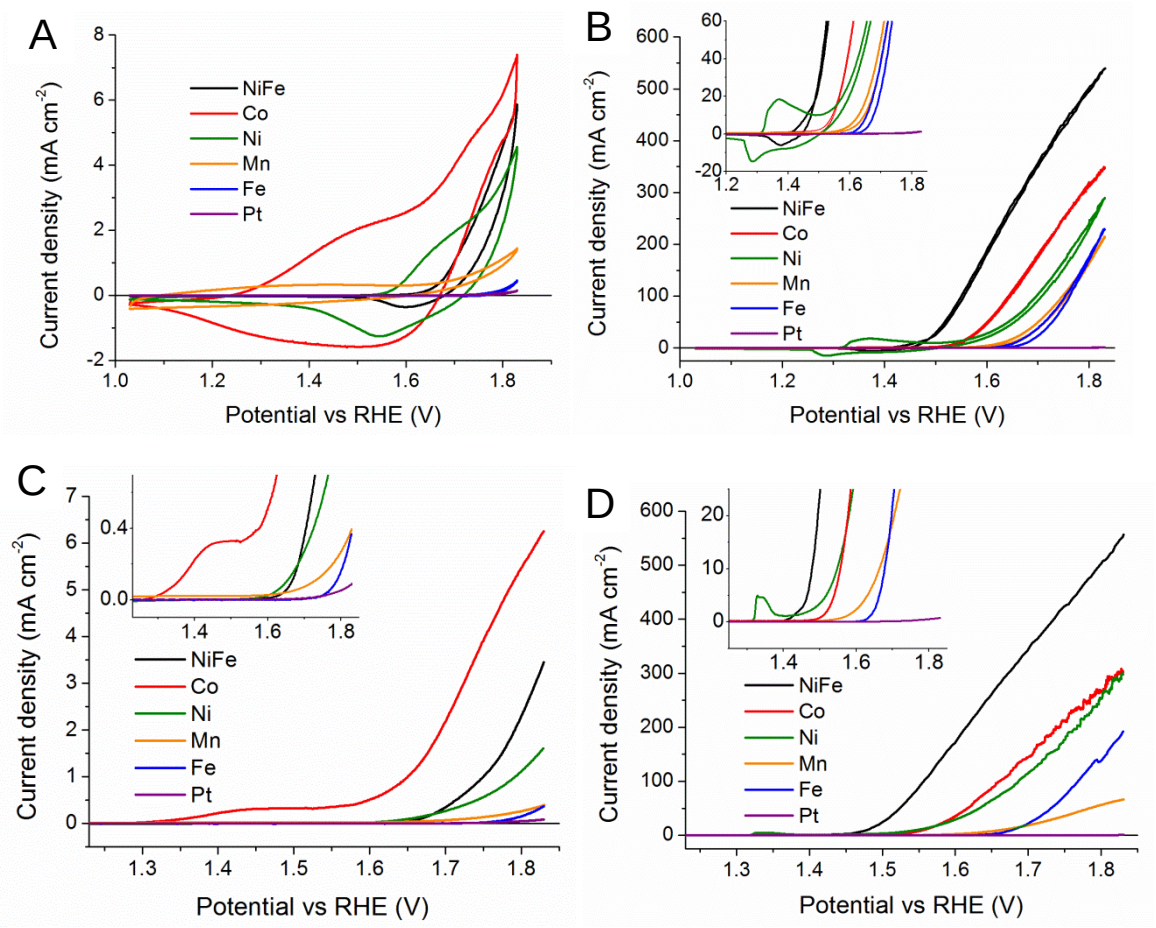

Figure 6.7. 10 mVs^{-1} CV (second scan) for cathodically deposited transition metal catalysts, measurements in 0.1 M phosphate pH 7 +1 M KNO_3 **(A)** and 1 M KOH **(B)**. And 1 mVs^{-1} forward (first) linear scan in 0.1 M phosphate pH 7 +1 M KNO_3 **(C)** and 1 M KOH **(D)**.

We extended the experiments from Merril also to measurements at pH 7 using 0.1 $molL^{-1}$ phosphate buffer with 1 $molL^{-1}$ KNO_3 to keep a comparable ionic strength. In Figure 6.7 the corresponding CV´s at 10 mVs^{-1} and upward linear scan at 1 mVs^{-1} at pH 7 and pH 14 are shown. The electrochemistry at pH 7 and in 1 mol L^{-1} KOH differs importantly. We can observe from comparison of the maximum current at 1.83 V versus RHE in the 1 mV s^{-1} scans that the catalytic activity is increased for all catalysts in 1 mol L^{-1} KOH. Also from comparison of the negative area of the CV´s at 10 mVs^{-1} at pH 7 and pH 14 (which is related to the portion of redox active species) we can observe that the trends in area magnitude also change. For example, meanwhile at pH 7 the highest redox area corresponds to the Co catalyst, in 1 $molL^{-1}$ KOH it corresponds to the Ni based catalyst. A comparison of redox area and maximum catalytic current at 1.83 V versus RHE is given in Table 6.2. Table 6.2 also shows the percentage of electroactive oxide calculated as the redox charge in the CV divided by the total amount of deposited oxide material shown in Table 6.5.

Table 6.2. Comparison of the negative integrated area of the CV´s at 10 mVs^{-1} in Figure 6.7A and 6.7B and current at 1.83 V versus RHE obtained from the 1 mVs^{-1} CV´s shown in Figure 6.7C and 6.7D for measurements at pH 7 and in 1 $molL^{-1}$ KOH. The % of electroactive oxide was calculated as the ratio between the redox charge in the CV and the total quantity of oxide deposited (excluding any metallic contribution.The estimation of the metallic contribution is explained in the EXAFS section).

	pH7			1 $molL^{-1}$ KOH		
	Charge (mC cm^{-2})	% of electroactive oxide	Current density at 1.83 V vs RHE (mA cm^{-2})	Charge (mC cm^{-2})	% of electroactive oxide	Current density at 1.83 V vs RHE (mA cm^{-2})
NiFe	5.0	2.0	3.46	56.0	22.1	556.5
Co	68.3	33.4	6.26	28.0	13.7	307.0
Ni	32.4	6.5	1.61	237.6	47.6	295.8
Mn	14.5	5.7	0.40	7.5	2.9	66.6
Fe	0.4	0.3	0.37	0.0658	0.04	192.9

From the data in Figure 6.7 it can be observed that the catalytic activity of the NiFe oxide at pH 7 is not so superior compared to other catalyst like Co oxide for example. On the other hand, in 1 mol L^{-1} KOH, the activity of the NiFe catalyst is especially high. Table 6.4 shows the overpotential required to hold a 10 mA cm^{-2} current density. In the case of the NiFe catalyst prepared in this study, this overpotential corresponds to some of the lowest reported 0.25 V (Gong and Dai 2014, Song and Hu 2014).

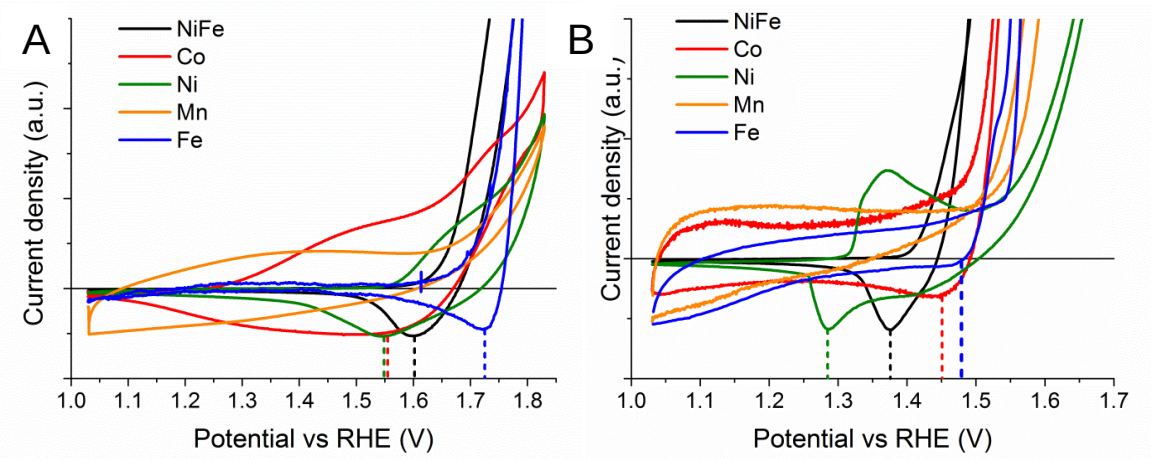

Figure 6.8. 10 mVs^{-1} CV (second scan) for cathodically deposited transition metal catalysts, measurements in 0.1 M phosphate pH 7 +1 M KNO_3 **(A)** and 1 M KOH **(B)**. The y-scale was normalized in a way that it is possible observing the more clearly the redox waves for all the films.

Figure 8 shows the 10 mVs^{-1} CV´s at pH 7 and pH 14 normalized to be able to observe the redox changes. The position of the cathodic wave is signaled with the dashed line. The corresponding values are shown in Table 6.3. With the exception of the Mn catalyst where individual redox waves cannot be clearly observed, for all the rest of the catalyst the cathodic wave at pH 14 is shifted to lower potentials versus RHE in comparison to the pH 7 values.

Table 6.3. Position of the reductive wave for each catalyst versus RHE at pH7 and pH 14.

	Reductive Potential (V)	
Catalyst	**pH 7**	**pH14**
NiFe	1.60	1.40
Co	1.55	1.45
Ni	1.55	1.30
Mn	--	--
Fe	1.73	1.50

Table 6.4. Overportential required for holding 10 mA cm^{-2} in 1 M KOH. The overpotential values were obtained from the 1 mVs^{-1} forward linear scan shown in Figure 6.7D.

Catalyst	Overpotential at 10 mA cm^{-2}
NiFe	0.25
Co	0.33
Ni	0.32
Mn	0.43
Fe	0.45

The striking differences in the catalytic activity of these materials could be affected not only from intrinsic electrochemical properties but also from other factors like catalyst load or important structural differences. For that reason we also focused on studying those aspects. The estimation of the quantity of metal deposited for every type of catalyst was determined by TXRF measurements. In this case the films are dissolved and a portion of the sample is placed on quartz plates to perform the measurements using Ga as internal standard (details in the experimental section). The results of the quantification are shown in Table 6.5. In all cases the quantity of deposited metal varied between 1500 and 5159 nmol cm^{-2}. We consider the catalysts to have a comparable magnitude order of metal deposited. We also performed some long term experiments in which we studied the quantity of remaining metal after applied for 5 minutes 0.4 V overpotential for catalyst operated in 1 $molL^{-1}$ KOH and 0.6 V overpotential for catalyst operated at pH 7. After this we also performed 3 CV´s at 20 mVs^{-1}, 2 CV´s at 10 mVs^{-1} and 1 CV at 1 mVs^{-1} between 1.03 and 1.83 V versus RHE. We observed for the NiFe catalyst leaching of Ni atoms to almost half of the initial quantity after operation in pH 7. This observation is consistent with previous similar observations (Görlin, Gliech et al. 2016). However the Fe content remained the same. In terms of stability, the Fe catalyst is especially problematic since falling of the catalyst from the electrode can be observed when operated in 1 $molL^{-1}$ KOH. The quantity of metal is diminished to approximately 40% of the initial quantity after operation. The Mn catalyst also loses material when operated in pH 7 to about 60% of the initial quantity. The cobalt catalyst after the operation in 1 $molL^{-1}$ KOH also looses around half of the initial quantity of metal. The Ni and NiFe samples are specially stable and robust in 1 $molL^{-1}$ KOH.

Table 6.5. Quantification of the deposited metals by TXRF.

Catalyst	Deposited material (nmol cm^{-2})	Deposited material (mC cm^{-2})
Ni	5159.1	499.6
Co	2120.4	204.6
NiFe	2623.5 Ni+ 1508.5 Fe	253.1 Ni+ 145.5 Fe
Mn	2619.0	256.5
Fe	1596.8	154.1

6.2.2 Structural properties of the cathodically deposited catalysts

To have a better understanding of the structure we performed X-ray absorption spectroscopy measurements at the K-edge of the corresponding metal. The samples were measured as deposited, and after applying 0.3 V overpotential for measurements at pH 14 and 0.4 V overpotential for samples conditioned in pH 7. To do so we used the freeze quenching approach in which the potential is applied for 5 min and the samples are frozen rapidly in liquid nitrogen (within a few seconds with no potential applied). Figure 6.9 shows the XANES for the different metal oxide catalyst. The EXAFS are shown in Figure 6.10 and the simulation data is shown in Figure 6.11 and Table 6.6. To do the simulations we performed a join fit for samples of the same type of catalyst with the three different conditionings. The Debye-Waller factor was also fixed. With this approach it is easier to distinguish changes in the portions of different phases in the film by checking the changes in the coordination number proportions.

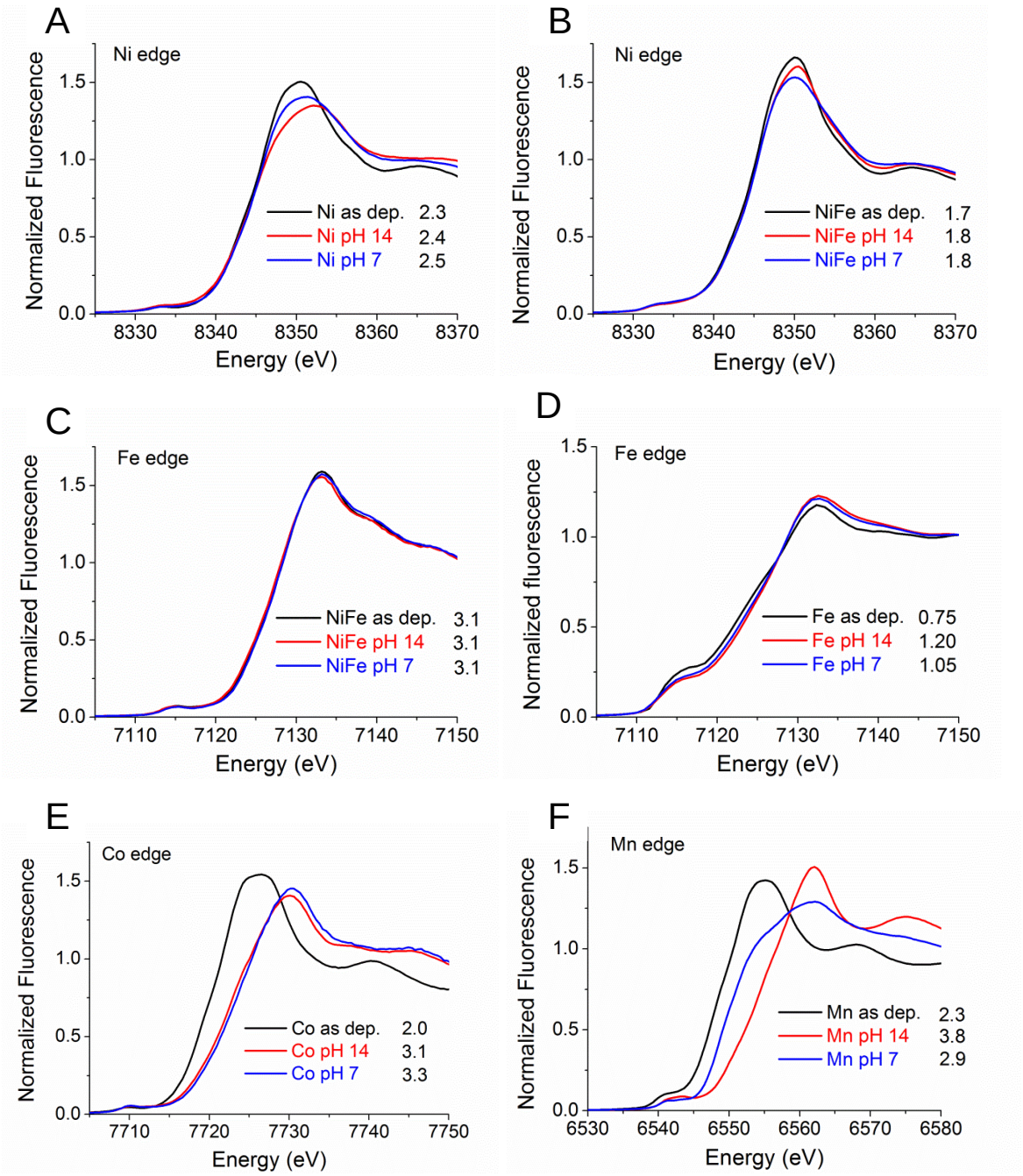

Figure 6.9. XANES spectra for transition metal oxides as deposited (black), after 5 min at 0.3 V overpotential in KOH (red) and after 5 min at 0.4 V overpotential in 0.1 molL^{-1} phosphate buffer pH 7. The images show cathodically deposited nickel oxide A), NiFe oxide at the Ni K-edge B), NiFe oxide at the Fe K-edge, Fe oxide D), Co oxide E) and manganese oxide F). The numbers after each sample name indicate the average oxidation state of the metal estimated from the edge position.

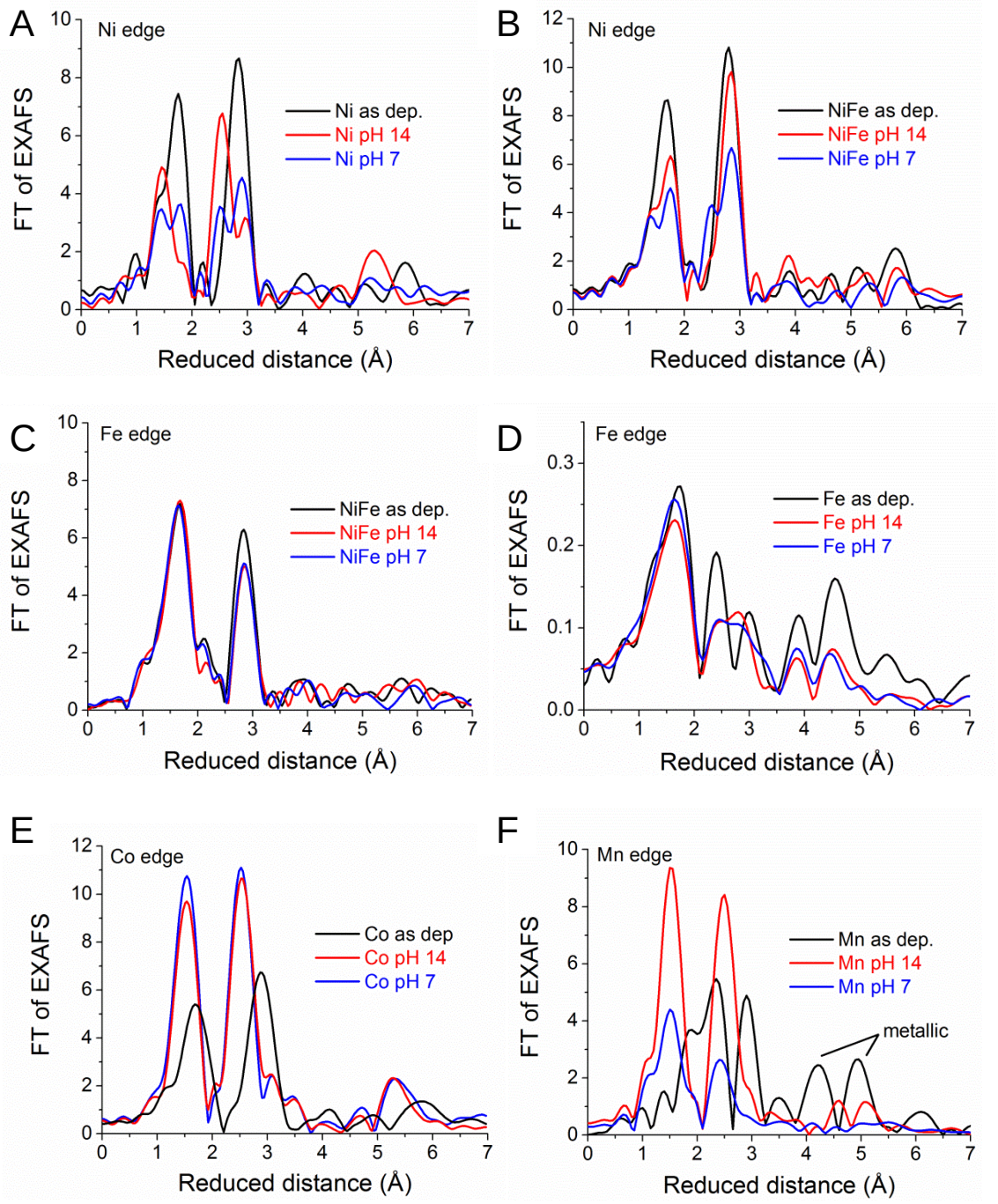

Figure 6.10. FT of EXAFS spectra for transition metal oxides as deposited (black), after 5 min at 0.3 V overpotential in KOH (red) and after 5 min at 0.4 V overpotential in 0.1 molL^{-1} phosphate buffer pH 7. The images show cathodically deposited nickel oxide A), NiFe oxide at the Ni K-edge B), NiFe oxide at the Fe K-edge C), Fe oxide D), Co oxide E) and manganese oxide F). All spectra are k^3 weighted except for the D which is k^1 weighted to damp the metal oscillations at high k and resolve better the oxide contribution. The samples were frozen without potential applied.

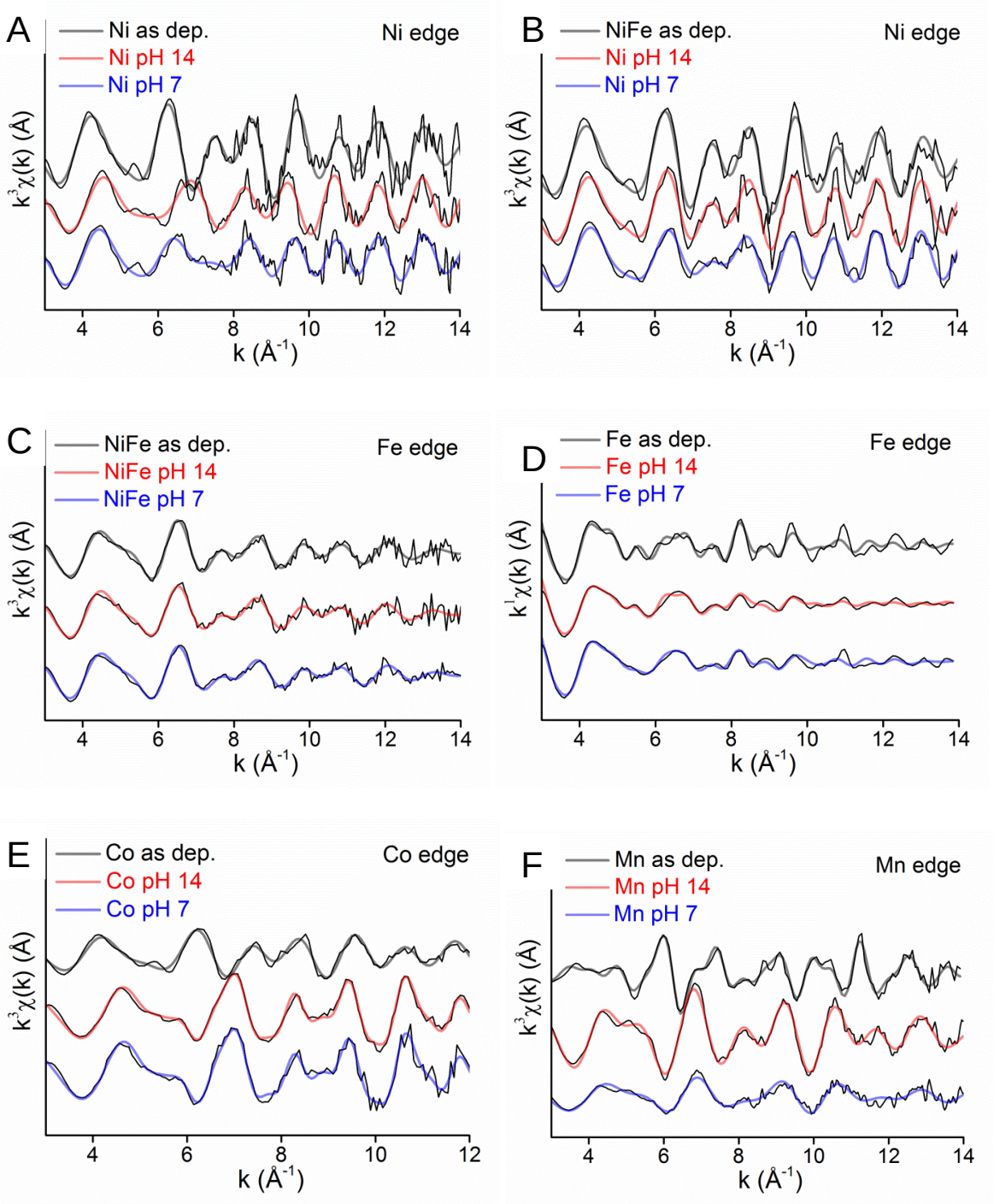

Figure 6.11. EXAFS spectra for transition metal oxides as deposited (gray), after 5 min at 0.3 V overpotential in KOH (red) and after 5 min at 0.4 V overpotential in 0.1 molL^{-1} phosphate buffer pH 7. The images show cathodically deposited nickel oxide A), NiFe oxide at the Ni K-edge B), NiFe oxide at the Fe K-edge C), Fe oxide D), Co oxide E) and manganese oxide F). All spectra are k^3 weighted except for the D with is k^1 weighted to damp the metal oscillations at high k and resolve better the oxide contribution. Note that the simulations in the Co catalyst were performed until k 12. The simulations are shown in color curves, and the experimental data is shown in black.

Table 6.6. Coordination numbers, N, and distances as determined from EXAFS simulation. The EXAFS Debye-Waller parameter, σ, was set to 0.063 Å to avoid overparameterization. The number in parenthesis corresponds to the uncertainty in the last digit. The simulations were done as a joint fit for the same type of sample, were the distances for a same type of bond were fitted as the same for the three types of conditioning. The metallic distances were not taken into account.

Type of bond	**Distance (Å)**	**Ni oxide as dep**	**Ni oxide pH 14**	**Ni oxide pH 7**
Ni-O_{short}	1.89(1)	1.0(4)	3.1(3)	2.1(3)
Ni-O_{long}	2.05(1)	6.1(4)	1.7(4)	3.5(4)
Ni-Ni_{short}	2.84(1)	0.1(3)	2.9(2)	1.5(2)
Ni-Ni_{long}	3.08(1)	4.6(3)	1.5(3)	2.4(3)
	Distance (Å)	**NiFe oxide as dep**	**NiFe oxide pH 14**	**NiFe oxide pH 7**
Ni-O_{short}	1.90(1)	0.8(4)	1.7(4)	1.9(4)
Ni-O_{long}	2.04(1)	5.9(4)	4.6(4)	3.9(4)
Ni-Ni_{short}	2.84(1)	0.0(3)	1.2(3)	1.7(3)
Ni-Ni_{long}	3.06(1)	4.6(3)	4.5(4)	3.4(4)
	Distance (Å)	**NiFe oxide as dep**	**NiFe oxide pH 14**	**NiFe oxide pH7**
Fe-O_{short}	1.94(1)	2.8(4)	2.7(4)	3.2(4)
Fe-O_{long}	2.05(1)	3.9(4)	4.0(4)	3.5(4)
Fe-Ni_{short}	2.86(1)	0.7(3)	1.1(3)	0.8(3)
Fe-Fe_{short}	3.03(1)	3.6(5)	3.1(5)	3.0(4)
Fe-Fe_{long}	3.14(1)	3.0(4)	2.6(1)	2.4(4)
	Distance (Å)	**Fe oxide as dep**	**Fe oxide pH 14**	**Fe oxide pH 7**
Fe-O_{long}	2.05(1)	6.0(3)	5.1(3)	5.7(3)
Fe-Fe_{long}	3.13(2)	4(1)	2.8(8)	1.7(8)
	Distance (Å)	**Co oxide as dep**	**Co oxide pH 14**	**Co oxide pH 7**
Co-O_{short}	1.89(1)	--	5.7(3)	6.3(3)
Co-O_{long}	2.09(1)	6.2(4)	--	--
Co-Co_{short}	2.83(1)	--	4.9(2)	5.1(2)
Co-Co_{long}	3.14(1)	4.1(3)	0.9(3)	0.4(4)
Co-$Co_{mono-\mu}$	3.42(2)	--	0.8(4)	1.3(4)
Co-$Co_{long-range}$	5.66(1)$^{+}$	--	3.2(6)	3.6(6)
	Distance (Å)	**Mn oxide as dep**	**Mn oxide pH 14**	**Mn oxide pH 7**
Mn-O_{short}	1.90(1)	--	5.5(2)	3.8(2)
Mn-O_{long}	2.20(2)	2.9(6)	--	2.2(2)*
Mn-Mn_{short}	2.88(1)	--	4.9(6)	1.2(2)
Mn-Mn_{long-1}	2.99(2)	--	3.1(7)	--
Mn-Mn_{long-2}	3.17(2)	--	2.1(5)	--

*In the case of this sample the sum of the coordination numbers of the first Mn-O shells was fixed to 6.

+This distance was set as twice the 2.83 Å Co-Co distance and simulated using multiple scattering as in reference (Risch, Klingan et al. 2012).

In the case of the cathodically deposited Ni catalyst we observe that the phase with the major fraction has Ni-O distances at 2.05 Å and Ni-Ni distances at 3.08 Å which are consistent with the structure of α-$Ni(OH)_2$. This kind of phase is composed by NiO_6 octahedra interconnected by protonated di-μ-oxo-bridges forming layers. Neighboring sheets are randomly oriented with distances superior to 8 Å between them. Inside the layers there are water molecules and ions which are not in specific positions (Pandya, O'Grady et al. 1990). The average oxidation state as estimated from the edge position is about 2.3 which is also consistent with a majority of α-$Ni(OH)_2$ phase with a small portion of another phase with higher oxidation state and shorter distances at 1.89 Å for Ni-O and 2.84 Å for Ni-Ni. These distances are consistent with formation of γ-NiOOH which results in formation of higher oxidation Ni species like Ni^{+3} accompanied by deprotonation of the di-μ-oxo-bridges (Glemser and Einerhand 1950, Delmas, Fouassier et al. 1980, Risch, Klingan et al. 2011, Bediako, Lassalle-Kaiser et al. 2012). In the films electrochemically operated in 1 $molL^{-1}$ KOH and pH 7 there is an increase in the portion of the γ -NiOOH phase which is followed by an increase in the oxidation state.

In the NiFe catalyst, at the Ni edge we observe an important metallic contribution manifested as a pronounced pre-edge feature, oxidation state bellow +2 and presence of a very short Ni-Ni distance at 2.5 Å. This metal contribution can be diminished by subtracting a fraction of a metal foil reference spectrum and renormalizing the resulting spectra as described in the experimental part. The portion of metallic contribution can be also calculated by simulation of the XANES spectrum as the linear combination of the metallic and metal oxide fractions as described in the experimental section. In the specific case of the NiFe catalyst this metallic contribution at the Ni edge corresponds to a 10 % approximately. To do the simulations we subtracted this contribution and fitted only the oxide part. After this, the trend is similar to the only Ni oxide film. The film as deposited corresponds mostly to a α-$Ni(OH)_2$ phase. Electrochemical operation in 1 $molL^{-1}$ KOH and pH 7 results in the formation of shorter Ni-O and Ni-Ni distances at 1.90 Å and 2.84 Å corresponding to γ-NiOOH. However, in this case we observed a lower proportion of γ-NiOOH formed and a less pronounced change in the edge position (all Ni species remained mostly like Ni^{+2}) in comparison to the only Ni sample. The discrepancies with other reports (Friebel, Louie et al. 2015) might come from the fact that we did not measure the samples under applied potential, and for instance the observed species correspond to a more relaxed state. According to some more recent reports (Goerlin, Chernev et al. 2016), in the case of a catalyst with high performance, a few seconds waiting before freezing the samples might be critical to be able to keep the species in the active state since the high catalytic rate might deplete fast the species in high oxidation state.

In the NiFe catalyst at the Fe edge, the metallic contribution is very small, present only like a Fe-Fe peak at 2.5 Å with a small coordination number (about 0.4) in the EXAFS spectrum. We did not observe any shifting in the edge position under applied potential. From the simulation of the EXAFS spectra we obtain Fe-O distances at 1.94 Å and 2.05 Å and Fe-Metal distances at 2.86 Å, 3.03 Å and 3.14 Å. The long Fe-O and Fe-Metal distances at 2.05 and 3.14 Å are consistent with formation of γ-FeOOH as observed before in other NiFe catalysts (Friebel, Louie et al. 2015, Wu, Chen et al. 2015, Li, Bai et al. 2016). The short 1.94 Å Fe-O and 2.86 Å Fe-metal distances are also consistent with the distances observed by Bell´s group for a NiFe catalyst under catalytic potentials. We observed a low proportion of these short distances; however, since we did not freeze the samples under applied potential, the observed proportion of phases might correspond to the more relaxed state. The absence of any long range order distances indicates a very amorphous Fe phase and that only a small fraction of the Fe content could have been incorporated into the Ni more ordered phase. The structural data implies the presence of at least the following phases: metallic Ni, metallic Fe, α-Ni(OH)2, γ-NiOOH, very amorphous γ-FeOOH and the possible mixture of the Ni phases with small fractions of Fe. The cathodically deposited NiFe catalyst is therefore more than a simple material, and seems to be composed of a complex mixture of phases and possibly undergoes some dynamical changes under electrochemical operation. We will discuss more deeply about the structure of the NiFe catalyst and its dynamical changes further in the chapter in the section about *in-situ* XAS measurements.

In the case of the only Fe catalyst the metallic contribution is over 60 % in all the films. This contribution can be easily observed in the XANES spectrum as described in the experimental part. The experimental spectra can be modeled as the linear combination of fractions of a metal Fe reference and a Fe(III) oxide reference spectra. However, since this metallic contribution is so high, it cannot be so easily subtracted from the EXAFS spectra due to high amplitude oscillations at high k values which are difficult to damp since they are re-scaled with the renormalization of the data. To diminish these high k oscillations we did the metallic contribution subtraction and k^1 weighted the spectrum. In this way we can observe an oxide phase formed, but we can only distinguish long Fe-O distances at 2.05 Å. However, due to the high noise in the data after the subtraction, we cannot discard possible formation of a small fraction of shorter Fe-O distances as well.

In case of the Co catalyst, the film as deposited presents long Co-O and Co-Co distances at 2.09 Å and 3.14 Å respectively with cobalt in an oxidation state close to +2. This type of distances are characteristic of formation of an $Co(OH)_2$ hydroxide phase. Similarly as in the nickel hydroxide the long distances are a result of the protonation of the di-μ-oxo-bridges and the low oxidation state of the cobalt. Formation of cobalt hydroxide under cathodic conditions has been observed before for

similar electrodepositions (Zhou, Zhang et al. 2008, Gao, Li et al. 2016). After electrochemical operation at pH 7 and pH 14, complete conversion to an oxide phase is observed as evidenced by the increase in the oxidation state to Co^{+3} and formation of shorter Co-O and Co-Co distances at 1.89 Å and 2.83 Å respectively. Formation of this type of oxide phases has also been widely studied (Risch, Khare et al. 2009, Kanan, Yano et al. 2010, Gerken, McAlpin et al. 2011). We also observed that the electrochemical operation results in formation of a more ordered phase for both pH conditions in comparison to the as deposited film. The formed oxide after operation at pH 7 and pH 14 also differs from the structure of cobalt oxide deposited anodically in pH 7 phosphate buffer. For example in the cathodically deposited Co oxides we observe a higher coordination number for the distances at 2.83 Å which is assigned to Co-Co di-μ-oxo-bridges. The distance at 5.66 corresponds to a multiple scattering pathway with two times the distance at 2.83 Å, and is for instance structurally conformed by three Co atoms in line connected by two di-μ-oxo-bridges. This distance was simulated as in the reference (Risch, Klingan et al. 2012) where they observed an amplitude of 0.4±0.4 for the cobalt oxide deposited in pH 7 phosphate buffer. In the cathodically deposited samples the coordination number for this distance is clearly higher with values over 3, which denotes again a structure with higher long range order. Another difference in the cathodically deposited oxide is the presence of the distance at 3.42 Å which corresponds to mono-μ-oxo-bridges in corner sharing octahedra. These types of distances are usually present in oxides which include tunnel kind of structures (Bergmann, Zaharieva et al. 2013).

The Mn catalyst as deposited shows a strong metallic contribution evidenced mostly by a Mn-Mn distance at 2.7 Å characteristic of metallic Mn phases. However, there is also a Mn-O contribution at 2.2 Å which denotes formation of an oxide phase on the Mn metallic layer. Upon electrochemical operation in pH 7 and pH 14 short Mn-O at 1.90 Å and Mn-Mn at 2.88 Å distances are formed and the oxidation state is increased. Formation of those distances in manganese based oxides have been widely described as birnessite type of structures (Zaharieva, Najafpour et al. 2011, Zaharieva, Chernev et al. 2012, Gorlin, Lassalle-Kaiser et al. 2013, Robinson, Go et al. 2013). The oxidation in pH 7 was more incomplete and formed a phase with higher amorphisity compared to the sample electrochemically operated in 1 M KOH. The Mn oxide operated in 1 M KOH shows the formation of a highly ordered oxide compared to the one deposited at pH 7 also with longer Mn-Mn distances at 2.99 Å and 3.17 Å. This type of distances have also been observed before in amorphous manganese oxides with structure similar to birnessite (Lee, Gonzalez-Flores et al. 2014).

In general, all the films show a very good performance at pH 14 with formation of similar structural features during electrochemical operation, this is formation of an oxy(hydroxide) phase

with short Metal-O and Metal-Metal distances accompanied by increase in the oxidation state, in consistency with most previous structural studies with electrodeposited transition metal catalyst. However, in some of the cases, differences in the structure compared to traditional oxy(hydroxide) phases can be observed as in the case of the Co catalyst for example.

Since during catalysis the intermediates are supposed to bond to the metal, many efforts have been made to corroborate trends in activity of transition metal oxides with the M-O bond strength according to the Sabatier principle (Morales-Guio, Liardet et al. 2016). In this case, the trends in activity result in a volcano type of plot. Very weak or very strong M-O bond results in poor catalytic activity. The maximum of the volcano plot corresponds to the optimal bond strength that leads to optimal catalysis (Rossmeisl, Qu et al. 2007, Man, Su et al. 2011).

Many of this kind of studies comparing activity trends in transition metal oxides have been made leading to different trends and mechanistic explanations (Hickling and Hill 1947, Trasatti 1980, Lyons and Brandon 2010, Suntivich, May et al. 2011). The differences in trends come for a series of factors like differences in microscopic surface area, contact with the electrode surface, differences in the electrical conductivity of the oxides and interference of impurities in the catalytic activity (Burke, Zou et al. 2015). All this effects are especially important in thick films as the ones we prepared in this study. For that reason our focus was not making another of those studies, but in a more simple way to describe how the observed redox charge of the metal and the catalytic activity are affected when the pH is changed from 7 to 14.

Even though the structural features determined by EXAFS are similar, the redox and catalytic behaviour is very different as we already mentioned previously. In the data shown in Table 6.2 we can observe some degree of correlation between the redox area and catalytic current. However, these correlations are obscured by the high convolution between the catalytic and redox waves. We decided then, to perform some more controlled experiments to quantify better these relationships in 0.1 M phosphate pH 7 with 1 M KNO_3 as supporting electrolyte and in 1 M KOH. To compare the performance of the catalysts at 0.4 V overpotential we used a jumping potential protocol in which we first applied a constant potential of 1.63 V versus RHE for 2 minutes which was then changed to 1.03 V versus RHE for 1 minute and recorded the current with 2 ms time resolution. These measurements were performed with no IR compensation, but we measured the Ohmic resistance after the experiment. From the integration of the current we can estimate the portion of redox equivalents at the applied potential. After this we measured 2 CV´s at 10 mVs^{-1} and 1 CV at 1 mVs^{-1} scan rates between 1.03 and 1.83 V versus RHE. These CV measurements were performed with 85 % IR compensation.

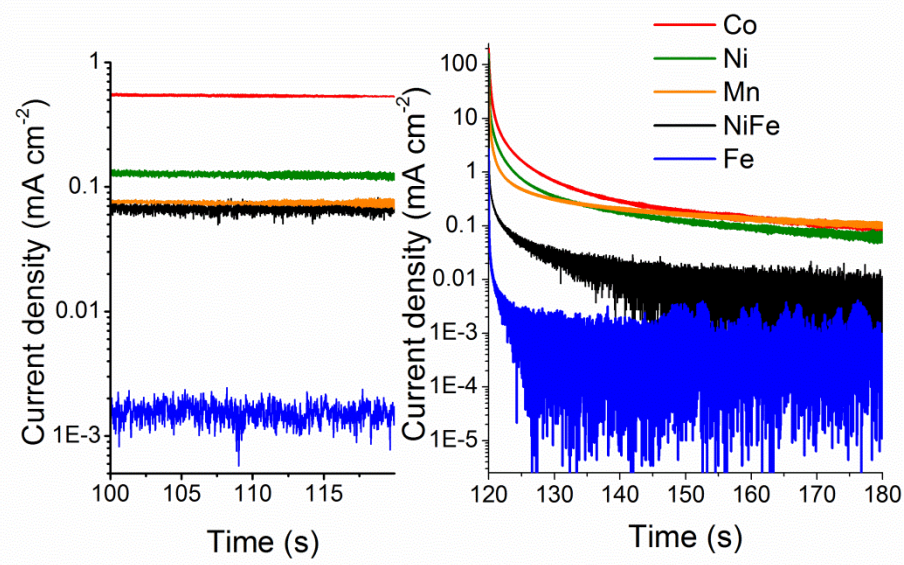

Figure 6.12. Jumping procedure switching from 1.63 V versus RHE for 2 minutes to 1.03 V versus RHE for 1 minute in a solution containing 0.1 M phosphate pH 7 +1 M KNO_3. The measurements were performed with 2 ms time resolution. The left panel shows the current in the last seconds of the first pulse at 1.63 V versus RHE which were used to estimate the catalytic current for the measurements at pH 7. The right panel shows the absolute current density at 1.03 V. Since the current density was negative, we took the absolute value to be able to use the logarithmic scale.

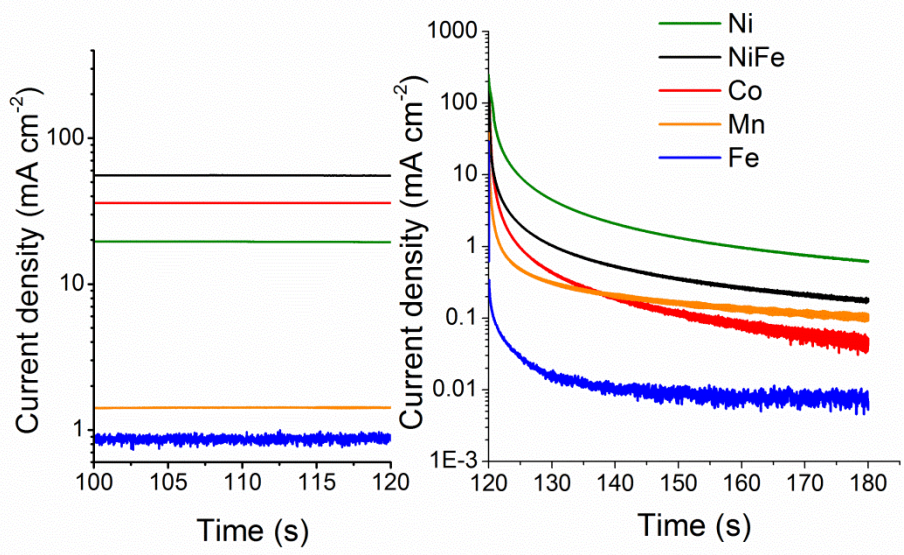

Figure 6.13. Jumping procedure switching from 1.63 V versus RHE for 2 minutes to 1.03 V versus RHE for 1 minute in a solution containing 1 M KOH. The measurements were performed with 2 ms time resolution. The left panel shows the current in the last seconds of the first pulse at 1.63 V versus RHE. The right panel shows the absolute current density at 1.03 V. Since the current density was negative, we took the absolute value to be able to use the logarithmic scale.

In the previously discussed TXRF experiments we observed that long term operation can affect the mechanical stability of some of the catalysts. To diminish the impact of the instability of the catalyst and have a better comparable data, we kept the experiments as short as possible. With the procedure described in the last paragraph, we observed that for all the samples after operation the quantity of deposited material diminished in less than 20 %, except for the only Ni sample operated in pH 7 and the only Fe sample operated in 1 $molL^{-1}$ KOH where the quantity of material in the electrode diminished by more than 40 % respect to the as deposited samples.

In the case of the measurements at pH 7 we observed that, since the currents are very low, the Ohmic loses are very insignificant, and for instance we used the stabilization current after 2 minutes at 1.63 V versus RHE (Figure 6.12) during the jumping protocol as the catalytic current. In the case of the measurements in 1 $molL^{-1}$ KOH, since the currents are much higher, the Ohmic drop can be as high as 40 mV. For this reason we decided to use the currents at 1.63 V versus RHE in the 1 mVs^{-1} forward scan as an estimation of the catalytic current. These 1 mVs^{-1} forward scans are the same shown in Figure 6.7.D. Also we assumed that the differences in effective applied potential due to the Ohmic losses do not affect dramatically the estimation of the redox charge using this step potential protocol in 1 $molL^{-1}$ KOH.

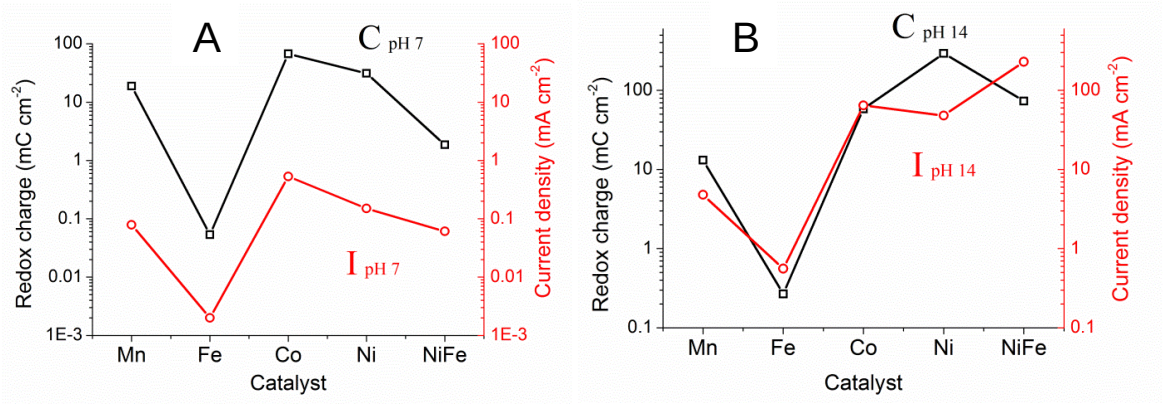

Figure 6.14. (A) Redox charge compared to the current density at 0.4 V overpotential at pH 7 for cathodically deposited transition metal catalyst and **(B)** Redox charge compared to the current density at 0.4 V overpotential at pH 14. In the case of the measurements at pH 7 the redox charge was obtained by integrating the current in Figure 6.12 after switching from **1.63 V** versus RHE to **1.03 V** versus RHE. The catalytic current was obtained as the stable current after 2 min at 1.63 V versus RHE also shown in the inset in Figure 6.12. In the case of the measurements at pH 14 the redox charge was calculated in a similar way as in pH 7. However, the catalytic current was obtained from the 1 mVs^{-1} forward scan shown in Figure 6.7D.

When we plot the redox charge and the catalytic current for the different metals in logarithmic scale (Figure 6.14), we can observe some clear correlations between them, especially a pH 7. The integrated redox charge is directly correlated to the number of redox-active metal centers undergoing oxidations state changes. The division of the estimated catalytic current by the redox charge can be seen as a turnover frequency (in s^{-1}) by redox-active metal as we have described before. In other words, it corresponds to an estimation of the normalized activity per catalytic center at 0.4 V overpotential. If we perform this estimation of the TOF for every studied transition metal catalyst at pH 7 and pH 14, we can observe for all the cases an increase of roughly 100 times in the catalytic activity (Figure 6.15). The similar increase for all metals suggests a common reason for the improvement. We will discuss more in depth this correlation further in the text using the NiFe catalyst as example.

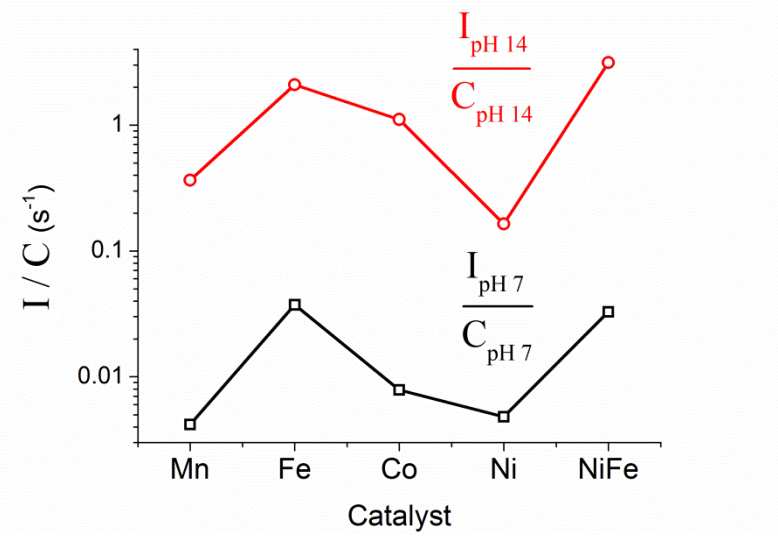

Figure 6.15. Ratio of the catalytic current and proportion of redox charge (q_{red}) at 1.63 V versus RHE in pH 14 (red) and pH 7 (black) for cathodically deposited transition metal catalysts. The ratio in both cases was obtained by dividing the values in Figure 6.14B (red) and Figure 6.14A (black) and may be viewed as a turnover frequency (TOF) rate of catalytic electron flow per redox-active cobalt ion. Both q_{red} and catalytic current are normalized to the macroscopic electrode area and they represent how the normalized activity changes when the pH is increased from pH 7 to pH 14.

6.2.3 Possible contaminations after operation in the samples

It is well known that certain levels of impurities can affect drastically the electrochemical properties of different transition metal oxides. Iron contaminations have shown to affect the redox potential and proportion of electroactive charge in cobalt oxides (Burke, Kast et al. 2015). Very small iron contaminations have also shown to be critical in the performance of nickel oxides in alkaline pH (Trotochaud, Young et al. 2014, Klaus, Cai et al. 2015). Table 6.7 shows the percentage of metal contaminations measured by TXRF. For comparison a clean platinum electrode with no catalyst deposited was used as a blank. This quantification suggests the possibility of contamination with other metals in some of the samples. In all cases we observed that the possible contamination levels were below 1% in metal content, except in the Fe catalyst in KOH, where the Ni is almost 3%.

Table 6.7. Estimation by TXRF of contamination with small portion of transition metals in the cathodically deposited catalyst after operation in 1 $molL^{-1}$ KOH and pH 7. The numbers shown correspond to the concentration in mg/L when the 1 cm^2 films are dissolved with 2 mL of concentrated HCl and diluted to 10 mL. The blank used for comparison corresponds to a platinum electrode that was rinsed with HCl and the solution diluted to 10 mL. The main possible contaminations in each film are highlighted in light red color.

		Concentration mg/L			
Catalyst	**Electrolyte**	**Mn**	**Fe**	**Co**	**Ni**
Blank	--	0.019	0.029	0.000	0.036
Fe	phosphate pH7 + 1 M KNO3	0.035	11.136	0.000	0.104
Fe	1 M KOH	0.017	3.012	0.000	0.084
Ni	phosphate pH7 + 1 M KNO3	0.015	0.049	0.000	18.614
Ni	1 M KOH	0.019	0.095	0.000	30.362
NiFe	phosphate pH7 + 1 M KNO3	0.024	8.788	0.000	8.283
NiFe	1 M KOH	0.025	7.994	0.000	10.027
Mn	phosphate pH7 + 1 M KNO3	9.834	0.040	0.000	0.120
Mn	1 M KOH	11.703	0.063	0.000	0.062
Co	phosphate pH7 + 1 M KNO3	0.017	0.024	11.753	0.071
Co	1 M KOH	0.017	0.036	9.210	0.117

6.2.4 pH dependence of the structural redox and catalytic properties in the NiFe catalyst

We performed grazing incident angle XRD measurements in the same NiFe catalyst samples that we used for the EXAFS experiments (Figure 6.16). The films as deposited and operated in pH 7 showed only strong reflections due to the platinum substrate (in orange). In the film operated in 1 $molL^{-1}$ KOH we observed the appearance of sharp reflextions at 12.0 and 24.1 2Θ degrees. These reflections are consistent with reports of NiFe layered double hydroxides with fougèrite/pyroaurite mineral structure which consist of layers of NiFe oxides with ions in the interlayer (Nakahira, Kubo et al. 2007, Trotochaud, Young et al. 2014). The reflections can be assigned to the (003) and the (006) planes respectively. There are also broad reflections at positions that correspond to a very amorphous α-$Ni(OH)_2$ phase as signaled with the green arrows. Some of these broad reflections are also present in the NiFe films operated in pH 7, but much less pronounced. The interlayer spacing can be calculated from the d spacing of the (003) plane. In the case of our oxides this spacing corresponds to about 7.2 Å. In this type of NiFe mixed oxides the interlayer spacing is larger than in pure Ni oxides since Fe^{+3} is incorporated in the structure and additional anions are required in the interlayer for stabilization and charge balance. Previous studies also showed an increase in the crystallinity of NiFe oxides upon electrochemical operation; however, they observed that catalytic activity was independent on the degree of crystalinity of the oxide, which suggest that the active sites are not affected by the crystallization process (Trotochaud, Young et al. 2014). We also observed the formation of similar reflections at 12.1 and 24.2 2Θ degrees in the case of the only Fe catalyst operated in KOH which also confirms the formation of an oxide phase presumably with similar characteristics to the NiFe oxide one (brown plot in Figure 6.16).

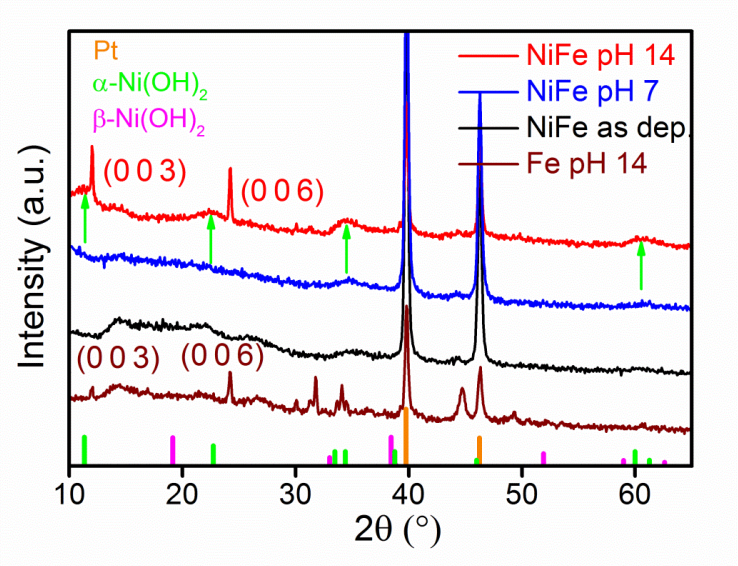

Figure 6.16. Grazing-incidence GIXRD patterns of NiFe catalyst as deposited (black), after 5 min at 0.3 V overpotential in KOH (red) and after 5 min at 0.4 V overpotential in 0.1 molL^{-1} phosphate buffer pH 7. The sloping background is due to the grazing-incidence geometry and has not been subtracted to preserve the peaks. The samples were kept dry under atmospheric conditions for several days before the XRD measurements. The measured samples correspond to the same used in the XAS experiments. The GIXRD for the only Fe sample after 5 min at 0.3 V overpotential in KOH is also shown (brown).

To study the long term stability of the NiFe catalyst we performed 200 CV cycles from 1.23 V to 1.63 V versus RHE in 1 molL^{-1} KOH at 10 mVs^{-1} scan rate (Figure 6.17A). We observed that particularly the first cycle is different from the rest, with a smaller oxidation wave overcrossing the reduction wave. After the second cycle the changes are more subtle, like broadening of the redox waves and a slight shift in potential, but in general the catalytic current remains quite stable. Under constant potential conditions at 1.53 V versus RHE for 4.5 h we observed a small decrease from 56 to 50 mA cm^{-2} (Figure 6.17B). However, we did not observe any evidence of long term activation under applied potential. We only observed a slight increase in the current during the first 50 s of electrochemical operation in 1 molL^{-1} KOH. This suggests that most changes in the catalyst happened already during the first seconds of electrolysis.

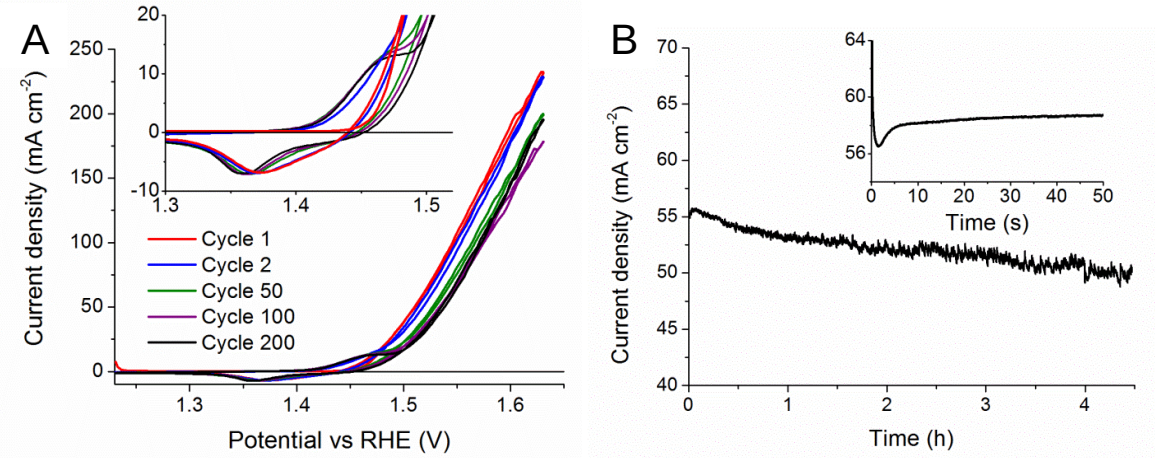

Figure 6.17. A) 10 mVs^{-1} CV´s of the NiFe catalyst in 1 $molL^{-1}$ KOH and B) long term stability of the NiFe catalyst at 1.53 V constant potential in 1 $molL^{-1}$ KOH (after iR compensation).

Since the NiFe catalyst is particularly interesting because of its high catalytic activity and low overpotential to deliver 10 $mAcm^{-2}$ as shown in Table 6.4, we decided to study more in detail the electrochemical properties of this material from neutral to strong alkaline pH conditions. We performed experiments in which CV´s at 20 mVs^{-1} were collected starting with 0.1 $molL^{-1}$ borate electrolyte at pH 8 and the pH was increased by adding KOH until pH 14. We observed that using KNO_3 as supporting electrolyte in this case produces changes in the shape of the CV at high pH values. For that reason we avoided using KNO_3 in this experiment. This observation might be related to some recent synthetic and electrochemical studies combined with XPS and DFT calculations suggesting that nitrite species can bond to Fe positions at the edge of the layers increasing the catalytic activity. They propose these sites as possible high catalytic activity sites (Hunter, Hieringer et al. 2016).

In the case of our experiment, before every CV, a constant potential of 1.63 V versus RHE was applied for 10 minutes to stabilize the film at every pH value. After every CV we used a similar potential step protocol as described before by applying a constant potential of 1.63 V versus RHE for 3 minutes and switching to 1.1 V versus RHE and the resulting current is integrated. The measured CV´s are shown in Figure 6.18A. The plot of redox charge increase calculated from the integration of the cathodic wave of the CV and from the integration of the current in the jumping protocol are shown in Figure 6.19. The maximum current in the CV at 1.63 V versus RHE and the steady state current at that potential after 3 minutes stabilization are also shown there.

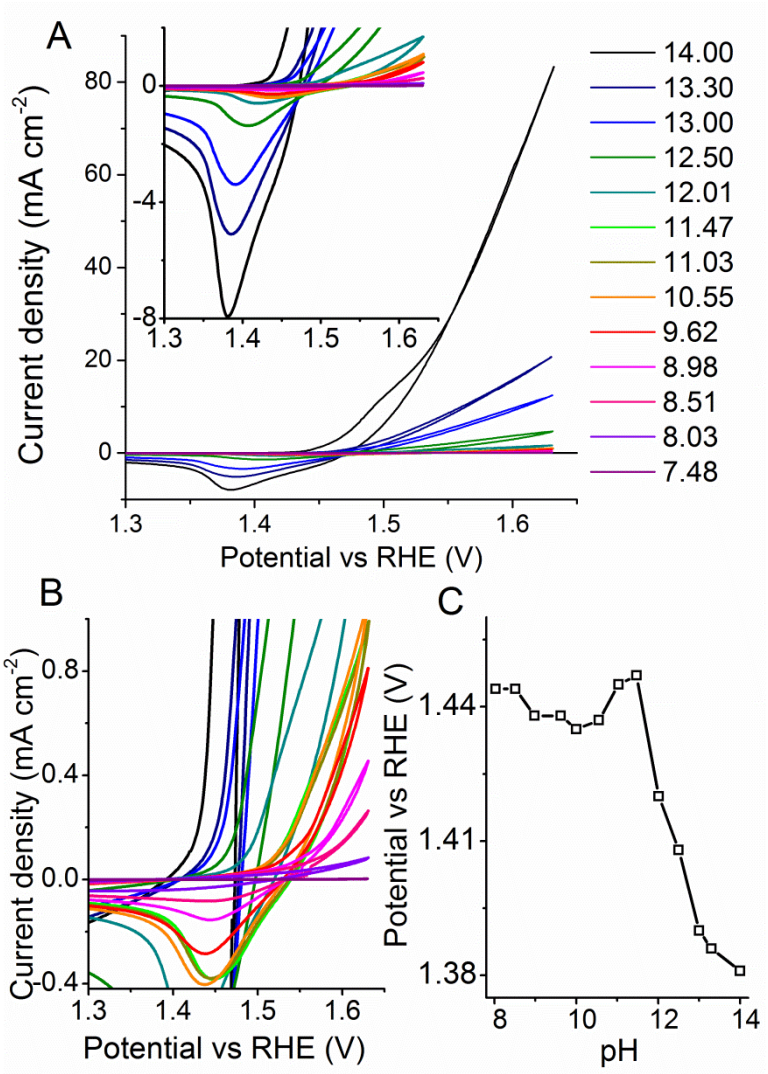

Figure 6.18. (A) CV´s collected at 10 mVs^{-1} scan rate for the NiFe catalyst starting with a 0.1 $molL^{-1}$ and pH 8 borate buffer solution and adding KOH until reaching pH 14. The inset shows the change in the cathodic wave. **(B)** Shows the cathodic wave for the films measured at pH values bellow 10.55. **(C)** Shows the shift in the cathodic peak position with the pH.

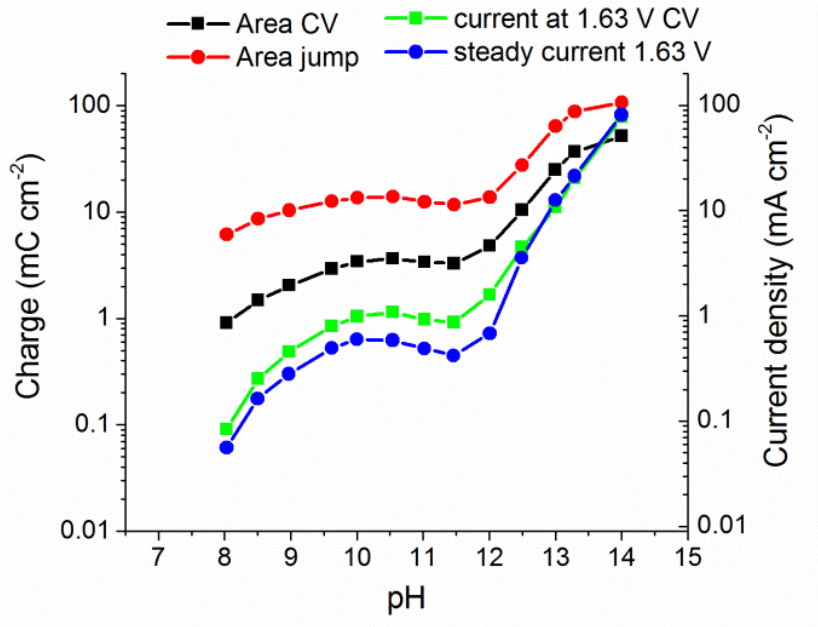

Figure 6.19. Changes in the catalytic current and redox charge with the pH for the NiFe catalyst. The catalytic current was calculated as the maximum of the CV´s in Figure 6.18 at 1.63 V versus RHE (green) and from the steady state current after 3 min operation at 1.63 V versus RHE (blue). The redox charge was calculated from the integration of the negative area of the CV´s in 18 (black) and from integration of the current after switching the potential from 1.63 V versus RHE to 1.23 V versus RHE (red).

What can be clearly observed from this data is that the increment in the catalytic current is also accompanied by a similar increase in the redox electroactive portion of the film. The redox electroactive portion is higher when calculated from the step potential than when obtained from integration of the redox wave. This behavior has been observed before in cobalt oxide catalyst (Risch, Ringleb et al. 2015). The interpretation for this behavior was that in the CV only the negative area is integrated. However, at high potentials, in the back scan of the CV there are both reduction of the metal and water oxidation. For instance some of the charge is already lost as water oxidation.The redox equivalents can be better observed from the jumping procedure were we used a higher time resolution than in the CV, and more charge is integrated before it is lost in the water oxidation process. We observed that from pH 8 to pH 14 the portion of redox electroactive species increased about 18 times, meanwhile the catalytic current increased 1700 times. This increase is fully consistent with the observed in Figures 6.14 A and B. We also observe a plateau in the redox area and current between pH 10.5 and 12. This behaviour seems to be related to the poor buffering capabilities of the borate electrolyte at pH values far from its pK_a where the borate buffering capabilities are optimal.

What can also be observed in Figure 6.18C is that the reductive wave is clearly shifted to lower potentials with the pH, at pH values higher than 11. This decrease might also be affected by the Ohmic drop as the current is increased with the pH. We cannot easily distinguish the shifting in the oxidative wave with the pH due to overlapping with the catalytic current. However, previous spectro-electrochemical experiments involving UV-Visible absorption studies on water-oxidizing transition-metal oxides, have shown that changes in absorption under applied potential can be used as a convenient in situ probe of changes in the metal oxidation state (Zaharieva, Chernev et al. 2012, Risch, Ringleb et al. 2015). From this combination of UV/Visible absorption and electrochemistry it is possible then to resolve the oxidation state changes from the catalytic wave.

To perform the *in-situ* absorption experiments we deposited cathodically the NiFe oxide on a transparent FTO electrode with the same procedure used in platinum. We corroborated that the film has simlar electrochemical properties as when it is deposited over platinum (Figure 6.20) and the same ratio of Ni:Fe. In this case the deposition for 1 s in FTO resulted in 199.1 nmolcm^{-2} in Ni and 131.4 nmolcm^{-2} in Fe according to the TXRF measurements. The deposited material in FTO for 1 s is about ten times less than the deposited for 30 s on platinum.

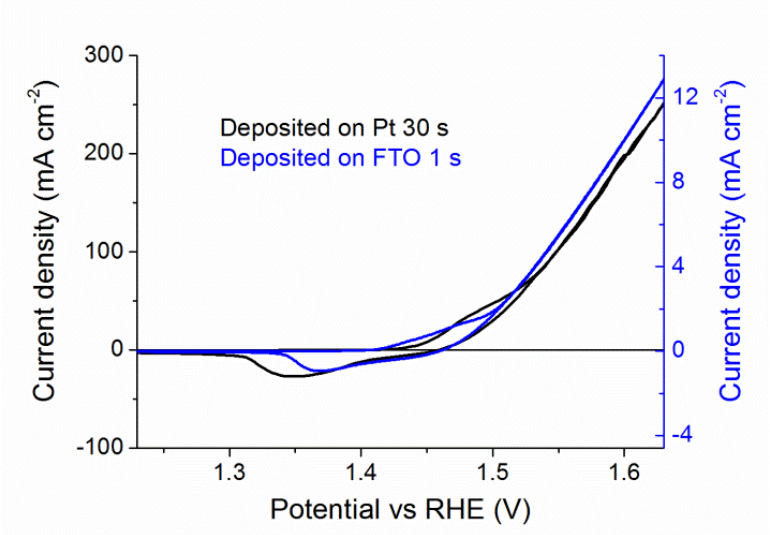

Figure 6.20. Comparison of a CV at 20 mVs^{-1} in 1 mol L^{-1} KOH for the NiFe catalyst deposited in FTO for 1 s and the film deposited in Pt for 30 s.

We used the electrodes deposited on FTO to record spectra at different potentials. The desired potential was applied for a stabilization time of 1 minute until the current reached a stable value. Then the spectrum was recorded while the potential was still applied. A blank FTO substrate spectrum was subtracted from all spectra as background (different samples were used to collect the

data at pH 7 and pH 14). In Figure 6.21 can be seen how there is less absorption change at pH 7 compared to 1 M KOH. As the potential is increased the absorption is also increased.

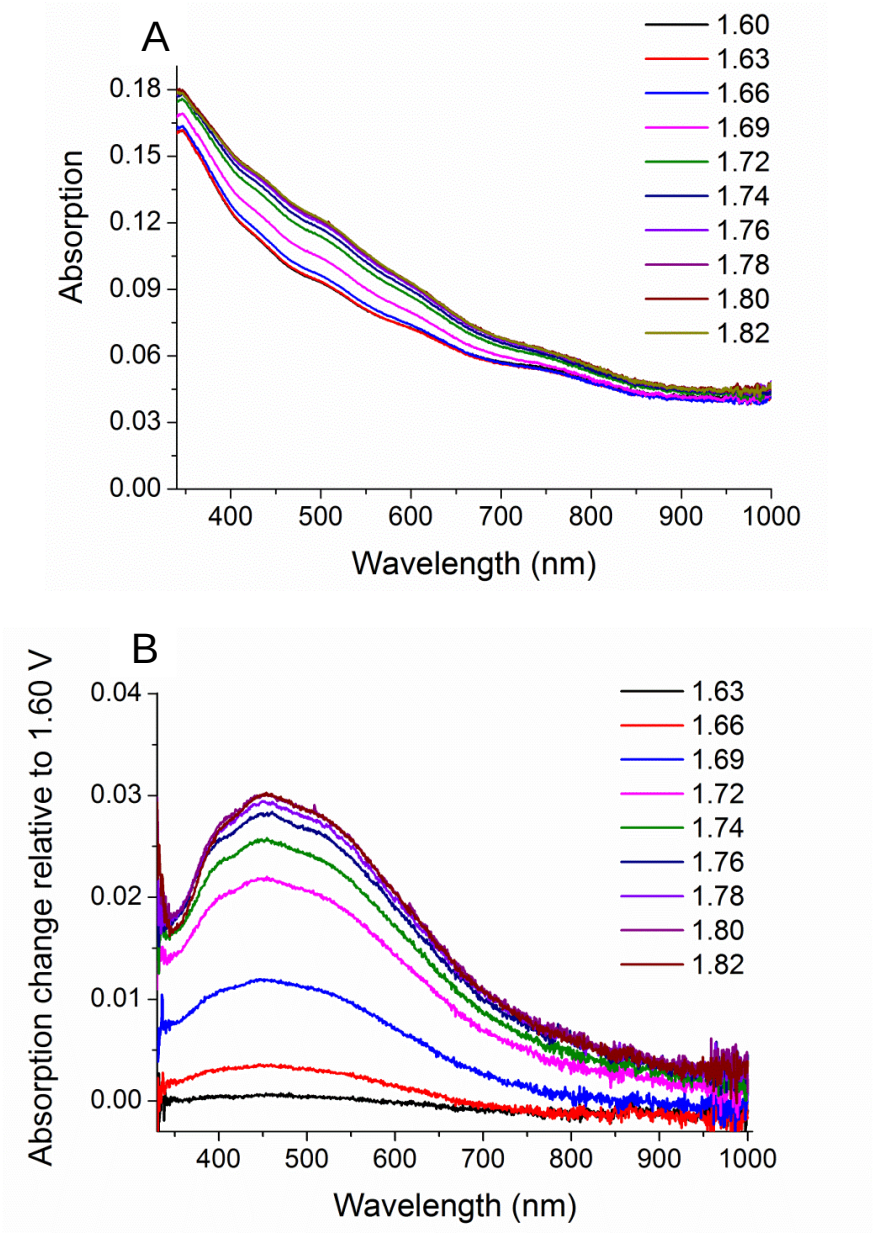

Figure 6.21. Absorption measurements for the cathodically deposited NiFe catalyst on FTO in **0.1 M phosphate pH 7 +1 M KNO_3**. Panel **(A)** shows the spectra using an clean FTO substrate as a blank. Panel **(B)** shows the spectra using the measurement at 1.60 V versus RHE as blank. The spectra were recorded under applied potential after 1 minute stabilization at the corresponding potential value shown. The potentials values are given in the RHE scale with no IR compensation applied. Measurements recorded from low to high potential.

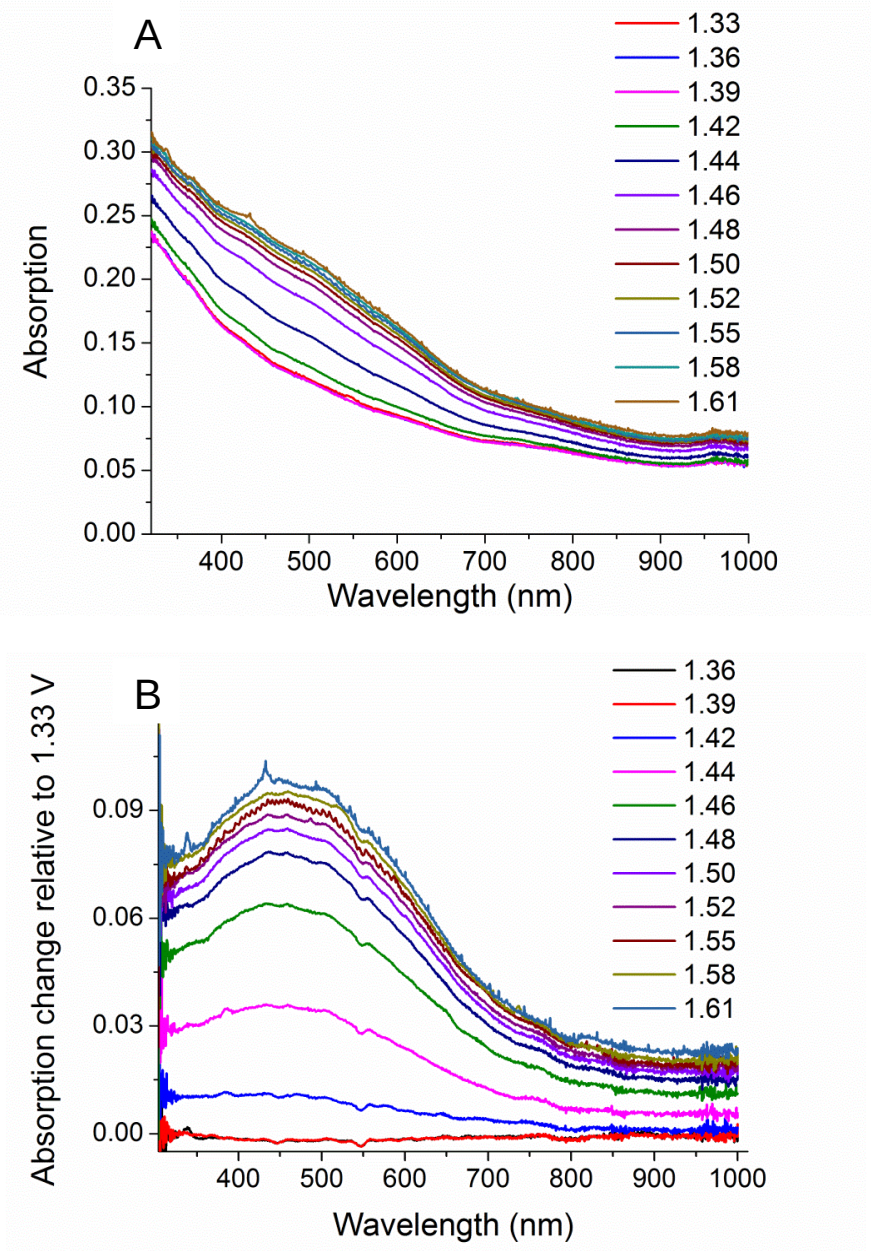

Figure 6.22. Absorption measurements for the cathodically deposited NiFe catalyst on FTO in **1 M KOH**. Panel **(A)** shows the spectra using a clean FTO substrate as a blank. Panel **(B)** shows the spectra using the measurement at 1.33 V versus RHE as blank. The spectra were recorded under applied potential after 1 minute stabilization at the corresponding potential value shown. The potentials values are given in the RHE scale with no IR compensation applied. Measurements recorded from low to high potential.

We estimated that the molar extinction coefficient at 470 nm wavelength changes from 496 to 642 $Lmol^{-1}cm^{-1}$ when the potential is increased from 1.60 to 1.82 V versus RHE at pH 7. In the case of measurements in 1 $molL^{-1}$ KOH solution the molar extinction coefficient changes from 658 to 1144 $Lmol^{-1}cm^{-1}$ when the potential is increased from 1.30 to 1.61 V versus RHE. We observed that a similar potential (1.6 V versus RHE for example) the molar extinction coefficient is several times higher in 1 $molL^{-1}$ KOH. For the calculation of the molar extinction coefficients we used only the Ni content in the film since as we will discuss later we only observed oxidation state changes at the Ni centres. We can observe that the shape of the absorption spectra is similar in both cases. We do not observe clear absorption peaks like it has been observed in Co oxide for example (Risch, Ringleb et al. 2015). The absence of clear absorption bands and the presence of a broad absorption at pH 7 and 14 indicates the presence of a distribution of different overlapping species that experience absorption changes with the potential. In the XAS and XRD experiments we observed that the deposited catalyst consists of a mixture of different phases that might result in this broad absorption spectrum shape.

When the absorption at 470 nm is plotted as a function of the applied potential, a sigmoidal plot is obtained (Figure 6.23). The midpoint of this plot corresponds to the midpoint potential at which the oxidation state changes take place. The catalytic current during the absorption measurements after 100 s time stabilization is also shown. From the Tafel plots in the region were the logarithm of the current varies linearly with the potential we can observe a change in the Tafel slope from about 25 mV/decade in 1 $molL^{-1}$ KOH to 78 mV/decade at pH 7. What is also interesting is that for both pH values the absorption increment follows the current increment very closely in the regions with Tafel behavior. Also the onset of this linear region is shifted in a similar way (about 240 mV) for the absorption and current, which denotes a correlation between the two parameters. This shift (assuming it is linear in this pH range) would correspond to approximately 36 $mVpH^{-1}$, which is similar to what has been observed for pure Ni oxides (Smith and Berlinguette 2016). These similarities in the shifting with the pH and in the increase with the potential that both current and absorption show, suggest that the position of the redox potential and the amplitude of the redox changes are strongly pH dependent and relate closely to the catalytic wave.

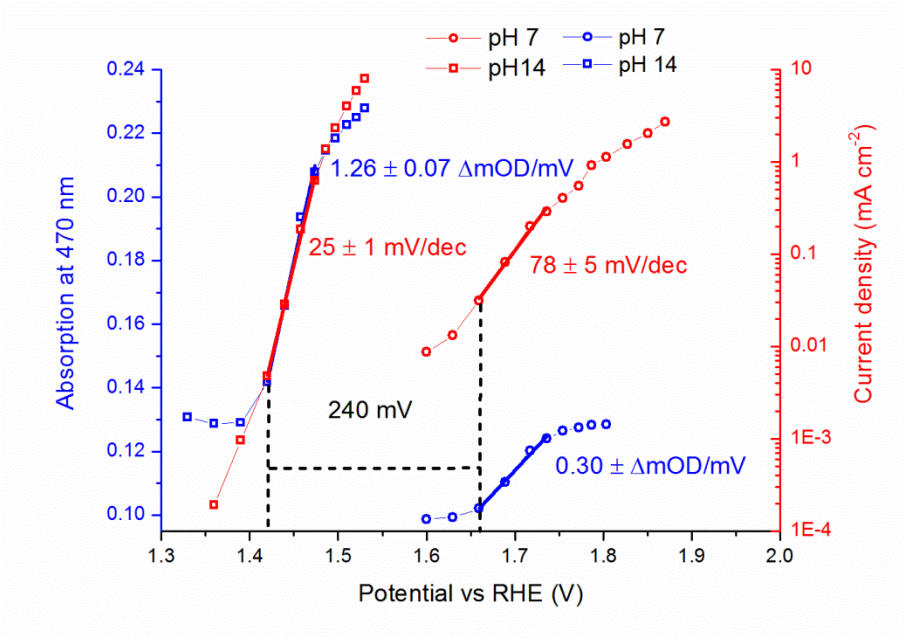

Figure 6.23. Absorption measurements for the NiFe catalyst deposited on FTO in 0.1 M phosphate pH 7 +1 M KNO_3 and 1 M KOH. Comparison of the increase in the absorption at 470 nm and current with the potential. The current value corresponds to the stabilization current after 100 s. The potential values were corrected for Ohmic losses after the measurement. The Ohmic resistance was 10 Ohm for pH 14 and 14.6 Ohm at pH 7.

The change in the average oxidation state in a redox system is determined by the concentration of oxidized and reduced species, which depend on the potential according to the Nernst equation for diluted systems. However, in a solid redox active material it is expected that ions interact strongly. For that reason a modified Nernst equation is required that includes a term E´ which depends on the concentration of oxidized and reduced species and accounts for the interaction energy between ions. This treatment has been used before for intercalation electrodes (Armand 1980, Julien 2003).

$$eV = E_m + k_B T \cdot \ln\left(\frac{[ox]}{[red]}\right) + E'\left(\frac{[ox]}{[red]}\right) \qquad (6.1)$$

The equation 6.1 shows the modified Nernst equation where e is the elementary charge, V the electrode potential, E_m the midpotential for equal concentrations of [ox] and [red], T the temperature, K_B the Boltzmann constant and E´ the interaction term between the redox species.

$$E'\left(\frac{[ox]}{[red]}\right) = E_w \ln\left(\frac{[ox]}{[red]}\right) \qquad (6.2)$$

For solving the equations a logarithmic dependence has been assumed according to equation 6.2, where E_w represents the interaction energy between cobalt sites (Risch, Ringleb et al. 2015). The ratio [ox]/ [red] can be expressed in terms of increase in the absorption in a similar way as in the reference leading to the equation

$$A = \frac{A_{\max} \cdot e^{\frac{eV - E_m}{k_B T + E_w}} + A_{\min}}{e^{\frac{eV - E_m}{k_B T + E_w}} + 1} \qquad (6.3)$$

Where A_{max} and A_{min} represent the maximum and minimum absorption respectively. A positive interaction energy represents repulsive interactions. This means that that each oxidation event increases the oxidation potential for remaining non-reacted species. On the other hand, negative interaction energies represent attractive interactions.

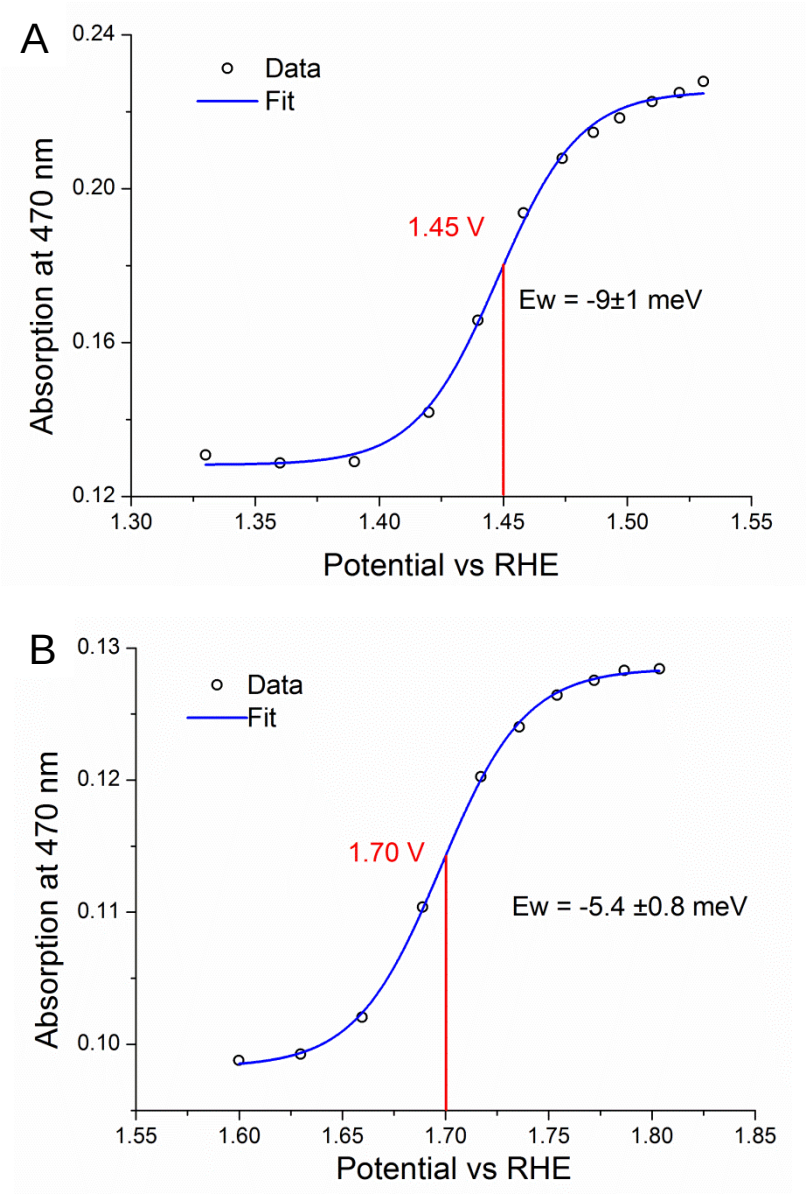

Figure 6.24. Oxidative charging of NiFe catalyst at **pH 7 (A)** and **pH 14 (B)** followed by absorption spectroscopy and simulated according to equation 6.3. The data corresponds to the same shown in Figure 6.23. The midpoint potential is signaled in red.

In the case of previous work in cobalt oxides, positive interaction energies were obtained indicating repulsive interactions between adjacent ions, causing increase in the oxidation potential of the still reduced species (Risch, Ringleb et al. 2015). In our measurements in NiFe oxides, we observed negative interaction energies, meaning that oxidation of some of the Ni species results in decrease in the oxidation potential for the still reduced species. This kind of negative interaction energies have been observed in intercalation electrodes where Li or H are intercalated related to a phase transition or formation of hydride phases (Barnard, Randell et al. 1980, Tsirlina, Levi et al. 2001). In the case of Ni (oxy)hydroxides it is well known the change of phases under potential conditions,

specially from the α-$Ni(OH)_2$ phase to the γ-NiOOH phase as discussed in the EXAFS simulations. It might be possible that in the case of Ni the phase transition facilitates the oxidation process. Also as observed by Risch, the interaction energy is also affected by the pH. In our case the interaction energy at pH 14 is larger indicating that the Ni ions require a smaller increase in potential at pH 14 to get oxidized in comparison to pH 7. Or in other words, the change of phase is favored at pH 14 which might be related to the increase in the catalytic activity observed.

Table 6.8. Simulation paramethers obtained from the modeling with equation 6.3. The thermal energy K_BT was 26 meV (T=300 K). R^2 denotes the Pearson correlation coefficient between the simulated curve and the experimental values provided by Origin 8.0.

Paramether	pH7	pH14
A_{max}	0.1284(2)	0.225(1)
A_{min}	0.0983(3)	0.128(1)
E_m (V)	1.6975(8)	1.448(1)
E_w (eV)	-0.0054(8)	-0.009(1)
R^2	0.999	0.997

The changes in oxidation state can be tracked in time together with the CV measurements by staying at a fixed wavelength (470 nm) and measuring the change in the absorption. The derivative of the absorption in time is directly related to the current due to oxidation state changes. In this kind of plot we can observe that the absorption changes at 470 nm are clearly related to the redox waves in the CV. The position of the redox waves and specially the oxidation wave can be better resolved from the catalytic wave. The cathodic and anodic waves are similarly shifted with the pH (around 240 mV) which results in a similar shift in the midpoint potential as observed in the measurements in Figure 6.23. The absorption measurements in Figures 6.23 and 6.25 together suggest that the observed absorption changes are related to the oxidation state changes in the oxidation wave of the CV and at the same time also closely related to the catalytic current. The pH of the solution affects how easy the phase transition associated to the redox process takes place in agreements with the high pH dependence of the catalytic activity.

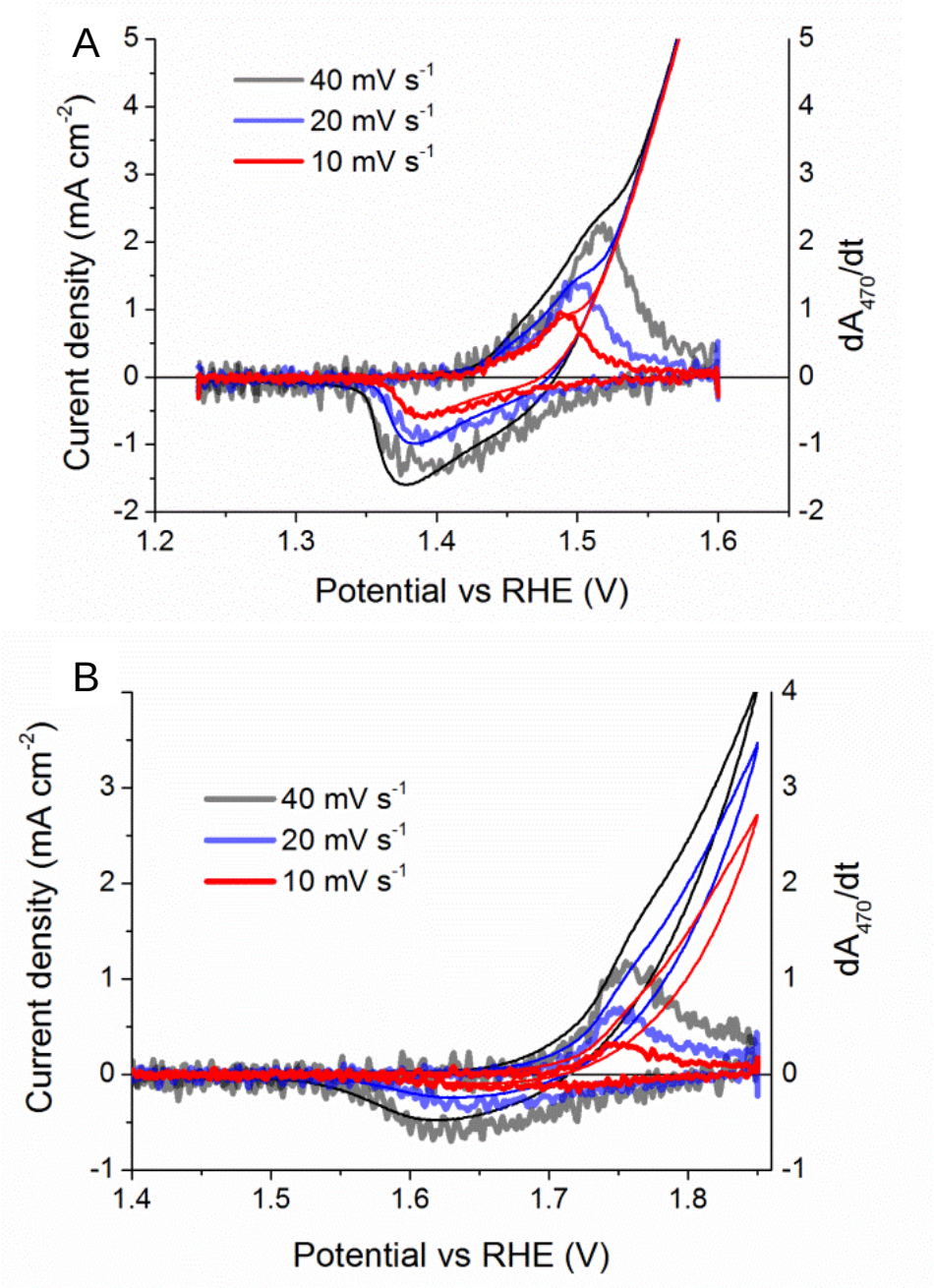

Figure 6.25. CV measurements at 40, 20 and 10 mVs^{-1} for the NiFe catalyst deposited on FTO in **1 M KOH (A)** and **0.1 M phosphate pH 7 +1 M KNO_3 (B)**. In the righ axis the derivative of the absorption at 470 nm with respect to the time is represented. The absorption derivative data correspond to the thicker red, blue and grey lines. Measurements performed using the blue light (470 nm) beam coming from a pulse driven 60 kHz light-emitting diode as described in the experimental section.

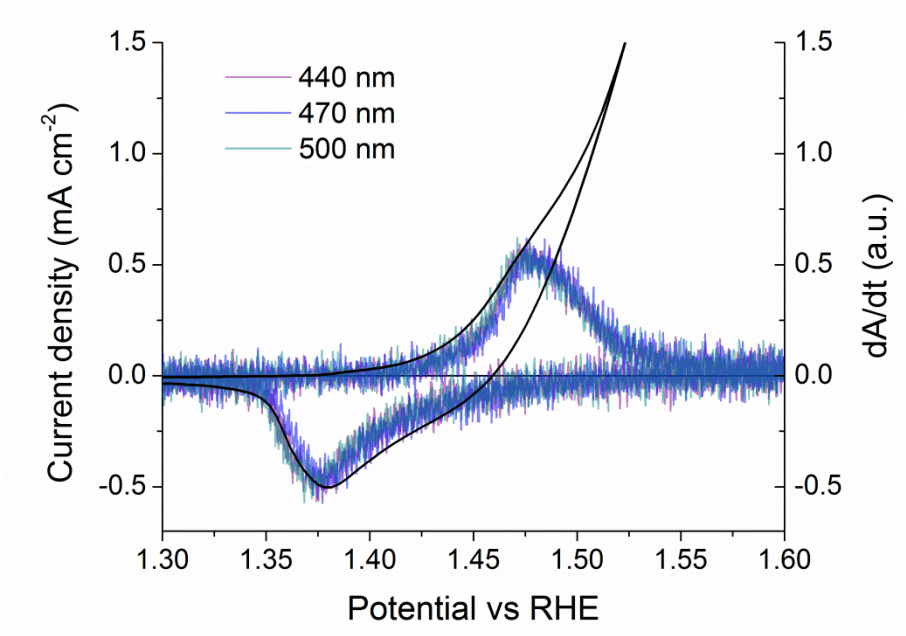

Figure 6.26. CV measurements at 10 mVs^{-1} for the NiFe catalyst deposited on FTO in **1 M KOH**, measurements at different wavelengths using an Agilent Cary 60 Uv-Vis spectrophotometer.

We also performed absorption measurements at different wavelengths. The derivative of the absorption for the 3 different wavelengths tested (440, 470 and 500 nm) lay over each other as observed in Figure 6.26, suggesting no effect of the wavelength in the shape of the derivative plot.

6.2.5 XAS study of the stability of the cathodically deposited NiFe catalyst in 1 M KOH

The absorption measurements alone cannot resolve if the oxidation state changes are associated to the nickel or the iron. To be able to describe this, we performed X-ray absorption spectroscopy *in-situ* measurements together with electrochemistry. To do the experiments we deposited the catalyst on carbon paper and placed it on a window of a Teflon self made electrochemical cell. The window was covered with Kapton tape and the detector is placed in front of the window. Details about the experimental set up are provided in the experimental section.

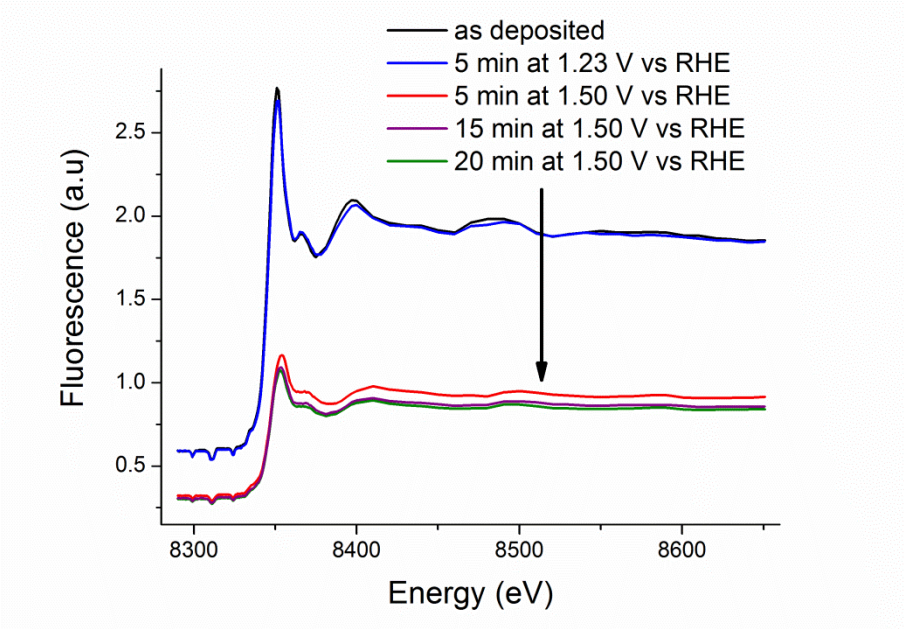

Figure 6.27. *In-situ* XAS measurements in the Ni K-absorption edge in 1 M KOH for the NiFe catalyst samples deposited on carbon paper for 5 s. All the XAS measurements except in the as deposited sample were collected with 1.23 V versus RHE applied. The color code corresponds to: black, sample as deposited; blue: sample measured with 1.23 V vs RHE potential applied; red: sample measured with 1.23 V vs RHE applied after conditioning at 1.50 V vs RHE for 5 minutes; purple: sample measured with 1.23 V vs RHE applied after conditioning at 1.50 V vs RHE for 15 minutes and green: sample measured with 1.23 V vs RHE applied after conditioning at 1.50 V vs RHE for 20 minutes. The decrease in the fluorescence reaches steady state after 20 min operation.

Before performing the *in-situ* measurements we performed a series of experiments to study the long term stability of the films and look for possible radiation damage in the samples. Understanding the long term behavior of the films is of major importance for the *in-situ* measurements to make sure that the measurements are meaningful and that the averaging of the data collected at different times is actually possible. We observed that the fluorescence at the Ni K-edge decreases to about half of the initial value when 1.50 V versus RHE are applied. However, this decrease reaches steady state after 20 minutes approximately. After this conditioning time it is possible to obtain reproducible edge measurements.

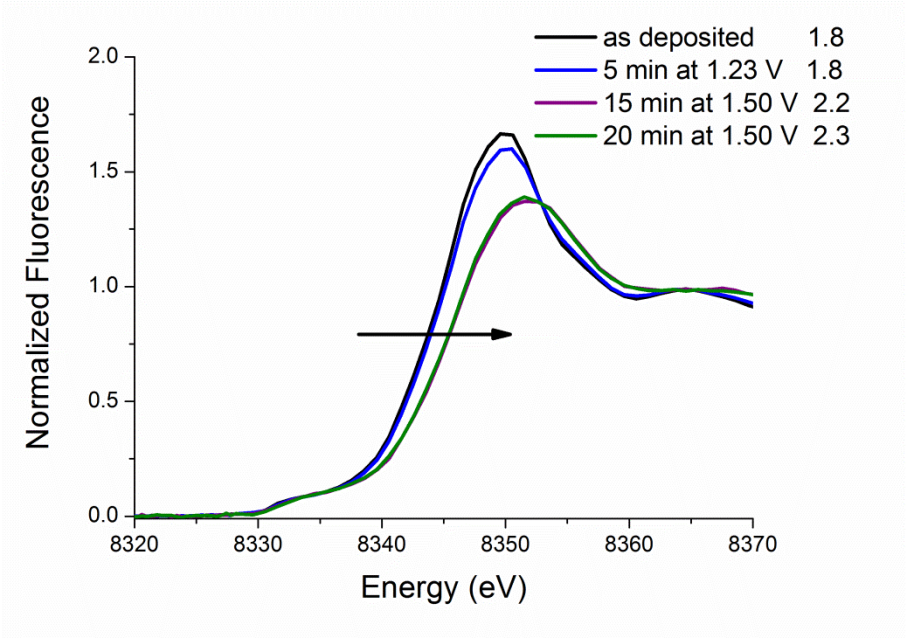

Figure 6.28. *In-situ* XANES measurements in the Ni K-absorption edge in 1 M KOH for the NiFe catalst samples desposited on carbon paper for 5 s. All the XAS measurements except in the as deposited sample were collected with 1.23 V versus RHE applied. The color code corresponds to: black, sample as deposited; blue: sample measured with 1.23 V vs RHE potential applied; red: sample measured with 1.23 V vs RHE applied after conditioning at 1.50 V vs RHE for 5 minutes; purple: sample measured with 1.23 V vs RHE applied after conditioning at 1.50 V vs RHE for 15 minutes and green: sample measured with 1.23 V vs RHE applied after conditioning at 1.50 V vs RHE for 20 minutes. The number shown in the inset corresponds to the estimated oxidation state of the sample.

Figure 6.28 shows the normalized XANES spectra from Figure 6.27. It can be observed that the sample as deposited and after applying 1.23 V has a very similar oxidation state. However, when 1.50 V versus RHE are applied for some time and the edge is measured again at 1.23 V versus RHE, the edge position remains at a higher oxidation state than the initial one in the samples as deposited. This seems to indicate that after operation at catalytic potential some of the Ni metal centres are trapped in a higher oxidation state. As it can be observed in Figure 6.29 the initial low oxidation state (around 1.8) can be slowly restored after long time exposure (more than 1 hour) to 1.23 V versus RHE.

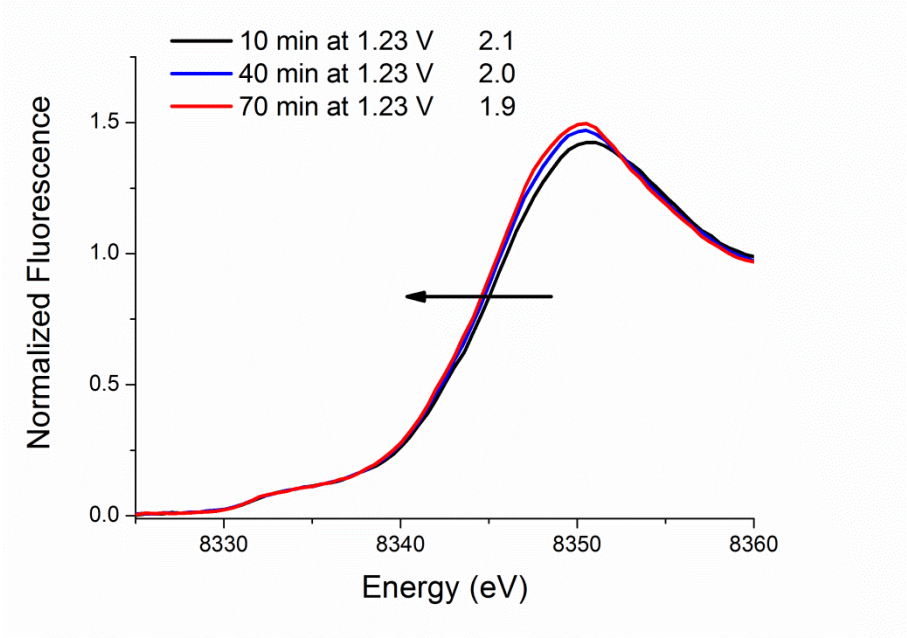

Figure 6.29. *In-situ* XANES measurements in the k-Ni edge in 1 M KOH for the NiFe catalst samples desposited on carbon paper for 5 s. The edge measurements were performed at 1.23 V versus RHE at different times of operation after having applied 1.55 V versus RHE for around 2 hours. The number shown in the inset corresponds to the estimated oxidation state of the sample.

Figure 6.30 shows the behavior of the fluorescence when the incident X-ray beam is set at an energy after the raising of the Ni K-edge (8520 eV). At this position the fluorescence is not importantly affected by changes in the oxidation state but only by the quantity of Ni in the film. We observed no fluorescence changes when no potential is applied. When 1.50 V versus RHE are applied, the fluorescence drops significantly. If the incoming beam is switched off and turned on again, after some minutes we observe that the fluorescence continued decreasing even with no X-rays applied on the film. This seems to indicate no apparent loss of material due to radiation damage but we observe loss of material during electrochemical operation possibly due to problems with the mechanical stability. However, according to this data and the edge measurements the loss of material reaches a steady state after 30 minutes operation.

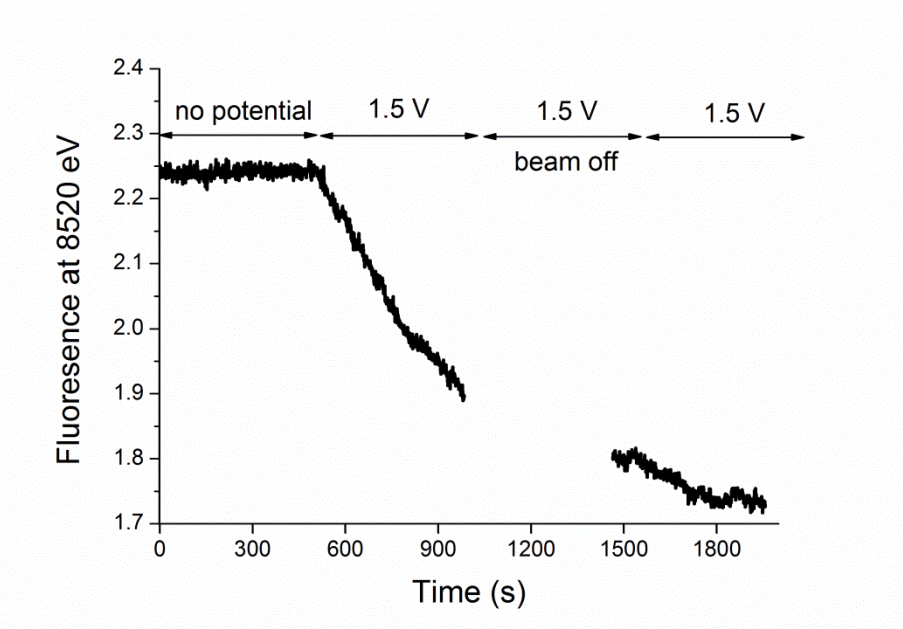

Figure 6.30. Study of the stability of the NiFe catalyst samples deposited on carbon paper for 5 s towards radiation damage in 1 M KOH. The film was first kept with no potential applied with the X-ray beam at an energy after the Ni K-edge (8520 eV). After that 1.50 V versus RHE was applied. After some time the X-ray beam was switched off and then switched on again.

The loss of material at the Fe-edge (Figure 6.31) seems to have a very similar behavior as the one observed at the Ni edge. It is possible to obtain reproducible edge measurements after 30 minutes operation at 1.55 V in 1 M KOH.

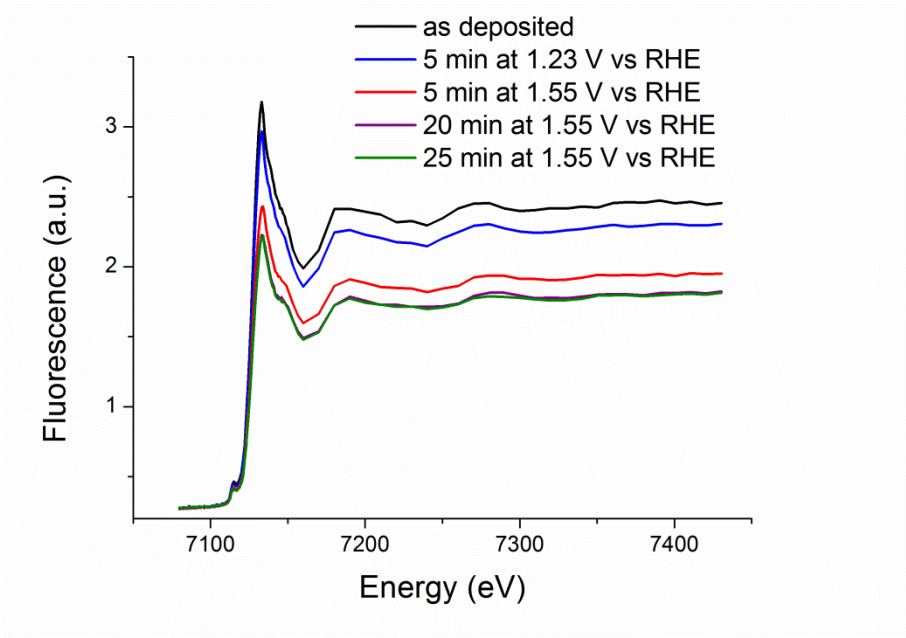

Figure 6.31. *In-situ* normalized XANES measurements in the Fe K-edge in 1 M KOH for the NiFe catalyst samples deposited on carbon paper for 5 s. The color code corresponds to: black, sample as deposited; blue: sample measured with 1.23 V versus RHE potential applied for 5 minutes; red: sample measured with 1.55 V vs RHE applied for 5 minutes; purple: sample measured with 1.55 V vs RHE applied for 15 minutes and green: sample measured with 1.55 V versus RHE applied for 20 minutes. The decrease in the fluorescence reaches steady state after 20 min operation.

6.2.6 XAS study of oxidation state changes in cathodically deposited NiFe catalyst in 1 M KOH

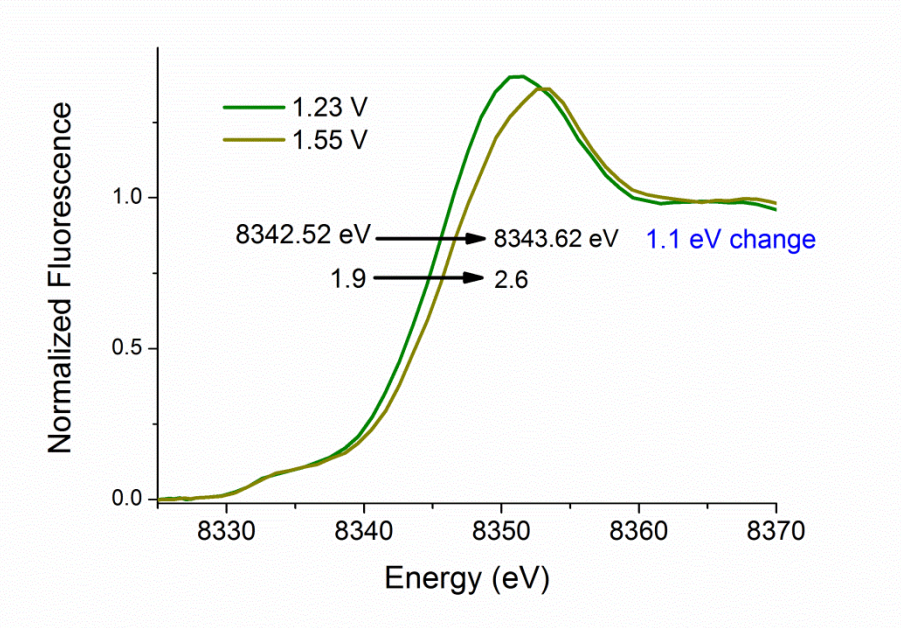

Figure 6.32. *In-situ* X-ray absorption measurements in 1 M KOH for the NiFe catalyst sample deposited on carbon paper for 5 seconds using the same deposition solution as in the rest of the experiments. The figure shows the normalized Ni K-edge at 1.23 V versus RHE and after applying 1.55 V versus RHE.

We measured the XANES spectra for the NiFe oxide at 1.23 and 1.55 V versus RHE. We observed a shift in the edge position of 1.1 eV between these two potentials. From measurements of Ni oxide references with known coordination environment and oxidation state (NiO, $Ni(H_2O)_6$, $LiNiO_2$, $K_2Ni(H_2IO_6)_2$) we know that a change of one oxidation state is associated to a 1.6 eV shift in the edge position. We observed a change in oxidation state from 1.9 (at 1.23 V versus RHE) to 2.6 (at 1.55 V versus RHE). The oxidation state lower than 2 at 1.23 V versus RHE accounts for 10 % Ni metal contribution. If we assume that the oxidation state changes take place mainly in the oxide phase, then we can subtract the metal contribution, in which case the change in the oxidation state will be from 2.1 to 2.9 in the oxide phase. Since we did not observe any change in the pre-edge features during operation we think that assuming the metal does not experience oxidation state changes is a good assumption. Now, according to the previous electrochemical measurements we observed that only about 30-40 % of the deposited material is electroactive. For instance, the oxidation state changes in the oxide phase will correspond to about 2 for the electroactive nickel. In the case of Bell and coworkers for example, they observed formation of Ni with +3.6 oxidation state (Friebel, Louie et al. 2015). Based on this, formation of Ni species with oxidation state higher

than +3 in our cathodically deposited NiFe catalyst seems rather likely. The fact that less charge (lower oxidation state) than expected is observed in this kind of oxides has also been recently interpreted as the consequence of a fast catalytic process which approaches the speed of the redox process of the Ni centers resulting in faster depletion of redox equivalents and as a result less redox charge is observed (Goerlin, Chernev et al. 2016).

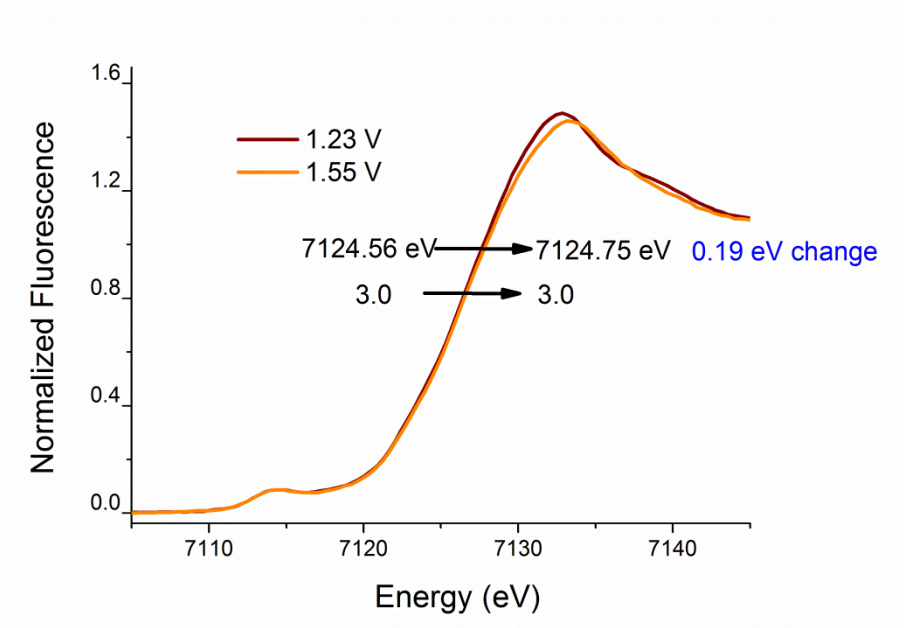

Figure 6.33. *In-situ* X-ray absorption measurements in 1 M KOH for the NiFe catalyst sample deposited on carbon paper for 5 seconds using same deposition solution as in the rest of the experiments. The figure shows the normalized Fe K-edge at 1.23 V versus RHE and after applying 1.55 V versus RHE.

In the case of the measurements at the Fe K-edge, we observed a change of about 0.19 eV when the potential is changed from 1.23 V to 1.55 V versus RHE. By comparison of reference iron compounds of know oxidation state (α-FeO(OH), α-Fe_2O_3, γ-Fe_2O_3, Fe3O4, FeO) we know that an oxidation state change is associated to a shift of 5.1 eV in the edge position. According to calibration with the Fe reference compounds we estimate that the change in the oxidation state of the oxide will correspond to only about 4 % of Fe atoms changing oxidation state by 1. The slight change in the edge position seems to be related to a change in the shape of the top of the edge more than a change in the oxidation state.

To study the structural changes under applied potential we performed EXAFS measurements at the Ni and Fe K-edge with 1.23 V and 1.55 V versus RHE potential applied. The data with the corresponding simulations are shown in Figure 6.34 and 6.35. The results from the simulations are shown in Table 6.9. The simulations were performed as a joint fit in which the distances at both

potentials are fitted to the same value and the Debye-Waller parameter is kept constant. With this methodology the amplitude of the coordination numbers are representative of the proportion of the different distances in the film, and for instance representative of the proportion of the different phases present in the catalyst.

From the simulations at the Ni K-edge it is clear that two types of distances are present at 1.23 V versus RHE: Ni-O and Ni-metal short distances at 1.90 and 2.87 Å respectively, corresponding to a γ-NiOOH phase; and long Ni-O and Ni-metal distances at 2.06 and 3.07 Å corresponding to α-$Ni(OH)_2$ phase. The proportion of both phases is similar. However, when 1.55 V are applied the proportion of the γ-NiOOH phase is clearly increased. The slow oxidation state changes towards a more reduced state observed in previous experiments in Figure 6.29 might be related to a slow transition from γ-NiOOH to α-$Ni(OH)_2$ when a reductive potential is applied.

In the case of the simulations at the Fe edge we observed an increase in the amplitude of short Fe-O distances at 1.92 Å. We also observed an increase in the coordination number of distances Fe-metal at 2.96 Å and Fe-metal at 2.85 Å. Formation of shorter distances is usually associated to increase in the oxidation state and deprotonation. In the case of the iron, we do not observe important oxidation state changes in the edge that account for the strong structural changes observed. The changes at the top of the edge seem to be rather associated to the formation of these short Fe-O and Fe-metal distances. Bell has suggested that in a mixed Ni-Fe oxide phase, the structural changes in the nickel associated to increase in the oxidation state and shortening of the metal-metal distances would also in this case affect the structure around the iron centers. Our results support this hypothesis of a strong correlation between the nickel and iron, which is possibly related to the formation of short Fe-Ni distances at 2.85 Å under catalytic potential. At non-catalytic potentials the amplitude of this distance is practically zero, and it is widely increased at 1.55 V versus RHE. We also corroborated that these structural changes are fully reversible and are the responsible of the changes at the top of the Fe edge in the XANES measurements.

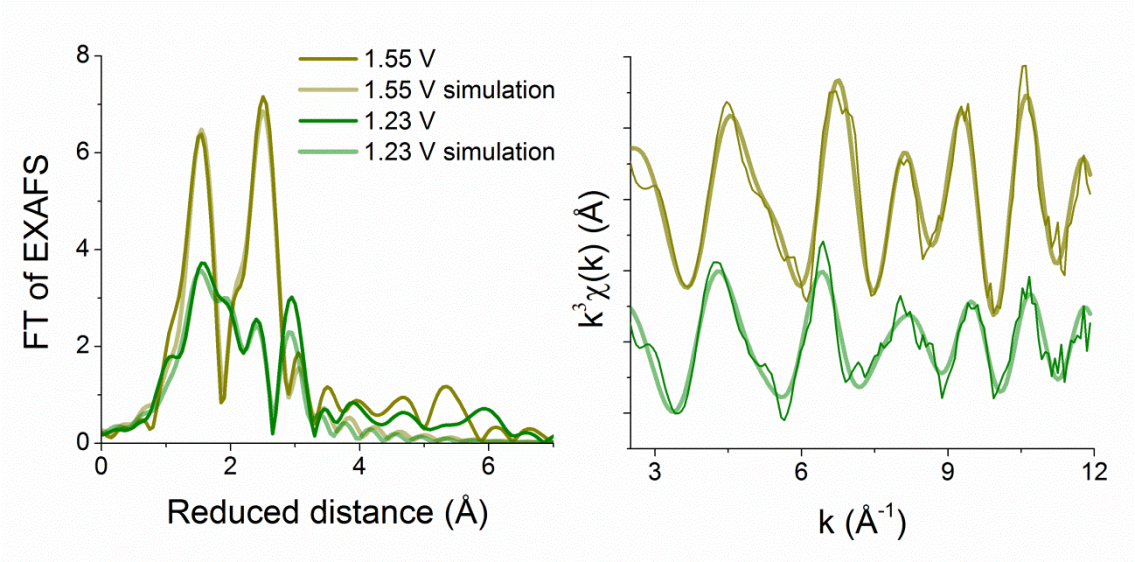

Figure 6.34. EXAFS spectra at the Ni K-edge for the NiFe catalyst sample deposited on carbon paper for 5 seconds in 1 M KOH at 1.23 V versus RHE and at 1.55 V versus RHE with the corresponding simulations. Left: Fourier-transformed EXAFS spectra (a cosine window covering 10% of the left and right side of the EXAFS spectra was used to suppress the side loops in the Fourier transforms). Right: k^3-weighted EXAFS spectra. The data was simulated after substracting a 10 % of metal contribution. The simulation parameters are provided in Table 6.9.

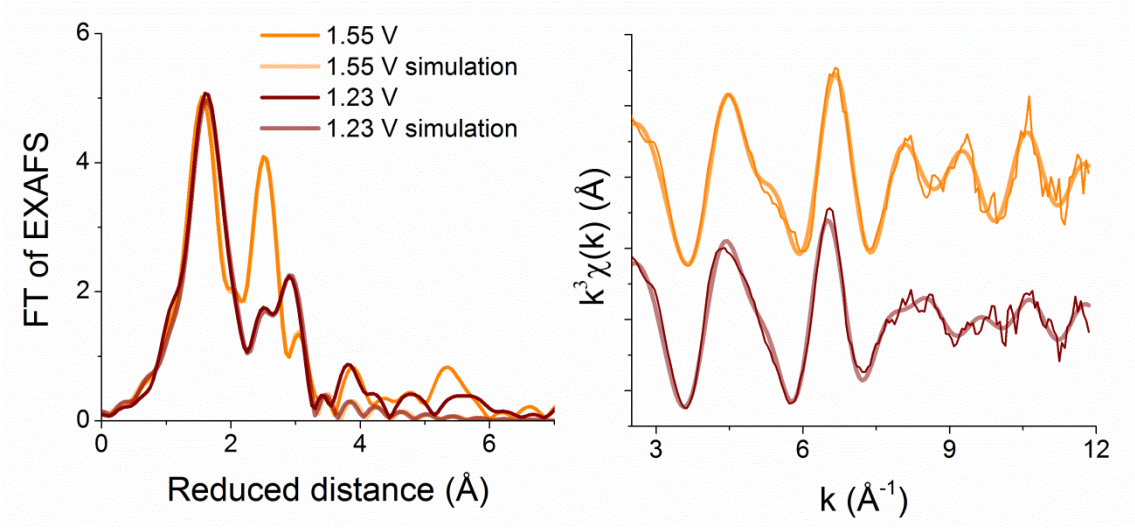

Figure 6.35. EXAFS spectra at the Fe K-edge for the NiFe catalyst sample deposited on carbon paper for 5 seconds in 1 M KOH at 1.23 V versus RHE and at 1.55 V versus RHE with the corresponding simulations. Left: Fourier-transformed EXAFS spectra (a cosine window covering 10% of the left and right side of the EXAFS spectra was used to suppress the side loops in the Fourier transforms). Right: k^3-weighted EXAFS spectra. The simulation parameters are provided in Table 6.9.

Table 6.9. Coordination numbers, N, as determined from EXAFS simulation. The EXAFS Debye-Waller parameter, σ, was set to 0.063 Å to avoid over-parameterization. The number in parenthesis corresponds to the uncertainty in the last digit. The simulations were done as a joint fit for the same type of sample, were the distances for a same type of bond were fitted as the same for the two types of conditioning.

Type of bond	Distance (Å)	1.23 V	1.55 V
Ni-O_{short}	1.90(1)	1.9(3)	3.2(2)
Ni-O_{long}	2.06(1)	2.6(3)	0.9(4)
Ni-Ni_{metal}	2.49(1)	0.4(2)	0.5(1)
Ni-Ni_{short}	2.86(1)	1.2(4)	3.1(4)
Ni-Ni_{long}	3.07(1)	1.7(4)	1.4(4)
	Distance (Å)	1.23 V	1.55 V
Fe-O_{short}	1.92(1)	2.5(3)	3.2(2)
Fe-O_{long}	2.05(1)	3.5(2)	2.4(3)
Fe-Fe_{metal}	2.52(1)	0.53(9)	0.58(9)
Fe-Ni_{short}	2.85(3)	0.2(7)	2(1)
Fe-Fe_{middle}	2.96(3)	2.0(3)	3.0(6)
Fe-Fe_{long}	3.12(2)	2.4(2)	2.1(4)

To study the dynamics of the oxidation state changes we performed cyclic voltammetry experiments together with fluorescence measurements *in-situ*. In the experiments we set the energy of the X-ray beam at a position in the middle of the edge for Ni (8337 eV) or Fe (7119 eV) and recorded the change in the fluorescence when a CV is performed on the film. The changes in the flurorescence are related to changes in the oxidation state. Figure 6.36A shows the Ni edge for the NiFe catalyst. The red dotted line represents the energy at which the X-ray was set. An oxidation of the Ni during the CV results in a shifting of the edge position to higher energy as illustrated by the blue arrow in the inset. This energy shift in the edge results in a decrease in the fluorescence intensity as illustrated by the red arrow in the inset. An increase in the oxidation state is then reflected as a decrease in the fluorescence and vice versa. The changes in fluorescence as the CV is performed are shown in Figure 6.36B. We can observe how as the oxidation wave appears in the CV, the fluorescence decreases, and it is again increased to the same level as the film is reduced in the backwards scan (signalled by the arrows). The observed change in fluorescence corresponds to about 0.4 eV in the middle of the edge in the non-normalized data.

The actual edge shift (estimated with the integral method) and change in oxidation state after normalization are shown in the green inset in Figure 6.36A. In this case we observed a change in oxidation state from 2.2 to 2.7 approximately. The oxidation state change obtained is smaller compared to the one in Figure 6.32. In the stability test measurements we already observed that during operation nickel ions are trap in high oxidation state and the low oxidations state can only be recovered after long term operation at reductive potentials.

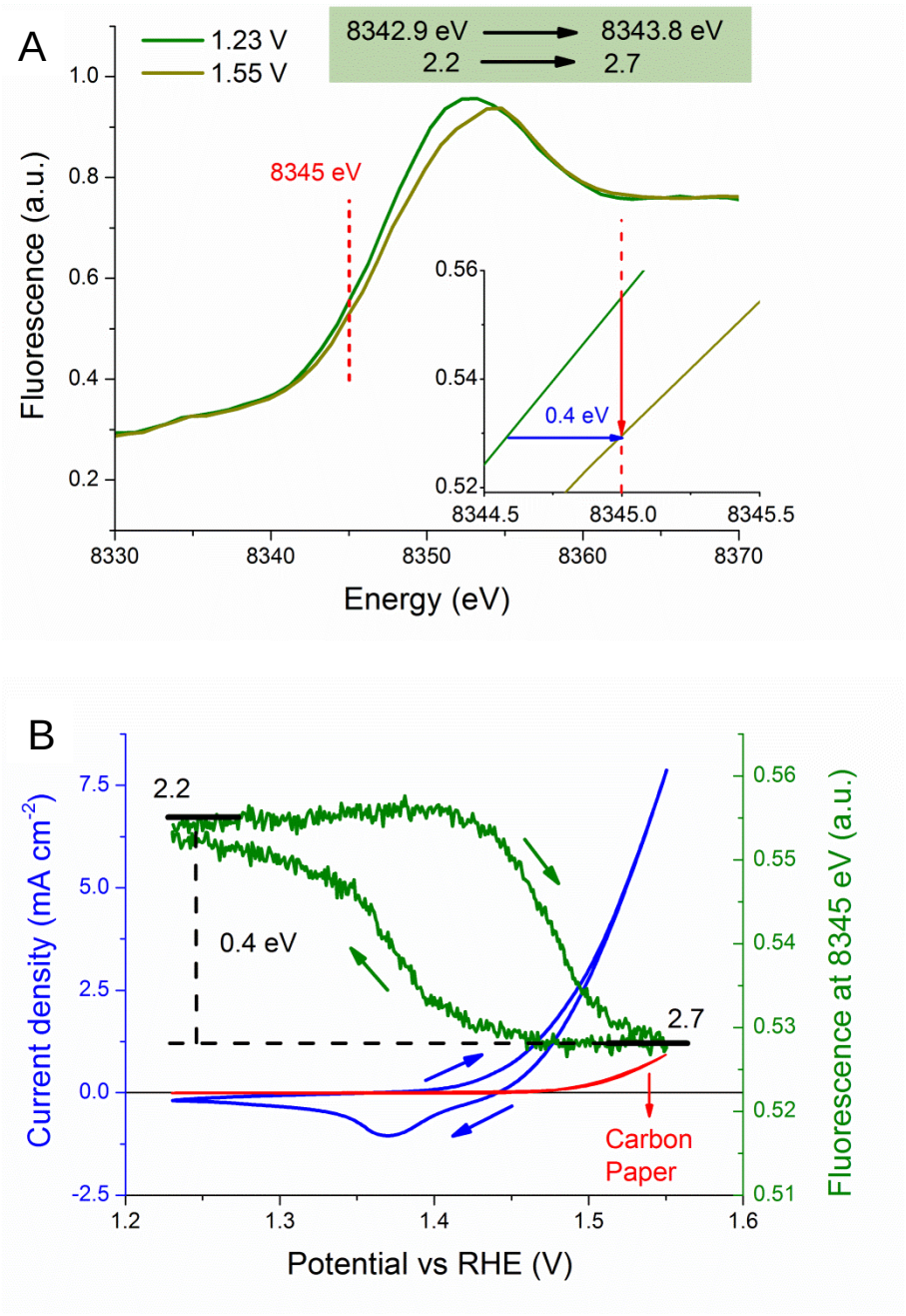

Figure 6.36. *In-situ* X-ray absorption measurements in 1 M KOH for the NiFe catalyst sample deposited on carbon paper for 5 seconds using the same deposition solution as in the rest of the experiments. (A) Shows the not normalized Ni K-edge at 1.23 V versus RHE and after applying 1.55 V versus RHE. In the inset the red arrow shows how the decrease in the fluorescence is related to a shifting in the energy of the edge (blue arrow). The red dotted line represents the energy at which the X-ray beam was set (8345 eV). (B) Corresponds to the 5 mVs^{-1} CV measurements at the Ni edge together with fluorescence measurements. The blue and green arrows show the direction of the scan. The decrease in the fluorescence is related to a shift of 0.4 eV in the edge position at this X-ray energy. The florescence data shown corresponds to the average of 7 measurements. The resistance was 3 Ω, no IR drop correction was applied.

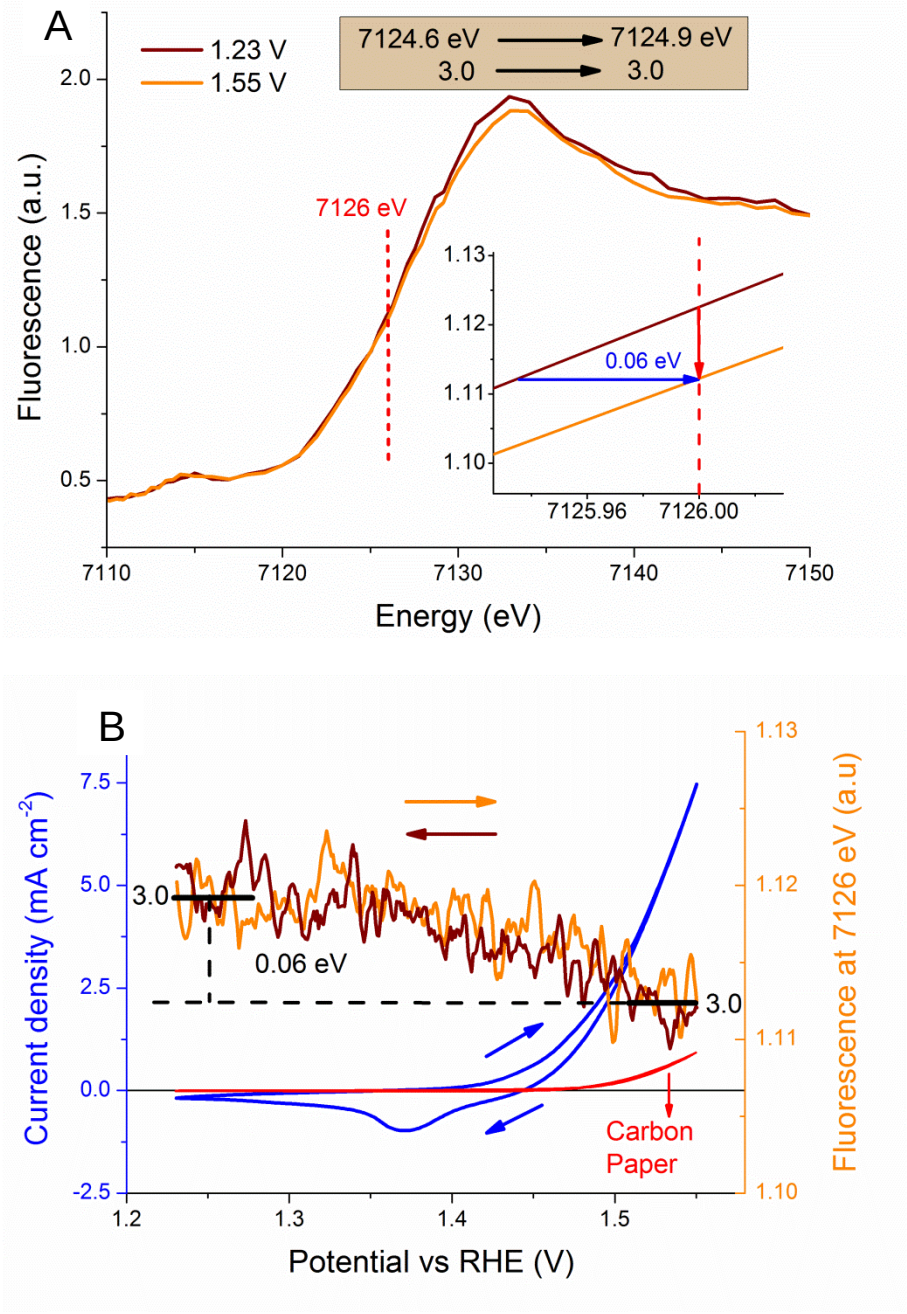

Figure 6.37. *In-situ* X-ray absorption measurements in 1 M KOH for the NiFe catalyst sample deposited on carbon paper for 5 seconds using same deposition solution as in the rest of the experiments. (A) Shows the not normalized Fe K-edge at 1.23 V versus RHE and after applying 1.55 V versus RHE. In the inset the red arrow shows how the decrease in the fluorescence is related to a shifting in the energy of the edge (blue arrow). The red dotted line in the edge Figures represents the energy at which the X-ray beam was set (7126 eV) . (B) Corresponds to the 5 mVs^{-1} CV measurements at the Fe edge together with fluorescence measurements. The arrows show the direction of the scan. The decrease in the fluorescence is related to a shift of 0.06 eV in the edge position. The florescence data shown corresponds to the average of 7 measurements. The resistance was 3 Ω, no IR drop correction was applied.

The measurements at the Fe edge are noisier due to the small edge changes that result in a low signal. We observed a 0.06 eV shift. If the edge measurements are normalized we observe a shift of 0.3 eV which accounts for a 6% of Fe atoms changing the oxidation state by 1. The corresponding edge shift and oxidation state change are shown in Figure 6.37A in the brown inset. In previous Mossbauer Spectroscopy experiments, they observed formation of Fe^{+4} in a portion of 20% for potentials above 1.7 V versus RHE has been observed (Chen, Dang et al. 2015). This would result in an increase in the oxidation state from 3.0 to 3.2. To corroborate that we performed a series of edge measurements with constant potential applied for potential values from 1.55 until values of 2.8 V versus RHE. The maximum oxidation state change observed from 1.23 V to the maximum potential 2.8 V versus RHE in the plot corresponds to about 8 % of Fe^{+4} atoms. However, this still does not result in an apparent change in the oxidation state. Based on this results we can say that in the most extreme of the cases the formation of Fe^{+4} in the oxide does not exceeds the 8 %, and most of this change in the edge position is possibly not due to and oxidation state change but mostly due to a change in the shape at the top of the edge.

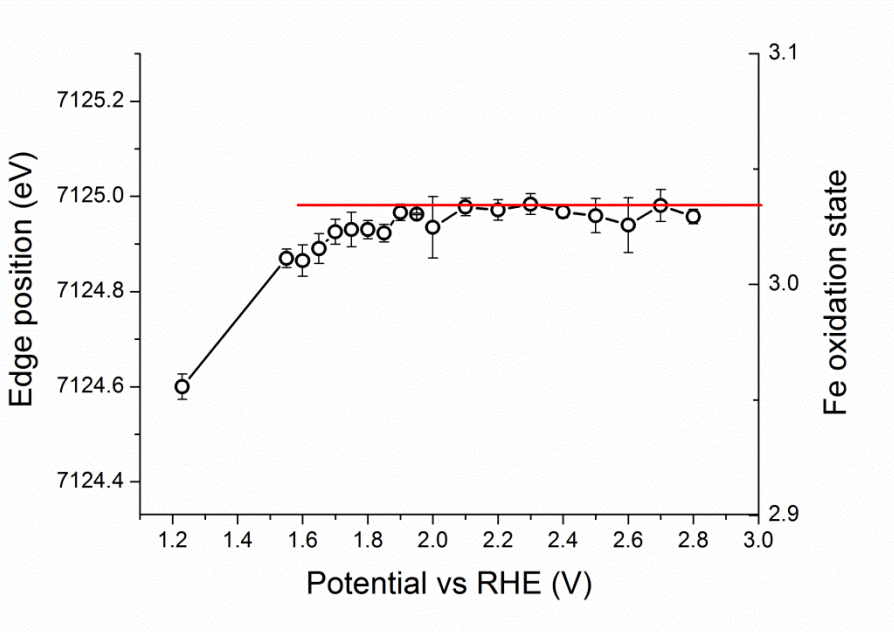

Figure 6.38. Edge position measured in 1 M KOH for the NiFe catalyst sample deposited on carbon paper for 5 seconds using same deposition solution as in the rest of the experiments. Each point corresponds to the average of 3 measurements; the standard deviations are also shown. The oxidation state was also determined according to calibration with reference compounds (α-FeO(OH), α-Fe_2O_3, γ-Fe_2O_3, Fe_3O_4, FeO). The resistance was 3 Ω, no IR drop correction was applied.

To study the kinetics of the redox process we designed a protocol in which the potential is switched between 1.55 V and 1.23 V versus RHE with 10 s pulses. The changes in the X-ray fluorescence were measured when the incident X-ray beam was kept at an energy in the middle of the edge (8345 eV for Ni and 7126 eV for Fe). The current and fluorescence decay after the pulse was measured simultaneously for 90 repetitions and the resulting plots averaged. The changes in the fluorescence are directly related to changes in the oxidation state of the metal. These changes can be compared to the decay of the integral of the current that represents the charge associated to the redox and catalytic process combined (Figure 6.39).

In the case of the measurements at the Ni edge (Figure 6.39A), when the potential is switched to 1.23 V versus RHE the fluorescence decay follows very closely the integral of the current for the reduction process in the slower domain (after 2 s). However, in the fast domain (before 1s) the decay of the fluorescence is faster than the integral of the current possibly because it is still affected by ongoing water oxidation. Continuation of the oxygen evolution reaction even after switching off the oxidative potential has been observed before for transition metal oxide catalyst (Risch, Ringleb et al. 2015). When the potential is switched to 1.55 V versus RHE the integral of the current shows a linear behavior almost since the beginning. After the oxidation of some Ni species, water oxidation is possible which leads to increase in the charge due to the catalytic current. The increase of this charge follows a Faradic linear behavior with time. This behavior indicates that it is strongly affected by the catalytic current that contributes since very early to the total charge observed.

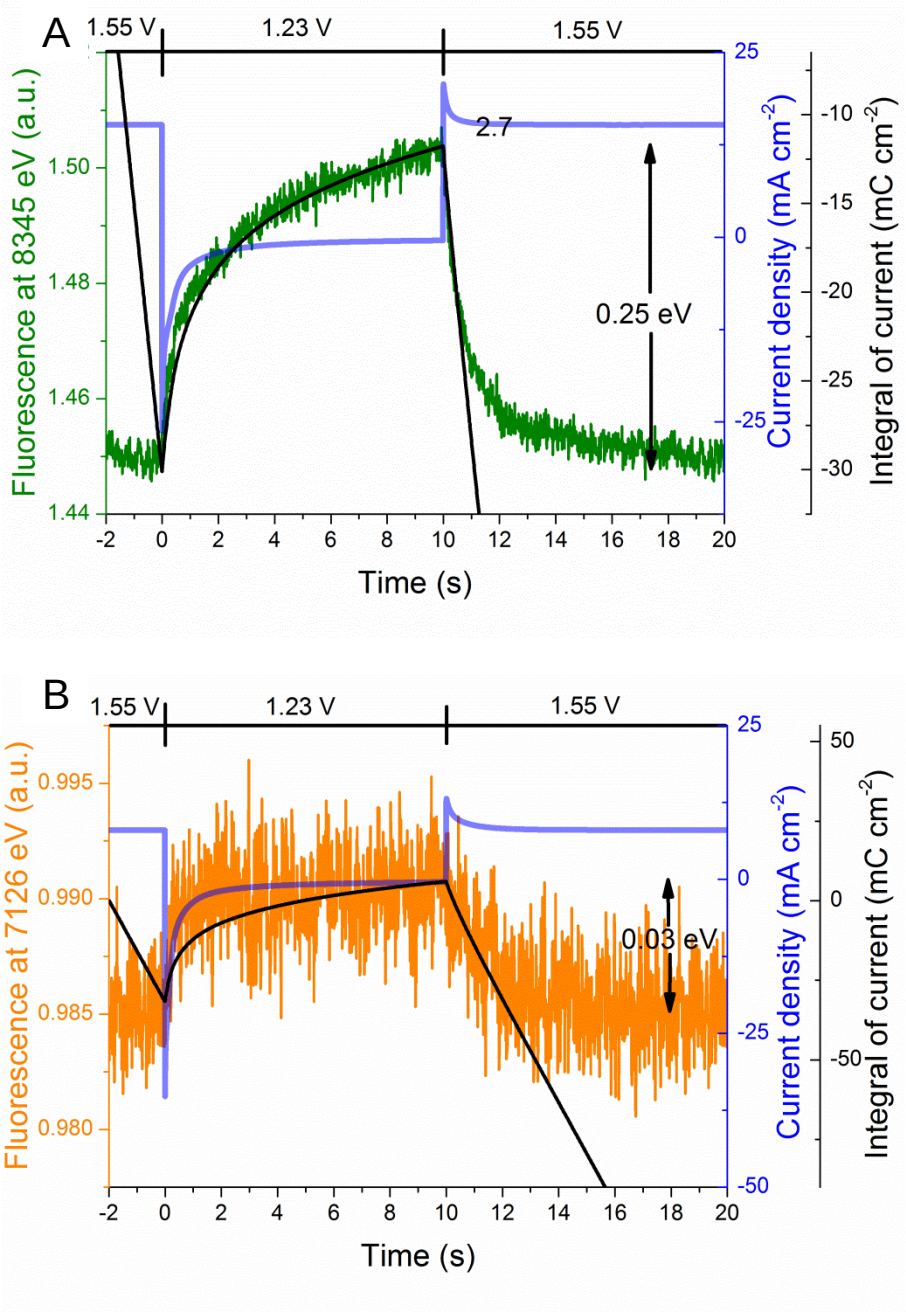

Figure 6.39. Time courses for the fluorescence, current and integral of current in the in-situ absorption measurements with step potential procedure for the NiFe catalyst sample deposited on carbon paper for 5 seconds. We stepped 90 times the potentials between 1.55 V versus RHE and 1.23 V versus RHE for measurements in 1 M KOH **(A)** in the middle of the Ni K-edge (8345 eV) **(B)** in the middle of the Fe K-edge (7126 eV). The data shown is the average of the 90 measurements in each case. The measurements were performed with 10 ms time resolution. The current shown in all cases corresponds also to the averaging of 90 measurements. For every sample all individual current measurements showed the same features.

The total change in the nickel fluorescence corresponds to about 0.25 eV, which is less than the changes previously observed in Figure 6.36. However, it is clear from the measurements that after 10 s the nickel fluorescence has not completely decay yet, especially in the reductive pulse. The fluorescence changes in the Fe edge (Figure 6.39B) are also smaller than the previously measured (0.03 eV compared to 0.06 eV), and the measurements appear much noisier due to these neglishable oxidation state changes. Also this change at the Fe edge seems to match much less the integral of the current changes.

Since the changes in the middle of the Fe edge (7126 eV) are very small and difficult to measure, we decided to study the dynamics of the changes at an energy at the top of the Fe edge (7131 eV). When the changes in the fluorescence at the top of the edge are collected, a very similar plot as the one for the oxidation state changes at the Ni-edge is obtained (Figure 6.40). However, one major difference in the case of the Fe edge is that the fluorescence changes are not related to oxidation state changes, but to structural changes that affect the shape of the top of the edge. This is, the formation of short Fe-O distances at 1.92 Å and short Fe-Ni distances at 2.85 Å as discussed in the EXAFS simulations. The dynamics of both processes follow a very similar behavior.

The fluorescence signal reflects the oxidation state; consequently the first derivative of the fluorescence represents a current that can be assigned either to oxidation or reduction of the metal centers. If the derivative of fluorescence plots are scaled to the current in the CV, they match very closely the reductive wave of the CV. It is also possible to resolve the oxidative wave from the catalytic wave. This data suggests that the redox waves observed in the CV are mostly related to redox and structural changes centered in the metal (Ni and Fe respectively) and not to redox changes in other species (formation of peroxides or superoxides for example). The iron redox waves seem to be slightly shifted around 5 mV to higher potentials. This might be related to the need of first oxidize the Ni metal centers before the structural changes can happened at the Fe edge as it has been suggested by Bell (Friebel, Louie et al. 2015).

To study the timescale of the events in the middle of the Ni edge (8345 eV) and at the top of the Fe edge (7131 eV) we performed also experiments in which the incident beam is set at these energies and the potential is switched 90 times from 1.55 V to 1.23 V with 10 s pulses. The resulting decay in the fluorescence is recorded with 10 ms time resolution and averaged (Figure 6.41).

The decay data can be modeled according to exponential first order decay functions. We observed that for every decay process (reduction or oxidation) at least two exponential functions were required to get a good fit of the data. For that reason we used the function shown in equation 6.4 for

the simulations, where F represents the fluorescence, t the time in seconds, A corresponds to an offset and t_1, t_2 correspond to the time constants related to how fast every decay is (the results from the fittings are shown in Table 6.10).

From the fitting of equation 6.4 two time constant can be obtained for each decay process. Interestingly, the time constants obtained from the measurements at the iron and nickel edge show very similar values, which suggest that the decay process in both cases follow very similar kinetics.

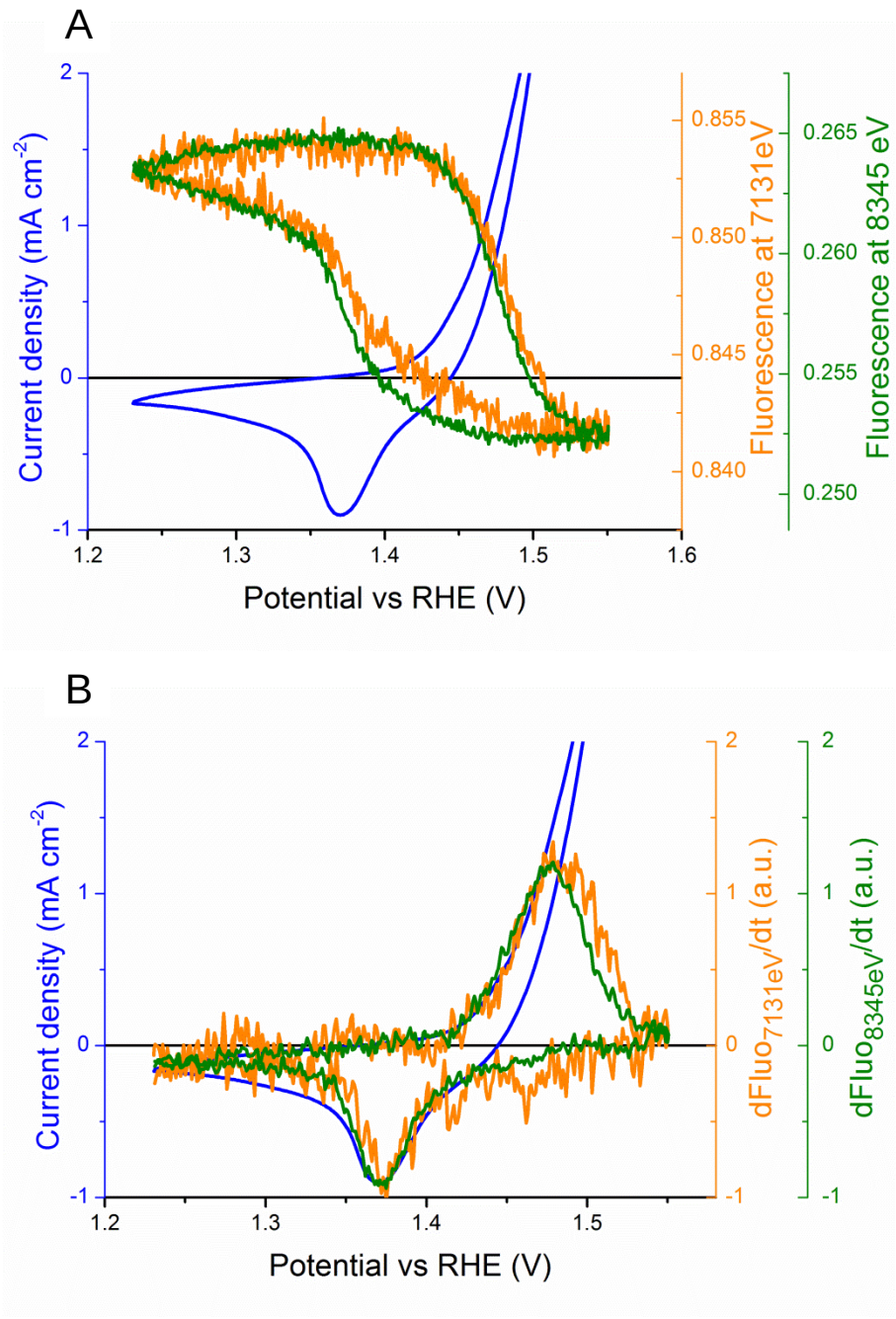

Figure 6.40. *In-situ* X-ray absorption measurements in 1 M KOH for the NiFe catalyst sample deposited carbon paper for 5 seconds using the same deposition solution as in the rest of the experiments. (A) Shows the 5 mVs^{-1} CV measurements at the Ni and Fe edge together with fluorescence measurements in the middle of the Ni k-edge (8345 eV) and at the top of the Fe edge (7131 eV). (B) Shows the derivative of the fluorescence in time which is related to the oxidation state changes or the corresponding structural changes. The resistance was 3 Ω, no IR drop correction was applied.

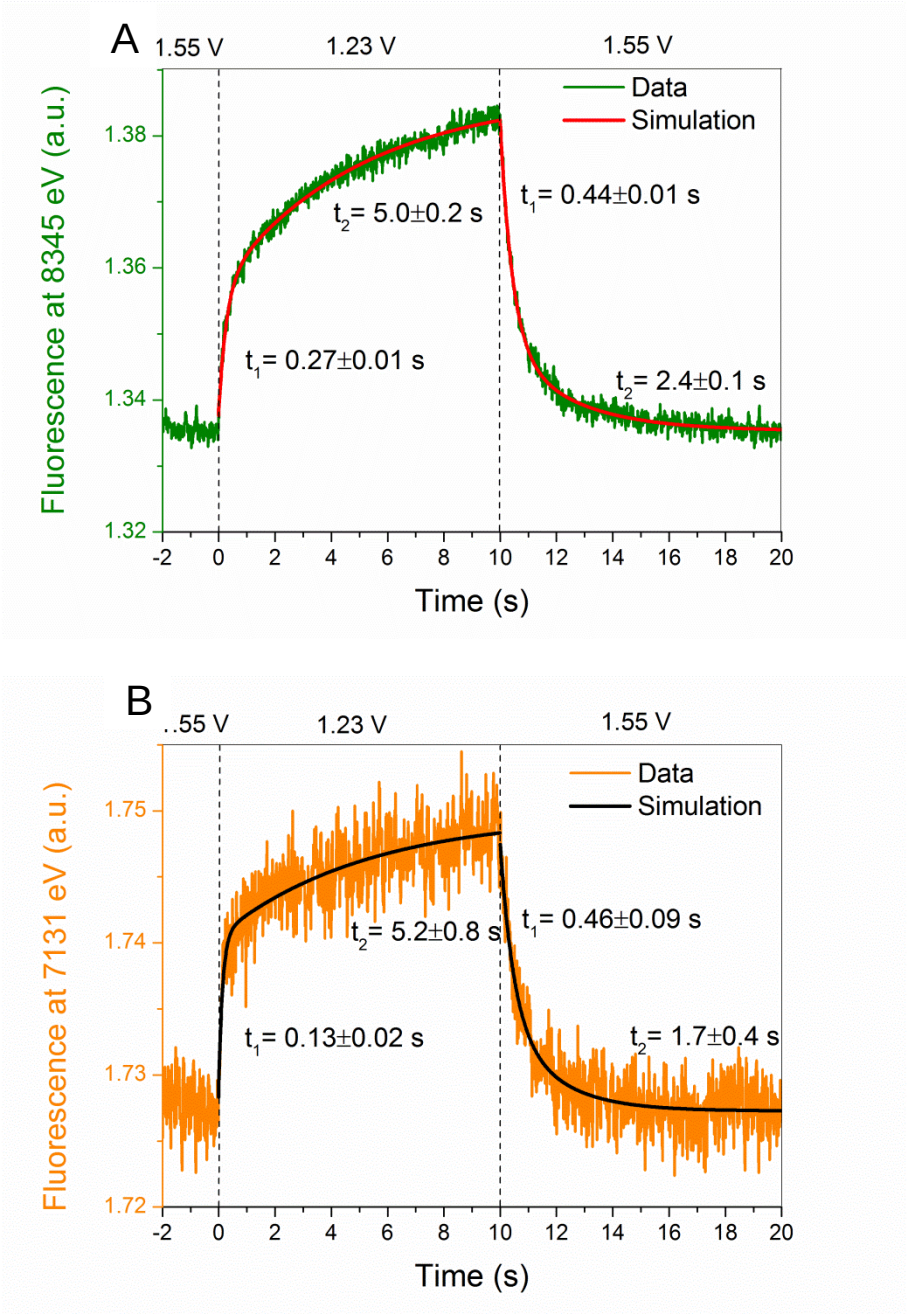

Figure 6.41. Time courses for the fluorescence in the *in-situ* absorption measurements with step potential procedure for the NiFe catalyst sample deposited on carbon paper for 5 seconds. We stepped 90 times the potentials between 1.55 V versus RHE and 1.23 V versus RHE for measurements in 1 M KOH **(A)** in the middle of the Ni K-edge (8345 eV) **(B)** in the top of the Fe K-edge (7131 eV). The data shown is the average of the 90 measurements in each case. The measurements were performed with 10 ms time resolution. The data was simulated using two exponential functions for the reduction and oxidation processes as described in the Table 6.10.

$$F = A + B \cdot e^{\frac{-t}{t_1}} + C \cdot e^{\frac{-t}{t_2}} \qquad (6.4)$$

Table 6.10. Simulation paramethers for the fitting with two exponential functions of the time courses of the fluorescence in the protocol with stepping potential between 1.55 V versus RHE and 1.23 V versus RHE from Figure 6.41. The number in parenthesis corresponds to the uncertainty in the last digit.

Paramether	Ni Oxidation	Ni Reduction	Fe Oxidation	Fe Reduction
A	1.3353(1)	1.3863(3)	1.7273(1)	1.7497(6)
B	3(2)E+8	-0.0188(4)	2.8(1)E+8	-0.0113(9)
C	0.9(3)	-0.0291(2)	3(5)	-0.0092(4)
t_1	0.44(1)	0.27(1)	0.46(9)	0.13(2)
t_2	2.4(1)	5.0(2)	1.7(4)	5.2(8)

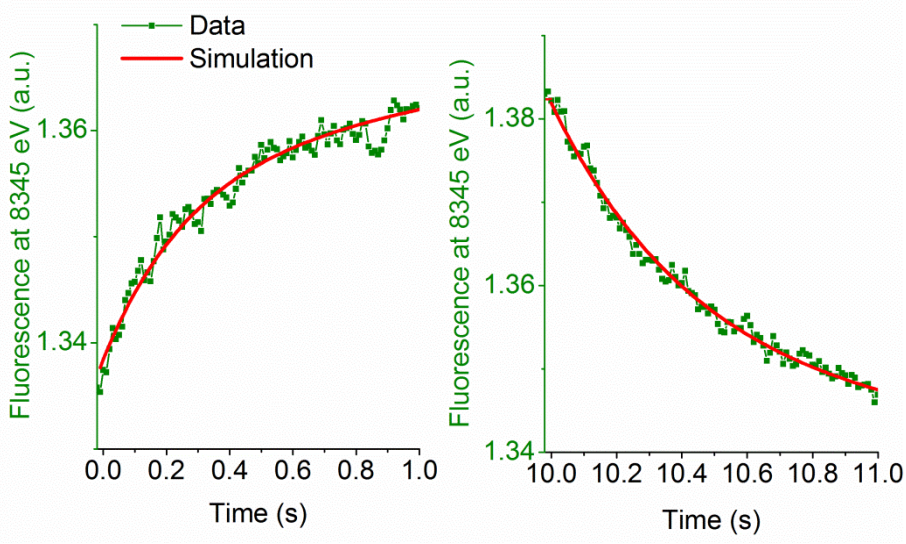

Figure 6.42. Time courses for the fluorescence in the in-situ absorption measurements with step potential procedure for the NiFe catalyst sample deposited on carbon paper for 5 seconds. Magnification of the data shown in Figure 6.41A between 0 and 1s after the potential pulse. We stepped 90 times the potentials between 1.55 V versus RHE and 1.23 V versus RHE for measurements in 1 M KOH in the middle of the Ni K-edge (8345 eV). The data shown is the average of the 90 measurements in each case. The measurements were performed with 10 ms time resolution. The data was simulated using two exponential functions for the reduction and oxidation processes as described in Table 6.10.

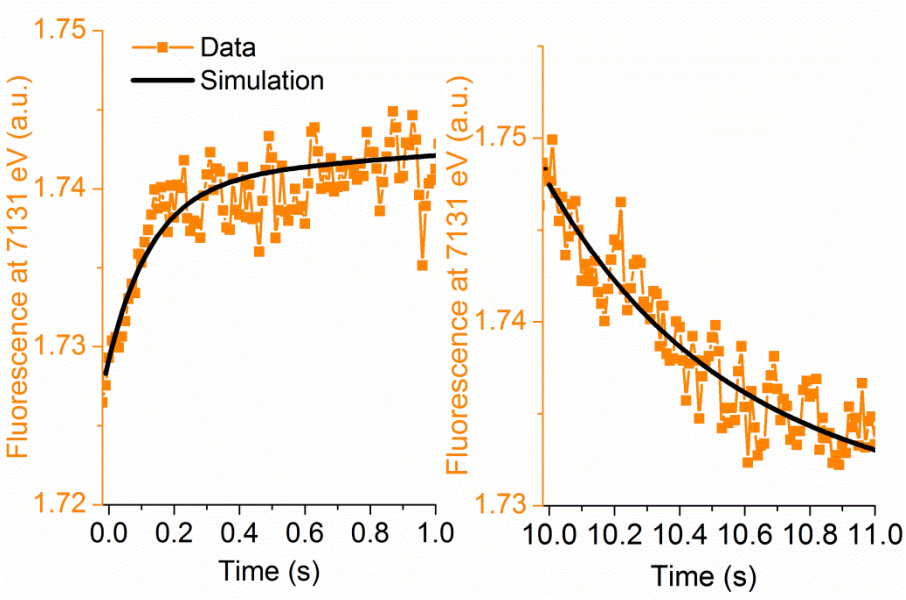

Figure 6.43. Time courses for the fluorescence in the in-situ absorption measurements with step potential procedure for the NiFe catalyst sample deposited on carbon paper for 5 seconds. Magnification of the data shown in Figure 6.41B between 0 and 1s after the potential pulse. We stepped 90 times the potentials between 1.55 V versus RHE and 1.23 V versus RHE for measurements in 1 M KOH in the top of the Fe K-edge (7131 eV). The data shown is the average of the 90 measurements in each case. The measurements were performed with 10 ms time resolution. The data was simulated using two exponential functions for the reduction and oxidation processes as described in Table 6.10.

6.2.7 *In-situ* time resolved UV-Vis absorption measurements

Previously in the CV experiments together with absorption measurements we observed that the absorption changes follow very closely the oxidation state changes related to the redox processes in the CV's. To study more in detail the kinetics of this redox process with a higher time resolution than in the fluorescence measurements (2 ms time resolution in this case) we performed absorption measurements together with chronoamperometry.

To study the relationship between the absorption and the current in the time domain we performed a series of measurements in which the potential was hold for 10 seconds at 1.55 V versus RHE and switched to 1.2 V versus RHE for another 10 seconds for measurements at pH 14. For measurements at pH 7 the potential was switched between 1.83 and 1.4 V versus RHE. The current and the absorption at 470 nm were recorded simultaneously with 1 ms time resolution. The measurements were performed 30 times in each sample and the corresponding currents and absorption values averaged. We also checked that the observed behaviour at each condition was

reproducible in at least 3 samples. The averaged absorption data was additionally treated to diminish the periodic noise by averaging every two points and also filtering the high frequencies using a Fourier transform filter. The details are described in the experimental part.

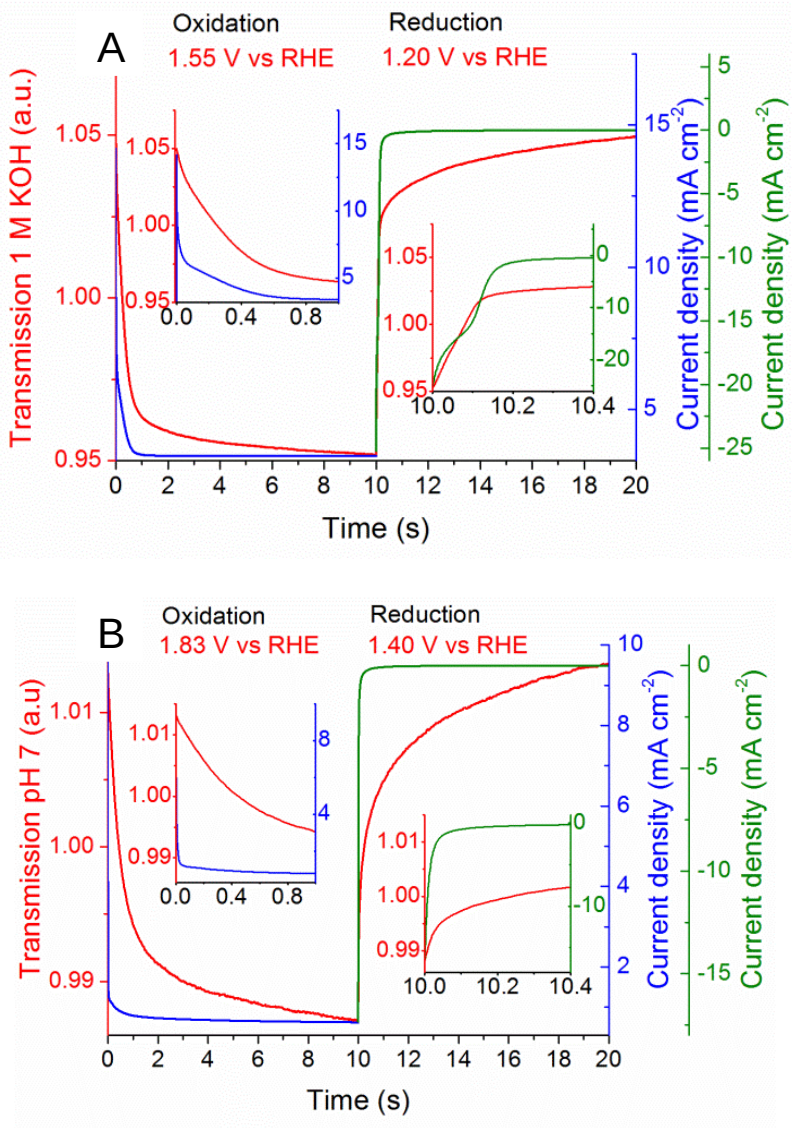

Figure 6.44. Time courses for the current and transmission at 470 nm wavelength in the *in-situ* absorption measurements with step potential procedure for the NiFe catalyst. We stepped 30 times the potentials between 1.55 V versus RHE and 1.2 V versus RHE for measurements in 1 M KOH **(A)** and between 1.83 V versus RHE and 1.4 V versus RHE for measurements at pH 7 **(B)**. The data shown is the average of the 30 measurements in each case. The measurements were performed with 1 ms time resolution and the data was averaged every two data points to decrease the noise. We also applied a filtering procedure to eliminate periodic noise. The current shown in all cases corresponds also to the averaging of 30 measurements. For every sample all individual current measurements showed the same features.

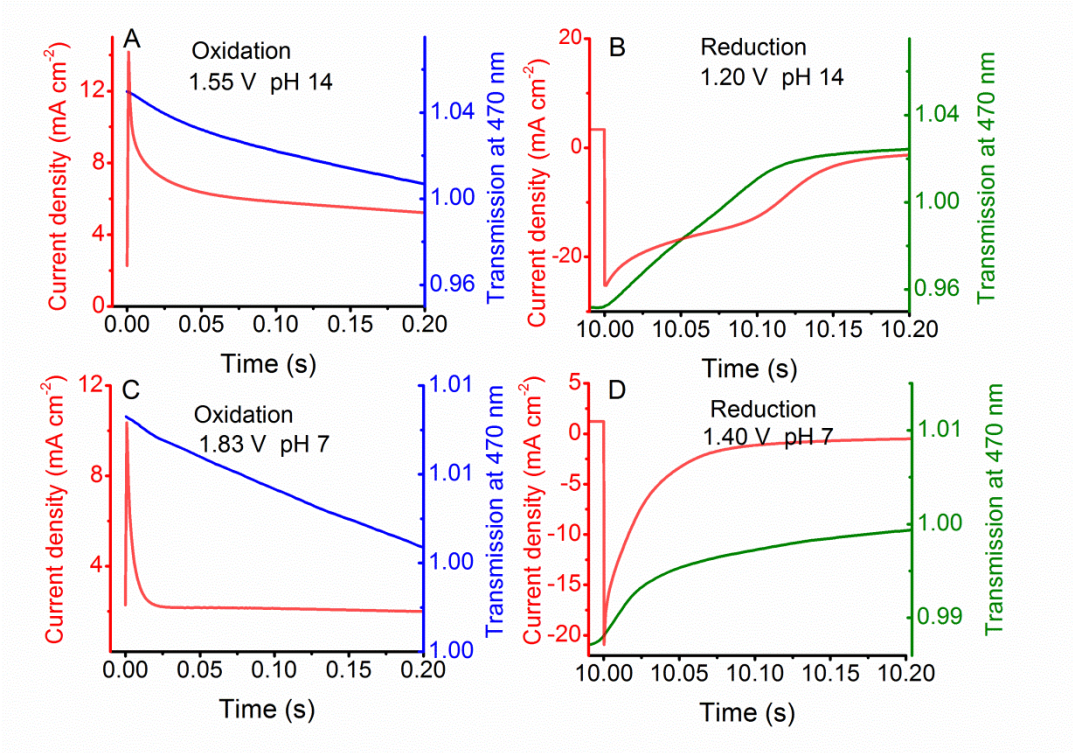

Figure 6.45. Time courses for the current and transmission at 470 nm wavelength in the in-situ absorption measurements with step potential procedure for the NiFe catalyst. Magnification of the data shown in Figure 6.44 between 0 and 200 ms after the potential pulse. The corresponding current and absorption at 470 nm wavelength are shown. We stepped 30 times the potentials between 1.55 V versus RHE **(A)** and 1.2 V versus RHE **(B)** for measurements in 1 M KOH and between 1.83 V versus RHE **(C)** and 1.4 V versus RHE **(D)** for measurements at pH 7. The data shown corresponds to the average of the 30 measurements.

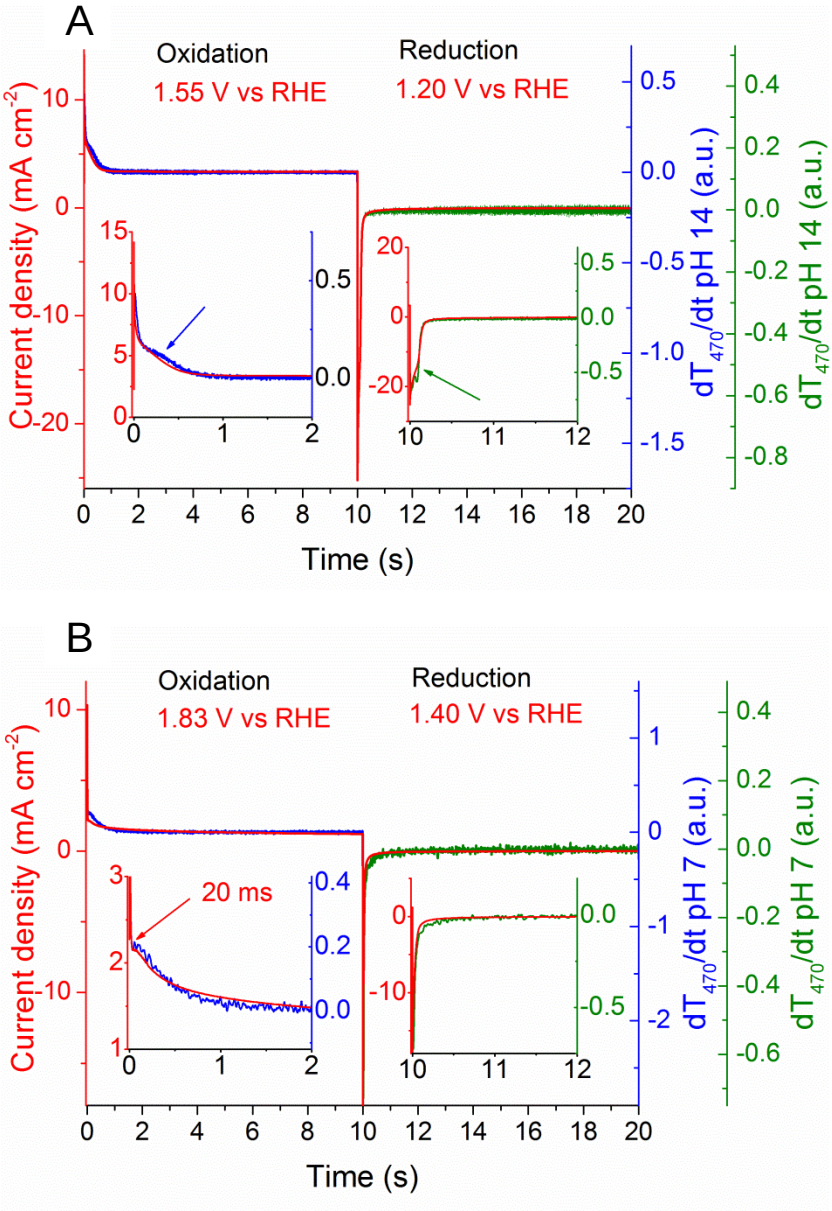

Figure 6.46. Time courses for the current and derivative of the transmission at 470 nm wavelength in the *in-situ* absorption measurements with step potential procedure for the NiFe catalyst. We stepped 30 times the potentials between 1.55 V versus RHE and 1.2 V versus RHE for measurements in 1 M KOH **(A)** and between 1.83 V versus RHE and 1.4 V versus RHE for measurements at pH 7 **(B)**. The data shown is the average of the 30 measurements in each case. The measurements were performed with 1 ms time resolution and the data was averaged every two data points to decrease the noise. We also applied a filtering procedure to eliminate periodic noise. Details about the measurement are described in the experimental part. The current shown in all cases corresponds also to the averaging of 30 measurements. For every sample all individual current measurements showed the same features. The derivative of the data is calculated by smoothing the data with an order 2 polynomial using 20 points in the window. The arrows show the inflection points observed during the current decay.

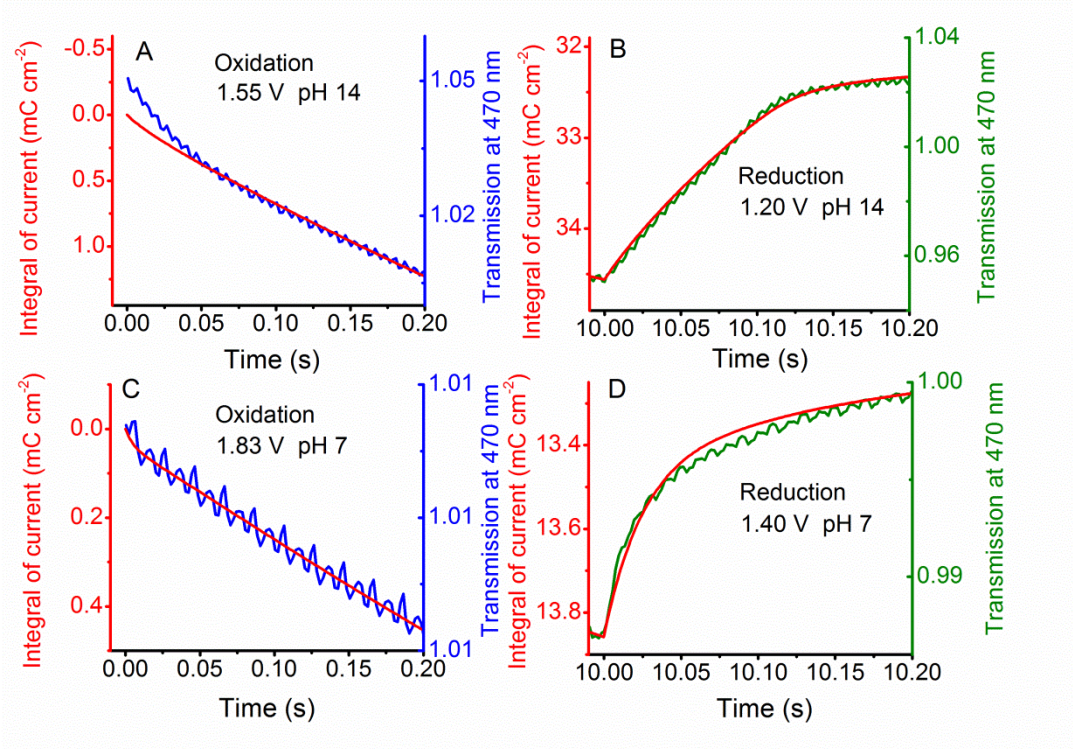

Figure 6.47. Time courses for the transmission at 470 nm wavelength and integral of current in the *in-situ* absorption measurements with step potential procedure for the NiFe catalyst. Magnification of the data between 0 and 200 ms after the potential pulse. We stepped 30 times the potentials between 1.55 V versus RHE **(A)** and 1.2 V versus RHE **(B)** for measurements in 1 M KOH and between 1.83 V versus RHE **(C)** and 1.4 V versus RHE **(D)** for measurements at pH 7. The data shown corresponds to the average of the 30 measurements. Before integrating, the data was averaged every two points and no Fourier filtering was applied.

Previously in Figure 6.25 we observed that the derivative of the absorption at 470 nm corresponds to the redox waves in the CV measurements at pH 7 and pH 14. For that reason we decided to take in this case the derivative of the transmission measured in the time resolved experiments and compare it to the current.

In the case of our electrode, the faradic current observed is composed by the current coming from the oxidation of the metal catalyst (redox process) and the current associated with the oxidation of the water (catalytic process). However, depending on the speed of both processes the catalytic current might affect the redox current since water oxidation results in reduction of the metal (Goerlin, Chernev et al. 2016). The derivative of the transmission at 470 nm (dT_{470}/dt), on the other hand, represents the current related to electron transfer that results in a change of color of the catalyst. As it was observed before, in the CV experiments the derivative of the absorption is directly related to the redox process due to oxidation and reduction of the Ni redox active sites.

Figure 6.46 shows the behaviour of the current and derivative of the transmission in a comparable scale. In both measurements at pH 7 and pH 14 we can observe that in general the behaviour of the derivative of the transmission follows very closely the behaviour of the current. In both cases we can observe that for times higher than 2 s after the pulse, dT_{470}/dt reaches already a value of zero (no oxidation state changes) where the current is also already stable and consist only of the catalytic current component. Most of the dynamical changes for current and dT_{470}/dt occur bellow 1 s after the switching in the potential.

In the case of Figure 6.46 it can be observed that after the pulse, in the oxidation region the current has a fast rising and decay but it gets slow down in the regions signalled with the arrows. Interestingly the dT_{470}/dt shows the same features of the current in this time domain. This suggests that the slowing down of the current in this region is strongly correlated to a process related to the oxidation and reduction of the metal. This type of features might appear from processes related to some kinetic limitations (like mass transfer or electron transfer).

The filtering of the transmission signal with the Fourier filter before the calculation of the derivative of the transmission might also affect the resulting shape, especially in the fast domain (around 200 ms after the pulse). For that reason we also show the fluorescence data with no filtering compared to the integration of the current. For pH 7 and pH 14 we observe that both, transmission and integral of current follow a very similar behavior (Figure 6.47). In general we observed that with the chosen potential values for the measurements at pH 7 and pH 14 we obtain

very similar current values and decay in the transmission (associated to the redox processes in the nickel centres). For instance the kinetics at pH 7 and pH 14 seem to be quite similar.

We also used another protocol in which we applied an oxidation potential (1.55 V versus RHE for pH 14 and 1.83 V versus RHE for pH 7) and then let the system relax at open circuit potential (OCP) and recorded how it changes in time (Figure 6.48 and 6.49). In previous experiments it has been observed that switching to OCP conditions after applying oxidizing potential results still in ongoing oxygen formation which results in reduction of the metal ions in the catalyst and for instance decrease in the OCP (Risch, Ringleb et al. 2015). In this way the changes in the OCP are strongly related to the ongoing water oxidation.

The same kind of behaviour is observed for the measurements in which the potential was switched between an oxidizing potential and the OCP. The derivative of the transmission follows again the decay of the current and the OCP (Figure 50). In Figure 6.49 (panels B and D) we can observe a very fast decay in the potential. From this decay an Ohmic resistance with a value around 10-15 Ω can be estimated, which is consistent with the usual values of Ohmic resistance in the electrochemical cell determined by impedance spectroscopy measurements at high frequencies (around 10 kHz) for films deposited on FTO. This suggests that the kinetics of the system in this case is limited by the Ohmic resistance of the electrochemical cell.

Figure 6.51 shows the transmission at 470 nm and the integral of the open circuit potential. In general, for this measurement at OCP we observe again that the transmission at 470 nm and the integral of the open circuit potential follow a very similar behaviour. Especially important is the decay during the reduction process that shows a linear behaviour, which as described before seems to be mostly limited by the resistance of the electrochemical cell.

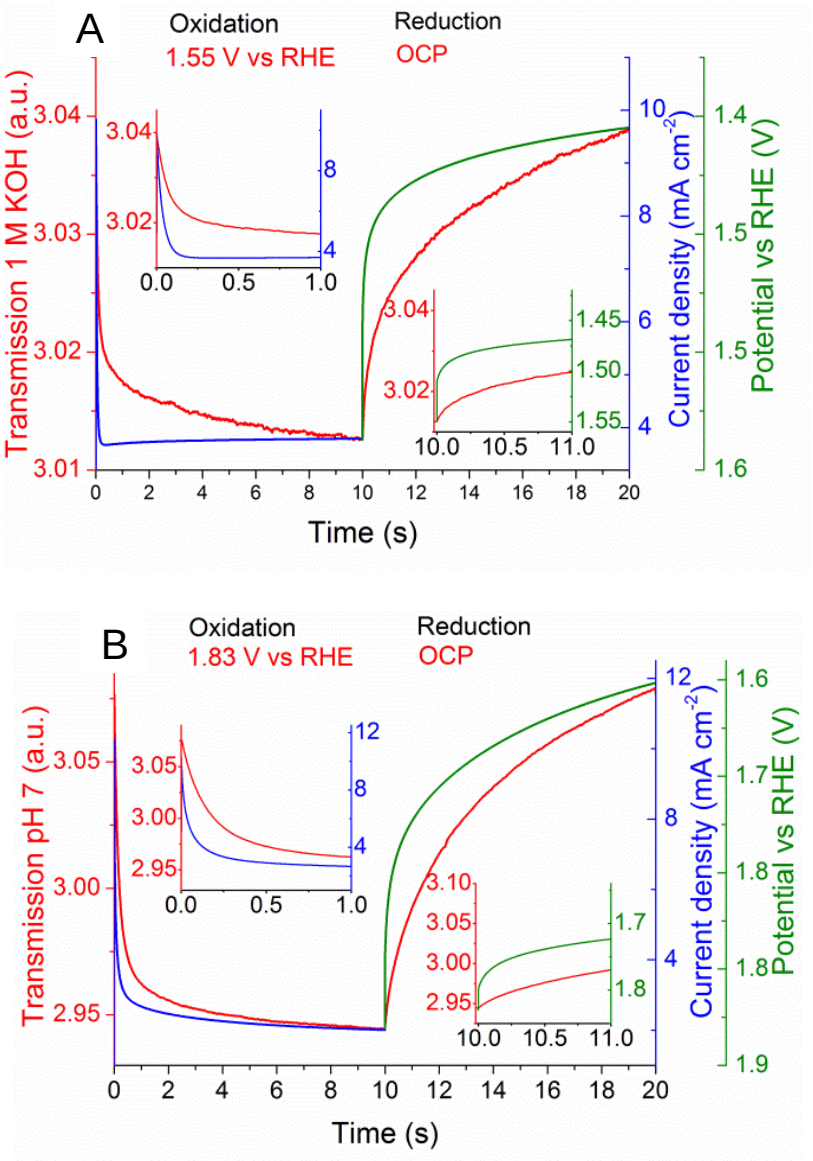

Figure 6.48. Time courses for the current, OCP and transmission at 470 nm wavelength in the *in-situ* absorption measurements with step potential procedure for the NiFe catalyst. We stepped the potential 30 times between 1.55 versus RHE and OCP for measurements in 1 M KOH **(A)** and between 1.83 V versus RHE and OCP for measurements in pH 7 **(B)**. All the measurements in pH 7 with phosphate buffer had also 1 M KNO_3 as supporting electrolyte. The data shown corresponds to the average of the 30 measurements. The measurements were performed with 1 ms time resolution and the data was averaged every two data points to decrease the noise. We also applied a filtering procedure to eliminate the periodic noise. The current shown in all cases corresponds also to the averaging of 30 measurements. For every sample all individual current measurements showed the same features.

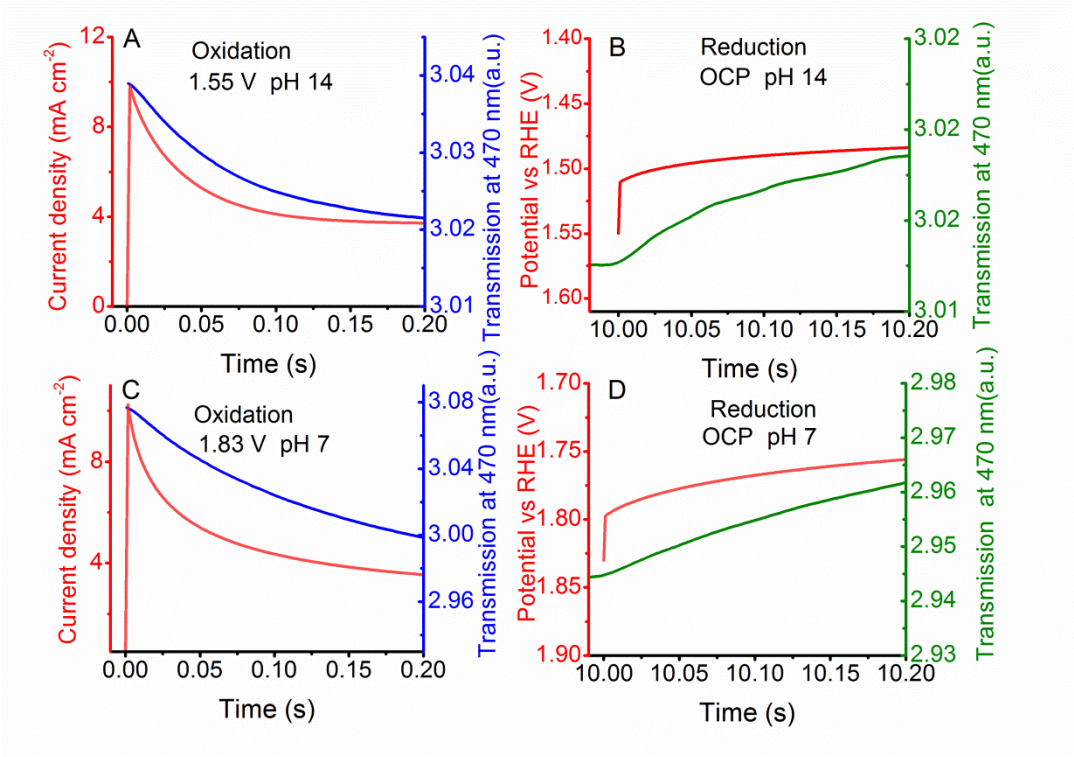

Figure 6.49. Time courses for the current, OCP and absorption at 470 nm wavelength in the *in-situ* absorption measurements with step potential procedure for the NiFe catalyst. Magnification of the data shown in Figure 6.48 between 0 and 200 ms after the potential pulse. We stepped 30 times the potentials between 1.55 V versus RHE **(A)** OCP **(B)** for measurements in 1 M KOH and between 1.83 V versus RHE **(C)** OCP **(D)** for measurements at pH 7. The data shown corresponds to the average of the 30 measurements.

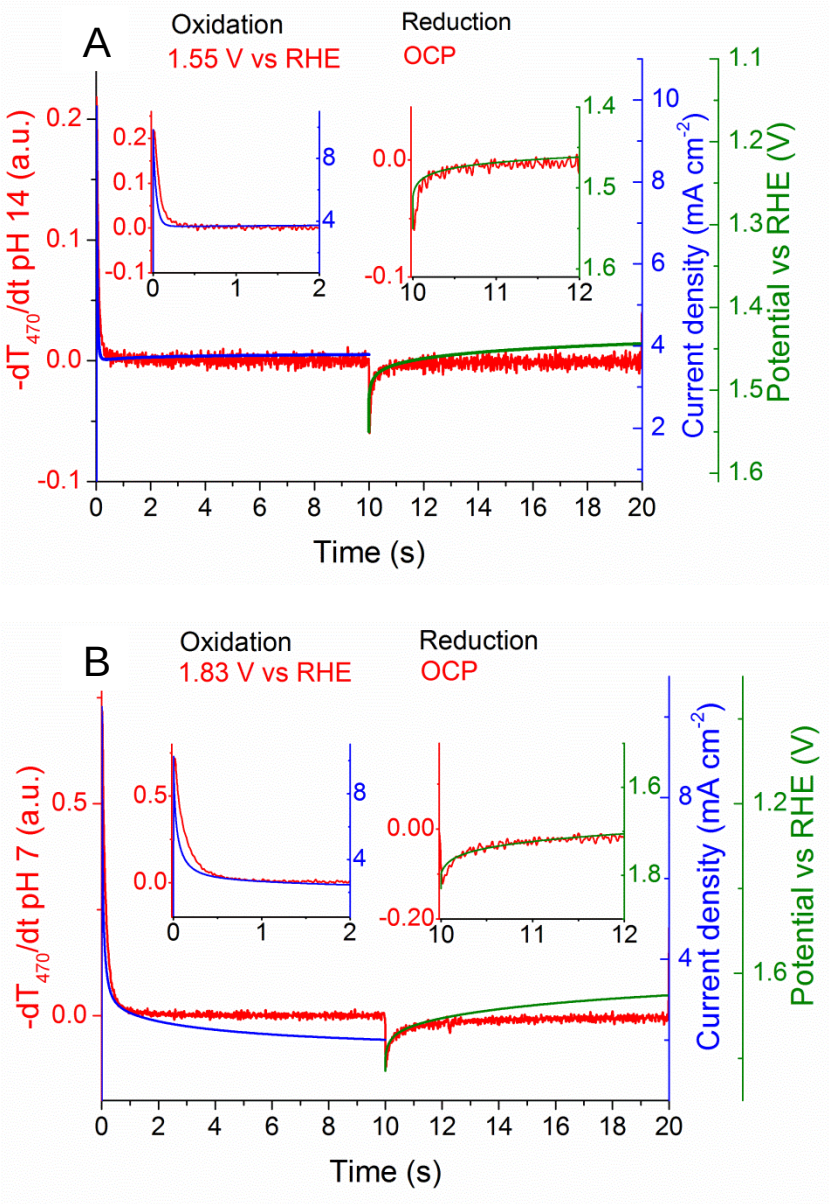

Figure 6.50. Time courses for the current, OCP and derivative of the transmission at 470 nm wavelength in the *in-situ* absorption measurements with step potential procedure for the NiFe catalyst. We stepped the potential 30 times between 1.55 V versus RHE and OCP for measurements in 1 M KOH **(A)** and between 1.83 V versus RHE and OCP for measurements in pH 7 **(B)**. All the measurements in pH 7 with phosphate buffer had also 1 M KNO_3 as supporting electrolyte. The shown data correspond to the average of the 30 measurements. The measurements were performed with 1 ms time resolution and the data was averaged every two data points to decrease the noise. We also applied a filtering procedure to eliminate the periodic noise. Details about the measurement are described in the experimental part. The current shown in all cases corresponds also to the averaging of 30 measurements. For every sample all individual current measurements showed the same features. The derivative of the data is calculated by smoothing the data with an order 2 polynomial using 20 points in the window.

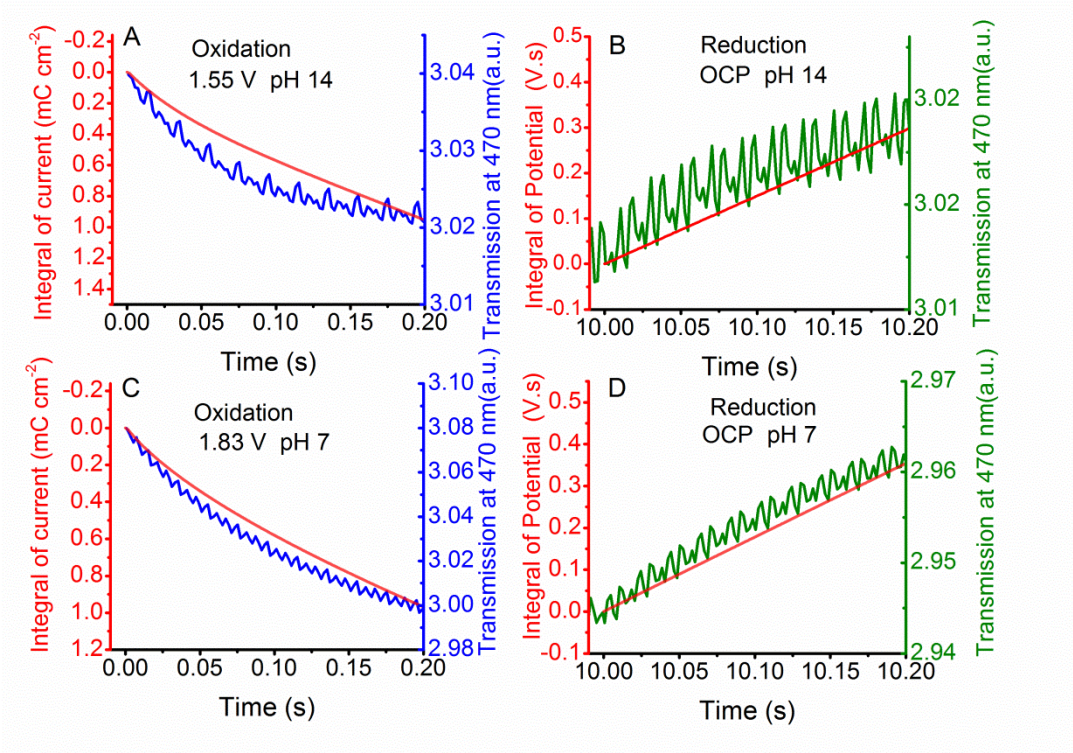

Figure 6.51. Time courses for the integral of current, transmission at 470 nm wavelength and the integral of OCP in the *in-situ* transmission measurements with step potential procedure for the NiFe catalyst. Magnification of the data between 0 and 200 ms after the potential pulse. The corresponding current, OCP and derivative of the absorption at 470 nm wavelength are shown. We stepped 30 times the potentials between 1.55 V versus RHE **(A)** OCP **(B)** for measurements in 1 M KOH and between 1.83 V versus RHE **(C)** OCP **(D)** for measurements at pH 7. The data shown corresponds to the average of the 30 measurements. Before integrating, the data was averaged every two points and no Fourier filtering was applied.

6.2.8 Analysis of the NiFe catalyst CV´s at different scan rates

To understand better the role of the Ohmic resistance in the redox and catalytic waves of the CV we performed a series of CV's at different scan rates for films deposited for 1 s in FTO and platinum substrate electrodes in 1 M KOH. We observed typical Ohmic resistance values around 10-14 Ω for films deposited on FTO and around 1-2 Ω for films deposited on platinum with the Ohmic resistance calculated from impedance spectroscopy measurements at high frequencies (10 kHz).

Figure 6.52 shows the CV´s for the 5 mV s^{-1} to 2000 mV s^{-1} scan rates for the NiFe catalyst deposited on FTO. Even though the cathodic wave can be directly observed, the anodic wave is

strongly embedded into the catalytic wave and cannot be clearly resolved in this case. If the magnitude of the maximum peak current in the cathodic wave is plotted versus the square root of the scan rate a pretty clear linear correlation can be observed (Figure 6.53B). However, the first 4 data points from 5 mV s^{-1} to 50 mV s^{-1} are outside this trend and follow a linear behavior rather when plotted just against the scan rate (Figure 6.53C). This data suggests two type of regimes present in the measurements. Bellow 50 mV s^{-1} a typical electron transfer controlled process for redox species confined on the surface of an electrode, and a behavior typical of a mass transport (diffusion) limited profess for scan rates over 50 mV s^{-1}, with the cathodic peak position varying also linearly with the scare root of the scan rate (Figure 6.54).

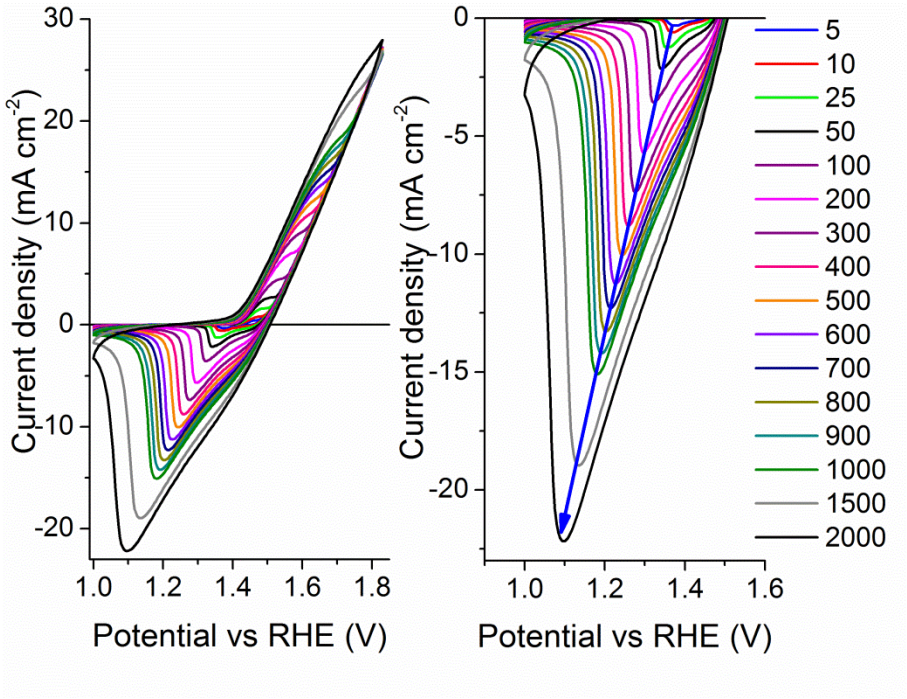

Figure 6.52. Cyclic voltammetries at different scan rates (shown in the figure legend, in mV s^{-1}) in 1 M KOH for the NiFe catalyst deposited on FTO. No IR drop correction was applied.

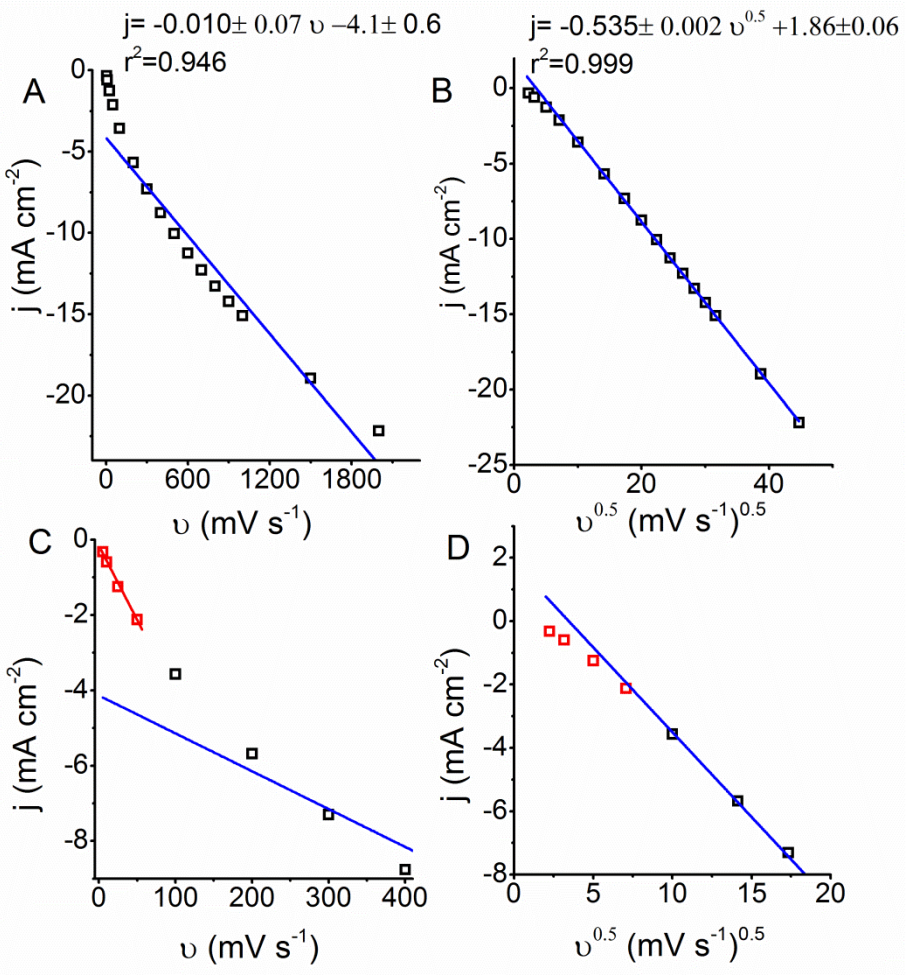

Figure 6.53. **(A)** Shows the linear fitting for the maximum reduction current (j) in the cathodic peak in Figure 6.52 plotted versus the scan rate (υ). **(B)** Shows the linear fitting for the maximum reduction current (j) plotted versus the square root of the scan rate ($\upsilon^{0.5}$). Panels **(C)** and **(D)** show how the first points at low scan rates (in red), these points do not follow the trend of the points at high scan rate.

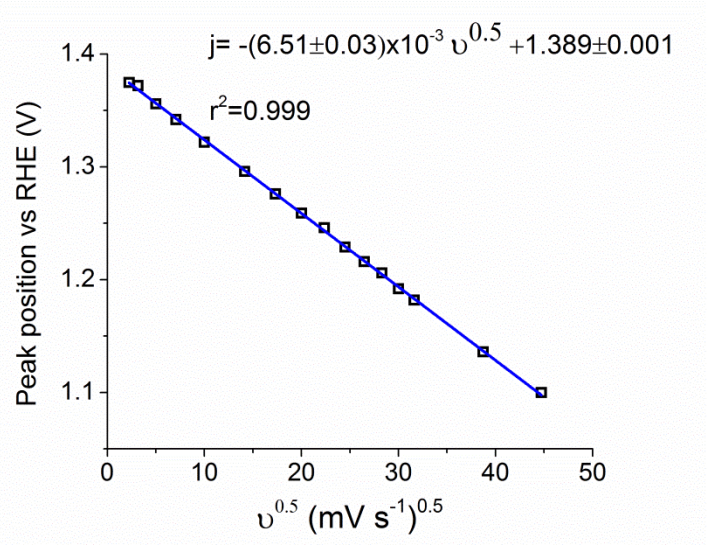

Figure 6.54. Linear dependence in the cathodic peak position versus the RHE in Figure 6.52 with the square root of the scan rate ($\upsilon^{0.5}$).

Traditionally a linear variation of the peak current with the square root of the scan rate is expected for a system in which the redox species are in solution and have to diffuse to the surface of the working electrode to experience the redox changes. However, in the case of our electrode, the redox species (nickel ions) are already attached to the substrate electrode (FTO or platinum). For instance, it is not completely clear what are the species that should diffuse in this case. Recent reports show that the catalysis in NiFe catalysts in alkaline pH is strongly dependant on the conjugated bases in the interlayer of the oxide and possibly associated to a deprotonation step during turnover (Hunter, Hieringer et al. 2016). Also Raman experiments by Trzésniewski et all (Trześniewski, Diaz-Morales et al. 2015) showed the formation of negatively charged species that they attributed to a deprotonation process and formation of active oxygen species as also observed previously in studies by Merrill (Merrill, Worsley et al. 2014). The studies by Trzésniewski suggested that the formation of oxygen active species is favored at alkaline pH and is inhibited when the electrolyte is borate buffer at pH 9.2. This suggests that the redox and catalytic processes might be (in this case of the films deposited on FTO) controlled by proton or hydroxide diffusion. To corroborate that possibility we performed the same type of measurements using the platinum substrate and the same type of electrolyte (1 M KOH).

We observed a very strong change in the shape of the CV just by changing the substrate electrode (Figure 6.55). The redox waves became sharper and it was possible in this case to observe better the oxidation wave. When we plot the maximum cathodic peak current versus the square root of the scan rate we observe again a linear correlation, but in this case the starting of the linear regime is shifted to 100 mVs^{-1} scan rate (Figure 6.56). The same kind of linear behaviour with the square

root of the scan rate is observed for the maximum peak current of the anodic wave and for the peak position of the anodic and cathodic waves as observed in Figures 6.57 and 6.58.

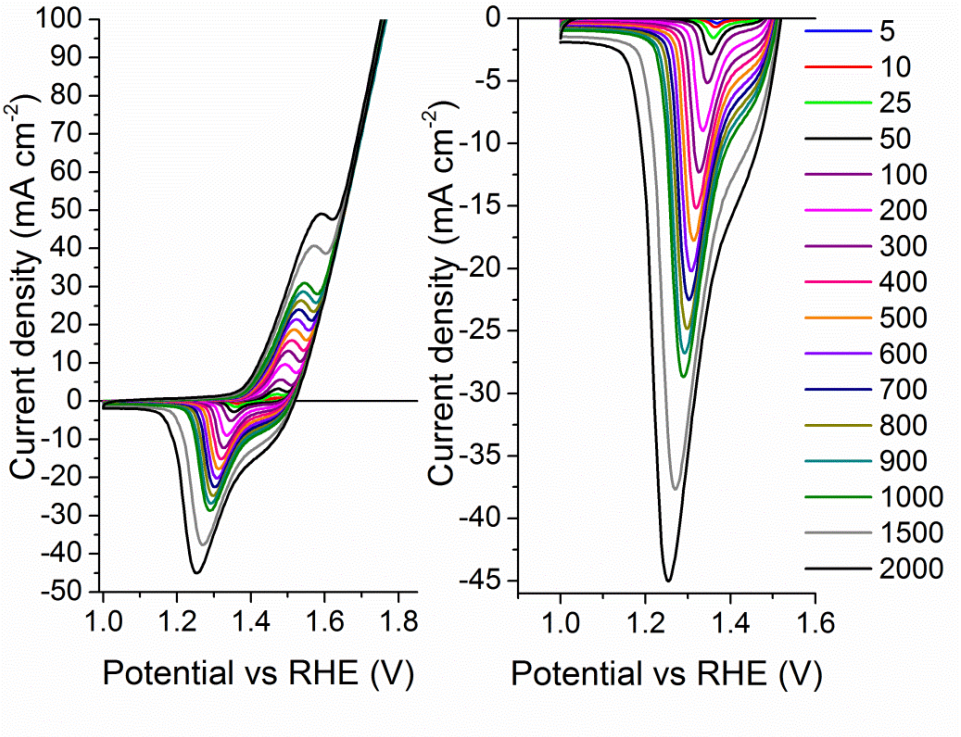

Figure 6.55. Cyclic voltammetries at different scan rates in 1 M KOH for the NiFe catalyst deposited on a platinum substrate. No IR drop correction was applied.

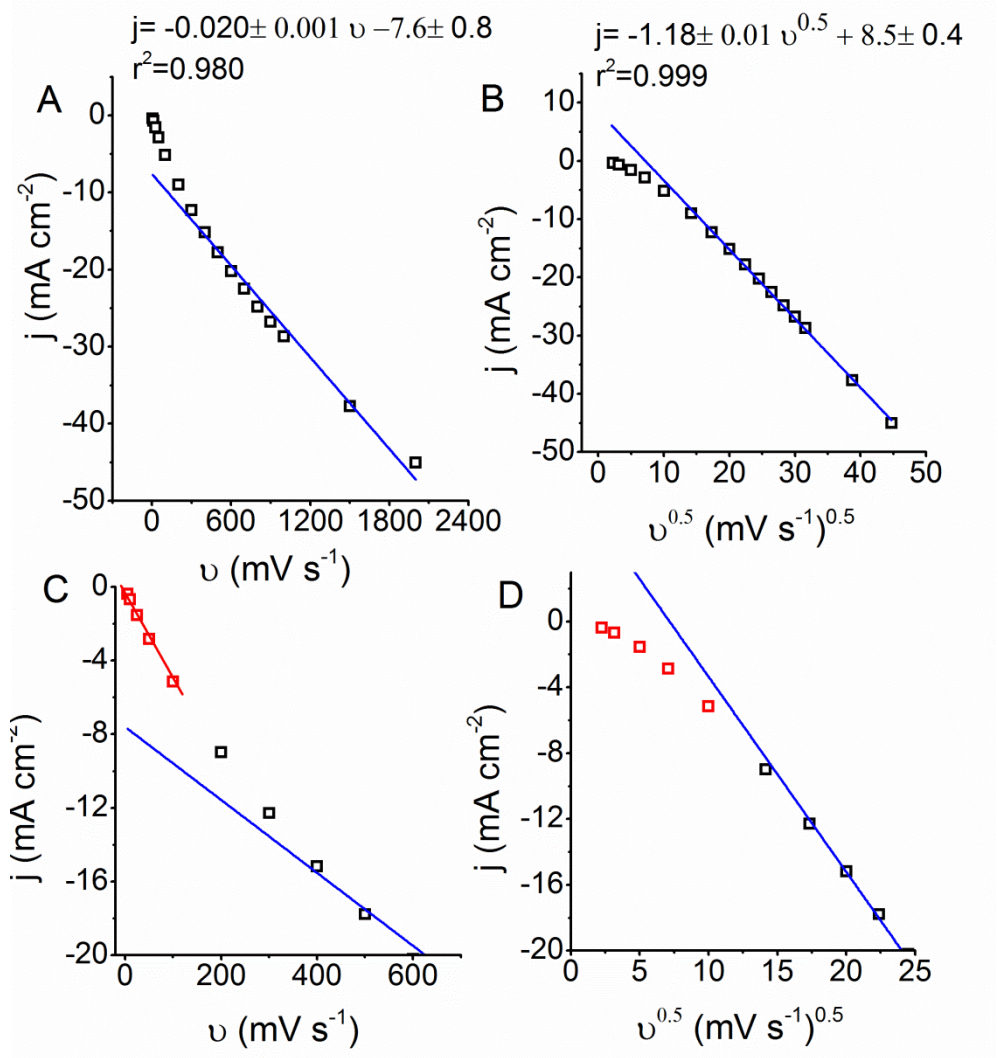

Figure 6.56. **(A)** Shows the linear fitting for the maximum reduction current (j) in Figure 6.55 plotted versus the scan rate (υ). **(B)** Shows the linear fitting for the maximum reduction current (j) plotted versus the square root of the scan rate ($\upsilon^{0.5}$). Panels **(C)** and **(D)** show how the first points at low scan rates (in red) do not follow the trend of the points at high scan rate.

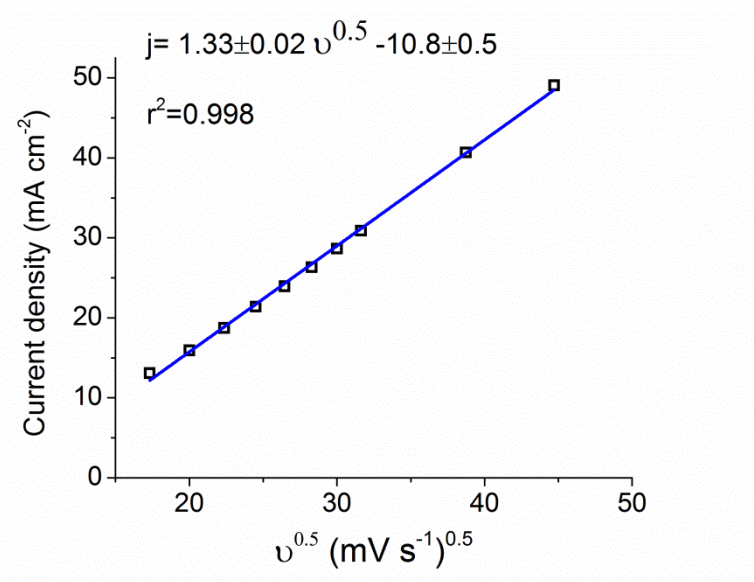

Figure 6.57. Linear fitting for the maximum reduction current (j) plotted versus the square root of the scan rate ($\upsilon^{0.5}$).

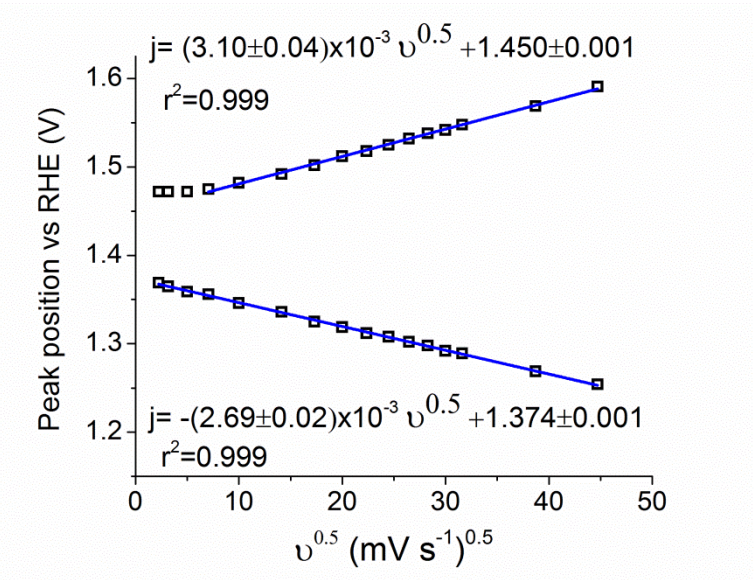

Figure 6.58. Linear dependence in the cathodic and anodic peak position in Figure 6.55 with the square root of the scan rate ($\upsilon^{0.5}$).

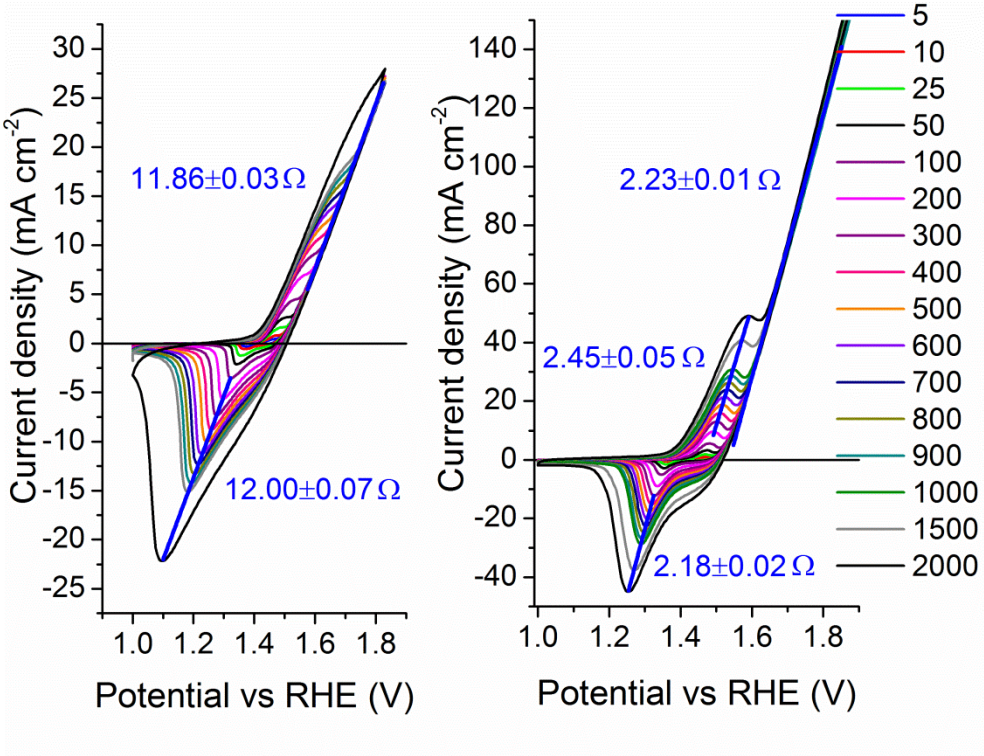

Figure 6.59. Comparison of the cyclic voltammetries at different scan rates in 1 M KOH for the NiFe catalyst deposited on FTO (left) and in platinum (right). The values shown in blue correspond to the ohmic resistance calculated from the linear fit of the peak position and current at different scan rates and the linear fit of the catalytic current in every corresponding case. No IR drop correction was applied.

Interestingly it is possible to trace a linear correlation of the redox peak position (in volts) and current magnitude (in $mAcm^{-2}$) as it varies with the scan rate (Figure 6.59). From the slope of this plot it is possible to obtain and estimation of an Ohmic resistance, which surprisingly shows approximately the same value of the Ohmic resistance obtained from the slope of the catalytic current. Even more interesting, the calculated Ohmic resistances show in every case very similar values to the ones obtained by impedance measurements for the electrochemical cell using FTO or platinum substrates.

Since we kept the same electrolyte in both cases (1 M KOH), the differences in Ohmic resistance come mostly from the variation of the electrode substrate and not from the electrolyte. This directly argues against mass transport limitations coming from diffusion of protons or hydroxide in the time resolved absorption measurements realized with the FTO electrodes. The strong correlation between the redox waves, the catalytic current and the Ohmic resistance suggests in this case that the redox and catalytic processes are fast in a way that the overall process is mostly limited by the Ohmic resistance of the electrochemical cell. This Ohmic resistance might not only be determined

by the material of the substrate electrode, but could also be strongly influenced by the conductivity of the oxide catalyst and its contact with the substrate electrode.

6.3 Summary

We observed very different catalytic and redox properties for all studied catalysts when compared at pH 7 and pH 14. All studied catalysts experience and increase of around 100 times in the TOF with the pH. The increase seems to be at the same time related to a shifting in the redox waves to lower potentials and also to a phase change towards shorter metal-oxygen and metal-metal bond distances.

In the specific case of the NiFe catalyst, we observed clearly that the increase in the catalytic activity is also related to a similar shifting in the redox waves to lower potentials. The absorption measurements together with EXAFS show that the redox changes are associated to a phase transition and this phase transition is more favourable at pH 14 than a pH 7.

The absorption and *in-situ* XAS measurements also show that the redox waves in the NiFe catalyst CV are mostly due to oxidation state changes in the nickel. At the iron edge we did not observe oxidation state changes higher than 8 % of Fe atoms changing oxidation state by one unit. However, the structure around the Fe atoms seems to be affected by the structural and oxidation state changes occurring in the nickel. These changes are observed in the XANES at the Fe edge as changes in the shape at the top of the edge. The strong interaction between nickel and iron might be related to the formation of short Fe-O distances at 1.92 Å and Fe-Ni distances at 2.85 Å induced by the nickel phase change as it was suggested by Bell before (Friebel, Louie et al. 2015). The in-situ XAS data also suggests that the structural changes in the Ni and Fe phases are reversible and follow very similar kinetics (perhaps the structural changes at the Fe edge are slightly shifted around 5 mV to higher potentials).

The *in-situ* time resolved absorption measurements suggest similar kinetics for the NiFe catalyst at pH 7 and pH 14. Again a strong correlation between the current and absorption changes is observed, suggesting that most absorption changes are related to oxidation state changes in the nickel. Under open circuit conditions, the system seems to be mostly controlled by the Ohmic resistance of the electrochemical cell. This is also supported by the CV measurements at different scan rates, which show that the position of the redox waves and the slope of the catalytic current in the measurements using FTO as substrate electrode are mainly determined by the Ohmic resistance of the electrochemical cell. We were able to decrease the Ohmic resistance of the electrochemical cell about 6 times just by changing the substrate electrode for a platinum one. This shows that when

1 M KOH is used as supporting electrolyte, the Ohmic resistance in the samples deposited on FTO is not determined by the electrolyte but by the material of the substrate electrode. This argues against the system limited by diffusion of protons or hydroxide species in the time resolved absorption measurements on FTO, and suggests a system controlled purely by the Ohmic resistance of the electrode. This Ohmic resistance in the electrode might have a strong contribution not only from the material of the substrate electrode, but also a component related to the interface conctact with the oxide catalyst and the conduction of charge through the oxide material itself.

Key results

Three different types of catalysts have been investigated: (1) an amorphous birnessite-type of manganese-calcium oxides, (2) a crystalline cobalt phosphate ($Co_3(PO_4)_2.8H_2O$), and (3) cathodically electrodeposited Mn, Fe, Co, Ni and NiFe oxides. The combination of different electrochemical techniques with UV-visible spectroscopy and X-ray absorption spectroscopy facilitated the establishment of the following structure-function relationships:

(1) Manganese-calcium oxides

It is possible to introduce a redox-inert cation (Ca^{+2}) into the structure of an amorphous manganese oxide by controlled anodic deposition at constant potential. However, there is a maximum amount of calcium that can be incorporated (around 0.5 Ca/Mn molar ratio).

All the prepared Mn-Ca films after deposition initially exhibit very low catalytic activity towards water oxidation (inactive oxides). However, they can become activated after annealing for 3 h at temperatures between 150 to 450 °C (in air).

Films with very high calcium content (like 0.5 Ca/Mn molar ratio) do not become active even after annealing. On the other hand, films without calcium can also present high catalytic activity after heating. This shows that in the case of inorganic manganese oxides, calcium is not essential for having catalytic activity for water oxidation in as it is in the case of the biological catalyst (where only strontium can substitute for calcium).

The Tafel slope decreases as calcium is incorporated, suggesting that it affects the mechanisms of water oxidation. This could be seen as an unfavorable effect; however, at low calcium contents the exchange current density increases resulting in an optimal catalytic activity at around 0.1 Ca/Mn molar ratio.

The structural analysis by XAS shows that the annealing procedure results in a decrease in the long-range order (formation of active sites) and reduction from Mn^{IV} to Mn^{III}. Upon electrochemical operation, the higher oxidation state is recovered, but the structure remains amorphous.

The XAS analysis also suggests that the calcium ions are not deposited in the form of calcium hydroxide, but it is rather incorporated in the layers forming a Mn_3CaO_4 cubane type of structure in close analogy to the Mn_4Ca complex of PSII.

UV-visible measurements indicate that low-activity catalysts reach high oxidation states (all Mn^{IV} level) at relatively low potentials. In contrast, active catalysts are characterized by the ability to undergo oxidation state changes also in the catalytic regime, facilitated by the stabilization of a small fraction of Mn^{III}.

Electrochemical UV-visible spectroscopy under steady-state conditions as well as during CV measurements, show that incorporation of calcium in the oxide films shifts the Mn^{III} to Mn^{IV} transitions to higher potentials, helping in that way to stabilize Mn^{III} species in the potential range of interest.

In a pre-synthesized birnessite type of oxide ($K_{0.20}Ca_{0.21}Mn_{2.21}\bullet 1.4H_2O$) screen-printed onto an FTO electrode, annealing to 450 °C also leads to decrease in the long-range order and increased formation of active sites.

(2) Crystalline cobalt phosphate $Co_3(PO_4)_2$ (Pakhomovskyite)

After long term operation at pH 7 (over 8h), the $Co_3(PO_4)_2$ shows complete transformation into an amorphous cobalt oxide.

For early stages of the electrochemical operation, electrochemical data supports high TOF values at the surface of the crystallites. This implies the possibility of having catalysts with higher activity than amorphous, electrodeposited (oxy)hydroxides and also the possibility of different reaction mechanisms depending on the nature of the catalyst.

Once the material becomes amorphous, bulk catalysis in the whole volume of the amorphous cobalt oxide prevails. The TOF of the amorphous cobalt oxide is lower compared to the crystalline material. However, the overall catalytic activity rises due to an increase in the redox active sites by amorphisation.

Wheter water oxidation in crystalline materials is always associated to amorphisation or restructuring of the surface of the crystal, still remains an open question. However, our study suggests that a good understanding of catalysis in crystalline materials should always include a good description of the amorphisation dynamics.

(3) Cathodically electrodeposited oxides

XAS analysis suggests that cathodic deposition of transition metal catalysts leads to formation of (oxy)hydroxide phases. Typically a hydroxide phase prevails after deposition. Operation at

catalytic potentials leads to formation of more "oxide-like" phases with higher oxidation states and shortening of metal-oxygen and metal-metal distances.

Even though in general the catalysts show structural similarities with anodically deposited catalysts, there also some differences. For example, there is more longer range order in the cathodic deposited cobalt catalyst in comparison to the CoCat (anodically electrodeposited), and formation of Co-Co distances at 3.45 Å not observed in most anodically deposited oxides. In the case of Ni, Fe and Mn containing catalysts, a metallic phase is detectable in the material.

All cathodically electrodeposited Mn, Fe, Co, Ni and NiFe catalysts exhibit a similar increase in TOF of about 100 times when the pH is increased from 7 to 14 (at an overpotential of 400 mV). The increase in the catalytic activity is accompanied by a shift of the redox waves to less positive potentials. The down shift in the redox wave likely explains the downshift of the catalytic wave, that is, lower overpotentials for catalysis. Data of electrochemical UV-visible spectroscopy and *in-situ* XAS of the NiFe catalyst confirm a similar shift to lower potentials of both redox and catalytic waves with increasing pH.

The *in-situ* XAS measurements in the NiFe catalyst, confirm that the redox transitions are related only to nickel oxidation state changes with formation of shorter Ni-O and Ni-Ni bond lengths. The oxidation state changes are associated to a phase change (from α-$Ni(OH)_2$ to γ –NiOOH) which is favoured at pH 14. No redox changes are observed at the Fe edge; however, the structural changes at the Ni edge induce also structural changes at the Fe edge forming also shorter Fe-metal bond distances at 2.85 Å.

The shape of the top of the iron K-edge changes under application of a catalytic potential. These changes in the shape of the iron K-edge are related to the oxidation state and structural changes observed in the nickel K-edge. Tracking of both process by *in-situ* time resolved XAS measurements suggests that both structural transformations follow similar dynamics.

References

Armand, M. B. (1980). Intercalation Electrodes. Materials for Advanced Batteries. D. W. Murphy, J. Broadhead and B. C. H. Steele. Boston, MA, Springer US**:** 145-161.

Bajdich, M., M. García-Mota, A. Vojvodic, J. K. Nørskov and A. T. Bell (2013). "Theoretical Investigation of the Activity of Cobalt Oxides for the Electrochemical Oxidation of Water." *J. Am. Chem. Soc.* **135**: 13521-13530.

Baktash, E., I. Zaharieva, M. Schroder, C. Goebel, H. Dau and A. Thomas (2013). "Cyanamide Route to Calcium Manganese Oxide Foams for Water Oxidation." *Dalton Trans.*: 16920–16929.

Balasubramanian, M., C. A. Melendres and S. Mini (2000). "X-ray absorption spectroscopy studies of the local atomic and electronic structure of iron incorporated into electrodeposited hydrous nickel oxide films." *J. Phys. Chem. B* **104**: 4300-4306.

Barber, J. (2009). "Photosynthetic energy conversion: natural and artificial." *Chem. Soc. Rev.* **38**: 185-196.

Barnard, R., C. F. Randell and F. L. Tye (1980). "Studies concerning charged nickel hydroxide electrodes. II. Thermodynamic considerations of the reversible potentials." *J. Appl. Electrochem.* **10**: 127-141.

Barra, M., M. Haumann, P. Loja, R. Krivanek, A. Grundmeier and H. Dau (2006). "Intermediates in assembly by photoactivation after thermally accelerated disassembly of the manganese complex of photosynthetic water oxidation." *Biochemistry* **45**: 14523-14532.

Bediako, D. K., B. Lassalle-Kaiser, Y. Surendranath, J. Yano, V. K. Yachandra and D. G. Nocera (2012). "Structure-activity correlations in a nickel-borate oxygen evolution catalyst." *J. Am. Chem. Soc.* **134**: 6801-6809.

Bergmann, A., E. Martinez-Moreno, D. Teschner, P. Chernev, M. Gliech, J. F. de Araujo, T. Reier, H. Dau and P. Strasser (2015). "Reversible amorphization and the catalytically active state of crystalline Co3O4 during oxygen evolution." *Nat Commun* **6**: 8625.

Bergmann, A., I. Zaharieva, H. Dau and P. Strasser (2013). "Electrochemical water splitting by layered and 3D cross-linked manganese oxides: correlating structural motifs and catalytic activity." *Energy Environ. Sci.* **6**: 2745-2755.

Burke, M. S., M. G. Kast, L. Trotochaud, A. M. Smith and S. W. Boettcher (2015). "Cobalt–Iron (Oxy)hydroxide Oxygen Evolution Electrocatalysts: The Role of Structure and Composition on Activity, Stability, and Mechanism." *J. Am. Chem. Soc.* **137**: 3638-3648.

Burke, M. S., S. Zou, L. J. Enman, J. E. Kellon, C. A. Gabor, E. Pledger and S. W. Boettcher (2015). "Revised oxygen evolution reaction activity trends for first-row transition-metal (oxy)hydroxides in alkaline media." *J. Phys. Chem. Lett.* **6**: 3737-3742.

Calle-Vallejo, F., N. G. Inoglu, H.-Y. Su, J. I. Martinez, I. C. Man, M. T. M. Koper, J. R. Kitchin and J. Rossmeisl (2013). "Number of outer electrons as descriptor for adsorption processes on transition metals and their oxides." *Chem. Sci.* **4**: 1245-1249.

Calvin, S. (2013). XAFS for Everyone. Boca Raton, CRC Press Taylor and Francis Group.

Chen, J. Y. C., L. Dang, H. Liang, W. Bi, J. B. Gerken, S. Jin, E. E. Alp and S. S. Stahl (2015). "Operando Analysis of NiFe and Fe Oxyhydroxide Electrocatalysts for Water Oxidation: Detection of Fe4+ by Mössbauer Spectroscopy." *J. Am. Chem. Soc.* **137**: 15090-15093.

Ching, S., J. A. Landrigan and M. L. Jorgensen (1995). "Sol-gel synthesis of birnessite from KMnO4 and simple sugars." *Chem. Mater.* **7**: 1604-1606.

Cobo, S., J. Heidkamp, P.-A. Jacques, J. Fize, V. Fourmond, L. Guetaz, B. Jousselme, V. Ivanova, H. Dau, S. Palacin, M. Fontecave and V. Artero (2012). "A Janus cobalt-based catalytic material for electro-splitting of water." *Nature Materials* **11**: 802-807.

Coehn, A. and M. Gläser (1902). "Studien über die Bildung von Metalloxyden I. Über das anodische Verhalten von Kobalt- und Nickel-Lösungen." *Zeitschrift für anorganische Chemie* **33**: 9-24.

Concepcion, J. J., J. W. Jurss, M. K. Brennaman, P. G. Hoertz, A. O. T. Patrocinio, N. Y. M. Iha, J. L. Templeton and T. J. Meyer (2009). "Making Oxygen with Ruthenium Complexes." *Acc. Chem. Res.* **42**: 1954-1965.

Corrigan, D. A. (1987). "The catalysis of the oxygen evolution reaction by iron impurities in thin film nickel oxide electrodes." *J. Electrochem. Soc.* **134**: 377-384.

Dau, H., A. Grundmeier, P. Loja and M. Haumann (2008). "On the structure of the manganese complex of photosystem II: extended-range EXAFS data and specific atomic-resolution models for four S-states." *Philos. Trans. R. Soc., B* **363**: 1237-1244.

Dau, H., P. Liebisch and M. Haumann (2003). "X-ray absorption spectroscopy to analyze nuclear geometry and electronic structure of biological metal centers—potential and questions examined

with special focus on the tetra-nuclear manganese complex of oxygenic photosynthesis." *Anal. Bioanal. Chem.* **376**: 562-583.

Dau, H., C. Limberg, T. Reier, M. Risch, S. Roggan and P. Strasser (2010). "The mechanism of water oxidation: from electrolysis via homogeneous to biological catalysis." *ChemCatChem* **2**: 724-761.

Dau, H. and I. Zaharieva (2009). "Principles, efficiency, and blueprint character of solar-energy conversion in photosynthetic water oxidation." *Acc. Chem. Res.* **42**: 1861-1870.

Debus, R. J. (1992). "The manganese and calcium ions of photosynthetic oxygen evolution." *Biochim. Biophys. Acta* **1102**: 269-352.

Delmas, C., C. Fouassier and P. Hagenmuller (1980). "Structural classification and properties of the layered oxides." *Physica B+C* **99**: 81-85.

Devaraj, S. and N. Munichandraiah (2008). "Effect of Crystallographic Structure of MnO2 on Its Electrochemical Capacitance Properties." *J. Phys. Chem. C* **112**: 4406-4417.

Dunn, S. (2002). "Hydrogen Futures: Towards a sustainable energy system." *Int. J. Hydrogen Energy* **27**: 235-264.

Esswein, A. J., Y. Surendranath, S. Y. Reece and D. G. Nocera (2011). "Highly active cobalt phosphate and borate based oxygen evolving catalysts operating in neutral and natural waters." *Energy Environ. Sci.* **4**: 499-504.

Faunce, T. A., W. Lubitz, A. W. Rutherford, D. MacFarlane, G. F. Moore, P. Yang, D. G. Nocera, T. A. Moore, D. H. Gregory, S. Fukuzumi, K. B. Yoon, F. A. Armstrong, M. R. Wasielewski and S. Styring (2013). "Energy and environment policy case for a global project on artificial photosynthesis." *Energy Environ. Sci.* **6**: 695-698.

Ferreira, K. N., T. M. Iverson, K. Maghlaoui, J. Barber and S. Iwata (2004). "Architecture of the photosynthetic oxygen-evolving center." *Science* **303**: 1831-1838.

Frey, C. E., M. Wiechen and P. Kurz (2014). "Water-oxidation catalysis by synthetic manganese oxides - systematic variations of the calcium birnessite theme." *Dalton Trans.* **43**: 4370-4379.

Friebel, D., M. W. Louie, M. Bajdich, K. E. Sanwald, Y. Cai, A. M. Wise, M.-J. Cheng, D. Sokaras, T.-C. Weng, R. Alonso-Mori, R. C. Davis, J. R. Bargar, J. K. Nørskov, A. Nilsson and A. T. Bell (2015). "Identification of highly active Fe sites in (Ni,Fe)OOH for electrocatalytic water splitting." *J. Am. Chem. Soc.* **137**: 1305-1313.

Frost, R. L., M. L. Weier, W. Martens, J. T. Kloprogge and Z. Ding (2003). "Dehydration of synthetic and natural vivianite." *Thermochim. Acta* **401**: 121-130.

Frost, R. L., M. L. Weier, W. Martens, J. Theo Kloprogge and Z. Ding (2003). "Thermal decomposition of the vivianite arsenates—implications for soil remediation." *Thermochim. Acta* **403**: 237-249.

Gao, Y. Q., H. B. Li and G. W. Yang (2016). "Amorphous Co(OH)2 nanosheet electrocatalyst and the physical mechanism for its high activity and long-term cycle stability." *J. Appl. Phys.* **119**: 034902.

Gardner, G. P., Y. B. Go, D. M. Robinson, P. F. Smith, J. Hadermann, A. Abakumov, M. Greenblatt and G. C. Dismukes (2012). "Structural Requirements in Lithium Cobalt Oxides for the Catalytic Oxidation of Water." *Angew. Chem.* **124**: 1648-1651.

Gerken, J. B., E. C. Landis, R. J. Hamers and S. S. Stahl (2010). "Fluoride-modulated cobalt catalysts for electrochemical oxidation of water under non-alkaline conditions." *ChemSusChem* **3**: 1176-1179.

Gerken, J. B., J. G. McAlpin, J. Y. C. Chen, M. L. Rigsby, W. H. Casey, R. D. Britt and S. S. Stahl (2011). "Electrochemical water oxidation with cobalt-based electrocatalysts from pH 0–14: The thermodynamic basis for catalyst structure, stability, and activity." *J. Am. Chem. Soc.* **133**: 14431-14442.

Giordano, L., B. Han, M. Risch, W. T. Hong, R. R. Rao, K. A. Stoerzinger and Y. Shao-Horn (2016). "pH dependence of OER activity of oxides: Current and future perspectives." *Catal. Today* **262**: 2-10.

Glemser, O. and J. Einerhand (1950). "*Die Chemischen Vorgange an Der Nickelhydroxydanode Des Edisonakkumulators." *Zeitschrift Fur Elektrochemie* **54**: 302-304.

Goerlin, M., P. Chernev, J. Ferreira de Araújo, T. Reier, S. Dresp, B. Paul, R. Kraehnert, H. Dau and P. Strasser (2016). "Oxygen evolution reaction dynamics, faradaic charge efficiency, and the active metal redox states of Ni-Fe oxide water splitting electrocatalysts." *J. Am. Chem. Soc.*

Gong, M. and H. Dai (2014). "A mini review of NiFe-based materials as highly active oxygen evolution reaction electrocatalysts." *Nano Research* **8**: 23-39.

Gong, M., Y. Li, H. Wang, Y. Liang, J. Z. Wu, J. Zhou, J. Wang, T. Regier, F. Wei and H. Dai (2013). "An Advanced Ni–Fe Layered Double Hydroxide Electrocatalyst for Water Oxidation." *J. Am. Chem. Soc.* **135**: 8452-8455.

Görlin, M., M. Gliech, J. F. de Araújo, S. Dresp, A. Bergmann and P. Strasser (2016). "Dynamical changes of a Ni-Fe oxide water splitting catalyst investigated at different pH." *Catal. Today* **262**: 65-73.

Gorlin, Y. and T. F. Jaramillo (2010). "A bifunctional nonprecious metal catalyst for oxygen reduction and water oxidation." *J. Am. Chem. Soc.* **132**: 13612-13614.

Gorlin, Y., B. Lassalle-Kaiser, J. D. Benck, S. Gul, S. M. Webb, V. K. Yachandra, J. Yano and T. F. Jaramillo (2013). "In Situ X-ray Absorption Spectroscopy Investigation of a Bifunctional Manganese Oxide Catalyst with High Activity for Electrochemical Water Oxidation and Oxygen Reduction." *J. Am. Chem. Soc.* **135**: 8525-8534.

H.-W. Tseng, R. Z., J. T. Muckerman, R. Thummel (2008). "Mononuclear Ruthenium(II) Complexes That Catalyze Water Oxidation." *Inorg. Chem.* **47**: 11763 - 11773.

Harriman, A., I. J. Pickering, J. M. Thomas and P. A. Christensen (1988). "Metal-oxides as heterogeneous catalysts for oxygen evolution under photochemical conditions." *J. Chem. Soc.-Farad. T 1* **84**: 2795-2806.

Haumann, M., C. Müller, P. Liebisch, L. Iuzzolino, J. Dittmer, M. Grabolle, T. Neisius, W. Meyer-Klaucke and H. Dau (2005). "Structural and oxidation state changes of the photosystem II manganese complex in four transitions of the water oxidation cycle ($S_0 \rightarrow S_1$, $S_1 \rightarrow S_2$, $S_2 \rightarrow S_3$, and $S_{3,4} \rightarrow S_0$) characterized by X-ray absorption spectroscopy at 20 K and room temperature." *Biochemistry* **44**: 1894-1908.

Hickling, A. and S. Hill (1947). "Oxygen overvoltage. Part I. The influence of electrode material, current density, and time in aqueous solution." *Discussions of the Faraday Society* **1**: 236-246.

Hocking, R. K., R. Brimblecombe, L.-Y. Chang, A. Singh, M. H. Cheah, C. Glover, W. H. Casey and L. Spiccia (2011). "Water-oxidation catalysis by manganese in a geochemical-like cycle." *Nat. Chem.* **3**: 461-466.

Hoffert, M. I., K. Caldeira, A. K. Jain, E. F. Haites, L. D. D. Harvey, S. D. Potter, M. E. Schlesinger, S. H. Schneider, R. G. Watts, T. M. L. Wigley and D. J. Wuebbles (1998). "Energy implications of future stabilization of atmospheric CO_2 content." *Nature* **395**: 881-884.

Hong, W. T., M. Risch, K. A. Stoerzinger, A. Grimaud, J. Suntivich and Y. Shao-Horn (2015). "Toward the rational design of non-precious transition metal oxides for oxygen electrocatalysis." *Energy Environ. Sci.* **8**: 1404-1427.

Hunter, B. M., W. Hieringer, J. Winkler, H. B. Gray and A. M. Muller (2016). "Effect of Interlayer Anions on [NiFe]-LDH Nanosheet Water Oxidation Activity." *Energy Environ. Sci.*

Huynh, M., D. K. Bediako and D. G. Nocera (2014). "A Functionally Stable Manganese Oxide Oxygen Evolution Catalyst in Acid." *J. Am. Chem. Soc.* **136**: 6002-6010.

Indra, A., P. W. Menezes, F. Schuster and M. Driess (2015). "Significant role of Mn(III) sites in eg1 configuration in manganese oxide catalysts for efficient artificial water oxidation." *J. Photochem. Photobiol., B*: doi:10.1016/j.jphotobiol.2014.1011.1012.

Indra, A., P. W. Menezes, I. Zaharieva, E. Baktash, J. Pfrommer, M. Schwarze, H. Dau and M. Driess (2013). "Active mixed-valent MnOx water oxidation catalysts through partial oxidation (corrosion) of nanostructured MnO particles." *Angew. Chem. Int. Ed.* **52**: 13206–13210.

Julien, C. M. (2003). "Lithium intercalated compounds - Charge transfer and related properties." *Mat. Sci. Eng. R* **40**: 47-102.

Kanan, M. W. and D. G. Nocera (2008). "In situ formation of an oxygen-evolving catalyst in neutral water containing phosphate and Co^{2+}." *Science* **321**: 1072-1075.

Kanan, M. W., J. Yano, Y. Surendranath, M. Dinca, V. K. Yachandra and D. G. Nocera (2010). "Structure and valency of a cobalt-phosphate water oxidation catalyst determined by in situ X-ray spectroscopy." *J. Am. Chem. Soc.* **132**: 13692-13701.

Khatib, H., A. Barnes, I. Chalabi, H. Steeg, K. Yokobori and O. o. A. O. P. C. the Planning Department (2000). Energy Security. World Energy Assessment Report: Energy and the Challenge of Sustainability. W. Communications Development Incorporated, D.C. United Nations, New York, United Nations Development Programme, Bureau for Development Policy.

Klaus, S., Y. Cai, M. W. Louie, L. Trotochaud and A. T. Bell (2015). "Effects of Fe electrolyte impurities on Ni(OH)2/NiOOH structure and oxygen evolution activity." *J. Phys. Chem. C* **119**: 7243-7254.

Klingan, K., F. Ringleb, I. Zaharieva, J. Heidkamp, P. Chernev, D. Gonzalez-Flores, M. Risch, A. Fischer and H. Dau (2014). "Water Oxidation by Amorphous Cobalt-Based Oxides: Volume Activity and Proton Transfer to Electrolyte Bases." *ChemSusChem*: 1301-1310.

Kok, B., B. Forbush and M. McGloin (1970). "Cooperation of charges in photosynthetic O_2 evolution - I. A linear four-step mechanism." *Photochem. Photobiol.* **11**: 457-475.

Landon, J., E. Demeter, N. İnoğlu, C. Keturakis, I. E. Wachs, R. Vasić, A. I. Frenkel and J. R. Kitchin (2012). "Spectroscopic Characterization of Mixed Fe–Ni Oxide Electrocatalysts for the Oxygen Evolution Reaction in Alkaline Electrolytes." *ACS Catalysis* **2**: 1793-1801.

Lee, S. W., C. Carlton, M. Risch, Y. Surendranath, S. Chen, S. Furutsuki, A. Yamada, D. G. Nocera and Y. Shao-Horn (2012). "The Nature of Lithium Battery Materials under Oxygen Evolution Reaction Conditions." *J. Am. Chem. Soc.* **134**: 16959-16962.

Lee, S. Y., D. Gonzalez-Flores, J. Ohms, T. Trost, H. Dau, I. Zaharieva and P. Kurz (2014). "Screen-Printed Calcium-Birnessite Electrodes for Water Oxidation at Neutral pH and an "Electrochemical Harriman Series"." *ChemSusChem* **7**: 3442-3451.

Lewis, N. S. and D. G. Nocera (2006). "Powering the planet: chemical challenges in solar energy utilization." *Proc. Natl. Acad. Sci. USA* **103**: 15729-15735.

Li, F., L. Bai, H. Li, Y. Wang, F. Yu and L. Sun (2016). "An iron-based thin film as a highly efficient catalyst for electrochemical water oxidation in a carbonate electrolyte." *Chem. Commun.*

Li, X., J. Liu, Y. Zhao, H. Zhang, F. Du, C. Lin, T. Zhao and Y. Sun (2015). "Significance of Surface Trivalent Manganese in the Electrocatalytic Activity of Water Oxidation in Undoped and Doped MnO2 Nanowires." *ChemCatChem* **7**: 1848-1856.

Limburg, J., V. A. Szalai and G. W. Brudvig (1999). "A mechanistic and structural model for the formation and reactivity of a Mn^{V}=O species in photosynthetic water oxidation." *Dalton Trans.* **1999**: 1353–1361.

Louie, M. W. and A. T. Bell (2013). "An investigation of thin-film Ni–Fe oxide catalysts for the electrochemical evolution of oxygen." *J. Am. Chem. Soc.* **135**: 12329-12337.

Lu, P. W. T. and S. Srinivasan (1978). "Electrochemical-ellipsometric studies of oxide film formed on nickel during oxygen evolution." *J. Electrochem. Soc.* **125**: 1416-1422.

Luo, J., J.-H. Im, M. T. Mayer, M. Schreier, M. K. Nazeeruddin, N.-G. Park, S. D. Tilley, H. J. Fan and M. Grätzel (2014). "Water photolysis at 12.3% efficiency via perovskite photovoltaics and Earth-abundant catalysts." *Science* **345**: 1593-1596.

Luo, J., Q. Zhang, A. Huang, O. Giraldo and S. L. Suib (1999). "Double-Aging Method for Preparation of Stabilized Na−Buserite and Transformations to Todorokites Incorporated with Various Metals." *Inorg. Chem.* **38**: 6106-6113.

Lutterman, D. A., Y. Surendranath and D. G. Nocera (2009). "A self-healing oxygen-evolving catalyst." *J. Am. Chem. Soc.* **131**: 3838-3839.

Lyons, M. E. G. and M. P. Brandon (2010). "A comparative study of the oxygen evolution reaction on oxidised nickel, cobalt and iron electrodes in base." *J. Electroanal. Chem.* **641**: 119-130.

Mahdi Najafpour, M., D. Jafarian Sedigh, S. Maedeh Hosseini and I. Zaharieva (2016). "Treated Nanolayered Mn Oxide by Oxidizable Compounds: A Strategy To Improve the Catalytic Activity toward Water Oxidation." *Inorg. Chem.* **55**: 8827-8832.

Man, I. C., H.-Y. Su, F. Calle-Vallejo, H. A. Hansen, J. I. Martínez, N. G. Inoglu, J. Kitchin, T. F. Jaramillo, J. K. Nørskov and J. Rossmeisl (2011). "Universality in oxygen evolution electrocatalysis on oxide surfaces." *ChemCatChem* **3**: 1159-1165.

Martin-Diaconescu, V., M. Gennari, B. Gerey, E. Tsui, J. Kanady, R. Tran, J. Pécaut, D. Maganas, V. Krewald, E. Gouré, C. Duboc, J. Yano, T. Agapie, M.-N. Collomb and S. DeBeer (2015). "Ca K-Edge XAS as a Probe of Calcium Centers in Complex Systems." *Inorg. Chem.* **54**: 1283-1292.

Mattioli, G., I. Zaharieva, H. Dau and L. Guidoni (2015). "Atomistic Texture of Amorphous Manganese Oxides for Electrochemical Water Splitting Revealed by Ab Initio Calculations Combined with X-ray Spectroscopy." *J. Am. Chem. Soc.* **137**: 10254-10267.

May, K. J., C. E. Carlton, K. A. Stoerzinger, M. Risch, J. Suntivich, Y.-L. Lee, A. Grimaud and Y. Shao-Horn (2012). "Influence of Oxygen Evolution during Water Oxidation on the Surface of Perovskite Oxide Catalysts." *J. Phys. Chem. Lett.* **3**: 3264-3270.

McCrory, C. C. L., S. Jung, J. C. Peters and T. F. Jaramillo (2013). "Benchmarking Heterogeneous Electrocatalysts for the Oxygen Evolution Reaction." *J. Am. Chem. Soc.* **135**: 16977-16987.

McKendry, I. G., S. K. Kondaveeti, S. L. Shumlas, D. R. Strongin and M. J. Zdilla (2015). "Decoration of the layered manganese oxide birnessite with Mn(ii/iii) gives a new water oxidation catalyst with fifty-fold turnover number enhancement." *Dalton Trans.* **44**: 12981-12984.

Menezes, P. W., A. Indra, P. Littlewood, M. Schwarze, C. Göbel, R. Schomäcker and M. Driess (2014). "Nanostructured Manganese Oxides as Highly Active Water Oxidation Catalysts: A Boost from Manganese Precursor Chemistry." *ChemSusChem* **7**: 2202-2211.

Merrill, M., M. Worsley, A. Wittstock, J. Biener and M. Stadermann (2014). "Determination of the "NiOOH" charge and discharge mechanisms at ideal activity." *J. Electroanal. Chem.* **717–718**: 177-188.

Merrill, M. D. and R. C. Dougherty (2008). "Metal oxide catalysts for the evolution of O-2 from H2O." *J. Phys. Chem. C* **112**: 3655-3666.

Młynarek, G., M. Paszkiewicz and A. Radniecka (1984). "The effect of ferric ions on the behaviour of a nickelous hydroxide electrode." *J. Appl. Electrochem.* **14**: 145-149.

Morales-Guio, C. G., L. Liardet and X. Hu (2016). "Oxidatively Electrodeposited Thin-Film Transition Metal (Oxy)hydroxides as Oxygen Evolution Catalysts." *J. Am. Chem. Soc.* **138**: 8946-8957.

Najafpour, M. M., T. Ehrenberg, M. Wiechen and P. Kurz (2010). "Calcium manganese(III) oxides ($CaMn_2O_4.xH_2O$) as biomimetic oxygen-evolving catalysts." *Angew. Chem. Int. Ed.* **49**: 2233-2237.

Najafpour, M. M., A. N. Moghaddam, H. Dau and I. Zaharieva (2014). "Fragments of Layered Manganese Oxide Are the Real Water Oxidation Catalyst after Transformation of Molecular Precursor on Clay." *J. Am. Chem. Soc.* **136**: 7245-7248.

Nakahira, A., T. Kubo and H. Murase (2007). "Synthesis of LDH-Type Clay Substituted With Fe and Ni Ion for Arsenic Removal and Its Application to Magnetic Separation." *IEEE Transactions on Magnetics* **43**: 2442-2444.

Newville, M. (2014). "Fundamentals of XAFS." *Reviews in Mineralogy and Geochemistry* **78**: 33-74.

Nocera, D. G. (2009). "Chemistry of personalized solar energy." *Inorg. Chem.* **48**: 10001-10017.

Pandya, K. I., W. E. O'Grady, D. A. Corrigan, J. McBreen and R. W. Hoffman (1990). "Extended x-ray absorption fine structure investigations of nickel hydroxides." *J. Phys. Chem.* **94**: 21-26.

Park, J., H. Kim, K. Jin, B. J. Lee, Y.-S. Park, H. Kim, I. Park, K. D. Yang, H.-Y. Jeong, J. Kim, K. T. Hong, H. W. Jang, K. Kang and K. T. Nam (2014). "A New Water Oxidation Catalyst: Lithium Manganese Pyrophosphate with Tunable Mn Valency." *J. Am. Chem. Soc.* **136**: 4201-4211.

Pecoraro, V. L., M. J. Baldwin, M. T. Caudle, W. Y. Hsieh and N. A. Law (1998). "A proposal for water oxidation in photosystem II." *Pure Appl. Chem.* **70**: 925-929.

Petit, J. R., J. Jouzel, D. Raynaud, N. I. Barkov, J. M. Barnola, I. Basile, M. Bender, J. Chappellaz, M. Davis, G. Delaygue, M. Delmotte, V. M. Kotlyakov, M. Legrand, V. Y. Lipenkov, C. Lorius, L. Pepin, C. Ritz, E. Saltzman and M. Stievenard (1999). "Climate and atmospheric history of the past 420,000 years from the Vostok ice core, Antarctica." *Nature* **399**: 429-436.

Pinaud, B. A., J. D. Benck, L. C. Seitz, A. J. Forman, Z. Chen, T. G. Deutsch, B. D. James, K. N. Baum, G. N. Baum, S. Ardo, H. Wang, E. Miller and T. F. Jaramillo (2013). "Technical and economic feasibility of centralized facilities for solar hydrogen production via photocatalysis and photoelectrochemistry." *Energy Environ. Sci.* **6**: 1983-2002.

Post, J. E. and D. R. Veblen (1990). "Crystal structure determinations of synthetic sodium, magnesium, and potassium birnessite using TEM and the Rietveld method." *Am. Mineral.* **75**: 477-489.

Press, W. H., S. A. Teukolsky, W. T. Vetterling and B. P. Flannery (1992). Numerical Recipes in C: The Art of Scientific Computing, Second Edition. Cambridge-New York-Port Chester-Melbourne-Sydney, Cambridge University Press.

Ramírez, A., P. Hillebrand, D. Stellmach, M. M. May, P. Bogdanoff and S. Fiechter (2014). "Evaluation of MnOx, Mn2O3, and Mn3O4 Electrodeposited Films for the Oxygen Evolution Reaction of Water." *J. Phys. Chem. C* **118**: 14073-14081.

Rehr, J. J. and R. C. Albers (2000). "Theoretical approaches to x-ray absorption fine structure." *Rev. Mod. Phys.* **72**: 621-654.

Riou, A., Y. Cudennec and Y. Gerault (1989). "Cobalt(II) orthophosphate octahydrate." *Acta Crystallographica Section C* **45**: 1412-1413.

Risch, M., V. Khare, I. Zaharieva, L. Gerencser, P. Chernev and H. Dau (2009). "Cobalt-oxo core of a water-oxidizing catalyst film." *J. Am. Chem. Soc.* **131**: 6936-6937.

Risch, M., K. Klingan, J. Heidkamp, D. Ehrenberg, P. Chernev, I. Zaharieva and H. Dau (2011). "Nickel-oxido structure of a water-oxidizing catalyst film." *Chem. Commun.* **47**: 11912-11914.

Risch, M., K. Klingan, F. Ringleb, P. Chernev, I. Zaharieva, A. Fischer and H. Dau (2012). "Water oxidation by electrodeposited cobalt oxides - role of anions and redox-inert cations in structure and function of the amorphous catalyst." *ChemSusChem* **5**: 542-549.

Risch, M., F. Ringleb, M. Kohlhoff, P. Bogdanoff, P. Chernev, I. Zaharieva and H. Dau (2015). "Water oxidation by amorphous cobalt-based oxides: in situ tracking of redox transitions and mode of catalysis." *Energy Environ. Sci.* **8**: 661-674.

Robinson, D. M., Y. B. Go, M. Mui, G. Gardner, Z. Zhang, D. Mastrogiovanni, E. Garfunkel, J. Li, M. Greenblatt and G. C. Dismukes (2013). "Photochemical Water Oxidation by Crystalline Polymorphs of Manganese Oxides: Structural Requirements for Catalysis." *J. Am. Chem. Soc.* **135**: 3494-3501.

Roger, I. and M. D. Symes (2016). "First row transition metal catalysts for solar-driven water oxidation produced by electrodeposition." *Journal of Materials Chemistry A*.

Rossmeisl, J., Z. W. Qu, H. Zhu, G. J. Kroes and J. K. Nørskov (2007). "Electrolysis of water on oxide surfaces." *J. Electroanal. Chem.* **607**: 83-89.

Rossouw, M. H., A. de Kock, D. C. Liles, R. J. Gummow and M. M. Thackeray (1992). "Synthesis of highly crystalline ramsdellite MnO2 and its lithiated derivative Li0.9MnO2." *J. Mater. Chem.* **2**: 1211-1211.

S. W. Gestern, G. J. Samuels and T. J. Meyer (1982). "Catalytic oxidation of water by an oxo-bridged ruthenium dimer." *J. Am. Chem. Soc.* **104**: 4029.

Shen, J. R. (2015). "The Structure of Photosystem II and the Mechanism of Water Oxidation in Photosynthesis." *Annu. Rev. Plant Biol.* **66**: 23-48.

Shevchenko, D., M. F. Anderlund, S. Styring, H. Dau, I. Zaharieva and A. Thapper (2014). "Water oxidation by manganese oxides formed from tetranuclear precursor complexes: the influence of phosphate on structure and activity." *Phys. Chem. Chem. Phys.* **16**: 11965-11975.

Siegenthaler, U., T. F. Stocker, E. Monnin, D. Lüthi, J. Schwander, B. Stauffer, D. Raynaud, J.-M. Barnola, H. Fischer, V. Masson-Delmotte and J. Jouzel (2005). "Stable Carbon Cycle-Climate Relationship During the Late Pleistocene." *Science* **310**: 1313-1317.

Smith, R. D. L. and C. P. Berlinguette (2016). "Accounting for the Dynamic Oxidative Behavior of Nickel Anodes." *J. Am. Chem. Soc.* **138**: 1561-1567.

Smith, R. D. L., M. S. Prévot, R. D. Fagan, S. Trudel and C. P. Berlinguette (2013). "Water Oxidation Catalysis: Electrocatalytic Response to Metal Stoichiometry in Amorphous Metal Oxide Films Containing Iron, Cobalt, and Nickel." *J. Am. Chem. Soc.* **135**: 11580-11586.

Song, F. and X. Hu (2014). "Exfoliation of layered double hydroxides for enhanced oxygen evolution catalysis." *Nat Commun* **5**.

Sowrey, F. E., L. J. Skipper, D. M. Pickup, K. O. Drake, Z. Lin, M. E. Smith and R. J. Newport (2004). "Systematic empirical analysis of calcium-oxygen coordination environment by calcium K-edge XANES." *Phys. Chem. Chem. Phys.* **6**: 188-192.

Spiro, T. G., J. R. Bargar, G. Sposito and B. M. Tebo (2009). "Bacteriogenic manganese oxides." *Acc. Chem. Res.* **43**: 2-9.

Suga, M., F. Akita, K. Hirata, G. Ueno, H. Murakami, Y. Nakajima, T. Shimizu, K. Yamashita, M. Yamamoto, H. Ago and J.-R. Shen (2015). "Native structure of photosystem II at 1.95 A resolution viewed by femtosecond X-ray pulses." *Nature* **517**: 99-103.

Suntivich, J., K. J. May, H. A. Gasteiger, J. B. Goodenough and Y. Shao-Horn (2011). "A Perovskite Oxide Optimized for Oxygen Evolution Catalysis from Molecular Orbital Principles." *Science* **334**: 1383-1385.

Surendranath, Y., D. A. Lutterman, Y. Liu and D. G. Nocera (2012). "Nucleation, growth, and repair of a cobalt-based oxygen evolving catalyst." *J. Am. Chem. Soc.* **134**: 6326-6336.

Swierk, J. R., S. Klaus, L. Trotochaud, A. T. Bell and T. D. Tilley (2015). "Electrochemical study of the energetics of the oxygen evolution reaction at nickel iron (oxy)hydroxide catalysts." *J. Phys. Chem. C* **119**: 19022-19029.

Takashima, T., K. Hashimoto and R. Nakamura (2011). "Mechanisms of pH-dependent activity for water oxidation to molecular oxygen by MnO_2 electrocatalysts." *J. Am. Chem. Soc.* **134**: 1519–1527.

Takashima, T., K. Hashimoto and R. Nakamura (2012). "Inhibition of charge disproportionation of MnO_2 electrocatalysts for efficient water oxidation under neutral conditions." *J. Am. Chem. Soc.* **134**: 18153-18156.

Toner, B., A. Manceau, S. M. Webb and G. Sposito (2006). "Zinc sorption to biogenic hexagonal-birnessite particles within a hydrated bacterial biofilm." *Geochim. Cosmochim. Acta* **70**: 27-43.

Trasatti, S. (1980). "Electrocatalysis by oxides -- Attempt at a unifying approach." *J. Electroanal. Chem.* **111**: 125-131.

Trasatti, S. (1984). "Electrocatalysis in the anodic Evolution of Oxygen and Chlorine." *Electrochim. Acta* **29**: 1503-1512.

Trotochaud, L. and S. W. Boettcher (2014). "Precise oxygen evolution catalysts: Status and opportunities." *Scripta Mater.* **74**: 25-32.

Trotochaud, L., J. K. Ranney, K. N. Williams and S. W. Boettcher (2012). "Solution-cast metal oxide thin film electrocatalysts for oxygen evolution." *J. Am. Chem. Soc.* **134**: 17253-17261.

Trotochaud, L., S. L. Young, J. K. Ranney and S. W. Boettcher (2014). "Nickel–Iron oxyhydroxide oxygen-evolution electrocatalysts: the role of intentional and incidental iron incorporation." *J. Am. Chem. Soc.* **136**: 6744-6753.

Trześniewski, B. J., O. Diaz-Morales, D. A. Vermaas, A. Longo, W. Bras, M. T. M. Koper and W. A. Smith (2015). "In Situ Observation of Active Oxygen Species in Fe-Containing Ni-Based Oxygen Evolution Catalysts: The Effect of pH on Electrochemical Activity." *J. Am. Chem. Soc.* **137**: 15112-15121.

Tsirlina, G. A., M. D. Levi, O. A. Petrii and D. Aurbach (2001). "Comparison of equilibrium electrochemical behavior of PdHx and LixMn2O4 intercalation electrodes in terms of sorption isotherms." *Electrochim. Acta* **46**: 4141-4149.

Tsui, E. Y. and T. Agapie (2013). "Reduction potentials of heterometallic manganese–oxido cubane complexes modulated by redox-inactive metals." *Proc. Natl. Acad. Sci. U.S.A.* **110**: 10084-10088.

Tsui, E. Y., R. Tran, J. Yano and T. Agapie (2013). "Redox-inactive metals modulate the reduction potential in heterometallic manganese–oxido clusters." *Nat. Chem.* **5**: 293-299.

Turner, J. A. (1999). "A Realizable Renewable Energy Future." *Science* **285**: 687-689.

Umena, Y., K. Kawakami, J.-R. Shen and N. Kamiya (2011). "Crystal structure of oxygen-evolving photosystem II at a resolution of 1.9 Å." *Nature* **473**: 55-60.

Vrettos, J. S., D. A. Stone and G. W. Brudvig (2001). "Quantifying the ion selectivity of the Ca^{2+} site in photosystem II: evidence for direct involvement of Ca^{2+} in O_2 formation." *Biochemistry* **40**: 7937-7945.

Wang, D., J. Zhou, Y. Hu, J. Yang, N. Han, Y. Li and T.-K. Sham (2015). "In Situ X-ray Absorption Near-Edge Structure Study of Advanced NiFe(OH)x Electrocatalyst on Carbon Paper for Water Oxidation." *J. Phys. Chem. C* **119**: 19573-19583.

Watson, I. P. o. C. C. b. o. a. d. p. b. R. T. (2001). Climate Change 2001: Synthesis Report, Summary for Policymakers Third Assessment Report. Washington, DC, Intergovernmental Panel on Climate Change.

Wiechen, M., I. Zaharieva, H. Dau and P. Kurz (2012). "Layered manganese oxides for water-oxidation: alkaline earth cations influence catalytic activity in a photosystem II-like fashion." *Chem. Sci.* **3**: 2330-2339.

Wu, Y., M. Chen, Y. Han, H. Luo, X. Su, M.-T. Zhang, X. Lin, J. Sun, L. Wang, L. Deng, W. Zhang and R. Cao (2015). "Fast and Simple Preparation of Iron-Based Thin Films as Highly Efficient Water-Oxidation Catalysts in Neutral Aqueous Solution." *Angew. Chem. Int. Ed.* **54**: 4870-4875.

Yachandra, V. K. and J. Yano (2011). "Calcium in the Oxygen-Evolving Complex: Structural and Mechanistic Role Determined by X-ray Spectroscopy." *Journal of photochemistry and photobiology. B, Biology* **104**: 51-59.

Yachandra, V. K. and J. Yano (2011). "Calcium in the Oxygen-Evolving Complex: Structural and Mechanistic Role Determined by X-ray Spectroscopy." *J. Photochem. Photobiol. B* **104**: 51-59.

Yakovenchuk, V. N., G. Y. Ivanyuk, Y. A. Mikhailova, E. A. Selivanova and S. V. Krivovichev (2006). "Pakhomovskyite, Co3(PO4)2·8H2O, a new mineral species from Kovdor, Kola Peninsula, Russia." *Can. Mineral.* **44**: 117-123.

Yeo, B. S. and A. T. Bell (2011). "Enhanced activity of gold-supported cobalt oxide for the electrochemical evolution of oxygen." *J. Am. Chem. Soc.* **133**: 5587-5593.

Yilanci, A., I. Dincer and H. K. Ozturk (2009). "A review on solar-hydrogen/fuel cell hybrid energy systems for stationary applications." *Prog. Energy Combust. Sci.* **35**: 231-244.

Yocum, C. F. (2008). "The calcium and chloride requirements of the O2 evolving complex." *Coord. Chem. Rev.* **252**: 296-305.

Zaharieva, I., P. Chernev, G. Berggren, M. Anderlund, S. Styring, H. Dau and M. Haumann (2016). "Room-Temperature Energy-Sampling Kβ X-ray Emission Spectroscopy of the Mn4Ca Complex of Photosynthesis Reveals Three Manganese-Centered Oxidation Steps and Suggests a Coordination Change Prior to O2 Formation." *Biochemistry* **55**: 4197-4211.

Zaharieva, I., P. Chernev, M. Risch, K. Klingan, M. Kohlhoff, A. Fischer and H. Dau (2012). "Electrosynthesis, functional and structural characterization of a water-oxidizing manganese oxide." *Energy Environ. Sci.* **5**: 7081-7089.

Zaharieva, I., D. Gonzalez-Flores, B. Asfari, C. Pasquini, M. R. Mohammadi, K. Klingan, I. Zizak, S. Loos, P. Chernev and H. Dau (2016). "Water oxidation catalysis - role of redox and structural dynamics in biological photosynthesis and inorganic manganese oxides." *Energy Environ. Sci.* **9**: 2433-2443.

Zaharieva, I., M. M. Najafpour, M. Wiechen, M. Haumann, P. Kurz and H. Dau (2011). "Synthetic manganese-calcium oxides mimic the water-oxidizing complex of photosynthesis functionally and structurally." *Energy Environ. Sci.* **4**: 2400-2408.

Zeng, K. and D. Zhang (2010). "Recent progress in alkaline water electrolysis for hydrogen production and applications." *Prog. Energy Combust. Sci.* **36**: 307-326.

Zhang, C. X., C. H. Chen, H. X. Dong, J. R. Shen, H. Dau and J. Q. Zhao (2015). "A synthetic Mn4Ca-cluster mimicking the oxygen-evolving center of photosynthesis." *Science* **348**: 690-693.

Zhou, F., A. Izgorodin, R. K. Hocking, V. Armel, L. Spiccia and D. R. MacFarlane (2013). "Improvement of catalytic water oxidation on MnO_x films by heat treatment." *ChemSusChem* **6**: 643-651.

Zhou, W.-j., J. Zhang, T. Xue, D.-d. Zhao and H.-l. Li (2008). "Electrodeposition of ordered mesoporous cobalt hydroxide film from lyotropic liquid crystal media for electrochemical capacitors." *J. Mater. Chem.* **18**: 905-910.

Zong, R. and R. P. Thummel (2005). "A New Family of Ru Complexes for Water Oxidation." *J. Am. Chem. Soc.* **127**: 12802 - 12803.

Abstract

The importance of fundamental research in the field of heterogeneous water oxidation is reflected on its impact in solar fuel production. In biological systems, solar energy capture to produce fuels (sugars) involves water oxidation catalyzed by a pentanuclear Mn_4CaO_5 complex which can be seen as a source of inspiration for the development of synthetic catalysts. However, a better understanding of the structure-function relationships is still required in both synthetic and biological catalysts. More detailed mechanistic insights in any of the two type of systems are important to draw parallelisms in the other.

In this thesis, I address this challenge by electrodepositing manganese-calcium oxides to study their properties by combining electrochemistry with UV-visible spectroscopy and X-ray absorption spectroscopy (XAS). The prepared oxides are amorphous with a birnessite type of structure. The developed synthesis protocol involves active site creation by annealing at moderated temperatures. Calcium can be introduced in the structure of the oxide by controlling the concentration in the solution during deposition. XAS studies suggest that reactive motives could involve $Mn_3Ca(\mu\text{-}O)_4$ cubane structures. However, calcium results inessential for water oxidation activity, but tunes the electrocatalytic properties of the manganese oxide. By UV-visible measurements it is observed that the ability to undergo redox transitions and the presence of a minor fraction of Mn^{III} is a prerequisite for catalysis. The redox tuning properties of the calcium might help to stabilize the corresponding active structures. Related to this study, I also investigated the effect of annealing of pre-synthesized manganese-calcium oxides attached to FTO electrodes by XAS. Similarly as in the electrodeposited oxides, it is observed that the annealing results in more defects and active site creation.

Studies in structure-function relationships might be in many cases influenced by structural rearrangement during catalysis. This is especially important in crystalline materials where it is still unclear whether catalysis is always associated with some degree of amorphisation and structural rearrangement of the surface of the crystallites. I addressed those questions by studying the amorphisation of a crystalline cobalt phosphate $Co_3(PO_4)_2.8H_2O$ under electrochemical operation combined with XAS measurements. By electrochemical analysis I observed a high catalytic activity at the surface of the cobalt phosphate catalyst; however, complete amorphisation (in the term of 5 to 8 h) results in bulk catalysis in all the volume of the amorphous oxide formed. In conclusion a good description of the kinetics of restructuring during operation is necessary to have a whole picture of catalysis in crystalline materials.

Finally, the role of the pH is essential for understanding the catalytic mchanism and for practical applications. This question was addressed by a comparative study of cathodically electrodeposited Mn, Fe, Co, Ni and mixed NiFe catalyst at pH 7 and pH 14. By estimating the turnover frequency (TOF) at both pH, I observe a similar increase of about 100 times at alkaline pH and a shift of the redox waves to lower potentials, which suggests a common reason for the increased catalytic activity. These observations are described in more detail by an elaborated investigation of NiFe oxides by UV-visible spectroscopy and in-situ XAS measurements.

Zusammenfassung

Die Relevanz grundlegender Forschung im Bereich der heterogen katalysierten Wasseroxidation besteht in ihrer Bedeutung für die Produktion von Solarbrennstoff. Zur Generation von Zucker wird Wasser in biologischen Systemen mit Hilfe von Sonnenenergie an einem fünfkernigen Mn_4CaO_5-Komplex oxidiert, der ebenso als Inspiration für synthetische Katalysatoren dient. Es ist jedoch sowohl für biologische als auch für synthetische Systeme ein besseres Verständnis der Struktur-Eigenschafts-Korrelationen notwendig. Eine detailliertere Kenntnis des Mechanismus der biologischen oder synthetischen Seite kann dabei ebenso wichtig für Einsichten in den jeweils anderen Bereich sein.

In dieser Arbeit wird dieser Umstand adressiert, indem Mangan-Calcium-Oxide elektrodeponiert und durch Kombination von elektrochemischen Methoden mit UV/Vis- und Röntgenabsorptionsspektroskopie untersucht werden. Die hergestellten Oxide sind amorph und weisen Birnessitstruktur auf. Die entwickelte Synthese beinhaltet die Erzeugung von aktiven Zentren durch Tempern unter milden Bedingungen. Calcium kann durch Steuerung der Konzentration in der Deponierungslösung gezielt in die Struktur eingebracht werden. Es beeinflusst das Redoxverhalten und die katalytischen Eigenschaften des Manganoxides, ist jedoch keine notwendige Voraussetzung, um überhaupt katalytische Aktivität zu erhalten. Durch UV/Vis Messungen beobachten wir, dass die Fähigkeit zu Oxidationszustandsänderungen und eine Mindestkonzentration an Mn^{III}-Ionen essentiell für die Katalyse sind. Dies kann durch die Feinabstimmung der Redoxeigenschaften durch Calcium erklärt werden, da es entsprechende Strukturen stabilisieren könnte. Damit verbunden haben wir die Auswirkungen des Temperns auf vorsynthetisierte Mangan-Calcium-Oxide durch Röntgenabsorptionsmessungen auf FTO-Substraten untersucht. Wie in gleicher Weise für die elektrodeponierten Oxide beobachtet, führt die thermische Behandlung zu einer größeren Zahl an Defekten und zur Bildung aktiver Zentren.

Für Studien zur Struktur-Eigenschafts-Korrelation sind in vielen Fällen strukturelle Umordnungsprozesse während der Katalyse zu berücksichtigen. Dies ist insbesondere für kristalline Materialien wichtig, da immer noch nicht klar ist, ob Katalyse in jedem Fall mit einer Teilamorphisierung und strukturellen Umordnungsprozessen einhergeht. Für ein kristallines Kobaltphosphat ($Co_3(PO_4)_2 \cdot 8\ H_2O$) haben wir diese Fragestellung durch Kombination von Elektrochemie und Röntgenabsorptionsmessungen unter *in situ* Bedingungen adressiert. Elektrochemische Analysen zeigen für das (kristalline) Kobaltphosphat eine hohe katalytische Aktivität an der Oberfläche, wohingegen eine vollständige Amorphisierung zu vollständiger Bulk-Aktivität im gebildeten, amorphen Oxid führt. Daraus folgern wir, dass ein vollständiges Bild der Katalyse an kristallinen Materialien nur bei Kenntnis der Kinetik der Umstrukturierungsprozesse während der Reaktion gezeichnet werden kann.

Der Einfluss des pH-Wertes ist essentiell für das Verständnis der katalytischen Aktivität in der Praxis. Dieser Frage sind wir durch vergleichende Studien an kathodisch abgeschiedenen Mn-, Fe-, Co-, Ni- und NiFe-Katalysatoren bei pH 7 und pH 14 nachgegangen. Eine Abschätzung der Umsatzfrequenz (TOF) zeigt einen Anstieg um den Faktor 100 vom neutralen zum alkalischen und eine Verschiebung der Redoxwellen zu niedrigeren Potentialen, was einen Grund für die erhöhte katalytische Aktivität liefert. Diese Beobachtungen werden im Detail am Beispiel der NiFe-Oxide durch UV/Vis- und *in situ* XAS-Spektroskopie beschrieben.

List of publications

Ivelina Zaharieva, **Diego González-Flores**, Baraa Asfari, Chiara Pasquini, Mohammed Reza Mohammadi, Katharina Klingan, Ivo Zizak, Stefan Loos, Petko Chernev, Holger Dau (2016). "Water oxidation catalysis - role of redox and structural dynamics in biological photosynthesis and inorganic manganese oxides." *Energy Environ. Sci.* **9**: 2433-2443.
DOI:10.1039/C6EE01222A

Diego González-Flores, Ivelina Zaharieva, Jonathan Heidkamp, Petko Chernev, Elías Martínez-Moreno, Chiara Pasquini, Mohammad Reza Mohammadi, Katharina Klingan, Ulrich Gernet, Anna Fischer, Holger Dau (2016). "Electrosynthesis of Biomimetic Manganese–Calcium Oxides for Water Oxidation Catalysis—Atomic Structure and Functionality." *ChemSusChem* **9**: 379-387.
DOI:10.1002/cssc.201501399
[Chapter 3 **Electrodeposited Manganese-Calcium Oxides for Water Oxidation Catalysis: Effect of the Ca content**]

Prashanth W. Menezes, Arindam Indra, **Diego González-Flores**, Nastaran Ranjbar Sahraie, Ivelina Zaharieva, Michael Schwarze, Peter Strasser, Holger Dau, Matthias Driess (2015). "High-Performance Oxygen Redox Catalysis with Multifunctional Cobalt Oxide Nanochains: Morphology-Dependent Activity." *ACS Catalysis* **5**: 2017-2027.
DOI:10.1021/cs501724v

Diego González-Flores, Irene Sánchez, Ivelina Zaharieva, Katharina Klingan, Jonathan Heidkamp, Petko Chernev, Prashanth W. Menezes, Matthias Driess, Holger Dau, Mavis L. Montero (2015). "Heterogeneous water oxidation: surface activity versus amorphization activation in cobalt phosphate catalysts." *Angew Chem Int Ed Engl* **54**: 2472-2476.
DOI:10.1002/ange.201409333
[Chapter 5 **Electrochemical Water Oxidation: Surface Activity versus Amorphization in a Crystalline Cobalt Phosphate**]

Seung Y. Lee, **Diego González-Flores**, Jonas Ohms, Tim Trost, Holger Dau, Ivelina Zaharieva, Philipp Kurz (2014). "Screen-Printed Calcium-Birnessite Electrodes for Water Oxidation at Neutral pH and an "Electrochemical Harriman Series." *ChemSusChem* **7**: 3442-3451.
DOI:10.1002/cssc.201402533
[Chapter 4 XAS **Study in Screen Printed Electrodes from Pre-synthesized Ca-Birnessite**]

Katharina Klingan, Franziska Ringleb, Ivelina Zaharieva, Jonathan Heidkamp, Petko Chernev, **Diego Gonzalez-Flores**, Marcel Risch, Anna Fischer, Holger Dau (2014). "Water oxidation by amorphous cobalt-based oxides: Volume activity and proton transfer to electrolyte bases." *ChemSusChem* **7**: 1301–1310.
DOI:10.1002/cssc.201301019

Selbständigkeitserklärung

Ich erkläre gegenüber der Freien Universität Berlin, dass ich die vorliegende Doktorarbeit selbstständig und ohne Benutzung anderer als der angegebenen Quellen und Hilfsmittel angefertigt habe. Die vorliegende Arbeit ist frei von Plagiaten. Alle Ausführungen, die wörtlich oder inhaltlich aus anderen Schriften entnommen sind, habe ich als solche kenntlich gemacht. Diese Arbeit wurde in gleicher oder ähnlicher Form noch bei keiner anderen Universität als Prüfungsleistung eingereicht und ist auch noch nicht veröffentlicht.

Berlin, den ……

……

Diego González-Flores